

COSMOLOGY USING PHOTOMETRIC SAMPLES OF
TYPE IA SUPERNOVAE: THE FIRST JOINT
PHOTOMETRIC LIGHT CURVE ANALYSIS

by

Brodie Popovic

Department of Physics
Duke University

Date: _____

Approved:

Daniel Scolnic, Supervisor

Michael Troxel

Chris Walter

Phil Barbeau

Thomas Mehen

Dissertation submitted in partial fulfillment of the
requirements for the degree of Doctor of Philosophy
in the Department of Physics
in the Graduate School of
Duke University

2023

ABSTRACT

COSMOLOGY USING PHOTOMETRIC SAMPLES OF
TYPE IA SUPERNOVAE: THE FIRST JOINT
PHOTOMETRIC LIGHT CURVE ANALYSIS

by

Brodie Popovic

Department of Physics
Duke University

Date: _____

Approved:

Daniel Scolnic, Supervisor

Michael Troxel

Chris Walter

Phil Barbeau

Thomas Mehen

An abstract of a dissertation submitted in partial fulfillment of the
requirements for the degree of Doctor of Philosophy
in the Department of Physics
in the Graduate School of
Duke University

2023

Copyright © 2023 by Brodie Popovic
All rights reserved

Abstract

Over the last twenty five years, type Ia supernova (SNIa) have been a crucial cosmological probe, responsible for the discovery of the accelerating expansion of the universe. But with the dawn of the next generation of telescopes and SNIa samples, new methods and techniques are needed to increase precision and provide ever-smaller systematics. The Dark Energy Survey (DES) Supernova program has recently completed taking data, and will be the first program whose success relies on the analysis of a sample in which we do not know the typing of the supernova. These ‘photometric samples’ are a significant switch from spectroscopic samples, in which every SNIa used in the analysis is spectroscopically typed. The motivation for this switch is the opportunity to have ~ 10 times larger samples than what would be feasible with spectroscopic identification; however, these analyses are replete with new and untested sources of systematic uncertainty. One less obvious, but equally significant, challenge is understanding the selection effects of this new survey strategy. This thesis serves to demonstrate the efficacy of modern photometric samples, such as DES, as a model for future analyses. Simultaneously, as our statistical constraints improve, a higher burden is placed on other systematic uncertainties, like a better understanding of the environment that supernovae occur in. Dust attenuates and reddens SNIa light curves, obscuring the true properties and astrophysical origins of the SNIa explosion. Here I combine the results of my four first-author papers in non-chronological order, laying out the steps I took to perform a cosmology analysis from start to finish.

In Figure 1.2, I provide a general overview and outline of the course of this thesis, and how my papers aid in answering these questions. My first question is *how do we*

observe the universe? I go over the surveys and experiments that have been used to peer back billions of years into cosmic history. I also discuss how our imperfect instruments and selection effects all impact our observations, alongside how non-cosmological effects make these observations even more challenging, and how we try to mitigate those issues.

To aid our methods of observing the universe, I ask - *how do we simulate the universe?* These simulations are able to create extremely realistic, catalogue level samples that can be tuned to mirror our data in every measurable metric. This question leads to the first published work in this thesis: *The Pantheon+ Analysis: Forward-Modeling the Dust and Intrinsic Colour Distributions of Type Ia Supernovae, and Quantifying their Impact on Cosmological Inferences*. The specific characteristics and modeling of dust distributions are drawn from the data using a multi-dimensional Markov Chain Monte Carlo method to infer and separate the intrinsic SNIa properties from those caused by external dust effects, informing us as to *how our measurements are biased*.

Given our improved simulations, I ask *how do we fix these biases?* In the next paper, *Improved Treatment of Host-Galaxy Correlations in Cosmological Analyses With Type Ia Supernovae*, I introduce a method to fix these biases using simulations by providing the first phenomenological model of correlating SNIa properties with that of their host galaxy. This framework is used as the basis for a novel set of bias corrections that are able to account for realistic correlations between SNIa properties, as well as separately introducing the first bias corrections methodology to correct dust models of SNIa scatter.

In the process of building up to cosmology measurements, I ask *what biases are*

unique to photometric surveys? In *Assessment of the Systematic Uncertainties in the Cosmological Analysis of the Sloan Digital Sky Survey Supernovae Photometric Sample*, I investigate a collection of potential biases and uncertainties that are unique to photometric samples: assessing the impact of mis-associating the host galaxy, modeling of non-Ia contamination, and changing the modeled efficiency of detecting the host galaxies.

My last paper puts all of these papers and methods together to answer the question: *What cosmological result do we find?* I create the first-ever joint analysis of two photometric SNIa samples, making the largest SNIa analysis to-date. I test for consistency between the samples with the first comparison of statistically-independent SNIa samples, and show that the results of this joint photometric analysis are competitive with the best spectroscopic SNIa analysis.

Contents

Abstract	iv
List of Tables	xii
List of Figures	xiii
1 Introduction	1
1.1 The Universe	1
1.1.1 Beginning of Modern Cosmology	3
1.1.2 Friedmann Equations	5
1.2 Cosmology Measurements	10
1.2.1 Type Ia Supernovae	10
1.2.2 Other Cosmology Probes	13
1.3 Data	15
1.3.1 Spectroscopic vs. Photometric Samples	16
1.3.2 Sloan Digital Sky Survey	17
1.3.3 Pan-STARRS Medium Deep	18
1.3.4 Low Redshift Surveys	19
1.3.5 Compilation	21
2 SNIa Distances and Simulations	23
2.1 Building a Modern Hubble Diagram	23
2.1.1 Initial Standardisation Modes	23
2.1.2 Light-curve Fitting	26
2.1.3 SALT	27

2.1.4	Light Curve Fitting with SALT	30
2.1.5	One SALT, Two SALT, Red SALT, Blue SALT	32
2.1.6	Distances Fitted Light Curves	35
2.1.7	Extensions to the Tripp Equation	36
2.1.8	Standardisation in Practice: The SALT2mu program	37
2.1.9	Building a Systematic Covariance Matrix	39
2.1.10	Bayesian Estimation Applied to Multiple Species	41
2.2	Simulations and Simulacra	45
2.2.1	Source Model	49
2.2.2	Noise Model	55
2.2.3	Trigger Model	57
2.3	Intrinsic Scatter	60
2.3.1	G10	60
2.3.2	C11	61
2.3.3	Dust Models	62
2.4	Intrinsic Populations	63
2.5	Simulating Non-Ia SNe	64
2.5.1	Core Collapse SNe	65
2.5.2	Non Core Collapse Contaminants	66
3	Intrinsic Populations of SNIa	68
3.1	Distance Biases from Correlations	68
3.1.1	Parent Populations	69
3.1.2	Extending Parent Populations	74
3.1.3	Measured Host Correlations	76

4	Dust in the Wind	85
4.1	Dust	86
4.1.1	BS20	88
4.1.2	Determining Dust Model Parameters	93
4.1.3	SALT2mu Fit	97
4.1.4	Dust2Dust Model Fitting	98
4.2	Results	105
4.2.1	Fit of Model Parameters	106
4.2.2	Comparison with Original BS21 Parameters	108
4.2.3	Systematic Uncertainties on Cosmological Parameters	109
5	Correcting Biases in SNIa	114
5.0.1	Improving Bias Corrections for SNIa-Host Correlations	116
5.0.2	Changes to the BBC formalism for BS20	120
5.0.3	Impact on Cosmology with Host Properties	123
5.0.4	Impact on Cosmology Using Bias Corrections for BS20	126
6	Biases in Photometric Samples	129
6.1	Analysis	130
6.1.1	Host Matching	131
6.1.2	Light-curve Fitting	132
6.1.3	Classification	133
6.1.4	BBC and Cosmology Fitting	134
6.2	Simulations	134
6.2.1	Host Galaxy Libraries	136
6.2.2	Core Collapse Simulations	141

6.2.3	SNIax Simulations	142
6.2.4	Simulation Analysis	142
6.3	Results	142
6.3.1	Galaxy Association and Mis-association	143
6.3.2	Impact of Host Galaxy Selection Efficiency	144
6.3.3	Impact of Core Collapse Templates	144
6.3.4	Data and Simulation Comparison	148
7	Amalgame	149
7.1	Introduction	149
7.2	Updates to Dust2Dust	150
7.3	Updates to σ_{int}	153
7.4	Sims and Data	154
7.5	Systematic Uncertainty Sources	154
7.5.1	Host-Galaxy Properties	157
7.5.2	Calibration	158
7.5.3	SALT3 Model	159
7.5.4	Survey Modeling	159
7.5.5	Intrinsic Scatter Models	160
7.5.6	Core Collapse Models	162
7.5.7	Redshift Evolution of Nuisance Parameters	163
7.5.8	Fixed Nuisance Parameters	164
7.5.9	Validation	164
7.5.10	Other	165
7.6	Results	166

7.6.1	Nominal Cosmological Results	166
7.6.2	Subsample Cosmological Results	166
7.6.3	Systematic Uncertainties	175
7.7	Discussion	182
7.7.1	SDSS Consistency	182
7.7.2	Cosmological Parameters	182
7.7.3	Comparison of Binned and Unbinned Results	183
8	Conclusions and Future Work	184
8.1	How do we observe the universe?	184
8.2	How do we simulate the universe?	185
8.3	How are our measurements biased?	186
8.4	How do we fix these biases?	188
8.5	What biases inhere in photometric surveys?	189
8.6	Cosmology	190
	References	191

List of Tables

1.1	A review of the fundamental differences between spectroscopic and photometric survey types for SNIa.	17
4.1	Fitted Parameters in BS20 Model	93
4.2	χ^2 Terms in Dust2Dust Population Fit	103
4.3	Ranges for Each Model Parameter	105
4.4	Results from Dust2Dust and Comparison With Original Model Parameters	105
4.5	Breakdown of different χ^2 criteria for the G10, C11, BS21-Original, and Dust2Dust scatter models.	106
4.6	Cosmology constraints with systematics with Ω_M prior	111
5.1	Fitted values and uncertainties ¹ averaged over 100 simulations	125
6.1	Sequential selection requirements on the SDSS transient sample.	133
6.2	w Differences for Systematic Tests	144
7.1	Number of SNe that pass SALT3 fitting before and after cosmology cuts.	150
7.2	P22 Model Parameters and Criteria Fit for this paper.	154
7.3	Comparison of BBC output between data and simulations.	167
7.4	Sources of Uncertainty	181

List of Figures

1.1	The velocity-distance relationship as measured by Hubble (1929) from a sample of 24 galaxies. Note the units of velocity.	3
1.2	Overview of information presented in this thesis.	4
1.3	Example Hubble Diagram showing magnitude vs. redshift for type Ia supernovae.	9
1.4	Non-exhaustive timeline of spectroscopic and photometric surveys. . .	15
2.1	Example light curves from PS1 at different redshifts.	25
2.2	The Spectral Energy Distribution of SN1998qu.	28
2.3	Filter response curves for SDSS.	29
2.5	An overview of the SALT fitting process.	33
2.6	Plot of the Hubble residuals vs. host galaxy stellar mass, the first evidence of the mass step.	36
2.7	Hubble diagram with non-Ia contamination.	42
2.8	Collection of supernovae light curves taken from literature.	44
2.9	An overview of the SNANA simulation process. Adapted from Kessler et al. (2019).	48
2.10	Example of the internal GENPDF file for SNANA.	51
2.11	Example of the HOSTLIB header for SNANA.	52
2.12	Spectroscopic efficiencies for SDSS and PS1 as a function of the redshift and r -band magnitude.	59
2.13	An example of measurement noise and selection effects biasing an observed colour distribution.	64

3.1	Visualisation of the Migration Matrix for the x_1 parameter.	72
3.2	Distributions of c and x_1 as a function of host galaxy mass.	75
3.3	The redshift evolution of c , x_1 , and host galaxy mass.	77
3.4	The x_1 distribution for Foundation and Low-z.	78
3.5	Intrinsic populations for c and x_1 as a function of host galaxy mass. . .	81
3.6	The G10 c parent populations as a function of host galaxy mass.	82
3.7	The G10 x_1 parent populations as a function of host galaxy mass.	83
4.1	Hubble scatter and Hubble residuals as a function of colour.	89
4.2	The observed colour distribution, Hubble scatter, and Hubble residuals as an example of the effects of dust.	91
4.3	Binned Hubble Residuals as a function of c , split on host galaxy mass.	94
4.4	Metric criteria for the Dust2Dust program: observed colour, Hubble residuals, and Hubble scatter.	95
4.5	Pictograph of the Dust2Dust process.	99
4.6	Example of the Dust2Dust reweighting process.	104
4.7	Triangle plot of posteriors from Dust2Dust	112
4.8	Metric criteria for Dust2Dust and results of the G10 scatter model.	113
4.9	Metric criteria for Dust2Dust and results of the C11 scatter model.	113
5.1	Bias Corrections for Tripp components as a function of redshift, split on c and x_1 values.	115
5.2	Diagram of fitting options for γ with BBC5D.	117
5.3	The δ_{x_1} component of BBC5D bias corrections as a function of the log host galaxy stellar mass.	118

5.4	Bias corrections vs. redshift for values of θ	121
5.5	The binned μ residuals for the G10 scatter model using three different BBC methods on the same set of simulations.	127
5.6	The Hubble scatter and BBC-fitted distance modulus uncertainties.	128
6.1	Comparison of data and fiducial simulations for observed parameters.	135
6.2	Distribution of angular separation, DLR, and d_{DLR} for simulations and data.	135
6.3	Measured r -band magnitude host galaxy efficiency for SDSS.	137
6.4	Summary of effect of systematics on binned distance modulus residuals.	139
6.5	Summary of mis-associated host galaxy information.	145
6.6	The Hubble residual distribution for data and simulations using different Core Collapse models.	146
7.1	The relationship between the colour of SNIa and the scatter in the Hubble Residuals, split on mass.	152
7.2	Metrics for goodness-of-fit for SDSS.	155
7.3	Metrics for goodness-of-fit for PS1.	156
7.4	A comparison of Hubble Residuals for SDSS and PS1 to illustrate the effects of non-Ia Contamination.	158
7.5	Comparison of the host galaxy redshift efficiencies for SDSS and PS1.	161
7.6	The Hubble Diagram and Hubble Residuals for the Amalgame sample.	165
7.7	Hubble Residuals for the Amalgame sample as a function of c and x_1	167
7.8	Comparison of blinded w and Ω_M values for the subsamples of Amalgame with the full sample.	168
7.9	The blinded w/Ω_{matter} contour for the Amalgame sample.	169

7.10	The w error budget for the Amalgame sample and subsamples.	171
7.11	Binned difference in Hubble Residuals between the fiducial Amalgame sample and the subsamples.	173
7.12	The Hubble Residuals for each subsample in Amalgame.	174
7.13	The blinded w/Ω_{matter} contour with only SN measurements.	176
7.14	The blinded w/Ω_{matter} contour for the Amalgame sample with Planck prior.	177
7.15	Model of the SDSS SNIa detection efficiency.	178
7.16	Changes in measured w for the Amalgame sample for various systematics.	180

Acknowledgements

First and foremost, to Dan - what do you say to someone that has so thoroughly and completely changed the arc of your life? What can be said? You've taught me science, but so much more than that. You've given me humour, patience, humility, and community. Even through my senior-in-high-school phase you've stuck next to me, and everything in this thesis is because of you. I know it's been a learning experience for both of us, but I can't imagine going through graduate school with anyone else as my supervisor. Thank you ever so for this and all the other opportunities, and I hope that your future students are better behaved than me.

To everyone else in the Supernova group: Bruno - The Big B himself. It's been such a journey from meeting you our first summer to saying au revoir. I've enjoyed and now missed seeing you realise the argument is going nowhere, and also refusing to back down. Despite your grouchiness, I appreciate and love your boundless optimism that you try to hide, and your special insights into the world.

Erik - When we first met, I was suspicious, because I had a hard time believing that anyone could be so charismatic and easygoing and not be up to something. I have never been more happy to be proven wrong. Never lose that ability of yours to make total strangers feel like you've been a lifelong friend.

Rebecca - Rebecca C'Gramercy Chen. Seeing you on campus for the first time, I was struck by the thought that this was a cool looking person with good hair. I was right, just in a way I didn't realise at the time. I think you're the secret sauce that holds this group together. Froggie Smalls sits on my bedside table much the same way you sit in my heart - a constant source of help, support, and silly inspiration. I hope that you manage to see the talent and ability that you have that the rest of us can see so clearly.

Kevin - I know we never really got much to talking. But still, it doesn't feel the

same without a classic Kevin interjection at group meetings or dinners. I hope you're doing well and figure out what you need to.

Ben - After adopting Maria and Kevin as your grad student children, you'll finally have the opportunity to build your own group at Baylor. I hope that you never get a demon child like myself, but even if you do, you've done a wonderful job of handling me and I know you'll look out for them.

Maria A. - You started your grad school career as baby, but it has been a joy and an honour to watch you grow up and take on all these responsibilities while you've been here, even at your great displeasure. You're in charge now, and I know you'll do great.

Maria V. - I am so sorry for taking your name. At the same time, I have never been more proud of a nickname sticking so well. I promise that wherever you end up next, you'll be the first and foremost Maria there.

Ava - I hope that one day you achieve your impossible dream of getting people to think that American artist Bruce Springsteen is, inexplicably, Italian.

Cosmology at large - I hope group meetings will go smoother now that I'm gone, but I leave happy knowing that this group is doing so well and is set up to keep succeeding.

To my cohort - Baran, Alexey, Adryanna, Jay, Drew, James, Nathan, Qiang and Wenkai; thank you for all the adventures, the late nights stressing over homework, the beer brewing and pirate captaining, the bizarre drawings and strange shrines. The cohort really is a community.

To Utsav and Masa, who have variously been subject to and instigators of shenanigans, thank you for all the adventures at 1406 and beyond. It won't be the same without waking up in the morning to find Masa meticulously making his coffee, or

going to bed at night soothed by the sweet sounds of Utsav shouting ‘No shot bro, no shot’ as he inevitably gets merked by some 12 year old on Apex or whatever the game is at that time. I’ll miss you.

To Shane, keep being a grouchy but delightful misanthrope while I’m gone, and never stop asking people at bars what they think about post cards.

To Phil (who still owes me a beer), Mat, Mark, and Marcus, and everyone else in DES - thanks for being a loveable bunch of goofballs, and I’ll be seeing more of y’all soon.

To Georgie - not everyone finishes the marathon. But that doesn’t make starting one any less meaningful. Thanks for running with me.

To Courtney, Taylor, Eli, John, Stephen, and Cole; thank you for being some of the best friends and siblings (not exclusive to Cole, first of equals on that list) a person could ask for. From the best of times - the DC trip, yee-ing and haw-ing through Seattle, suffering through Riverdale with Courtney, late night talks at weird bars with Cole - to the worst of times - post break ups, the Taylor dark age, the lockdowns - y’all have been with me through thick and thin. Some of you I’ve known since I was a child, others it just feels like that. I love you all.

And last, but absolutely not least, my parents. As I write this you’re travelling to Lisbon on yet another adventure. For all my life you’ve been the world travellers, the parents that have given sometimes helpful, sometimes obvious advice. I know it’s hard to believe that I’m leaving the country, that I’m finally graduating and leaving school for the first time in my life; it’s hard for me to believe too. But I think I’ll be ok. After all, I’ve had the best teachers in the world. And as I’ve gone through school, undergraduate, and now grad school, one of the most important things I’ve learned is how lucky I’ve been to have you as parents; how kind and supportive and helpful you’ve been my entire life. I don’t know how to express how much you’ve

done for me and how much it's meant; I don't think a thesis acknowledgement can ever be enough. But this is for you. Thank you for everything, mom and dad.

Chapter 1

Introduction

1.1 The Universe

Leopold von Ranke is often considered the father of source-based history. His driving principle was to report history ‘as it happened’, drawing events from available sources to tell the story of a given event. It is entirely excusable that he was victim to the shortcomings pointed out by modern day critics such as E.H. Carr, that the historian is, as it were, not immune from history - they choose which events to include, which to discard, and what story they wish to tell. History is not simply best understood as a narrative, it *is* a narrative.

Cosmology a scientific history of the universe. Today we have answered a great number of questions about the universe - it came to be from the rapid expansion of everything, everywhere, a process known as the Big Bang. Proof of this hid literally outside of our sight, in the cosmic microwave background radiation, the static in a dead channel. Clusters of galaxies, which did not contain enough visible matter to justify their existence, coursed with ‘dark matter’, something matter-like that seemingly does not interact with the electromagnetic spectrum. Our best description of the universe rests on an exact solution to Einstein’s field equations of general relativity: the Friedmann-Lemaître-Robertson-Walker (FLRW) metric, which describes a changing, isotropic, and homogeneous universe. With the FLRW metric and cosmological measurements, we have constructed the Lambda Cold Dark Matter (Λ CDM) model as today’s standard model of cosmology. Λ CDM posits a universe with a cosmological constant, or some form of dark energy equivalent to it — the eponymous

Λ — which drives the accelerating expansion of the universe.

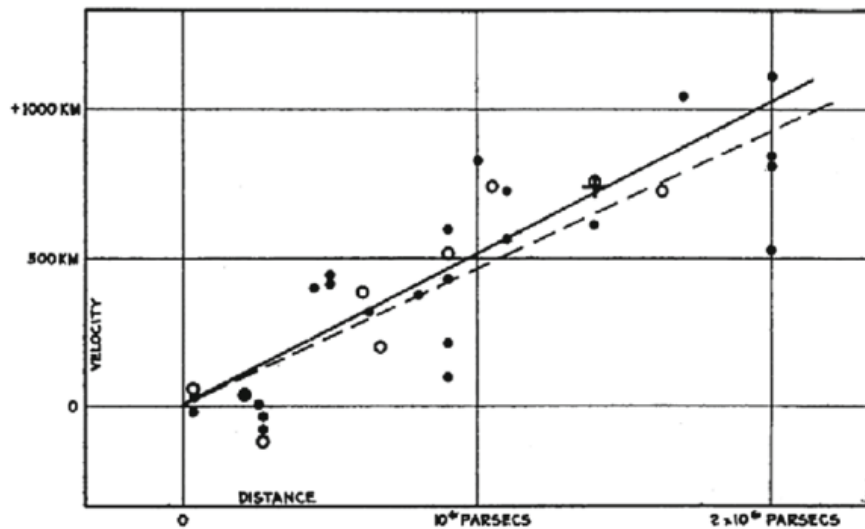
Alongside dark energy, Λ CDM presents a universe with a matter component that is primarily dark matter; that is, matter that does not interact strongly with the electromagnetic spectrum. Further, this dark matter in Λ CDM is non-relativistic and non-interacting. Λ CDM is able to describe the whole of existence in only 6 parameters - three densities for matter, dark matter, and dark energy; and a spectral scalar index, the amplitude of curvature fluctuations, and the optical depth of reionisation.

But there are still parts of our history that we do not understand. Today, we know that dark matter exists, but are in many ways not any closer to understanding what it is than when it was first discovered. Dark energy comprises 68% of the modern universe, driving the accelerating expansion of the universe, but we know precious little about it still. One thing that we do know is that our measurements of dark energy from cosmology are in conflict with the values predicted arising from quantum mechanics: anywhere from 60 to 120 orders of magnitude off (Martin (2012)).

Like any historians, we have primary sources. This thesis is concerned with the use of supernovae to map the history of the universe, specifically to improve the accuracy of these ‘standard candles’. These improvements come in many forms: better standardisation, incorporating real physics into our standardisation, improved bias corrections, and identifying sources of errors that may arise when we find new ways to use these tools. The amalgamation of this thesis, and the work of my graduate school career, is to put together the largest sample of supernovae in history, and attempt to measure cosmology with it.

1.1.1 Beginning of Modern Cosmology

We shall choose 1929 as a somewhat-arbitrary starting point for this thesis, with Edwin Hubble's paper "*A relation between distance and radial velocity among extra-galactic nebulae*" Hubble (1929). Figure 1.1 shows that the recession velocity of 'nebulae' (later renamed to galaxy) increases with distance from the earth. This discovery provided definitive proof that the universe was changing, with galaxies receding from the earth. These velocities were measured using spectroscopic observations from Slipher (1917); Humason (1931); Hubble & Humason (1931) and distances from the still quite-new Cepheid period-luminosity relationship discovered by Leavitt & Pickering (1912).



Velocity-Distance Relation among Extra-Galactic Nebulae.

Figure 1.1: The velocity-distance relationship as measured by Hubble (1929) from a sample of 24 galaxies. Note the units of velocity.

<p>The Universe</p>	<p>Chapter 1: Cosmology and the Universe</p>	<p>An overview of the universe, Cosmology background, and the data we use</p>
<p>How do we observe the universe?</p>	<p>Chapter 2: Fitting SNIa Light Curves</p>	<p>How we get our measurements of SNIa light curves, including dust effects and light curve fitting overview</p>
<p>How do we simulate the universe?</p>	<p>Chapter 4: Simulating Dust Effects</p>	<p>The SuperNova ANALYSIS simulation package, and how we use it to infer dust and intrinsic SNIa properties from SNIa light curves</p>
<p>How are our measurements biased?</p>	<p>Chapter 3: Parent Populations</p>	<p>Our data is biased by selection effects, non-continuous cadence, measurement noise, and dust.</p>
<p>How do we fix these biases?</p>	<p>Chapter 5: BEAMS with Bias Corrections</p>	<p>We use simulations to provide a statistical correction to our data</p>
<p>What biases are unique to photometric surveys?</p>	<p>Chapter 6: Host Galaxy Spectroscopy</p>	<p>SNIa surveys without spectroscopic measurements of the SNe face a host of problems such as acquiring the redshift, associating the right host galaxy, and mitigating non-Ia contamination</p>
<p>Cosmology</p>	<p>Chapter 7: The Amalgam Cosmology Results</p>	<p>We put all the previous chapters together to perform a measurement of cosmological parameters using SNIa</p>

Figure 1.2: An overview of the information presented in this thesis. The ultimate aim is to provide a measurement of cosmological parameters using SNIa. To do so, we must understand the universe and how to measure it, alongside modeling and correcting biases using simulations.

1.1.2 Friedmann Equations

The best understanding of the universe, after Edwin Hubble's discovery, was of a homogeneous, isotropic, expanding universe that is path connected. These assumptions allow for a solution to Einstein's field equations of general relativity under the assumption that the universe is well-described by a perfect fluid: the Friedmann-Lemaître-Robertson-Walker (FLRW) metric.

The FLRW metric, which at its most generic takes the following form,

$$-c^2 d\tau^2 = -c^2 dt^2 + a(t)^2 d\Sigma^2 \quad (1.1)$$

where $d\Sigma^2$ represents a three-dimensional space of uniform curvature, and $a(t)$ is a time-dependent 'scale factor', can be inserted into the field equations to derive two equations that describe the change of the universe with time, dubbed the Friedmann equations:

$$\frac{\dot{a}^2 + kc^2}{a^2} = \frac{8\pi G\rho}{3} \quad (1.2)$$

and

$$\frac{\ddot{a}}{a} = -\frac{4\pi G}{3}\left(\rho + \frac{3p}{c^2}\right) \quad (1.3)$$

where p and ρ are the pressure and energy density in the universe, G is Newton's gravitational constant, k is the curvature of the universe, and $a \equiv (1+z)^{-1}$.

It is expedient to rewrite Equation 1.2 in terms of energy densities:

$$\frac{\dot{a}^2}{a^2} = H(a)^2 = H_0^2(\Omega_M a^{-3} + \Omega_r a^{-4} + \Omega_\Lambda a^{-3(1+w)}) \quad (1.4)$$

where H_0 is the current expansion rate of the universe (e.g the Hubble Constant) equivalent to $\frac{\dot{a}}{a}$ when $a = 1$, Ω_M is the matter energy density today, Ω_r is the radiation energy density today, Ω_Λ is the energy density associated with ‘dark energy’, and w is the dark energy equation-of-state parameter. Here we are rewriting the expansion of the universe as a function of time, $H(a)^2$, as a function of the current properties ($H_0, \Omega_M/\Omega_r/\Omega_\Lambda$). I have introduced dark energy rather suddenly, in concordance with its mysterious nature. We shall delve into some explanation of what its effect is later, but for now we need the tools necessary to describe it effectively. We have assumed a flat universe, $k = 0$, because by most accounts the universe is *consistent* with being flat, and it makes defining the critical density Ω_c simpler:

$$\Omega_c = \frac{\rho}{\rho_c} = \frac{8\pi G\rho}{3H_0^2} \quad (1.5)$$

with $\rho_c \sim 10^{-29} \text{g cm}^{-3}$, the density in a matter-only universe that would cause it to stop expanding.

We have elided an important definition in our rush to get to the dark energy equation-of-state w ; that is, the relationship between energy density and pressure follows that of a perfect fluid with $w = p/\rho$. This perfect-fluid behaviour, as a function of the scale factor a , is described as

$$\rho(a) \propto \exp\left(3 \int_a^1 \frac{1 + w(a')}{a'} da'\right) \quad (1.6)$$

where w is the dark energy equation-of-state parameter. If we assume that w is constant in time, e.g not a function of a , then Equation 1.6 simplifies to

$$\rho(a) \propto a^{-3(1+w)} \quad (1.7)$$

This $\rho(a)$ relationship holds for not just dark energy, but all energy components of the universe. We have already solved for the matter and radiation equations-of-state in Equation 1.4, for as we shall see, the equations-of-state for matter and radiation are well-understood. This leaves w as the de-facto ‘dark energy equation-of-state’ parameter. The equation-of-state for matter is $w_M = 0$, such that $\rho_M \propto a^{-3}$. This is fairly intuitive, as one might expect the density of a constant amount of matter in an expanding volume to shrink proportionally to the volume. The radiation equation-of-state is $w_r = 1/3$, such that $\rho_r \propto a^{-4}$. This is a bit less intuitive, but if one considers light bouncing back and forth between the boundaries of a box, then we should expect an energy density decrease proportional to the volume \times the $1/\lambda$ decrease in the wavelength of the light due to the expanding volume.

So we have seen that Equation 1.4 contains two familiar and well defined terms, Ω_r and Ω_M , and one stranger one that does not have an earthly equivalent, dark energy: Ω_Λ . This naturally leads to the question: what is dark energy?

The nature of dark energy is not well understood. It is, by definition, a proposal for the observed expansion of the universe; from this, we can make a reasonable estimate that dark energy has a negative w . If $w = -1$, then Ω_Λ has no z -dependence and is a cosmological constant, that of Einstein fame. A cosmological constant represents something with pressure exactly equal and opposite that of its energy density. However, a cosmological constant is not the only solution consistent with the available data: w could also be a constant other than -1 : so long as $w < 0$, the universe is expanding, even if it is decelerating. w could change with redshift as often parametrised as $w(z) = w_0 + w_a(1 - a)$. Unfortunately, detecting w_a with the systematic uncertainties of today is not possible, but the next generation of telescopes should provide the data to constrain w_a . Below, I provide a summary of the most commonly accepted cosmologies that we will be probing. The ‘CDM’ below refers to

‘Cold Dark Matter’, dark matter which is non-relativistic and only weakly interacting with electromagnetic radiation and ordinary matter.

- Flat Λ CDM: A flat universe with non-relativistic dark matter, relativistic radiation, and a cosmological constant $w = -1$.
- Flat w CDM: A flat universe with non-relativistic dark matter, relativistic radiation, and constant w .
- Flat w_0w_a CDM: A flat universe with non-relativistic dark matter, relativistic radiation, and redshift-varying $w(z) = w_0 + w_a(1 - a)$.

We *do* know that $\sim 70\%$ of the energy density of the universe is dark energy, but to explain how we know this, we need to understand how to measure distances in a given cosmology.

In a spacetime that is expanding, defining ‘distance’ is not trivial. It helps to start with the ‘comoving’ distance; that is, the distance of an object that is also moving with the expansion of the universe. For that object at redshift z , the comoving distance is this,

$$D(z) = \int_0^z \left(\frac{c}{H(z')} dz' \right) = \frac{c}{H_0} \int_0^z \frac{dz'}{\sqrt{\Omega_M(1+z')^3 + \Omega_r(1+z')^4 + \Omega_\Lambda(1+z')^{3(1+w)}}} \quad (1.8)$$

where $H(z)$ is defined as in Equation 1.4, and we have begun to write in terms of z rather than a .

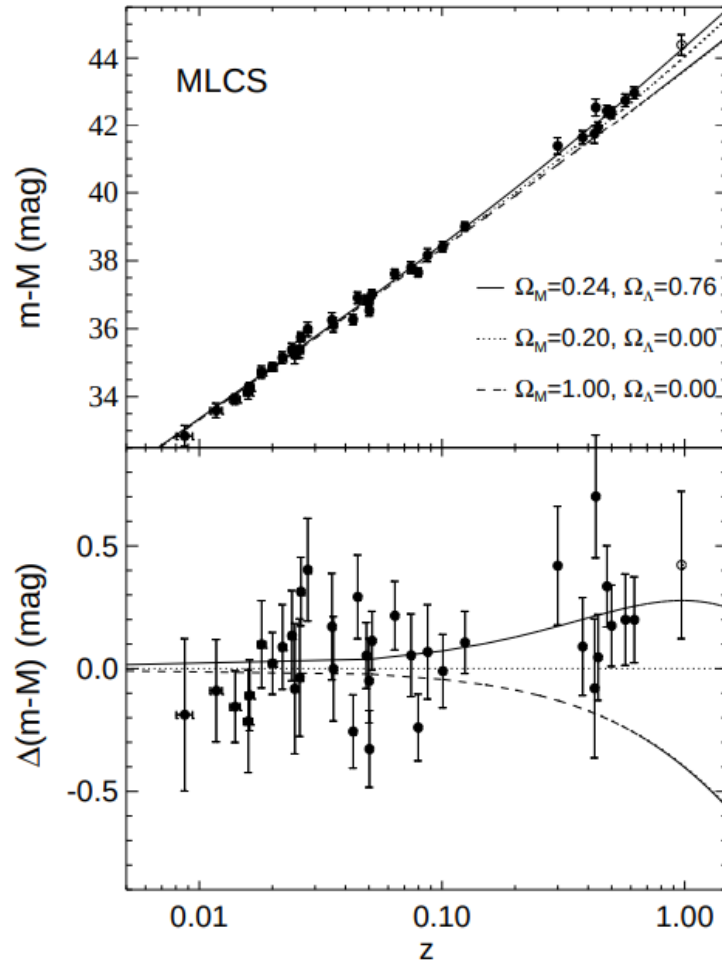


Figure 1.3: An example Hubble Diagram showing magnitude vs redshift for type Ia supernova. The top panel shows the magnitude-redshift relationship with different cosmologies. The bottom panel shows the ‘Hubble Residuals’, the difference between individual SNIa distances and the chosen fitted cosmology. The bottom panel shows clearer proof that the data favours a cosmology with $\Omega_\Lambda = 0.76$. From Riess et al. (1998). © AAS. Reproduced with permission

1.2 Cosmology Measurements

1.2.1 Type Ia Supernovae

And so we reach our standard candles: astronomical objects with a known, consistent absolute magnitude. Type Ia supernovae, and their position as standard candles, directly led to the discovery of the accelerating expansion of the universe in Riess et al. (1998) and Perlmutter et al. (1999).

A standard candle, with a given intrinsic luminosity L and flux f , allows us to measure the luminosity distance D_L of this candle as follows:

$$D_L = \sqrt{\frac{L}{4\pi f}}. \quad (1.9)$$

To capture the comoving distance, d_L is written as

$$D_L = (1 + z) \times D(z) \quad (1.10)$$

where $D(z)$ is expressed as Equation 1.8.

In the case of a type Ia supernova (SNIa), the cosmological luminosity distance D_L and a measurable distance can be linked together. This measurable distance is the difference between the absolute magnitude (how bright the object is at 10 parsecs) M of an SNIa and its apparent magnitude (how bright an object appears to be) m :

$$M - m = -5 \log_{10} \frac{D_L}{10\text{pc}} \quad (1.11)$$

where D_L here is measured in parsecs. This definition comes from, in part, the

conversion of flux to magnitudes,

$$F = 10^{0.4(m)} \tag{1.12}$$

where F is the flux of an object and m is the magnitude.

Thus, we are able to observe distances from a collection of standard candles out in the universe. We need not actually know the intrinsic luminosity L nor the absolute magnitude M : to compare distances we only need to ensure that the intrinsic luminosity of these standard candles is the same. This gives us a set of *relative* distance measurements, from which we can measure the universe, as shown in Figure 1.3.

What SNIa lack in absolute distance measurements, they make up for in other ways. SNIa are:

- Bright. At -19 magnitudes in rest-frame, it is ~ 6 orders of magnitude brighter than the full moon, and 20 orders of magnitude brighter than Vega.
- Common. While 1 SNIa per galaxy per 100 years (Perrett et al. (2012)) does not sound frequent, there are a great number of galaxies, and the universe is ~ 14 billion years old.
- Long lasting. An SNIa lasts about 1 month; for a transient object this is plenty of time to observe with a telescope.
- Standard. The scatter in distances with SNIa is as low as ~ 0.15 magnitudes, enough to detect the accelerating expansion of the universe.

SNIa are the thermonuclear explosion of a white dwarf star. A white dwarf is the remains of a main-sequence star with a solar mass less than 8 times that of our own

sun. In this scenario, the star will fuse elements until it reaches carbon and oxygen. At this point, the future white dwarf is not heavy enough to fuse carbon, nor dense enough to implode when it runs out of fuel. Instead, the carbon-oxygen core is stable due to electron degeneracy pressure, that is, the Pauli exclusion principle forcing an exertion of pressure against further compression. With time, the outer layers of the star drift away, leaving only the stable carbon-oxygen core, the white dwarf star. A type Ia supernova occurs when the white dwarf accretes matter from its binary star system partner, and exceeds the maximum stable mass provided by electron degeneracy pressure, 1.44 solar masses.

SNIa are a specific subtype of supernovae, phenomenologically defined as lacking hydrogen and having a strong silicon signal in their spectra. What this actually means is that SNIa are not core-collapse supernovae, which are SNe caused by stars whose core collapses in upon itself when it has burned out its fuel. We shall not discuss core collapse SNe, except to say that they can be easily distinguished from Ia by their spectra and that *only* type Ia are precise enough to be used as standard candles. There is too much variance in the potential progenitor masses of other SNe, and not presently enough knowledge to extract from their light curves to reduce this variance, for them to be effective standard candles.

The question of what the white dwarf accretes from is an ongoing area of research. Very little is left over from the thermonuclear explosion, which so far has been too far away to see beforehand. The progenitor question, ‘what goes into the white dwarf to trigger the explosion’, is an ongoing one. Certainly we can say that a white dwarf requires some form of binary star system, and that the impact of progenitors on their status of standard candle is still a subdominant systematic. We do know that there is likely more than one progenitor channel from the sheer diversity of progenitor ages and masses; see Sullivan et al. (2006). Suffice to say, we may not know what causes

the explosion, but the white dwarf explodes.

We also still do not understand how the white dwarf explodes. The post-explosion stage is very well understood: the peak brightness of the SNIa light curve is driven by the radioactive decay of ^{56}Ni , into ^{56}Co , and then ^{56}Fe . It is the ^{56}Co decay that drives the light curve decay and is responsible for SNIa taking course over the timespan of a month rather than days.

The actual explosion is likely more complicated than a single mechanism being solely responsible for all SNIa explosions. A conflagration, that is to say sub-sonic explosion velocities, would not generate bright enough SNIa, but the supersonic velocities of a detonation would cause significantly brighter SNIa than we observe.

1.2.2 Other Cosmology Probes

While SNIa are near-unparalleled in their ability to measure cosmic distances, their use is susceptible to a degeneracy between the value of w and the energy density of matter Ω_M . Hence, their true constraining power is only seen when combined with other probes that break the Ω_M/w degeneracy. We shall briefly review two other geometric cosmology probes here, and leave discussion of probes of structure growth for another thesis.

Cosmic Microwave Background

The Cosmic Microwave Background radiation (CMB) is electromagnetic radiation from shortly after the Big Bang, and constitutes the first strong evidence of the big bang 14 billion years ago. First discovered in 1965 by Arno Penzias and Robert Wilson, it is very nearly a perfect blackbody at 2.7 Kelvin, and is strong proof of a Big Bang. It was not till Smoot et al. (1990) and the first space telescope launched

to measure the CMB that it was discovered that the CMB is not a perfect blackbody. Instead, the discovery of anisotropies in the CMB power spectrum offered something else: a strong constraint on the early-time universe. These anisotropies, caused by non-uniformity in the early universe, preserve a snapshot of the universe near $z \sim 1100$.

The CMB therefore makes a good complement to distance measurements with SNIa. The CMB is from a high redshift, sensitive to the curvature of the universe and matter. SNIa distance measurements probe low redshifts, sensitive to the expansion of the universe (a recent phenomenon) and matter. Together, they provide a strong constraint on the dark energy equation-of-state w and the total matter density at the present, Ω_M .

Baryon Acoustic Oscillations

In the aftermath of the Big Bang, the universe was an incredibly hot and energetic plasma of baryonic and lepton matter. Gravity and radiation pressure exacerbated early inhomogeneities, causing acoustic oscillations to reverberate through the plasma. When the plasma cooled enough to allow the formation of neutral hydrogen, the era known as recombination, these oscillations were crystallised into what would become the matter distribution of the universe. This presents cosmologists with a ‘standard ruler’. Because CMB very accurately measures the early universe, the distance that these baryonic acoustic oscillations could have traveled before recombination, the sound horizon at the time of recombination is very well constrained. This provides an accurate ruler for distances imprinted on the CMB. The universe has expanded since then, and BAO set the seed for the current matter distribution of the universe. By comparing the clustering of galaxies in the modern day with the CMB inhomogeneities, one can see how much the standard ruler has changed,

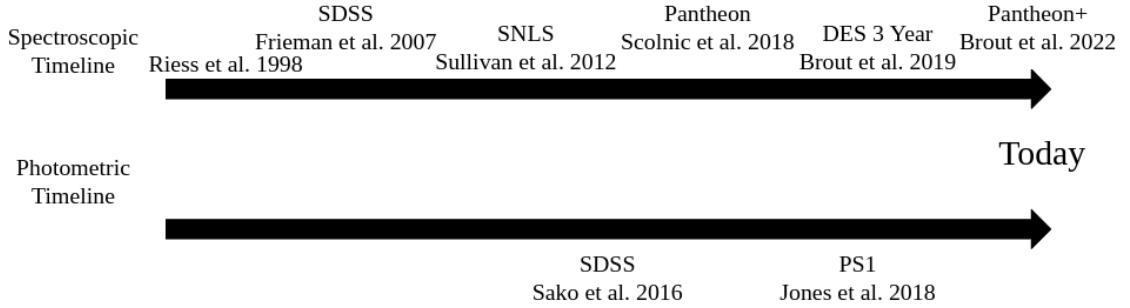


Figure 1.4: A non-exhaustive list of the timeline of spectroscopic and photometric supernova surveys. The Vera Rubin and Nancy Grace Roman supernova surveys, launching in the mid to late 2020s, will be photometric and observe orders of magnitude more supernovae than the combined spectroscopic surveys.

giving access to distance measurements entirely independent of SNe. Of note, BAO give *angular distance* measurements rather than luminosity measurements; that is, we derive distances not from the brightness of an object but their angular separation in the sky. These distances, using clusters of galaxies (see Bautista et al. (2021)) or quasars (see du Mas des Bourboux et al. (2020)), can be measured to an uncertainty of less than 3%.

1.3 Data

Here we give a brief overview of the data used in the analyses presented in this thesis. We focus primarily on the Sloan Digital Sky Survey (SDSS), the Pan-STARRS Medium Deep survey (PS1), two distinct low redshift surveys, Low-z and Foundation, and a combination of surveys named Pantheon+. We also briefly review the difference between spectroscopic surveys and photometric ones.

1.3.1 Spectroscopic vs. Photometric Samples

The past 2 decades of SNIa cosmology have been dominated by spectroscopic surveys, shown in Figure 1.4. The discovery of dark energy was made with spectroscopic surveys, and this spectroscopic trend has only recently begun to slow down. The next generation of telescopes, namely Vera Rubin and Nancy Grace Roman, are planned to run primarily-photometric surveys. Here we provide a brief review of the differences between spectroscopic and photometric surveys.

In both cases, data is collected with broadband photometry and some amount of spectra is required for determining redshift. In the case of spectroscopic surveys, the SNIa spectrum is measured. This has two distinct benefits. The first is that the typing of the SN is known. The most reliable way to distinguish the standardised SNIa light curves from non-standard core collapse light curves is through the silicon absorption lines in the spectrum, so spectroscopic surveys have the guarantee that there is no non-Ia contamination. The second benefit is the redshift. While host galaxy redshifts are more precise, and therefore used over the SNIa-measured redshift, having the SNIa redshift ensures that there is no mis-association of the host galaxy, which would potentially provide an incorrect redshift and therefore bias the measurement.

However, spectroscopic surveys also come with downsides. The biggest drawback is sample size. Live spectroscopy of a transient event is time-limited, and spectrographs are expensive and limited in their field of view. Approximately 10% of observed SNIa have spectroscopic followup - this significantly constrains the sample size. Furthermore, the question of *how* those SNIa are selected can cause issues. Because spectroscopic time is limited, the SNe most likely to be type Ia are selected. These are inherently brighter SNe, causing a selection effect that must be accounted for. But this accounting can be difficult at the best of times, as it necessitates ap-

Table 1.1: A review of the fundamental differences between spectroscopic and photometric survey types for SNIa.

Sample Type	Spectroscopic	Photometric
% Of Sample	$\sim 10\%$	$\sim 100\%$
Is the SN a Ia?	Identified With Spectrum	Estimated From Light Curve
Host Galaxy	Confirmed	Small Uncertainty

proximating human decision making with a function.

Photometric samples, on the other hand, have no spectroscopic followup for the supernova. Instead, only the host galaxy redshift is acquired, a significantly easier and less time-constrained process. Photometric samples alleviate the tight statistical constraints, but now some element of typing the SNe and matching the host galaxy is needed. The specific details of classifying the SNe and matching the host galaxy are given later in this thesis. The differences between the approaches are given in Table 1.1 as an overview.

It is important to note that the sample percentages given in Table 1.1 are for the surveys of today: next generation telescopes are likely to acquire far less than 10% spectroscopic followup. Maintaining a spectroscopic survey for Vera Rubin will be prohibitively difficult, with the photometric SNe sample in the range of millions by the time Vera Rubin finishes. This impending abundance of SNIa photometric data makes the move to photometry all the more important.

1.3.2 Sloan Digital Sky Survey

The Sloan Digital Sky Survey (SDSS) is considered to be the first modern ‘all-sky’ survey. Run off of the 2.5 meter telescope at Apache Point Observatory in New Mexico, SDSS began in 2000 as the first survey to use charge-coupled devices. A review of the SDSS Supernova Survey is given in Frieman et al. (2008). In brief, Stripe 82 (from Right Ascension of 20h to 04h and 2.5 degrees wide along the equator

in Declination) was repeatedly scanned every four days using *ugriz* filters¹. The processing pipeline for the images is described in Stoughton et al. (2002) and potential SNe were identified in subtracted images with the method developed by Alard & Lupton (1998). Candidate selection and spectroscopic identification are described by Sako et al. (2008). The photometry is described in Holtzman et al. (2008). The spectroscopically confirmed subset of this data was used in several analyses to measure cosmological parameters such as Kessler et al. (2009); Betoule et al. (2014); Scolnic et al. (2018). Through three observing seasons (Fall 2005 through Fall 2007), the SDSS supernova program discovered 10,258 new variable objects and measured their *ugriz* light-curves - the procession of light from a celestial transient with time. Further specifics of the supernovae population statistics can be found within Sako et al. (2018). A component of the SDSS supernova survey included spectroscopic follow-up for a limited number of identified host galaxies. A separate SDSS spectroscopic survey (the Baryon Oscillation Spectroscopic Survey, or BOSS) acquired a significant fraction of potential host galaxy redshifts (Dawson et al. (2013)). For 4,680 candidates, they obtained an accurate spectroscopic redshift of the corresponding host galaxy. Since the conclusion of the SDSS Supernova Survey in 2008, BOSS has acquired an additional 1,294 host galaxy spectroscopic redshifts.

1.3.3 Pan-STARRS Medium Deep

The Pan-STARRS Medium Deep (PS1) Survey was operated from 2009 to 2013 in Hawaii near the summit of Haleakala using a 1.8 meter telescope. With a cadence of 8 observations every 4 days in 10 fields with 5 filters, *grizy* (detailed further in Chambers et al. (2016)), PS1 discovered thousands of transients through its run

¹I give a slightly more in-depth description of what a filter is later; but in short it is part of the telescope that measures specific ranges of wavelengths of light.

time. The Medium Deep survey, through which the SN program was run, covered a 70 square degree patch of sky for 6 months out of the year. The PS1 supernova survey data, along with information about how candidates were selected and identified, was released in Jones et al. (2018a)². Host galaxy redshifts are drawn from a compilation of sources detailed in Jones et al. (2018a).

1.3.4 Low Redshift Surveys

The modern collection of low redshift supernovae primarily comes from three different surveys. The first two of these, the Center for Astrophysics (CfA) and Carnegie Supernova Project (CSP) are commonly grouped together and referred to as the ‘Low- z ’ sample. The reason for this grouping is historical - these first two low redshift surveys started in the 1990s, and were therefore available before the third of these low redshift surveys: the ‘Foundation’ survey.

Low- z

As mentioned above, the ‘Low- z ’ sample is split into two separate samples: the CfA and CSP. In total, these releases represent ~ 150 SNIa, depending on the cuts made on the sample.

The CfA sample can be further split into 4 parts, starting with the release of 22 light curves, CfA1, in 1990 by Riess et al. (1999). The releases continued with Jha et al. (2006), Hicken et al. (2009), and Hicken et al. (2012); CfA2, CfA3, and CfA4 respectively. The telemetry of the collective CfA sample is too complicated to describe in detail here³; instead, I shall give an illustrative example of these complications.

²<https://archive.stsci.edu/prepds/ps1cosmo/>

³See Hicken et al. (2009) and Hicken et al. (2012)

CfA4 was observed on the 1.2 meter KeplerCam telescope at the Fred Lawrence Whipple Observatory in Arizona. The same $BVUr'i$ filters from CfA3 were used until the U band filter broke, after which it was replaced with an SDSS-like u' filter. During this observing process, the primary 1.2 meter mirror degraded, affecting the quality of the CfA4 measurements.

The supernova selection process in CfA is not, like SDSS or PS1, an untargeted search. Untargeted surveys repeatedly scan patches of the night sky and wait for supernovae to occur; CfA (and CSP) instead wait for supernovae to occur before targeting them for observation. Relying on these external observations, which in general had limiting magnitudes of 19.5, introduces even more complicated selection effects on top of those introduced by using different telescopes and filters over the years.

The Carnegie Supernova Project (CSP) is composed of the data releases from Contreras et al. (2010) and Stritzinger et al. (2011). CSP is situated at the Las Campanas Observatory with the 1 meter Swope telescope and the 2.5 meter du Pont telescope. These telescopes use the $UBVRIYJH$ filters, with access to optical spectroscopy. CSP similarly uses a targeted survey approach, same as CfA.

Foundation

In contrast to CfA and CSP, the Foundation survey, introduced by Foley et al. (2018), is quite simple. Foundation uses the PS1 camera and runs an untargeted supernova survey with 4 images per night in the same PS1 footprint. This approach provides obvious and immediate benefits over the CfA and CSP approaches, not the least of which are a significantly less complicated selection function, and the presence of a high redshift survey (PS1) on the same telescope. At its conclusion, Foundation acquired 225 light curves, approximately 180 of which pass common light curve cuts.

1.3.5 Compilation

One main tool in cosmology analyses with SNIa in the past decade has been the use of compilations of different spectroscopic SNIa samples. Combining different samples provides better statistics and a greater redshift range, but requires some level of homogeneity between the samples, and increased difficulty in modeling the interplay of the different selection effects across samples. Nonetheless, recent compilation surveys have provided the most accurate constraints on w ; starting from Union (Amanullah et al. (2010)), the Joint Light Curve Analysis (JLA) from Betoule et al. (2014) and the original Pantheon sample from Scolnic et al. (2018).

Pantheon+

The Pantheon+ survey, from Brout et al. (2022), is, as of time of writing, the largest sample of SNIa and the tightest constraint on w . As several of the sections of this thesis are predicated on the Pantheon+ sample, it is worth a brief review.

Pantheon+ contains several samples we have already discussed: SDSS, PS1, Low- z , and Foundation. It additionally includes supernovae from the Dark Energy Survey (DES) three year analysis from Brout et al. (2018) and the SuperNova Legacy Survey (SNLS). More information can be found in Scolnic et al. (2022).

Pantheon+ additionally includes numerous low redshift supernovae from an assortment of surveys and a handful of SNe observed by the Hubble Space Telescope. The work contained in this thesis removes these extra supernovae: the Hubble supernovae due to low statistics, and the extra low redshift supernovae are not present due to high uncertainties in their measurements.

This is the Accepted Manuscript version of an article accepted for publication in The Astrophysical Journal. IOP Publishing Ltd is not responsible for any errors

or omissions in this version of the manuscript or any version derived from it. The Version of Record is available online at the following doi: [10.3847/1538-4357/ab6deb](https://doi.org/10.3847/1538-4357/ab6deb)

Chapter 2

SNIa Distances and Simulations

Some portions of text from this chapter are from Popovic et al. (2021). The text represents my own work, and the contributions of other authors is presented as such:

- *Daniel Scolnic: Analysis and advising.*
- *Richard Kessler: Implementation of code and analysis construction.*

In this chapter, I discuss the generation and use of simulations in the field of SNIa cosmology for modeling systematics and performing validation testing.

The SNIa simulations that we utilise are inextricably linked to the Spectral Adaptive Light Curve Template (SALT) light-curve fitting model; we begin this chapter by explaining the SALT model before moving onto simulations of SNe Ia.

2.1 Building a Modern Hubble Diagram

2.1.1 Initial Standardisation Modes

SNIa are *standardisable* candles. On their own, without corrections, Phillips (1993) and Riess et al. (1996) find that SNeIa have a dispersion of ~ 0.8 magnitudes in the B band at peak magnitude¹. There is a ~ 0.25 magnitude signal difference between an accelerating expansion of the universe and a decelerating one; clearly the non-corrected dispersion is not sufficient for an accurate cosmological probe. Happily, great research has been done into reducing the dispersion through the use of empirical

¹This is the brightest point in an originally arbitrary, but historically important, filter.

relations down to a scatter of ~ 0.16 magnitudes, now accurately able to probe the depths of the universe. These empirical corrections broadly come in two flavours, with their veracity confirmed by comparisons of distance to galaxies with surface brightness fluctuations:

Light Curve Width

The first discovered relationship is that between the luminosity of the SNIa and the light-curve width, also interchangeably referred to as ‘stretch’. Discovered by Phillips (1993), SNIa with broader light curves (e.g. higher stretch) are more luminous than their narrower counterparts. This phenomenon is best understood as the amount of ^{56}Ni in the explosion. Kasen & Woosley (2007) provide some research into the relationship between light curve width and brightness, but research is still ongoing. In short, there is either less mass or more inefficiently produced ^{56}Ni in the narrower, fainter SNIa, resulting in a less luminous explosion. This less luminous explosion is also less opaque, allowing for the photons to more quickly exit the explosion and a thereby narrower light curve.

Colour

The second correction is the relationship between the luminosity and the $B - V$ colour at peak brightness. Riess et al. (1996) was the first to observe that redder SNIa are fainter than bluer SNIa. Here I shall take a moment to define ‘colour’ in the astronomical context - it is best understood as the difference in flux between two passbands, in this case B and V , rather than a single wavelength as in normal conception. An initial suggestion for the presence of some $B - V$ colour correlation was dust causing astronomical reddening $E(B - V)$, defined as

$$E(B - V) = (B - V)_{\text{observed}} - (B - V)_{\text{intrinsic}} \quad (2.1)$$

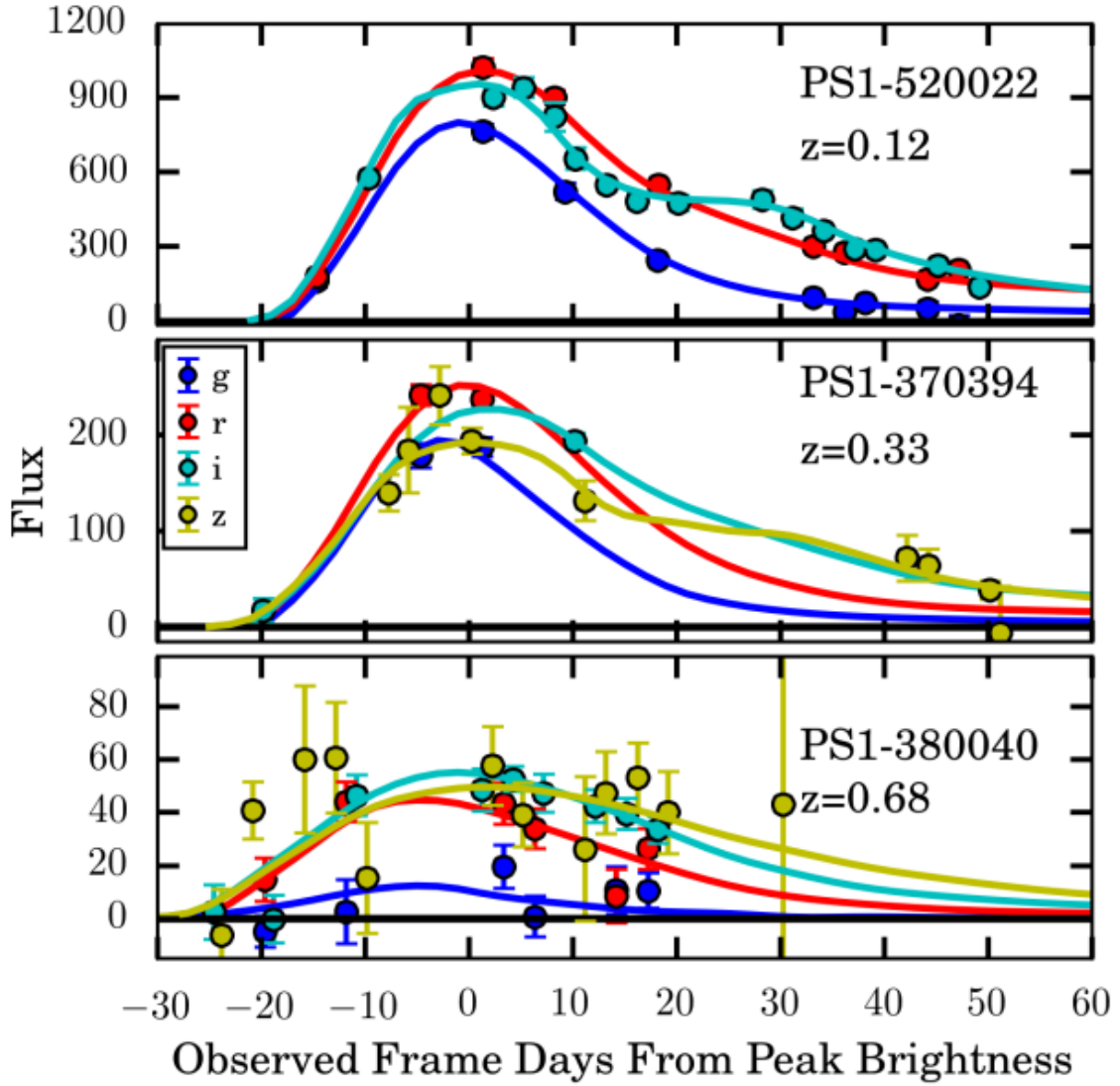


Figure 2.1: Three example light curves from PS1 at different redshifts. The rest-frame phase is shown in days, with 0 being time of peak brightness, and the y-axis is flux. From Scolnic et al. (2018). © AAS. Reproduced with permission

or, the flux difference between the $B - V$ bands that is observed and the ‘true’ not-attenuated flux difference in the $B - V$ bands in the restframe. Different wavelengths of light undergo different attenuation by dust: redder wavelengths are able to penetrate further through a medium than bluer wavelengths, the attenuation is approximately $1/\lambda$. The specifics of this attenuation are discussed later on in this chapter, as it is a key component of standardisation.

A simple reddening law is not sufficient to describe this colour-luminosity relationship. The slope of the SNIa colour-luminosity relationship is ~ 3.0 , a statistically-significant departure from the galactic colour-luminosity relationship of the Milky Way discovered by Schlafly et al. (2016): 4.1 ± 0.18 . We shall come back to dust, and alternate theories on the colour-luminosity relationship later in this work, but for now we have knowledge that some colour correction is needed.

2.1.2 Light-curve Fitting

So far we have limited our discussion to corrections at the peak brightness of supernovae. This is desirable for multiple reasons, not the least of which are that it has the best Signal-to-Noise Ratio and that the peak brightness is best calibrated for distance estimation. However, supernovae are rarely observed at time of maximum light, and never observed in their own rest frame.

We must make use of a model that is able to synthesize existing data and interpolate between observations in order to

- Convert observer frame data into rest frame.
- Convert data into appropriate bands.
- Estimate time of peak brightness.

- Estimate the flux at time of peak brightness.
- Provide necessary stretch and colour corrections.

While multiple methods do exist, here we shall focus exclusively on the SALT model family. The SALT family is the most widely-used light curve fitter of the past decade, and much research has gone into validation and improving the ease of propagating systematics for study.

2.1.3 SALT

The SALT model, originally introduced by Guy et al. (2005) and updated in Guy et al. (2010), Taylor et al. (2021), and Kenworthy et al. (2021) is a spectro-photometric empirical model of fitting SNIa light curves. SALT models the flux of a SNIa (SN) with time (here, as the phase p) as

$$F(\text{SN}, p, \lambda) = x_0 \times [M_0(p, \lambda) + x_1 M_1(p, \lambda) + \dots] \times \exp[c CL(\lambda)], \quad (2.2)$$

where x_0 is the overall amplitude of the light-curve, x_1 is the observed light-curve stretch, and c is a parameter describing the colour of the SNIa. The M_0 , M_1 , and $CL(\lambda)$ parameters are global model parameters: M_0 is the average Spectral Energy Distribution (SED) at each phase, M_1 describes the x_1 -dependence of SED variability, and $CL(\lambda)$ is the average colour law. The x_1 and c terms are familiar: they are the light-curve width correction, ‘stretch’, and the light-curve colour correction, colour, here given their proper designations.

The other three parameters, M_0 , M_1 , and $CL(\lambda)$, are new, alongside the SED terminology. These are all heavily interconnected, and necessitate a short digression into the difference between broadband photometry and spectroscopy.

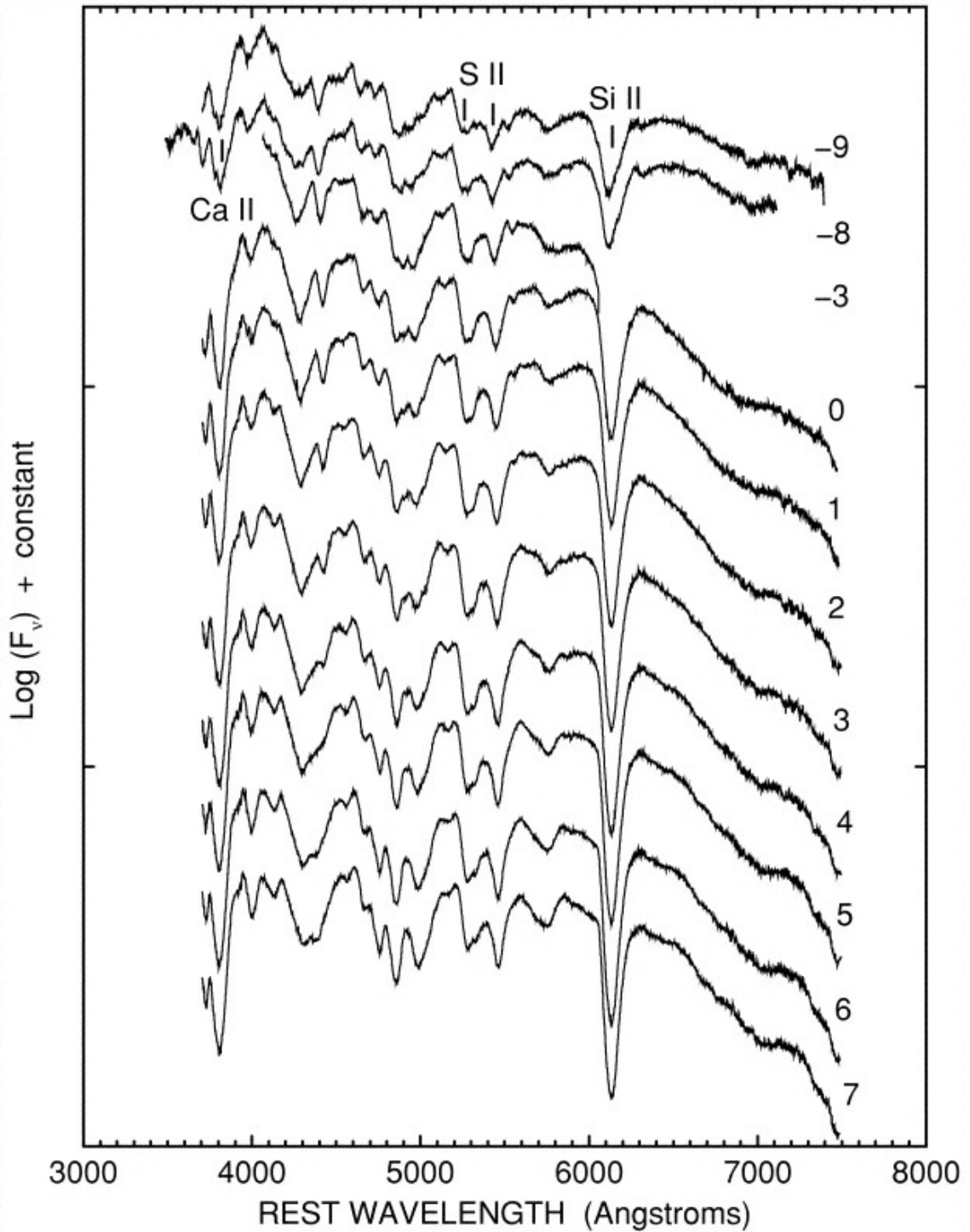


Figure 2.2: The Spectral Energy Distribution of SN1998qu in the rest frame. The flux is shown in log space with an arbitrary offset, and the numbering on the far right indicates the number of days since or before peak brightness. The absorption lines for elements are noted for reference. From Branch et al. (2003). © AAS. Reproduced with permission.

The SED of a celestial object is a collection of the spectral measurements taken of that object as a function of time, encompassing multiple continuous wavelength-range measurement as the object evolves. Figure 2.2 shows the SED of SN1998qu as reference for what a typical SNIa SED looks like.

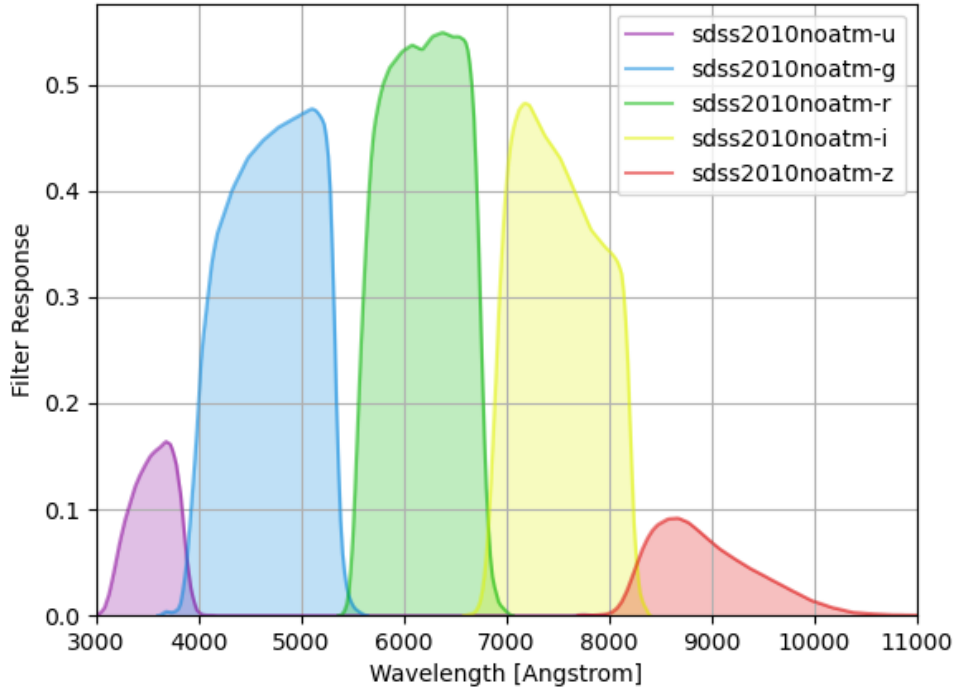


Figure 2.3: The filter response curves for the Sloan Digital Sky Survey. The atmospheric response has been subtracted out.

In contrast, Figure 2.3 shows the broadband photometry filters for SDSS. Each filter corresponds to an integrated wavelength range convolved with its response. Rather than a continuous wavelength measurement at a given time, the bandpasses return N -number of separate flux measurements. When put together with time, these measurements represent the SNIa light curve; therefore, the light curve can be understood to be a lower-information version of an SED.

SALT uses a combination of photometry and spectroscopy to train a working

model and determine M_0 , M_1 , and $CL(\lambda)$. Photometry contains less information than spectroscopy; spectral features are washed out in photometry, but photometry is cheaper and easier to obtain. SALT trains on data and converges to a model that is acquired via a χ^2 minimisation method, providing a model to fit SNIa light curves. Once the SALT training process is complete, SALT can be used to fit individual SNIa.

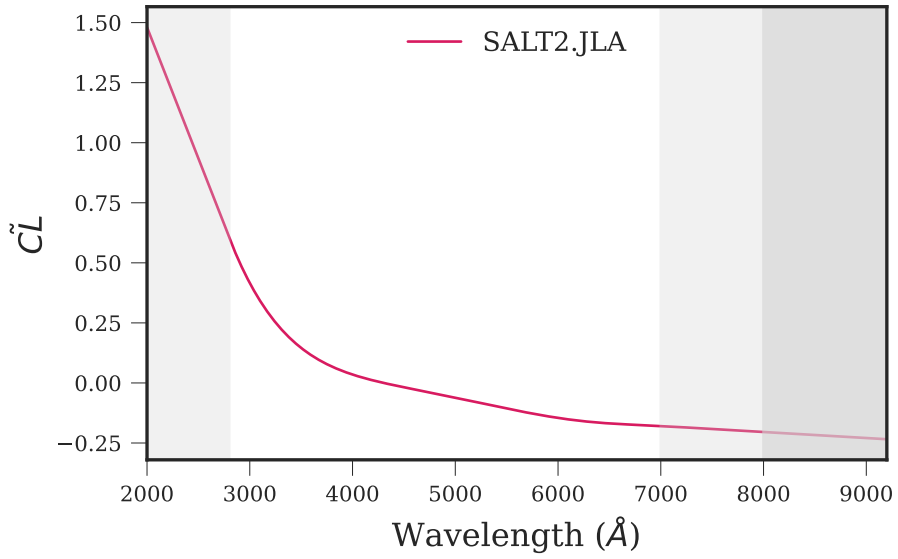
Figure 2.4a shows the SALT2² colour law $CL(\lambda)$, trained on the Joint Lightcurve Analysis (JLA) data from Betoule et al. (2014). The colour law is not time dependent, and assumes a universal behaviour for all supernovae. This means that SALT does not permit variance in the amount of reddening SNIa may go through: effectively, all supernova occur in the same environs, with no variance between their host galaxies. This is of course not true, but it is a starting point as an empirical model.

Figure 2.4b shows the M_0 and M_1 components for the JLA sample. Since M_0 and M_1 are both a function of wavelength and time, we only show the component for time of peak brightness as an example. The M_0 component is defined as the average SED for the sample, with $c = x_1 = 0$. M_1 encapsulates the average variability of this M_0 component.

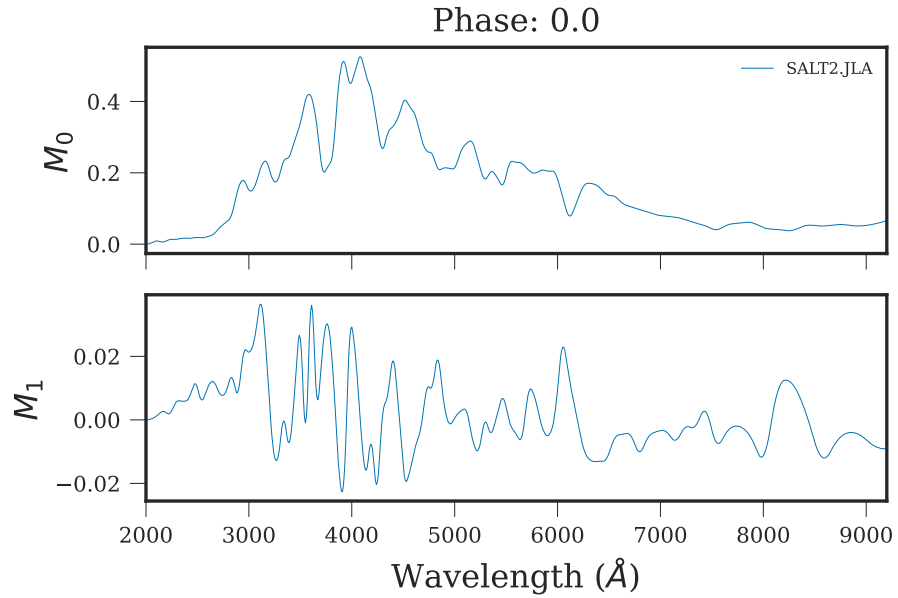
2.1.4 Light Curve Fitting with SALT

Discussion in the previous section has alternated between spectroscopic measurements in the form of SEDs and photometric light curves. The vast majority of SNIa light curve measurements are done with photometry alone. Spectroscopy is expensive, narrow, and time consuming, and it is not feasible to have every, or even a majority of, measurements using spectroscopy. Instead, most supernovae measurements are

²Section 2.1.5 gives more detail on the different SALT models. For now, it suffices to say that there is little difference between the SALT colour laws.



(a) The colour law $CL(\lambda)$ from the SALT2 model trained on the JLA sample. This models the attenuation of light at different wavelengths. The model is trained in the white region, and extrapolated by a 4th order polynomial in the light grey region and a 5th order polynomial in the dark grey region.



(b) The SALT2 M_0 and M_1 components at peak brightness as trained on the JLA sample. Both M_0 and M_1 are a function of time and wavelength, so we show only the components at peak brightness as an example.

done with photometry, which is relatively faster and able to cover a broader area of the night sky.

Recall that the SALT model is defined primarily by the M_0 , M_1 , and $CL(\lambda)$ components, which correspond to the average SED, SED variability, and an overall colour law, respectively. Because photometry is a lower-informational space version of spectroscopy, SALT is able to fit real data with photometry alone by estimating an SED and integrating into photometric measurements to then compare with the data. An example of this is shown in Figure 2.5. 2.5(a) shows the initial M_0 component, which is then scaled by $x_1 \times M_1$ in 2.5(b) and reddened by the colour law $\exp(c \times CL(\lambda))$ in 2.5c. These three steps provide an SED, which can then be redshifted and observed in the relevant bandpasses by integrating the flux with the filter transmissions as in 2.5(d) and 2.5(e). Finally the model covariance is added as in 2.5(f), which allows a comparison between the predicted fit and the real data. This process is iterated in the SALT fitting process until a best fit has been found.

2.1.5 One SALT, Two SALT, Red SALT, Blue SALT

We have kept our discussion of the SALT framework general up until this point, but here we shall take a moment to discuss the different implementations of SALT. The original SALT framework was introduced in 2005 by Guy et al. (2005) and shares few similarities with the more recent implementations. We shall not discuss it here.

SALT2, however, was introduced in 2010 by Guy et al. (2010) and comprised the primary SNIa light curve fitter for 10 years, until the introduction of SALT3 by Kenworthy et al. (2021).

SALT2 and SALT3 are broadly similar in their approaches. Indeed, SALT3 was an attempt to replicate SALT2 in a more accessible format, as the original SALT2

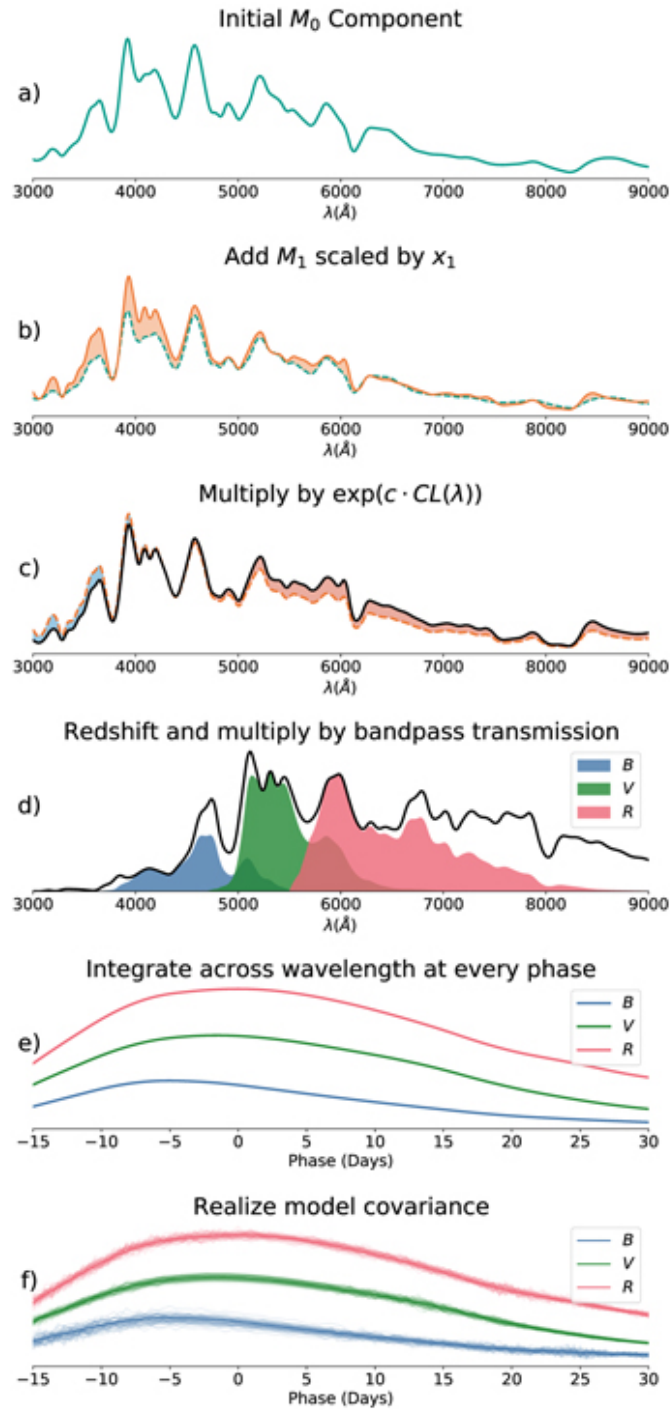


Figure 2.5: An overview of the SALT fitting process. Firstly, the average SED (M_0) component is generated as in (a). Then, the $x_1 \times M_1$ component to describe SED variability is added in (b) and the SED is reddened by $\exp(c \times CL(\lambda))$ in (c). The SED is then redshifted and integrated with the filter response curves in (d) and (e), before the model covariance is added in (f). From Kenworthy et al. (2021)

used proprietary code to train the model that made retraining difficult. The open source nature of the SALT3 training code is its primary benefit over SALT2, but also included the following differences.

- **Increased model range:** SALT2 is defined over the wavelength range 2000Å–9200Å; SALT3 increased this range to 2000Å – 11000Å.
- **Colour Law:** Extrapolation from the defined Colour Law range is done with a 5th order polynomial in SALT2, and a 6th order polynomial in SALT3.
- **Enforced Independence:** SALT3 requires that x_1 and c are uncorrelated in the training, whereas SALT2 only requires that $x_1 = 0$ at time of peak magnitude. In practice, both of these approaches find similar results.

We leave the discussion of SALT light curve fitting with a couple of comments. There is a difference between the SALT frameworks, SALT2 and SALT3, and an individual realisation of the SALT framework being trained on data, e.g. SALT2.B14. This second option, the individual training realisation, is referred to as a SALT surface. It is most expedient to think of the SALT frameworks as a functional form, and the surfaces are the functions output from this functional form, where the input is the data. As both are empirical methods to describe the variability of SNIa, we expect these surfaces to approximate what we see in the data.

Furthermore, while it is tempting to compare distributions of c and x_1 across SALT trainings, this is not feasible. The center of the distribution is set based on the mean value of the training sample, so comparisons across different training samples should not be expected to have the same center distribution. While it may seem that at the present moment there is a surfeit of available SALT surfaces to use, this is not yet the case.

2.1.6 Distances Fitted Light Curves

From a given SALT framework training, individual SNIa can then be fit and used to estimate distances using the Tripp Equation (Tripp (1998)), for use in inferring cosmological parameters. Tripp (1998) finds that using both correction modes for SNIa, the colour and the stretch, results in more precise measurements of cosmology and smaller χ^2 than a single correction mode. The Tripp equation is as follows:

$$\mu = m_B + \alpha x_1 - \beta c - M_0 \quad (2.3)$$

where $m_B = -2.5 \log_{10}(x_0)$; x_1 and c are the stretch and colour, and α and β are global nuisance parameters for the stretch-luminosity and colour-luminosity relationships respectively. M_0 is the supernova magnitude at restframe, ~ -19.35 magnitudes. Confusingly the same designation is used for the average SED and the restframe brightness of an SNIa; rest assured that beyond this section we will rarely reference the average SED. Each individual SNIa has its own m_B , c , and x_1 value, while every SNIa shares the same M_0 , and every cosmology fit has an α and β associated with the sample used for that fit. Unlike the other parameters, α and β have no SALT equivalent.

The c and x_1 values are well-defined between the ranges of $-0.3 \leq c \leq 0.3$ and $-3 \leq x_1 \leq 3$ respectively. The colour and stretch distributions are constructed such that the mean value of the training sample is set to $c = x_1 = 0$. The α and β parameters typically range between $0.14 \leq \alpha \leq 0.16$ and $2.8 \leq \beta \leq 3.2$, and are determined for an entire sample, separately from the training process, whereas m_B , c , and x_1 exist per-supernova.

2.1.7 Extensions to the Tripp Equation

However, the Tripp Equation alone is not able to encompass the full variability of SNIa distances. The most famous of the shortcomings of the Tripp Equation is colloquially referred to as the ‘mass step’. The mass step was discovered in Sullivan et al. (2011); Lampeitl et al. (2010); Childress et al. (2014) as a difference in the post-standardisation luminosity of SNIa between SNIa hosted in low and high mass galaxies. While the original mass step was discovered in SNLS using the original SALT light-curve fitter, it has persisted into SALT2 and SALT3 and every SNIa data set since - see Brout et al. (2018); Jones et al. (2018a); Scolnic et al. (2018); Brout et al. (2022).

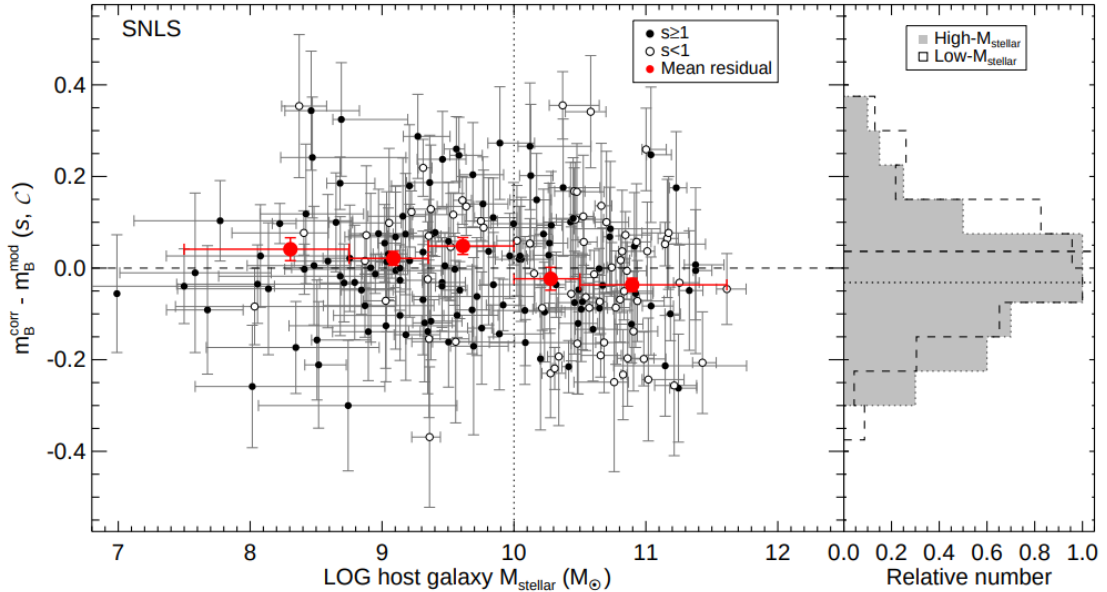


Figure 2.6: A plot of the Hubble Residuals (the difference in best fit cosmology and the individual SNIa distance) vs log of the host galaxy stellar mass for SNLS using the original SALT light-curve fitter. The data here was fit with the original SALT model, which contained different nomenclature than the modern SALT model. SNe Ia with $s < 1$ (comparable to $x_1 < 0$) are shown in open circles and SNe Ia with $s \geq 1$ (comparable to $x_1 \geq 0$) are shown in filled circles. Red circles represent the average residual in bins of log stellar mass. There is a 3.1σ significant difference in the low ($M_{\text{stellar}} < 10$) and high ($M_{\text{stellar}} > 10$) average residuals. From Sullivan et al. (2011).

Strangely, Sullivan et al. (2011) do find that a step, rather than a linear relation, more preferentially fits the data. Following Sullivan et al. 2011, the mass step, represented as γ , is incorporated into the modified Tripp estimator as $\delta\mu_{\text{host}}$:

$$\delta\mu_{\text{host}} = \gamma \times (1 + e^{(X_{\text{stellar}} - S)/\tau_X})^{-1} - \frac{\gamma}{2}, \quad (2.4)$$

where γ is the magnitude of the SNIa luminosity difference between SNIa in high and low mass galaxies, X_{stellar} is $\log_{10}M_{\text{stellar}}$, $S \sim 10$ is the step location, and τ_X is the width of the step. This step size is typically ~ 0.001 , approximating a step function.

2.1.8 Standardisation in Practice: The SALT2mu program

The α and β are, as mentioned, fit for the entire sample by minimising a χ^2 function of the supernova distances to a particular cosmology. This process obviously requires an assumed cosmology, which then presents an issue - α and β are cosmology-dependent. A cosmology-dependent set of nuisance parameters requires iterative re-fitting every time a new cosmology is tested, a highly resource and time intensive process.

The SALT2mu program, introduced by Marriner et al. (2011) and implemented by Kessler & Scolnic (2017), aimed to fix this process. SALT2mu fits a Hubble Diagram χ^2 function — the redshift vs. distance relation as showed in Fig. 1.3 — expressed as

$$\chi_{\text{HD}}^2 = \sum_i (\mu_i - \mu_{\text{model},i} - \Delta_{\mu,z})^2 / \sigma_{\mu,i}^2 \quad (2.5)$$

where (we drop subscript i for clarity here)

$$\sigma^2 = \sigma_{\text{int}}^2 + (\sigma_{\mu}^z)^2 + C_{m_B, m_B} + \alpha^2 C_{x_1, x_1} + \beta^2 C_{c, c} + 2\alpha C_{m_B, x_1} - 2\beta C_{m_B, c} - 2\alpha\beta C_{x_1, c} \quad (2.6)$$

and

$$\sigma_\mu^z = \left(\frac{5}{\ln 10} \right) \frac{1+z}{z(1+z/2)} \sqrt{\sigma_z^2 + (\sigma_{\text{vpec}}/c)^2}. \quad (2.7)$$

α , β , σ_{int} , and $\Delta_{\mu,z}$ (a distance offset in a given z bin) are the fitted parameters; the distance uncertainty is σ_μ with fitted covariance matrix C along the $\{m_B, x_1, c\}$ parameters, σ_{int} is the intrinsic scatter, σ_z is the redshift uncertainty, and σ_{vpec} is the peculiar velocity uncertainty.

σ_{int} is a measure of the additional scatter needed in cosmology fits using SNIa distances to achieve a reduced χ^2 of 1. For real data without any corrections, Conley et al. (2011) and Betoule et al. (2014) give a $\sigma_{\text{int}} \approx 0.1$. The σ_{int} value should be understood to be an underestimate of the true scatter in the Hubble Diagram, as it does not take into account the SALT parameter errors (e.g. $c_{\text{err}}, x_{1\text{err}}, m_{B\text{err}}$). Were a sample to have perfect measurements of SNIa and therefore perfect SALT parameters, then σ_{int} would be identical to the RMS of the Hubble Diagram, though neither would be zero.

SALT2mu does not fit for cosmological parameters, but rather an arbitrary reference cosmology w_{ref}, Ω_M is used for the $\mu_{\text{model},i}$. The deviation from this arbitrary cosmology is fit in N_z redshift bins of $\Delta_{\mu,z}$, giving a redshift-binned residual to the arbitrary cosmology that is degenerate with M_0 . All SNe in a given redshift bin share the same $\Delta_{\mu,z}$. Each SALT2mu fit does not return cosmology parameters w and Ω_M , but rather, N_z fitted $\Delta_{\mu,z}$ values with (now) the cosmology-independent α , β , and σ_{int} values. This SALT2mu process does necessitate a redefinition of M_0 , which now effectively changes with z : M_0 is redefined as the average of all the $\Delta_{\mu,z}$ bins, and then $\Delta_{\mu,z}$ becomes $\Delta_{\mu,z} - M_0$.

2.1.9 Building a Systematic Covariance Matrix

After the SALT2mu fitting, cosmological parameters can be obtained by a separate fit of $\mu_{\text{ref},z} + \Delta_{\mu,z}$ vs. redshift, with $\mu_{\text{ref},z}$ being the distances from assuming the reference cosmology $w_{\text{ref}}, \Omega_{\text{M}}$ that was given in the SALT2mu program. This final fitting of a specific cosmology is done by minimising a new χ^2 ,

$$\chi_{\Delta}^2 = \vec{D}_{\mu,z} C^{-1} \vec{D}_{\mu,z} \quad (2.8)$$

where $\vec{D}_{\mu,z} \equiv \Delta_{\mu,z} + \mu_{\text{ref},z} - \mu_{\text{model},z}$ and $\mu_{\text{model},z}$ is the distance from the now-fit ‘final’ cosmology, not to be confused with the reference cosmology. The $\mu_{\text{ref},z}$ and $\mu_{\text{model},z}$ values are error-weighted, with weights of σ_{μ}^{-2} . C is the total covariance matrix for the sample that includes both statistical and systematic uncertainties.

Conley et al. (2011) defines the statistical covariance matrix C_{stat} is defined as

$$C_{\text{stat}}(i, j) = \begin{cases} \sigma_{\mu}^2 & i = j \\ \sigma_{\text{int}}^2 + \sigma_z^2 + \sigma_{\text{vpec}}^2 & i \neq j \ \& \ \text{SN}_i = \text{SN}_j \end{cases}, \quad (2.9)$$

where i and j are the column and row indices for each entry and the diagonal is the full distance error. Occasionally, the same SN might be observed by two different surveys; this is accounted for by the requirement that $\text{SN}_i = \text{SN}_j$. The off-diagonal contains measurement noise from non light-curve components.

The systematic covariance matrix is created by defining the set of distance uncertainties for a given systematic ψ :

$$\Delta\mu_{\psi}^i \equiv \mu_{\psi}^i - \mu_{\text{BASE}}^i - (\mu_{\text{ref}}(z_{\psi}) - \mu_{\text{ref}}(z_{\text{BASE}})). \quad (2.10)$$

The derivative for each ψ is used to build the systematic covariance matrix as

$$C_{\text{syst}}^{ij} = \sum_{\psi} \frac{\partial \Delta \mu_{\psi}^i}{\partial S_{\psi}} \frac{\partial \Delta \mu_{\psi}^j}{\partial S_{\psi}} \sigma_{\psi}^2, \quad (2.11)$$

which gives the covariance between the i^{th} and j^{th} entry, marginalised over the systematic uncertainties ψ with their uncertainty, σ_{ψ} .

Lastly, the systematic covariance matrix is combined with the statistical covariance matrix:

$$C = C_{\text{stat}} + C_{\text{syst}}. \quad (2.12)$$

There are two options for the size of both $\vec{D}_{\mu,z}$ and C . Kessler & Scolnic (2017) sets the size to be N_z^2 by binning the SNIa into discrete redshift bins for both the construction of $\vec{D}_{\mu,z}$ and C . This choice was motivated by the N^2 growth of a per-SNIa entry covariance matrix, but as we shall see in a later section, an unbinned covariance matrix is preferable. In either case, the prescription for use does not change after the construction of the covariance matrix; the size is either N_z^2 or N_{SNe}^2 .

Rudimentary Bias Corrections

Here we will take a brief moment to discuss an extant issue in astronomy, Malmquist bias. Malmquist bias is the preferential detection of brighter objects, which are easier to see in the night sky, over fainter ones. Malmquist bias is capable of skewing the inferred brightness distribution of a set of stars, or in our case, SNIa. Should this effect correlate with redshift, which it does, this can result in biases that are indistinguishable from cosmology. Here we shall discuss a simplistic correction to SNIa distance measurements inspired by the SALT2mu process.

The SALT2mu process uses z -binning as part of the cosmology fitting and deter-

mination of nuisance parameters. It is a natural place to include some element of Malmquist bias correction, which worsens with decreasing brightness of the supernova. This decreasing brightness largely correlates with redshift.

Kessler & Scolnic (2017) introduced the idea of including a redshift-binned correction to SNIa distances. The question of how these corrections can be calculated is a trivial one with the simulations from Section 2.2 in hand. With a ‘true’, simulated luminosity $m_{B,\text{SIM}}$ and an observed $m_{B,\text{obs}}$ a change in the m_B parameter for a simulated SNIa can be calculated as $\Delta_{m_B} = m_{B,\text{SIM}} - m_{B,\text{obs}}$.

This Δ_{m_B} information can be leveraged for use on real data by calculating the average Δ_{m_B} in a given redshift bin. This average value is defined as $\delta\mu_{\text{bias}}(z)$, and is only a function of z . This 1D bias correction is then appended to the SALT2mu Tripp Estimator for each SNIa,

$$\mu = m_B + \alpha x_1 - \beta c - M_{z_i} - \delta\mu_{\text{bias}}(z) \quad (2.13)$$

where M_{z_i} is now the redshift-dependent M_0 that includes the $\Delta_{\mu,z}$ term from SALT2mu. While every SNIa distance includes a bias correction term $\delta\mu_{\text{bias}}(z)$, all SNe in a given redshift bin share the same $\delta\mu_{\text{bias}}(z)$, much like $\Delta_{\mu,z}$.

2.1.10 Bayesian Estimation Applied to Multiple Species

Here we briefly allow the idea that not all SNe that make it to the Hubble Diagram are SNIa. While spectroscopic surveys have no non-Ia, such a guarantee is not possible for photometric surveys. Here we review the process of mitigating non-Ia contamination.

Figure 2.7 shows an example Hubble Diagram with non-Ia contamination, colour coded by Ia probability. The non-Ia contamination is centered at higher magnitudes on the Hubble Diagram, rather than being evenly distributed. This is because non-Ia

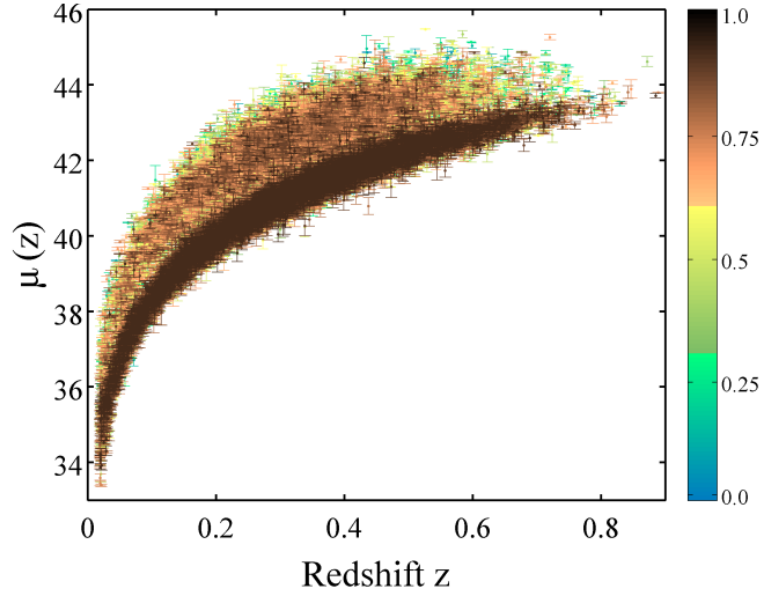


Figure 2.7: An example of a Hubble Diagram with non-Ia contamination. The probability of each SN being a Ia is colour coded, with brown being most likely a Ia and blue being highly unlikely. It can be seen that the non-Ia contamination is gathered at higher magnitudes on the Hubble Diagram. From Hlozek et al. (2012).

SNe have, on average, a lower luminosity and are therefore dimmer than their Ia counterparts.

The Bayesian Estimation Applied to Multiple Species (BEAMS) approach uses these two separate populations to marginalise over non-Ia contamination while performing the SALT2mu fit. BEAMS simultaneously maximises two likelihoods to model distinct SN populations. The first likelihood models the SNIa population \mathcal{L}_{Ia} and the second models the non-Ia contaminants \mathcal{L}_{CC} such that

$$\mathcal{L}_{\text{tot}} = \sum_{i=1}^{N_{\text{SNe}}} \mathcal{L}_{\text{Ia}}^i + \mathcal{L}_{\text{CC}}^i. \quad (2.14)$$

These likelihoods are defined as

$$\begin{aligned}\mathcal{L}_{\text{Ia}}^i &= \tilde{P}_{\text{Ia}}^i \times \exp\left(-\frac{(\mu_{\text{obs},i} + \Delta\mu^b - \mu_{\text{ref}}(z_i))^2}{\sigma_{\mu,i}^2}\right) \\ \mathcal{L}_{\text{CC}}^i &= (1 - \tilde{P}_{\text{Ia}}^i) \times D_{\text{CC}}(z_i, \mu_{\text{obs},i}, \mu_{\text{ref}}),\end{aligned}\tag{2.15}$$

where, following SALT2mu, $\mu_{\text{ref}}(z_i)$ is the distance modulus at a given redshift z_i assuming a fixed reference cosmology, $\mu_{\text{obs},i}$ is the observed distance of a supernova i , and $\Delta\mu^b$ is the offset between observed distance $\mu_{\text{obs},i}$ and reference cosmology $\mu_{\text{ref}}(z_i)$ in each redshift bin. $\sigma_{\mu,i}$ is the distance uncertainty from SALT2mu.

\tilde{P}_{Ia}^i is the scaled likelihood of the i th SN being a type Ia supernova, such that

$$\begin{aligned}\tilde{P}_{\text{Ia}}^i &= \frac{P_{\text{Ia}}^i}{P_{\text{tot}}^i} \\ \tilde{P}_{\text{non-Ia}}^i &= \frac{S_{\text{non-Ia}}(1 - P_{\text{Ia}}^i)}{P_{\text{tot}}^i} \\ P_{\text{tot}}^i &= (P_{\text{Ia}}^i + S_{\text{non-Ia}}(1 - P_{\text{Ia}}^i))\end{aligned}\tag{2.16}$$

where P_{Ia}^i is the probability of being a Ia and $S_{\text{non-Ia}}$ is a free parameter in the maximisation of the likelihood that acts as a scaling factor to correct for inaccurate probabilities. A perfect classifier would have $S_{\text{non-Ia}} = 1$.

Finally, D_{CC} is the contamination likelihood term

$$D_{\text{CC}} = \exp\left(-\frac{(\mu_{\text{obs},i} - \mu_{\text{ref,CC}}(z_i))^2}{\sigma_{\mu,i}^2}\right)\tag{2.17}$$

where $\mu_{\text{ref,CC}}$ and $\sigma_{\mu,i}^2$ can be modeled in two ways. The first is a second-order polynomial describing the brightness offset of non-Ia SNe and their error respectively, as in Hlozek et al. (2012). This approach, while analytical, requires an extra six parameters. The approach we instead take is to use simulations of non-Ia SNe to model $\mu_{\text{ref,CC}}$ and $\sigma_{\mu,i}^2$, as in Kessler & Scolnic (2017). More information on simulations of Ia and non-Ia SNe are given in Section 2.2.

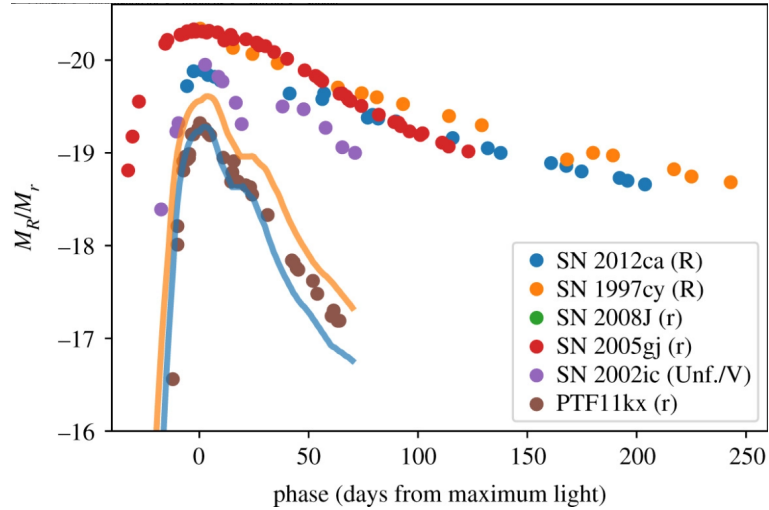


Figure 2.8: A collection of supernova light curves in a single band (R,r, or V) taken from literature. The variation between light curves of different types of supernova is comparable to the variation between light curves from the same type of supernova, making classification difficult. From Fraser (2020).

We have spoken recently of assigning probabilities of being an SNIa. Figure 2.8 shows an example of the light curves from different types of supernova in a single band, collected from several surveys. Without spectra, it is not obvious to differentiate type Ia light curves from non-Ia light curves by eye, and it is in fact quite impressive that the field has developed photometric classifiers with as high a degree of accuracy as we have. In Section 7, we make use of the SuperNNova photometric classifier from Möller & de Boissière (2019) to assign probabilities. SuperNNova trains on a simulated sample of equal parts Ia and non-Ia light curves using a recurrent neural network. After training, SuperNNova classifies directly on SN light curves, assigning a probability for each event ranging from 0 to 1.

2.2 Simulations and Simulacra

The SALT framework is well suited to generating simulations of SNIa light curves. I do not perform simulations of the explosion mechanism itself - if that were possible, empirical corrections would likely not be needed, as the explosion mechanism would be well understood enough to accurately model the data. Figure 2.5 provides an illustrative example of the light curve simulation process with SALT. The initial M_0 component is taken from the SALT surface, and x_1 and c values are selected for the SNIa, after which the M_0 component is changed by the addition of M_1x_1 and the multiplication by $\exp(c \times CL(\lambda))$. In large, survey-level simulations, the process of selecting c and x_1 becomes more complicated, requiring a method of scatter and a population-level description of x_1 and c , but this is discussed more in Sections 2.3 and 2.4. Once the SALT model SED is created, it is redshifted to the appropriate redshift and integrated with the bandpass transmissions to give measurements in different telescope filters. After this process, the model covariance is added, resulting in a simulated light curve that closely resembles real data. In this Section, we review the process of simulating and fitting SNIa.

Modern cosmology analyses with SNIa are complicated. Even a single survey requires modeling complex selection effects based off of cadence, measurement noise, and a secondary follow-up program to acquire either live SNIa spectroscopy or host galaxy redshifts, or both. An analytical model that simultaneously captures all these effects is prohibitively difficult, so instead we use rigorous simulations of SNIa light curves to recreate the observed behaviour. The use of simulations not only enables more accurate modeling of survey effects, but provides a useful tool for validation testing. Simulations are generated with the SuperNova ANAlysis software (SNANA, Kessler et al. (2009), with updates from Kessler et al. (2019)). The simulation process

occurs broadly in three steps, shown in Figure 2.9: Source Model, Noise Model, and Trigger Model. Before diving into the weeds, we will go over each of these steps to give an overview.

The Source Model stage aims to replicate SNe as they exist in nature, before being observed by a telescope. This process requires several inputs: the SALT model, redshift rates to determine how frequently SNe occur, a library of galaxies that SNe can occur in, and a model of intrinsic scatter and intrinsic populations. The specifics of the intrinsic scatter and populations are complicated, and they are covered on their own in Sections 2.3 and 2.4; that they are used can be considered a given for now. With these inputs, SNANA selects a redshift from the input rate, alongside the distance for the input cosmology, and creates an SED as per Figure 2.5, drawing c and x_1 from the intrinsic scatter and intrinsic populations provided while simultaneously selecting a host galaxy. After this, the SED is redshifted out of its rest frame and other cosmological effects (such as dimming, lensing, or Galactic Extinction) are applied, before the SED is integrated with the desired bandpass functions to give measurements in different filters.

From the Source Model, we transition to the Noise Model, which aims to replicate the process of observing SNe. For this, a simulation library is needed. The simulation library contains the metadata for a survey of observation cadence, telescope zeropoints, sky noise, and other instrument effects. Through the Noise Model stage, these effects are applied, starting with using the noise, zeropoints, and instrumental effects to calculate the flux error and convert the true flux from Source Model to a ‘measured’ flux. This flux error is then added to the measurement data as the error, before the telescope cadence is applied to mimic the process of a survey observation strategy.

The final stage of the simulation process is the Trigger Model, which follows how

surveys are designed to detect, store, and follow up observations. The Trigger Model stage requires information about how the survey is designed: if it is photometric or spectroscopic, how likely host galaxies are to have spectroscopy, and a model of SNIa Signal to Noise Ratio. With these inputs, the Trigger Model stage first applies detection cuts, such as multiple observations in a single band over a given period of time. After this, the SN detection efficiency is applied to the SNe, and finally either a SNIa-spectroscopy or a host galaxy spectroscopy followup model is applied.

At the conclusion of this simulation process, we are left with a catalogue of light curves that are indistinguishable from real data. These simulated light curves can be fine tuned to match the real data on a variety of observable metrics, from distributions of fitted light curve parameters to things such as Signal to Noise Ratio.

SuperNova ANALYSIS (SNANA) Simulations

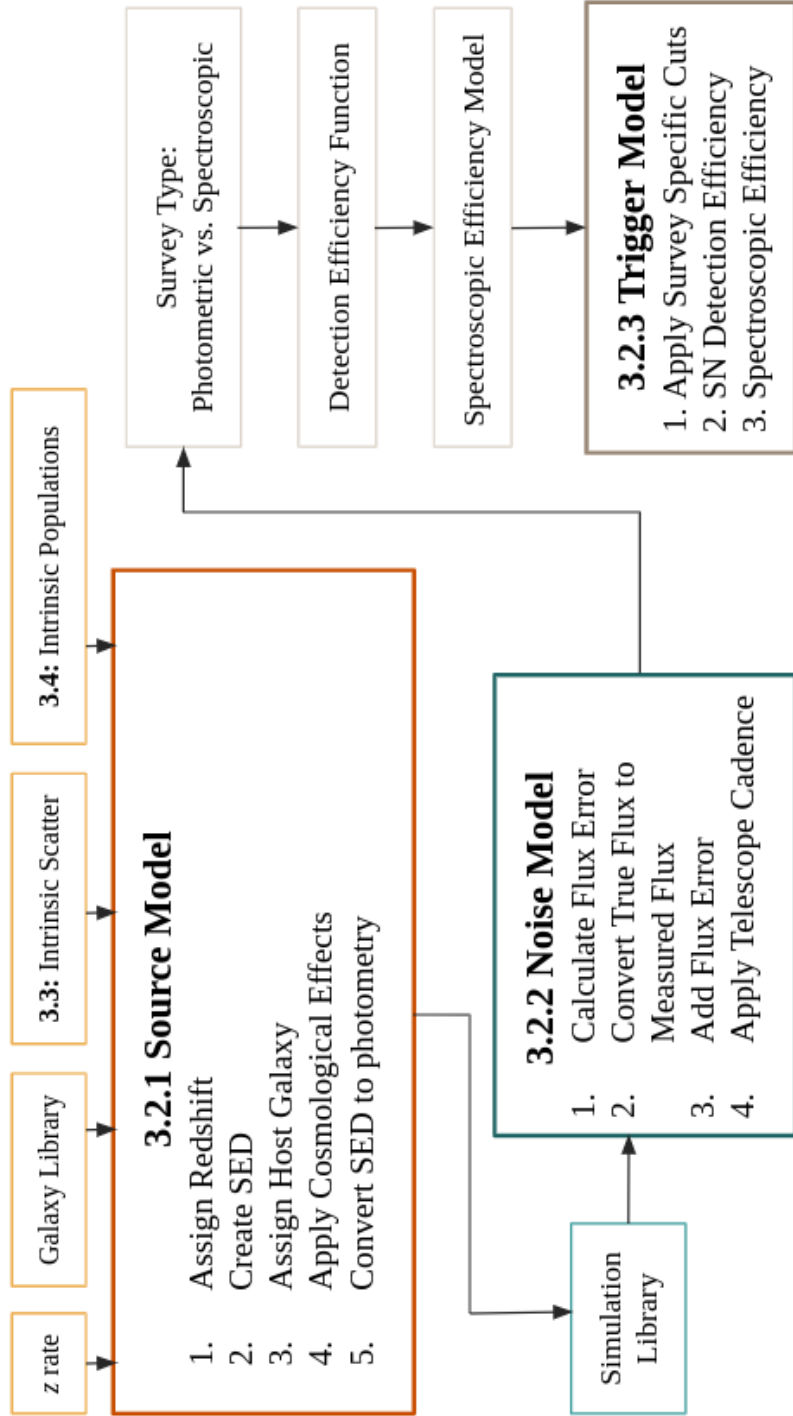


Figure 2.9: An overview of the SNANA simulation process. Adapted from Kessler et al. (2019).

2.2.1 Source Model

Source Model covers the process of simulating SNe light curves and SEDs as they exist in nature, assuming, effectively, perfect measurements and sky coverage. In all cases, a cosmology must be assumed to simulate distances for. SNANA has the capability to simulate many cosmologies, but in most cases we assume a w CDM cosmology.

The SNIa is simulated, in order, across the following steps:

- Assign Redshift.
- Create SED.
- Assign Host Galaxy.
- Apply Cosmological Effects.
- Convert SED to broadband filters.

Assign Redshift

First, a supernova redshift must be generated from a rate function created from data. An example of this rate is from Perrett et al. (2012):

$$R(z) = 1.75 \times 10^{-5} (1 + z)^{2.11} \text{yr}^{-1} \text{Mpc}^{-3} \quad (2.18)$$

Create SED

With a supernova redshift, we generate an SNIa SED from a selected SALT surface. A model distance μ_{model} is generated from the luminosity distance for the assumed simulated cosmology, and the SNIa parameters are assigned so as to match the distance. This process is similar to that of Figure 2.5: the M_0 component is generated before

the $x_1 \times M_1$ and $\exp(c \times CL(\lambda))$ components are added and multiplied respectively, e.g.

$$F(\text{SN}, p, \lambda) = x_0 \times [M_0(p, \lambda) + x_1 M_1(p, \lambda) + \dots] \times \exp[cCL(\lambda)], \quad (2.19)$$

The α and β values in Equation 2.3 and, by extension, 2.13, are given in the simulation input file, and are the same for all SNIa, whereas each SNIa has its own c , x_1 , and x_0 . Recall that x_0 corresponds to m_B , which is used in the Tripp equation; during the simulation process SNANA defines

$$\log_{10}(x_0) = -0.4(\mu_{\text{model}} - \alpha x_1 + \beta c - M_0) \quad (2.20)$$

which should be recognisable as the inverted Tripp Equation. Hence, with the model distance μ_{model} (which is entirely determined by redshift for a given cosmology), the nuisance parameters α and β , and c and x_1 , the simulated SNIa is fully described.

However, the question of what c and x_1 values to select is not trivial. First, a model of intrinsic scatter, σ_{int} , must be selected. The different ways of modeling intrinsic scatter are given in Section 2.3, as it is a topic worthy of its own section entirely, but the choice of intrinsic scatter model does impact the distributions of c and x_1 used. After the choice of intrinsic scatter model is made, a distribution of x_1 and c values must be given so as to match the data; this is briefly discussed in Section 2.4 and in greater detail in Section 3.1.1. The process of understanding the intrinsic scatter models and the selection of c and x_1 distributions is made significantly easier with the general knowledge of how an SNIa is simulated, so we will leave the much more complicated specifics of these two aspects for later. For now, there are three

```

VARNAMES: SALT2x1 LOGMASS PROB
PDF: -5.000 8.40 0.000
PDF: -4.900 8.40 0.000
PDF: -4.800 8.40 0.000
PDF: -4.700 8.40 0.000
PDF: -4.600 8.40 0.000
PDF: -4.500 8.40 0.000
PDF: -4.400 8.40 0.000
PDF: -4.300 8.40 0.000
PDF: -4.200 8.40 0.000
PDF: -4.100 8.40 0.000
PDF: -4.000 8.40 0.000
PDF: -3.900 8.40 0.000
PDF: -3.800 8.40 0.000
PDF: -3.700 8.40 0.000
PDF: -3.600 8.40 0.000

```

Figure 2.10: An example GENPDF file. SALT2x1 is the internal designation for x_1 , LOGMASS refers to the host galaxy stellar mass, and PROB is the probability of generating a supernova in the given 2D probability space.

methods to select c and x_1 distributions.

The first method is via random draw from an asymmetric Gaussian specified within the simulation input file. In the case of the x_1 distribution this is represented as

$$P(x_1) = \begin{cases} e^{-(x_1 - \bar{x}_1)^2 / \sigma_-^2} & \text{if } x_1 \leq \bar{x}_1 \\ e^{-(x_1 - \bar{x}_1)^2 / \sigma_+^2} & \text{if } x_1 > \bar{x}_1 \end{cases} \quad (2.21)$$

where \bar{x}_1 is the value at peak probability of the asymmetric generalised normal distribution, and σ_- and σ_+ are the width parameters for negative and positive x_1 values, respectively. The same form of equation is used for the colour c .

The second method is via the use of a GENPDF file. The GENPDF is a binned probability distribution function that SNANA is able to read in place of the aforementioned asymmetric Gaussian. An example of a GENPDF file is given in Figure 2.10, containing a Gaussian distribution of SNIa stretch probabilities as a function of the host galaxy mass.

The GENPDF file is capable of defining a multi-dimensional probability space, as

```

VARNAMES: GALID RA_GAL DEC_GAL ZTRUE g_obs r_obs i_obs z_obs Y_obs n0_Sersic a0_Sersic b0_Sersic a_rot LOGMASS LOGMASS_ERR X1
GAL: 1 34.4579 -4.70279 0.908506 26.5384 25.7263 23.5751 22.6917 23.034 0.5 0.286538 0.854813 86.6227 9.23965 0.2 1.28735
GAL: 2 34.7423 -4.70316 1.03694 23.9878 23.6814 23.2397 22.9509 24.6508 0.5 0.974762 0.688614 -56.0862 9.15756 0.2 0.449782
GAL: 3 34.9884 -4.70419 1.03077 22.6348 22.3853 21.8954 21.5255 21.272 0.5 1.1701 1.13566 57.3089 8.65909 0.2 0.352447
GAL: 4 34.9154 -4.70552 0.610123 21.9055 20.4269 19.6386 19.2496 19.1131 0.5 0.878139 2.19186 12.917 9.08866 0.2 -1.86042
GAL: 5 34.368 -4.70245 1.46711 23.9215 23.7939 23.8668 23.2683 23.2935 0.5 0.81753 1.11262 63.4521 11.216 0.2 1.79685
GAL: 6 34.3359 -4.70219 1.34426 24.4587 24.7415 24.251 23.9385 25.1445 0.5 0.929519 1.05107 -35.1383 8.65494 0.2 0.640691
GAL: 7 34.7635 -4.70222 1.58874 24.9358 25.2404 25.3813 25.7084 24.949 0.5 1.46478 0.65625 5.16143 9.08221 0.2 -0.196146

```

Figure 2.11: An example HOSTLIB header. X1 is equivalent to SALT2x1 in the GENPDF.

shown in 2.10. SNANA can read in an arbitrary probability distribution function provided, allowing for more complex systems than a(n) (asymmetric) Gaussian. GENPDF files are able to provide distributions for more than c and x_1 ; a non-exhaustive list is given here.

SALT2x1, SALT2c, LOGMASS, SIM_zCMB, SIM_RV, SIM_EBV³

Assign Host Galaxy

The final method for assigning c and x_1 is the HOSTLIB. SNe do not occur in an entirely empty vacuum of space. Instead, they most often occur in galaxies, where stars are. The HOSTLIB, short for ‘Host Library’, is a collection of galaxy information that a supernova can be associated with. A typical example of information stored in the HOSTLIB is shown in Figure 2.11.

The header information in Figure 2.11 is not enough to fully encompass all information present in the galaxy, nonetheless, it is sufficient to give the brightness of the galaxy in different bands (g_obs , r_obs , i_obs , z_obs , Y_obs), the location in the sky (RA_GAL , DEC_GAL), size ($n0_Sersic$, $a0_Sersic$, $b0_Sersic$, a_rot) and orientation (a_rot), stellar mass ($LOGMASS$), and redshift ($ZTRUE$). The X1 column contains the SNIa x_1 information for an SNIa hosted in the galaxy. The contents

³SIM_RV, SIM_EBV will become important later, but it is important to note that we can easily set them with the GENPDF.

of the `HOSTLIB` can be filled in a number of ways, from a rigorous galaxy properties simulation such as the Marenstrum Institut de Cincies de l’Espai Simulations Catalogue (`MICECAT`, Croce et al. (2015)), or in the case of this thesis, by compiling a library of real galaxies from SDSS data.

Host galaxy matching is nominally done via redshift matching between the supernova and the host galaxy. As the SNIa already has an assigned redshift from the rate function, a redshift tolerance can be defined as a polynomial

$$\Delta z = a + b \times z + c \times z^2 \tag{2.22}$$

where a, b, c are arbitrary coefficients and z is the redshift. This polynomial allows for more tight matching requirements at low redshifts, where redshift constraints are more impactful.

The host galaxy matching process, by default, places no priors on the host galaxy stellar mass distribution. This is not desirable, as there is no guarantee that the `HOSTLIB` has the same mass distribution as a given SNIa sample. In fact, it is incredibly unlikely. Instead, SNANA is able to accept a binned 1D probability density function, similar to the `GENPDF`, for the host-galaxy stellar mass. This PDF function, the `WEIGHTMAP` allows for tailoring of the host galaxy masses in the simulation to match that of the data.

The `WEIGHTMAP` is also the place where the mass step is conventionally included in the simulation. This is a convenient place, given that the `WEIGHTMAP` is a 1D function of the host galaxy mass. The mass step is included as an optional secondary column with the size of the magnitude shift $\pm\gamma/2$.

Apply Cosmological Effects

From here, cosmological effects are applied. These are dependent upon the redshift of the SNIa and the host galaxy:

Lensing Effects

In the real universe, objects exist between us and a given supernovae. This necessitates some modeling of lensing effects on the supernova. The lensing is split into two regions, $z < 0.4$ and $0.4 < z < 1.4$. For $0.4 < z < 1.4$, the lensing is approximated as

$$\mu_{\text{lens},z} = 5 \log_{10}(1 - \kappa) \quad (2.23)$$

where κ is the convergence distribution from MICECAT. For $z < 0.4$, the lensing is given as $\mu_{\text{lens},z} = \mu_{\text{lens},0.4} \times z/0.4$ with $\mu_{\text{lens},0.4}$ as defined in Equation 2.23 at a redshift of 0.4.

Lensing is a relatively subdominant effect, but one included in SNANA for completeness.

Peculiar Velocity

The SNIa is simulated with a given z in the CMB frame. However, celestial objects may have some motion that is not part of the expansion of the universe. This motion is given the catchall name ‘peculiar velocity’. It is at this stage that the peculiar velocity is added to the redshift of the supernova. Peculiar velocities are an important consideration for low redshifts, where they may cause significant bias. At higher redshifts, which this thesis focuses on, the contribution is negligible.

Cosmological Dimming

There is some dimming caused by the expansion of the universe. This dimming is applied here following the assumed cosmology.

Galactic Extinction

The earth is situated in the Milky Way, causing a blanket level of dust extinction for any supernova we observe. This extinction (see Chapter 4.1 for more on extinction and dust) is applied here following the dust extinction maps given by Schlafly et al. (2016) using the reddening law from Fitzpatrick (1999).

Redshift SED

The wavelength range and features of the SED are changed to the appropriate redshift as $1 + z = \frac{\lambda_{\text{obs}}}{\lambda_{\text{true}}}$.

Convert SED to Broadband Filters

We have already made reference to the difference between spectroscopy and photometry. It is at this stage that the SED is converted to broadband photometry using filter response curves as in Figure 2.3. The filter response curves are supplied from either the measured responses for an existing telescope, or the predicted response for a planned telescope.

2.2.2 Noise Model

At this point, we have an exactly perfect supernova measurement with our unrealistically good telescope. This is not of much use to us. The Noise Model stage is the first stage at which SNANA replicates the conditions of observing, so as to more accurately recreate the desired data.

The bulk of this work is done with the **SIMLIB**, a collection of observation metadata from a survey. The **SIMLIB** contains the sky coverage, cadence strategy, and telescope information for a given survey. A **SIMLIB** is comprised of multiple entries, each corresponding to metadata taken from a real supernova. For each entry, the **SIMLIB** contains the following information:

- MJD (modified Julian Date, e.g. the day)
- Telescope Filter
- Gain of the CCD
- Sky noise, including CCD noise
- Point Spread Function (PSF)
- Zero Point, including atmospheric and telescopic transmission. (ZPTADU)

This information, convolved with the SNe from Section 2.2.1, accurately replicates the set of observed SNe. That is, of course, after we convert the true flux of the simulated supernova into observed flux.

We have been primarily working with magnitudes so far, but a magnitude can be converted into flux via

$$F = 10^{0.4(m-ZPT)} \quad (2.24)$$

where m is the magnitude and ZPT is the zeropoint of the telescope. In general, the zeropoint of a telescope is the magnitude of an object that produces 1 count per second on the detector. This is critical to ensure that different telescopes are able to agree on the same brightness for the same object. In this case, SNANA processes ZPT as

$$ZPT = ZPTADU + 2.5 \log_{10}(\text{GAIN}) \quad (2.25)$$

where ZPTADU is the zero point provided by the SIMLIB and GAIN is the Gain provided by the SIMLIB.

The true flux of the SNe is then converted to observed flux using the information

provided by the SIMLIB:

$$\sigma_{F_{\text{true}}}^2 = (F_{\text{true}} + (4\pi\sigma_{\text{PSF}}^2) \times b + \sigma_{\text{host}}^2) \times \hat{S}_{\text{sim}} \quad (2.26)$$

where F_{true} is the true flux, σ_{PSF} is the PSF provided by the SIMLIB, b is the background noise including sky and CCD noise, and \hat{S}_{sim} is an empirically-determined fudge factor to ensure the simulated measured uncertainty matches the data. Kessler et al. (2019) gives a more detailed description of how \hat{S}_{sim} is calculated; we do not need to pursue it further.

σ_{host} is the Poisson noise of the host galaxy. SNANA places the SNIa at a random point in the host galaxy, whose shape is determined from parameters given in the HOSTLIB. From there, the σ_{host} is calculated by integrating the host galaxy flux with the PSF of the telescope.

It is worth noting that Equation 2.26 gives $\sigma_{F_{\text{true}}}^2$, the uncertainty on the true flux. A random draw of $\sigma_{F_{\text{true}}}^2$ is used to convert the true flux to the observed flux, and then the measured flux uncertainty is given by

$$\begin{aligned} \sigma_F &= \sqrt{\sigma_{F_{\text{true}}}^2 + (F - F_{\text{true}})^2} \quad (F > 0) \\ \sigma_F &= \sqrt{\sigma_{F_{\text{true}}}^2 - F_{\text{true}}^2} \quad (F < 0). \end{aligned} \quad (2.27)$$

2.2.3 Trigger Model

This takes us to the final stage of simulation. We have made no considerations, as of yet, for the limitations on magnitude that our telescope has, or the volume of data that a survey may have to process. The Trigger Model section takes place in two steps:

Detection Efficiency

Not all SNe are detected. This is due to a variety of factors - mostly revolving around being too dim to observe. Rather than process every pixel at every second and store the massive volume of resulting data, surveys elect to establish candidate logic to identify potential transients. Firstly, a transient must be detected in a single night in a single band above a given SNR. The specific SNR is determined by the survey construction. This detection must then be matched with other bands and nights in order to identify a single, continuous transient event.

This process can be approximated by modeling the efficiency of detecting a transient as a function of the SNR of the event, typically as a sigmoid function. This efficiency function is able to effectively account for the telescope missing supernovae in the universe that are too dim to observe.

Spectroscopic Efficiency

Within the simulation framework, it is the Spectroscopic Efficiency stage that constitutes the major difference between a spectroscopic and photometric survey. SNe photometry alone is not enough to do a cosmological measurement: a redshift is required. Since the field of photometric redshift is not developed enough to measure redshifts from photometry with the precision required for SNIa (on the order of $\times 10^{-4}$), some spectroscopic element is needed. This comes in two forms.

The first is a spectroscopic followup on the supernova itself. This followup is obviously time-limited, and is dependent on the supernova, not the host galaxy. The upside to this is easy typing of the supernova from the spectrum.

The second is a spectroscopic followup of the host galaxy. This followup is not time limited, and is dependent on the host galaxy magnitude. Host galaxy spectro-

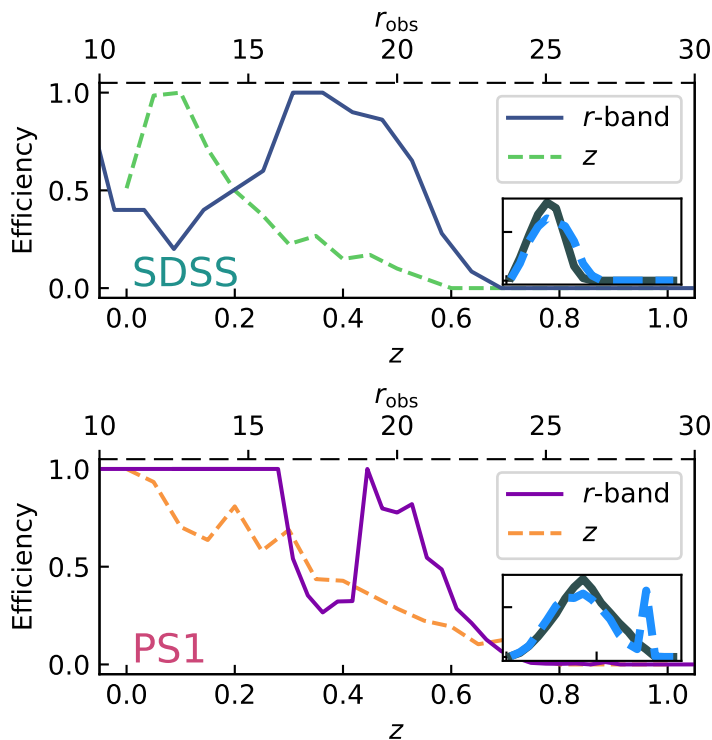


Figure 2.12: Spectroscopic efficiencies for SDSS and PS1 as a function of the host galaxy r -band magnitude (a telescope band in the redder range of the visible spectrum) and the host galaxy redshift. In both cases, the r -band magnitude efficiency is shown in solid line and the redshift efficiency is shown in dashed line. The inset shows the resulting redshift distribution from the r -band magnitude modeling (solid histogram) and the redshift modeling (dashed histogram).

spectroscopic measurements are required because they provide a redshift that is 2 orders of magnitude more accurate than the SNe redshift.

‘Spectroscopic’ surveys require both of these follow-ups, though the limiting factor is the SNIa redshift. ‘Photometric’ surveys only require the second. In both cases, the spectroscopic efficiency is calculated as a smooth function of either the redshift or a bandpass magnitude, typically i or r .

Figure 2.12 shows an example of the two approaches. The statistical redshift approach is less realistic, as the magnitude is typically the physically limiting factor in measuring a redshift, but it may provide some advantages in easier modeling of

the redshift distribution. The bandpass magnitude method is more realistic, but may present issues if the host galaxy magnitudes do not realistically align with the expected magnitude-redshift relationship. It is worth noting that this stage is the most responsible for the output redshift distribution of the simulations, as it governs how effective we are at ‘observing’ a given simulated supernovae.

With the Trigger Model finished, all that is left to do is write the events that pass all the required cuts onto disk, and we will have successfully created a universe simulacrum.

2.3 Intrinsic Scatter

As we have seen, simulating a perfect SNIa is relatively straightforward with a SALT surface. Unfortunately, we also know that SNIa are not perfect. If the name of the game is simulating SNe that best replicate the data, then we need a method of explaining the intrinsic scatter. We shall focus on 2.5 models of intrinsic scatter in this section: two SED-variational methods, G10 and C11, and one dust model framework.

2.3.1 G10

The first of these models of intrinsic scatter is G10, named for Guy et al. (2010). While this model was technically implemented in Kessler et al. (2013), it is constructed using the data from Guy et al. 2010. As mentioned above, G10 is an SED-variational method, which means the scatter modeling comes from modifying the SED flux in the simulation stage. This is done in two parts, a wavelength-dependent portion and a coherent scatter portion.

The coherent scatter portion will be covered first. Put simply, the entire SED is

shifted by a random magnitude drawn from a Gaussian. The standard deviation of this coherent-shift Gaussian is $\sigma_{\text{COH}} = 0.09$ mag. This coherent, or "gray" (e.g. not colour-dependent) scatter comprises $\sim 75\%$ of the scatter in the G10 model.

The wavelength-dependent scatter is a little trickier. A 'node' is placed every 800\AA , and each node is given a random Gaussian scatter. The standard deviation of the Gaussian is determined from data in Guy et al. (2010), hence the name. From the G10 data set, the average difference between the predicted peak brightness of the SALT model and the observed peak brightness of that SN is calculated every 800\AA , and this difference is used as the standard deviation for the node at that wavelength. This only needs to be calculated once to determine the standard deviation for the Gaussians, but a new random draw is done at each node for every SNIa simulated.

Before the magnitude at each node has been scattered, a wavelength-dependent function is applied:

$$\sigma_{\text{node}} = 1 + (\lambda_{\text{rest}} - 2157)/9259. \quad (2.28)$$

This function ensures that the scatter better matches the data. Once the nodes have been scattered, the points between them are interpolated with a continuous series of sine functions such that the derivative of the function is zero at each node. The rest of the SED is then shifted accordingly. This wavelength-dependent portion accounts for $\sim 25\%$ of the scatter in the G10 model.

2.3.2 C11

The C11 model, named for Chotard et al. (2011), can broadly be understood as the inverse of the G10 model. Where G10 had $\sim 75\%$ coherent scatter, $\sim 75\%$ of the scatter in the C11 model is wavelength-dependent.

The C11 process is also extrapolated from the data, but this time from a covari-

ance matrix between broadband filters. The C11 covariance matrix is given in Kessler et al. (2013), but the process of generating scatter is broadly similar. 6 nodes are created at specific wavelengths corresponding to the *UBVRI* filters (and one extra node is centered at 2500Å) and given random magnitude shifts taken from the C11 covariance matrix. The 6 nodes are then interpolated between using sine functions, and the entire SED is then shifted accordingly.

2.3.3 Dust Models

Considering that this is the simulations section, and a large part of this thesis will be on the effects of dust, it is worth briefly reviewing how simulating dust works. Unlike G10 and C11, dust is not done with an SED-variational method. In fact, the first step in simulating with dust is to set the magnitude smearing of C11 to zero.

Scatter, therefore, comes from a different place, namely the stochastic selection of model parameters. We will very briefly review the three primary components of scatter within a dust model.

- Colour is generated from a linear combination of SNIa colour and a dust effect.
- Each SNIa is given a random value of the nuisance parameter β drawn from a distribution, rather than a single value for all SNe.
- The SNIa luminosity is dimmed by a physical dust effect, rather than a random SED shift.

More information is given in Section 4.1.

2.4 Intrinsic Populations

Equation 2.3 relies on accurate measurements of SNIa parameters. However, there are variations in brightness in SNIa; the linear Tripp equation cannot capture these variations - and furthermore, it is not able to separate the different sources of fitted parameter deviation from the ‘truth’.

The distribution of supernova fitted parameters, such as c , is well approximated by a Gaussian. The Tripp estimator on its own is not sufficient to differentiate between the colour (or stretch) that correlates with luminosity from either scatter intrinsic to SNIa or scatter caused by measurement noise. The first of these three effects, colour and stretch that correlate with luminosity, are called ‘intrinsic populations’ or ‘parent populations’ from Scolnic & Kessler (2016). Not accounting for the natural deviations away from this correlation over the course of a survey can impart biases on the measured distances. Take, as an illustration, a SNIa with a ‘true’ colour of $c = 0$. If this SNIa is observed with a colour of $c = 0.1$, then the expected bias would be $-\beta(c_{\text{obs}} - c_{\text{True}}) \sim -0.3$ magnitudes, for an expected $\beta \sim 3$.

Because of this measurement noise and other deviations from the ‘true’ intrinsic populations, simply using the observed c or x_1 distributions as an input to SNANA will not recreate the observed data, instead further skewing it. Therefore we need a method of extracting the intrinsic populations from the data; this is discussed in detail in Section 3.1.1. An illustrative example of the expected change to the c distribution is shown in Figure 2.13.

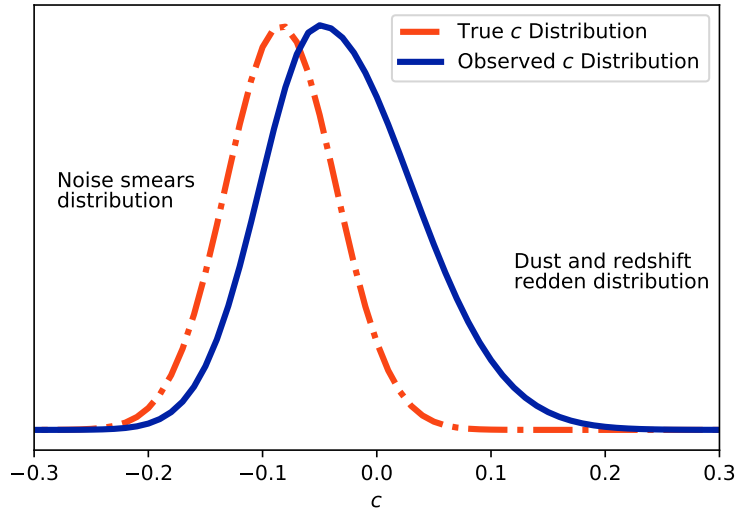


Figure 2.13: A true c distribution is smeared and skewed through the observation process, resulting in an observed distribution that is not reflective of SNIa. This process must be modeled properly to correct for any biases arising from not using luminosity correlations in the Tripp Equation.

2.5 Simulating Non-Ia SNe

We come to the final section in this Chapter. So far we have limited our discussion to only simulating SNe Ia. Unfortunately, there are more types than just Ia, and this is a thesis focused on photometrically confirmed SNIa samples, so it is necessary to consider how non-Ia may impact our samples. The process of actually simulating non-Ia is conceptually simple: the Noise and Trigger models are applied in the same way, but the Source Model section changes. We do not have a SALT-equivalent model for non-SNIa, so there is no scatter model or intrinsic populations. Instead of taking the SALT surface, Vincenzi et al. (2019a) gathers a collection of 67 templates of Type Ibc and Type II SNe, and provides a random, coherent magnitude to the SED template drawn from the luminosity distributions from Li et al. (2016).

We take care to simulate these non-Ia supernovae for good reason. Simulated non-Ia form the training sample for photometric classifiers, allowing us to identify non-Ia

SNe in the data. Furthermore, the simulated non-Ia can be used to characterise BEAMS more accurately than a polynomial, better equipping us to marginalise non-Ia contamination. After the simulation process and subsequent classifier training, simulated non-Ia are effectively treated as SNIa (with their probability) through the analysis.

However, this description does not illuminate the different types of non-Ia SNe, so we will go over them briefly here.

2.5.1 Core Collapse SNe

Core collapse is the process that happens to a star with a mass 8 to 10 times greater than that of our sun. Towards the end of their life, the core of the star is made predominantly of iron, the last energetically-favourable fusion element. With fusion no longer possible, the only pressure that the core can exert to stop gravitational collapse is that of electron degeneracy pressure, the same force that powers white dwarf stars. But this electron degeneracy pressure is only stable up to 1.4 times the mass of our sun, and when that mass is exceeded, the core collapses, producing a shockwave that tears through the star and triggers the supernova. Despite a core collapse supernova's prodigious explosion, most of the energy is carried by neutrinos generated at the core. Core collapse SNe are classified into two different types: Type Ib/Ic and Type II.

Type Ib/Ic

Type I(a/b/c) supernovae lack hydrogen lines in their spectrum. This taxonomic approach, assigned before the explosion mechanism of these three categories was understood, is why type Ia, despite not being core collapse, share a typing with Ib

and Ic: Ia supernovae also lack hydrogen lines. This is due to the progenitors of all three types having a ‘stripped’ envelope: the outer layer of the star, where the hydrogen would be, is not present. In the case of Ib/Ic supernovae, this is likely either from binary interactions stripping the hydrogen from the star, as proposed in Eldridge & Maund (2016), or it has been theorised that the progenitors are Wolf-Rayet stars (stars fusing heavier elements and missing hydrogen from their spectra) with initial masses more than 25 times that of our sun, as in Gaskell & Sparke (1986).

Type Ib supernovae have strong helium absorption lines in their spectra, whereas type Ic do not, instead characterised by oxygen and silicon. Unlike type Ia supernovae, neither Ib nor Ic supernova present the silicon or sulphur lines that would indicate a thermonuclear explosion.

Type II

While type I supernovae are characterised by their lack of hydrogen, type II supernova *do* show hydrogen lines in their spectra. The typical progenitor for type II supernovae is a massive red giant, anywhere from 8-20 times the mass of our sun.

2.5.2 Non Core Collapse Contaminants

There are two commonly observed types of poorly-understood, non-standardisable type Ia supernovae: ‘91bg’ and ‘Iax’. The first is named for the eponymous SN1991bg discovered by Filippenko et al. (1992), which is noticeably less luminous than normal Ia, and has much faster declining and redder light curves. These occur at about 1/8th the rate of normal Ia.

Iax on the other hand, named by Li et al. (2003); Foley et al. (2013), are more peculiar. Iax are best characterised by their spectra, but in lieu of spectral measure-

ments, they present a much quicker rise and decline time than normal Ia. Iax are approximately 1/4th as common as normal Ia.

Base SED templates for both of these are taken from Photometric LSST Astronomical Time Series Classification Challenge (PLAsTiCC, Modelers (2019)). 35 91bg templates and 1000 Iax templates were provided.

Interestingly, the Iax templates provided by PLAsTiCC were all based off of a single supernova, 2005hk. The templates were generated by warping the SEDs to capture the observed diversity in light curve width, but the peak colour in the templates was left unchanged. This caused the issue that PLAsTiCC templates of Iax did not properly reproduce the observed Iax colour distribution, leading to an overestimation of Iax contamination in Popovic et al. (2019). This issue would later be fixed by Vincenzi et al. (2021).

Chapter 3

Intrinsic Populations of SNIa

3.1 Distance Biases from Correlations

The results presented in this chapter, as well as some portions of text, are from Popovic et al. (2021). The text represents my own work, and the contributions of other authors is presented as such:

- *Dillon Brout: Implementation of code for work not covered in this section. Dillon was instrumental in aiding with changes to SNANA code to enable bias corrections, which are covered in a later section.*
- *Richard Kessler: Implementation of code and analysis construction. Rick, alongside Dillon, aided in changing SNANA code for bias corrections. Provided many statistical definitions including a way to account for correlated bins in the analysis.*
- *Daniel Scolnic: Analysis and advising, particularly with respect to suggestions for honing the migration matrix implementation.*
- *Lisa Lu: Code refactoring. After the initial results were obtained, Lisa aided in refactoring the code for ease-of-use and futureproofing for additional features.*

Simulations are effective at offering insights into the process of observing SNIa. One of the greatest, even though it is quite obvious, strengths of simulations is the presence of a known truth value. Seeing a shift from the simulated truth to the

observed, simulated value would hint that the fitted parameters in our data are not the ‘true’ ones - they are instead skewed and smeared through the observation process. We can use this knowledge to correct biases in the data - but only if we understand what the true parameters are, and how they migrate from true to observed. In this chapter, we shall concern ourselves with creating the tools to extract these true parameters from the data, so that we can use them for bias corrections later on. Along the way, we will answer a question that has been haunting the SNIa community for years. For the last decade, we have been seeing a strong correlation between fitted SNIa parameters and the mass of their host galaxy. This is surprising, because the mass of the host galaxy is not a standardisation parameter. Is this effect simply observational, or do the true SNIa parameters actually correlate with the host?

3.1.1 Parent Populations

One of the inputs in the Source Model stage in Figure 2.9 is the ‘Intrinsic Population’, also referred to as parent populations. This refers to the distributions of fitted SNIa parameters x_1 and c as they exist in nature, before selection effects and measurement noise. These are, by definition, impossible to directly observe, but they constitute a vital part of the simulation pipeline: without knowledge of the intrinsic populations, it would be impossible to recreate the data with simulations. We need a way to infer the parent populations from the data.

With realistic simulations and fitted data in hand, it is possible to recover the parent populations by accounting for the migration of ‘true’ parameters to observed ones due to the myriad sources of noise and bias in a survey. This is done with the ‘Migration Matrix’, which is a statistical approximation of the likelihood of a supernova with a given true property to be observed with a given observed property.

The Migration Matrix, created in Scolnic & Kessler (2016), provides a simulation-free method to quickly compute the transformation of a distribution of true parameters into an approximate distribution of observed parameters. When we say ‘simulation free’, this means that once the Migration Matrix is generated from simulations, we need not invoke SNANA any further. It is worth noting that this Migration Matrix approach does not provide individual, supernova-level predictions of how fitted parameters change, but does allow for population level predictions. In short, we cannot predict how any single supernova will turn out, but we create a probability distribution for how likely we are to observe a supernova with a given parameter.

A simulation with a flat distribution of true colour and true stretch is generated, and SALT light-curve fits determine the measured colour and measured stretch for the SNIa that pass light-curve quality cuts. The true and measured values from these flat simulations are used to compute the migration matrix (X for stretch and C for colour) that captures the migration from the input distribution to the observed distribution through selection effects, measurement noise and intrinsic scatter. Each component of the matrix, X_{ij} , describes the likelihood that a true value in an input stretch bin i (x_{1_i}) migrates to a measured value in stretch bin j (x_{1_j}), and similarly for colour.

For an underlying stretch population, $P(x_1)$, we define a binned distribution \vec{P}_x with components P_{xi} . Scolnic & Kessler (2016) defines $\vec{\Delta}_x$, the data-simulation difference vector, as

$$\vec{\Delta}_{x_1} = \begin{bmatrix} O_{x1} \\ O_{x2} \\ \vdots \\ O_{xn} \end{bmatrix} - \begin{bmatrix} X_{1,1} & X_{1,2} & \cdots & X_{1,n} \\ X_{2,1} & X_{2,2} & \cdots & X_{2,n} \\ \vdots & \vdots & \ddots & \vdots \\ X_{d,1} & X_{d,2} & \cdots & X_{d,n} \end{bmatrix} \times \begin{bmatrix} P_{x1} \\ P_{x2} \\ \vdots \\ P_{xn} \end{bmatrix} \quad (3.1)$$

where the measured distribution vector \vec{o}_x has the same binning as X and \vec{P}_x .

Figure 3.1 shows an visualisation of the migration matrix for x_1 . The scatter is focused around the diagonal, indicating useful constraints on the observed properties. The highest scatter is focused around the high ($x_1 > 0$) stretch values. This is expected given that high stretch values correspond with fainter SNIa, which are less well constrained.

The mathematics up to this point show how to transform a proposed distribution of ‘true’ SNIa fitted parameters into the observed distribution, but this matrix alone has no constraining power.

Scolnic & Kessler (2016) performed a grid search for their parameters, where here we use a Monte Carlo minimisation procedure using the `emcee` python package from Foreman-Mackey et al. (2013). We wish to minimise $\vec{\Delta}_{x_1}$ to provide the best-fit to our data. For the χ^2 calculation, the associated data error vector is $\vec{e}_x = [e_{x1}, e_{x2}, \dots, e_{xn}]$, where $e_{x_i} = \sqrt{o_{x_i}}$ for $o_{x_i} > 0$ and $e_{x_i} = 1$ for $o_{x_i} = 0$; while not technically correct for a Poisson distribution (Baker & Cousins (1984)), Scolnic & Kessler (2016) has shown this this error approximation is sufficient.¹ The four parameters that describe $P(x_1)$

¹This construction leaves out the off-diagonal errors that may contribute later in the χ_x^2 determination, but the impact of this omission remains unmodeled.

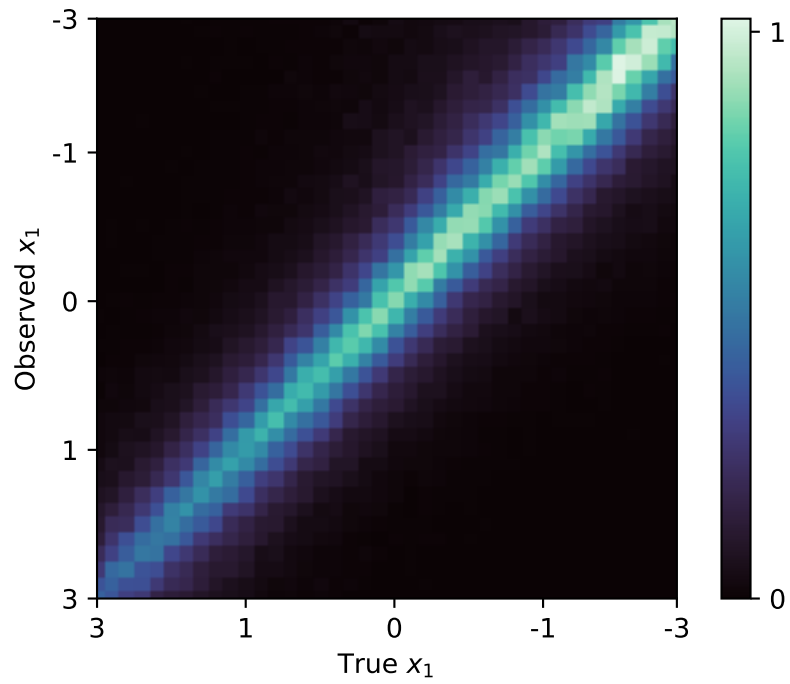


Figure 3.1: An example of the Migration Matrix for the x_1 parameter. The colourmap represents the probability of the true SNIa stretch being observed at a given value. The probability is normalised to the peak value, not the cumulative distribution.

are determined by minimising the χ_x^2 defined as

$$\chi_x^2 = \sum_{i=1}^n \left(\frac{\Delta_{xi}}{e_{xi}} \right)^2. \quad (3.2)$$

For the colour distribution, χ_c^2 is defined similarly using $\vec{\Delta}_c$ and \vec{e}_c .

We have only the choice of proposed true distribution to consider. Here we begin to diverge more from the groundwork laid out in Scolnic & Kessler (2016) and reviewed above. Unlike Scolnic & Kessler (2016), we replace an asymmetric Gaussian with an asymmetric generalised normal distribution that depends on four parameters,

$$P(x_1) = \begin{cases} e^{(-|x_1 - \bar{x}_1|^n / n\sigma_-^n)} & \text{if } x_1 \leq \bar{x}_1 \\ e^{(|x_1 - \bar{x}_1|^n / n\sigma_+^n)} & \text{if } x_1 > \bar{x}_1 \end{cases} \quad (3.3)$$

where \bar{x}_1 is the value at peak probability of the asymmetric generalised normal distribution, n is the shape, and σ_- and σ_+ are the width parameters for negative and positive x_1 values, respectively.

The choice of input distribution shape is arbitrary, so long as it is parameterised. Low redshift surveys show a distinctive double peak in the stretch distribution; we include a double Gaussian model

$$P(x_1) = A_1 \times e^{(-|x_1 - \bar{x}_{11}|^2 / 2\sigma_1^2)} + A_2 \times e^{(-|x_1 - \bar{x}_{12}|^2 / 2\sigma_2^2)} \quad (3.4)$$

where A_i is the weight, \bar{x}_{1i} is the mean value, and σ_i is the standard deviation of the respective Gaussian.

3.1.2 Extending Parent Populations

Figure 3.2 shows the distributions of c and x_1 for the Pantheon+ data set as a function of host-galaxy mass. There exists a clear correlation between the stretch x_1 and the host galaxy mass of the supernova. A weaker trend exists for c .

These correlations do not arise solely from selection effects. A naive attempt at simulating SNIa without host galaxy correlations does not recover the x_1 -mass relationship that is present in the data.

These shortcomings of a host-galaxy independent simulations indicate that another approach is necessary. If selection effects are not sufficient to explain the observed correlations of SNIa with their host galaxy, it is worth investigating whether or not the parent populations of SNIa change with host-galaxy mass.

The ideal approach for including mass-dependent correlations is to replace \vec{o}_{x_1} in Equation 3.1 with a 2-dimensional array of stretch and host-galaxy mass, $\vec{o}_{x_1, M}$, where the subscript is $M = M_{\text{stellar}}$. Similarly, the migration matrix X and probability vector \vec{P}_x would also be extended to include M_{stellar} .

However, the M_{stellar} measurements lack a well defined uncertainty and therefore the migration matrix is not as well determined in the M_{stellar} dimension as it is for c or x_1 . We therefore assume that the measured M_{stellar} is the true M_{stellar} . To reduce the dependence on M_{stellar} uncertainties, we implement a 2 step process. First, we fit the parent populations by minimising χ_x^2 and χ_c^2 (Eq. 3.2) in M_{stellar} bins. Ideally we would perform this minimisation in small M_{stellar} bins, however, the statistics of SNIa per bin is insufficient. As a compromise, we fit in relatively large M_{stellar} bins of $1.2 \times 10^{10} M_{\odot}$ but use a small step size of $0.2 \times 10^{10} M_{\odot}$. Although the M_{stellar} bins are strongly correlated, we have used simulated data samples to validate our method. In the second step, we re-weight the simulated M_{stellar} distribution to match

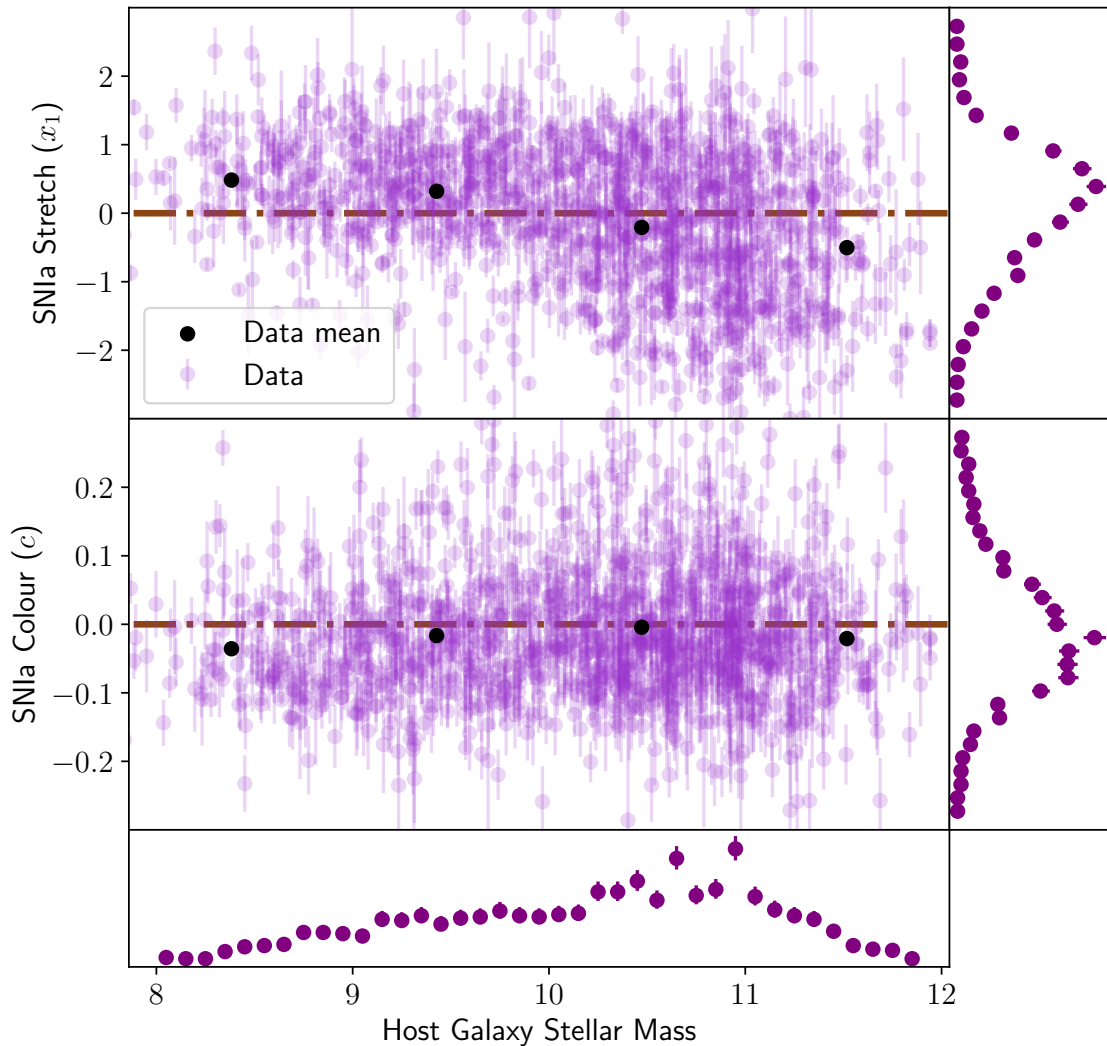


Figure 3.2: The distributions of c and x_1 for the combined Low- z , DES, PS1, Foundation, SNLS, and SDSS spectroscopic samples as a function of host-galaxy mass. Circles are the data; purple represent individual data points and black are the average value for that bin. The mass here is given as a logarithm, such that a value of 10 on the x-axis corresponds to a host galaxy mass of 10^{10} times the mass of our sun. The uncertainty on these averages is not shown here, but is present in Figure 3.5. The dash-dotted line is 0.

the data.

3.1.3 Measured Host Correlations

Here we present the results of fitting the parent populations as they correlate with stellar mass. The data presented here is a collection of spectroscopic high- z surveys (Pantheon+) and low- z surveys Foundation and Low- z .

We choose spectroscopically confirmed surveys here for two reasons. The first is historical - the infrastructure for creating robust simulations of photometric surveys did not exist. The second reason is the question of core collapse SNe. The question of core collapse contamination and its effects on standardisation and cosmological measurements has been well detailed in previous sections. The combination of high redshift surveys into a single sample is motivated by a need for improved statistics and a confidence in the survey modeling of the individual surveys. For Low- z , such confidence does not exist, so it is fit separately from Foundation.

These choices may nonetheless raise the question - "why not combine all surveys simultaneously? Why bother with the split between 'low redshift' and 'high redshift'?"

As we shall see, the redshift dependence of c and x_1 are a natural consequence of the selection effects of the survey. Figure 3.3 shows that the observed colour and stretch distributions depend on redshift for two reasons: 1) separate populations for low and high z , and 2) selection effects. The data-simulation agreement is reasonable, with $\chi^2/N = 4.8, 1.5,$ and 3.5 for stretch, colour, and M_{stellar} , respectively, where the number of degrees of freedom is $N = 10$.

We maintain the split between low and high redshift surveys because we still recover the desired redshift dependence, and because we need to remain consistent in

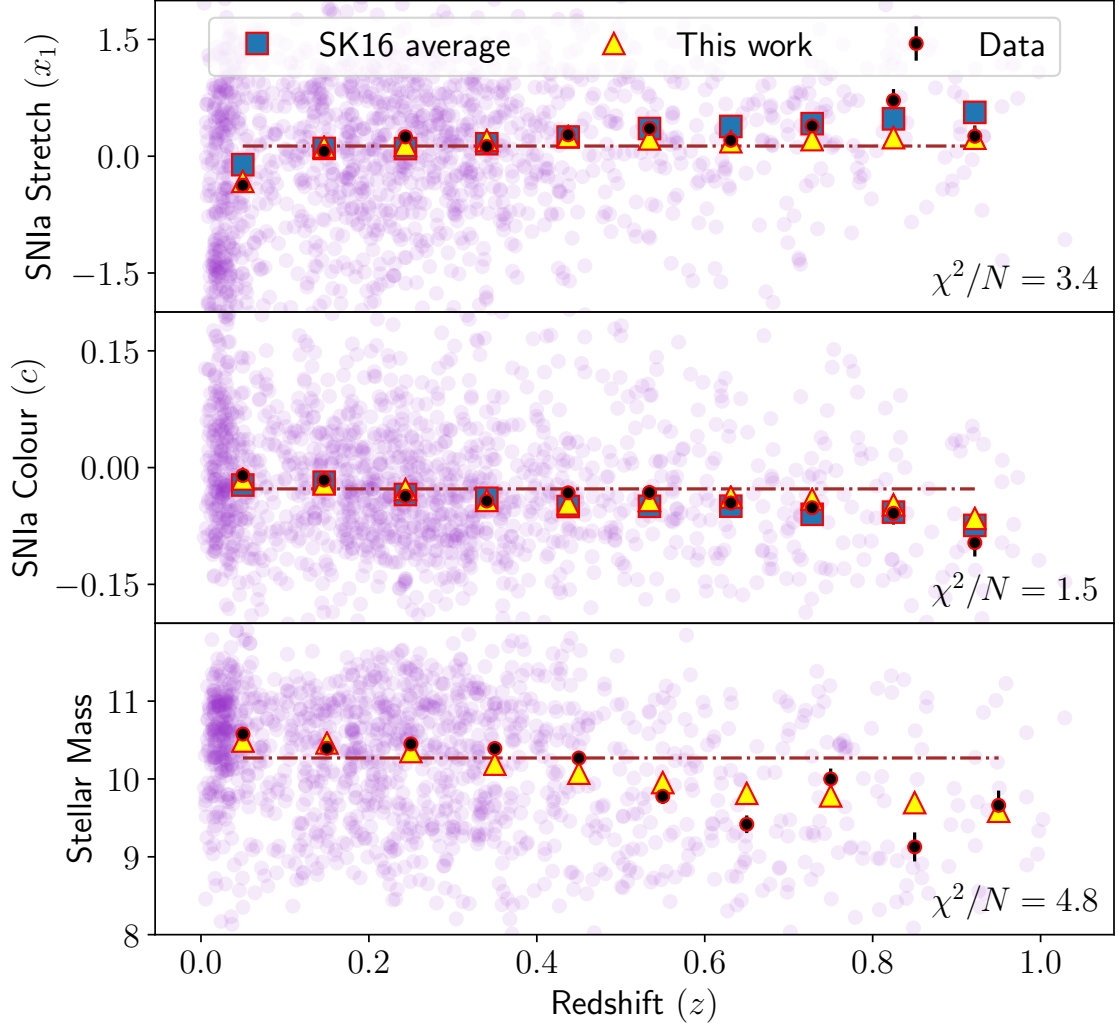


Figure 3.3: The redshift evolution of c , x_1 , and host-galaxy stellar mass for the combined sample. The data is presented in purple circles, and averaged bin values for the data are shown in red-lined black circles. The averaged bin values for the SK16 simulations are shown in red-lined blue squares, red-lined yellow triangles represent the average bin values for this work. Individual simulated events are not shown for clarity. We present the χ^2/N values for each parameter. SK16 assumes a flat distribution of M_{stellar} with redshift.

how we fit for populations. Because the low-redshift surveys have a double peaked x_1 distribution, we need to fit them separately from the high redshift surveys. While this does imply an evolution of the x_1 distribution with redshift, we are able to recover this behaviour without explicitly simulating it.

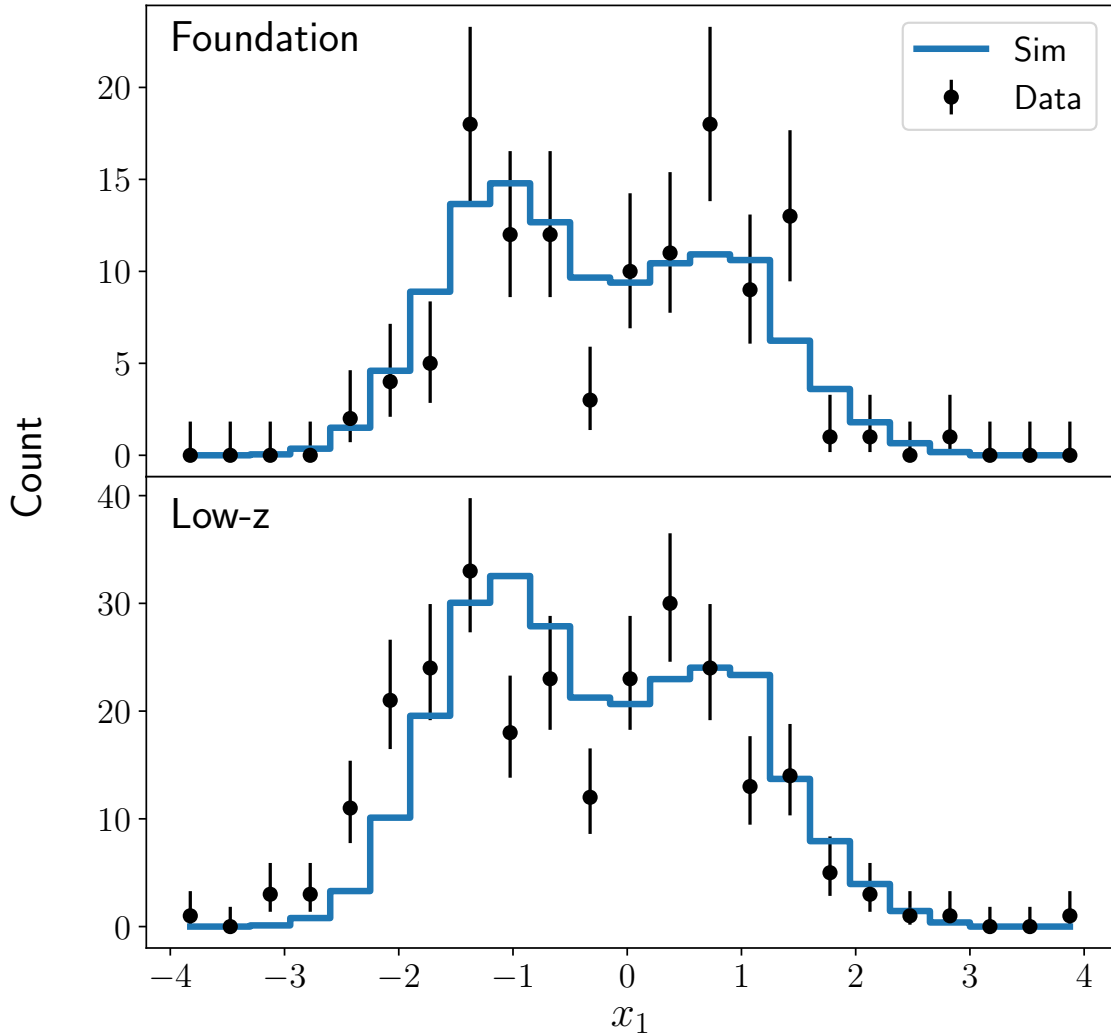


Figure 3.4: The x_1 distributions for Foundation and Low- z surveys. Data is presented in black circles and simulation is presented in blue histogram. The second low x_1 peak is present in both surveys, indicating that it is not caused by selection effects.

To model the double-peaked x_1 distribution in Low- z and Foundation, we found it

necessary to implement a prior requiring that $\overline{x}_{11} < 0$ and $\overline{x}_{12} > 0$ (Eq. 3.4). While we are able to capture the double-peak behaviour for both surveys, shown in Figure 3.4, there is a slight data-sim discrepancy near $x_1 \sim -2$ for the Low- z sample.

In Figure 3.5, we show the comparison between sim and data for c vs. M_{stellar} and for x_1 vs. M_{stellar} . We also show the M_{stellar} dependence of the underlying combined SDSS, DES, SNLS, and PS1 parent population. The Foundation and Low- z parent populations are shown separately in Figures 3.6 and 3.7 for colour and stretch respectively. There are three notable results. First, there is excellent agreement between the observed mean values for data and simulation. In the combined SDSS, DES, SNLS, and PS1 sample, this parent population also characterises the constituent individual surveys. Second, we find that both the intrinsic x_1 and c populations depend on M_{stellar} .

We evaluate the significance of M_{stellar} dependence by comparing each curve in Figure 3.5 to a null model that has no M_{stellar} dependence. For the x_1 distribution, σ_+ is consistent with no M_{stellar} dependence with a confidence of 99.9%. The probability that σ_- has no M_{stellar} dependence, however, is 1E-8. This means that the observed x_1 dependence on mass is driven by σ_- increasing with increasing masses. Similarly, \overline{x}_1 has a low probability of being independent of M_{stellar} at only 0.01%, but does not correlate with the observed distribution and is therefore unlikely to be the primary driver. For the colour distribution, σ_- and \overline{c} are consistent with no M_{stellar} dependence with a confidence of 90%. Similarly to x_1 , the probability that the faint-side σ_+ has no M_{stellar} dependence is 99.9%. Taken together, this constitutes the third notable result: the M_{stellar} dependence of the observed c and x_1 distributions is driven by increasing faint-side widths (σ_- for x_1 and σ_+ for c) rather than a shift in the mean values.

The evolution of the parent populations with M_{stellar} is shown in Figures 3.6 and

3.7 respectively. We find evidence for two distinct populations of x_1 in the low redshift samples, with little overlap between them.

This discovery leaves us with a host of problems. The first is the (relatively) simple finding that there is a difference between the observed SNIa light curve fit parameters and the true ones. This presents difficulties in using the Tripp formula (2.3), as the naive choice of c and x_1 are likely to be divergent from the expected luminosity correlation. The second issue is a further incompleteness of the Tripp formula: it has no dependence on the host galaxy. If the true populations of SNIa light curve fit parameters are not an uncorrelated draw from an underlying distribution, and are instead strongly correlated with the properties of their hosts, then some correction is needed to account for this correlation. While the mass step does work as an *ad-hoc* solution to the anomalous luminosity difference, it is not sufficient to explain these host-galaxy correlations, nor is it desired.

Before we address these issues, we need to take a detour to discuss an alternative methodology for describing SNIa scatter: dust.

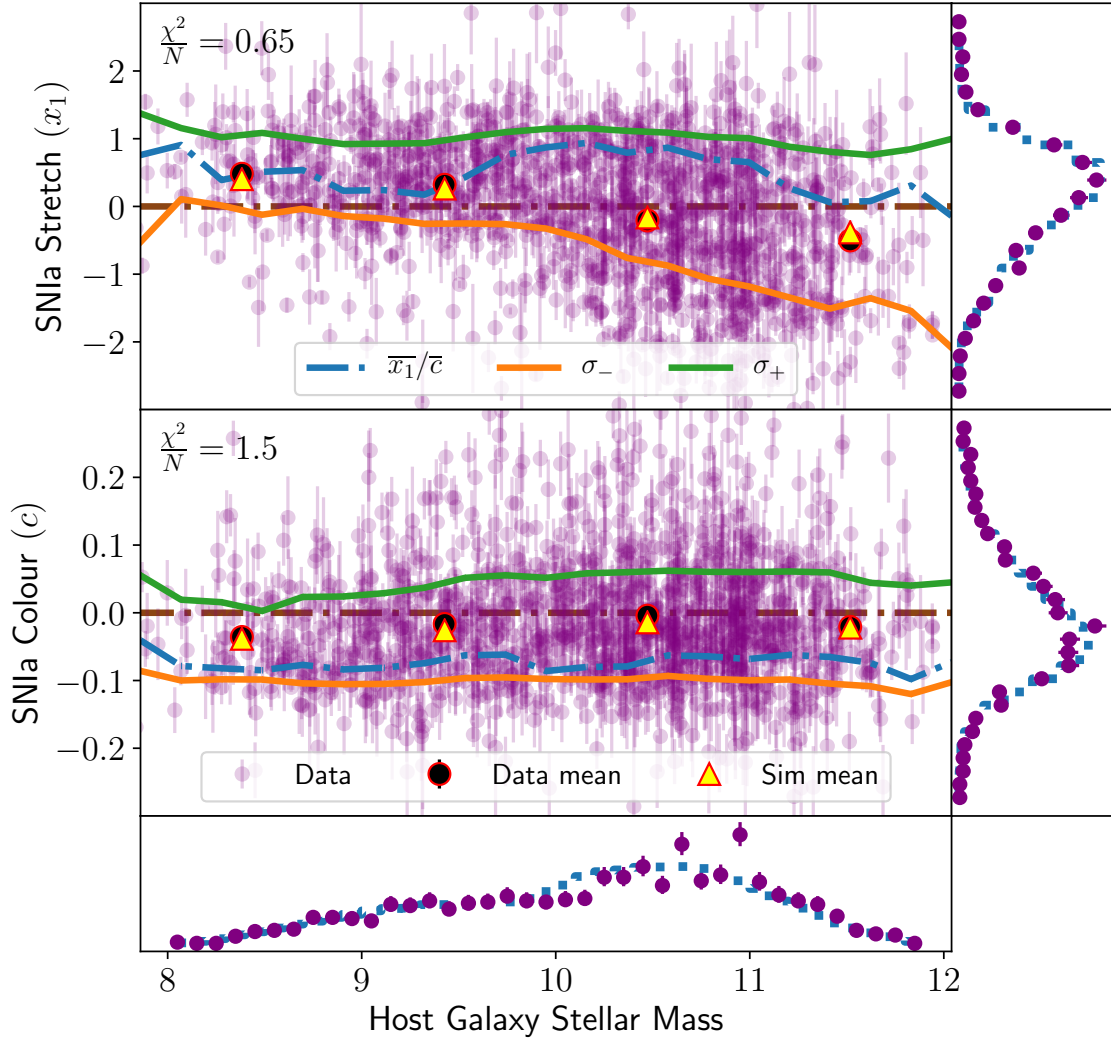


Figure 3.5: The distributions of c and x_1 for the combined DES, PS1, SNLS, and SDSS spectroscopic samples as a function of host-galaxy mass. Circles are the data; purple represent individual data points and black are the average value for that bin. Solid lines are the G10 parent population parameters: green is σ_+ , blue is the peak value, and orange is σ_- . The dash-dotted line is 0. The bin averages for the data are presented in red-lined black dots, for the simulations, red-lined yellow triangles. The histograms on the side show data in circles and simulated results in dashed line. For both c and x_1 we find good agreement between the mean value in data and sims, with a $\chi^2/N = 1.5$ and $\chi^2/N = 0.65$ respectively.

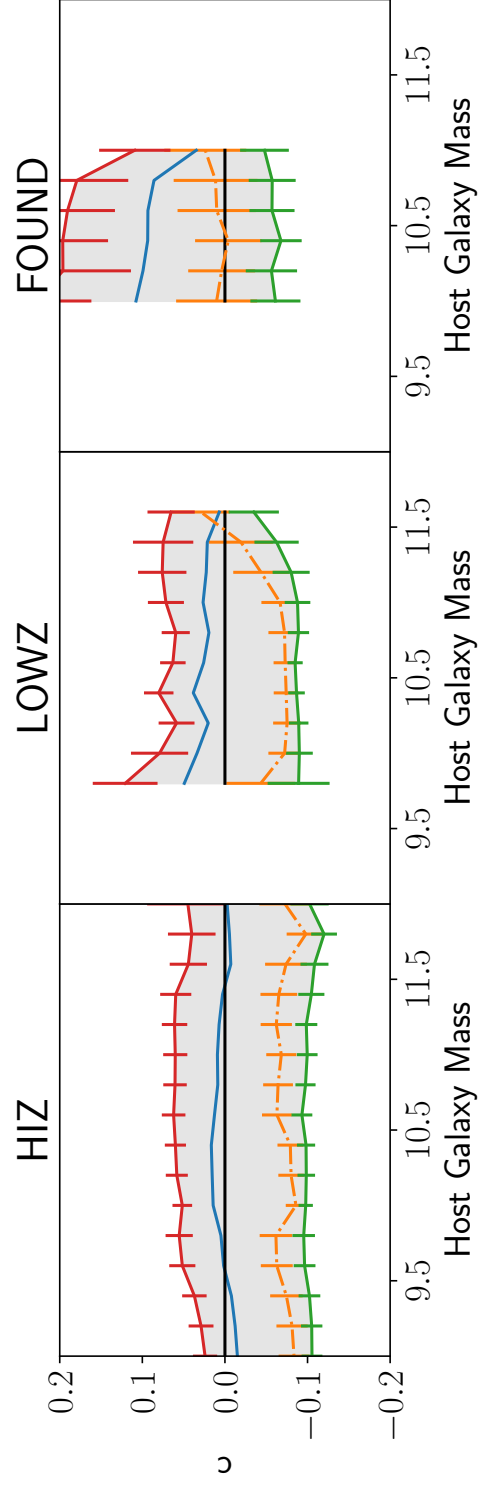


Figure 3.6: The G10 c parent populations as a function of host-galaxy mass for several spectroscopic surveys. The mean of the asymmetric distribution is presented in blue, the peak in orange, the bright-side standard deviation in green, and the faint-side standard deviation in red. Errors are included for each parameter and the 68% confidence interval for each is shown in grey fill.

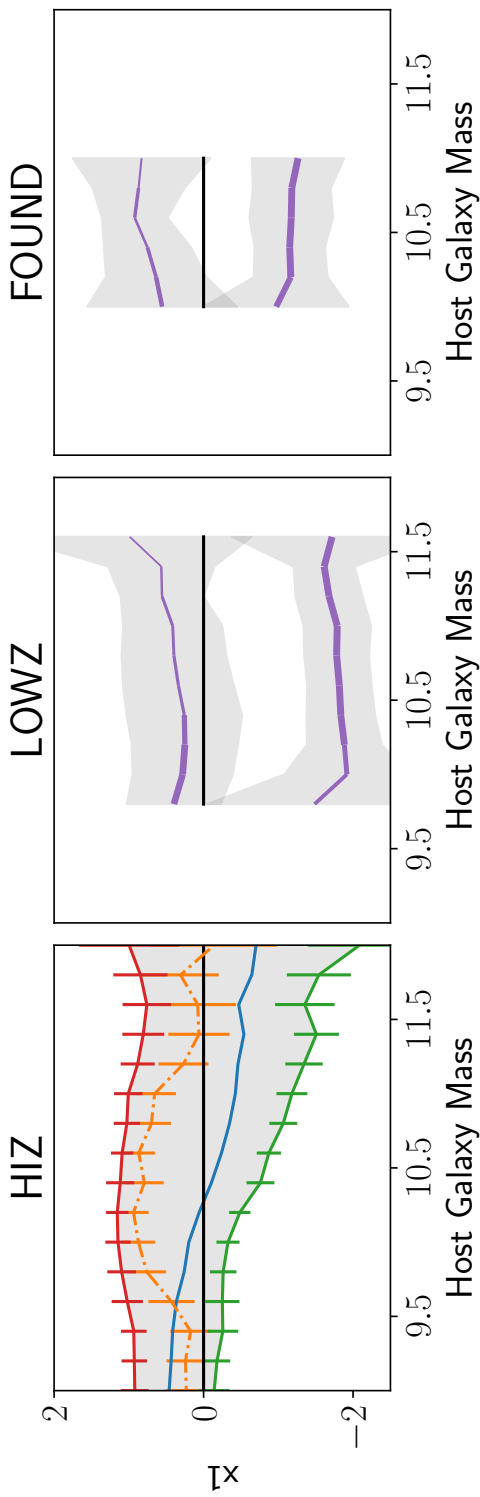


Figure 3.7: The G10 x_1 parent populations as a function of host-galaxy mass for several spectroscopic surveys. The mean of the asymmetric distribution is presented in blue, the peak in orange, the faint-side standard deviation in green, and the bright-side standard deviation in red. Errors are included for each parameter and the 68% confidence interval for each is shown in grey fill. For Foundation and Low-z, two peak values are shown by purple lines, and the line thickness denotes the relative weight of each peak.

This is the Accepted Manuscript version of an article accepted for publication in The Astrophysical Journal. IOP Publishing Ltd is not responsible for any errors or omissions in this version of the manuscript or any version derived from it. The Version of Record is available online at the following doi: [10.3847/1538-4357/abf14f](https://doi.org/10.3847/1538-4357/abf14f)

Chapter 4

Dust in the Wind

The results presented in this chapter, as well as some portions of text, are from Popovic et al. (2021). The text represents my own work, and the contributions of other authors is presented as such:

- *Dillon Brout: Implementation of initial codebase. Responsible for the idea to implement a wrapper program for SALT2mu, and wrote the early function definitions. These would end up being entirely rewritten by me, though I did take cues from the code structure.*
- *Richard Kessler: Implementation of code within SNANA to interact with the Dust2Dust program I wrote.*
- *Daniel Scolnic: Advising, including suggesting additional metrics to determine goodness of fit and aid with non-code related conceptual issues.*

SNIa cosmology is, as has been previously mentioned, an empirical science. Our lack of understanding on the exact explosion mechanism of type Ia supernovae requires approximations. Light curve fitters, and standardisation, are a good example of this. We make some sacrifices in completeness for gains in usefulness as a cosmological measurement. One of the biggest sacrifices in the ‘modern’ cosmological era — 2014 and beyond — has been disregarding the effects of dust on our observed light curves. Betoule et al. (2014) presented the SALT2.JLA surface, and along with it one of the most robust cosmological measurements with SNIa at the time (and still an impressive measurement today). But SALT2.JLA had a knock-on effect. By being

an important and widely-used light curve fitter that ignored the impact of dust on light curves, it would influence the next 6 years to similarly disregard dust. In 2021, Brout (2021) released a paper that incorporated dust into the SALT light curve fitter for the first time. A robust framework was established, but the question of how to tune the model parameters for that framework was left largely unaddressed. In this chapter, we shall prescribe a method to extract information about dust parameters from SNIa data.

4.1 Dust

Here we switch tactics from the previous section. Chapter 3 focused on intrinsic populations, yes, but specifically intrinsic populations through the lens of conventional, SED-variational scatter models such as G10 and C11 (see Section 7.5.5). These scatter models, by construction, assume a single dust law for all supernovae. This is rather unphysical, and many of the shortcomings of conventional simulations that we shall address in this section stem from this assumption. Consider this chapter to present an alternative approach to the beginning of Figure 2.9, a new way of interpreting intrinsic populations and scatter models.

Recall that we defined astronomical reddening in Equation 2.1 as

$$E(B - V) = (B - V)_{\text{observed}} - (B - V)_{\text{intrinsic}}, \quad (4.1)$$

a common cause of which is dust (see the SALT colour law in 2.1.3 as an example of a rough estimation of reddening effects).

Obviously nature does not particularly care which band is used, or even have a conception of what a band is, so the choice of bands is a historical artifact. We need

not even observe in the B or V bands to calculate reddening; converting between bandpasses is a relatively simple linear equation.

Measuring reddening relies on knowing the intrinsic colour of an astronomical body - for SNIa we have already explained how the SALT model accomplishes a rough estimation of reddening by assuming a single R_v , though we left a detailed explanation of why R_v is important till now.

R_v is defined as

$$R_v = A_v / E(B - V) \tag{4.2}$$

where $E(B - V)$ is the reddening term and A_v is the circularly-defined ‘total extinction’. R_v can be understood as a measurement of the particulate size and orientation of dust in a region. While any celestial object will have an A_v measurement (and therefore an associated R_v and $E(B - V)$, though these may be difficult to ascertain), R_v is most important as a measurement in those most dusty regions: galaxies. Studies have shown a wide range of R_v values for galaxies: the Milky Way has an R_v of 3.1 on average, but even the Large Magellanic Cloud and the Small Magellanic Cloud exhibit variations with R_v ranging from 2 to 5.

History is unfortunately a matter of convenience rather than rigour. Much like how Equation 2.1 favours the B and V bands, the concept of a variable R_v was largely dropped in SNIa cosmology at the turn of the 2010s. This is largely due to the convenience of SALT2 incorporating native k-corrections and updated calibration compared to its main competitor, Multicolor Light Curve Shapes (MLCS2k2), developed by Jha et al. (2007). While we shall not delve too much into MLCS2k2 in this thesis, as it is largely ancillary to the research being done here, it is worth noting a feature of this light curve fitter that the SALT model lacked. MLCS2k2 attempted to assign each SNIa its own physical extinction law as part of the fitting

process, rather than assuming a non-physical universal colour law like SALT. This R_v modeling, alongside attributing a large part of intrinsic scatter to colour variations, were the first modern steps into modeling the astrophysical processes behind SNIa measurements. Unfortunately, the idea of incorporating external effects was largely left in the dust in the coming years.

4.1.1 BS20

It was not until Brout & Scolnic (2021), hereafter BS20 (or BS21; they are used interchangeably), was published that dust once again came to fore. Inspired by papers such as Mandel et al. (2017) and Scolnic et al. (2014, 2018), BS20 investigated the impact of including dust in the SALT framework.

Figure 4.1 shows the Hubble Residuals (4.1b) and the RMS of the Hubble Residuals (4.1a) for real data and three models of intrinsic scatter. The first two, G10 and C11, are familiar, but noticeably fail to capture the trend of increasing Hubble Residual RMS with SALT colour c . The third one, BS20, does.

Here we present a review of the BS20 model. BS20 attributes observed SNIa colours to two components: a colour component intrinsic to SNIa properties, c_{int} , and a dust component described by a distribution of reddening values drawn from the extinction ratio R_V (E_{dust}). The observed colour, c_{obs} , is modeled as

$$c_{\text{obs}} = c_{\text{int}} + E_{\text{dust}} + \epsilon_{\text{noise}}. \quad (4.3)$$

where ϵ_{noise} is measurement noise otherwise unaccounted for.

The dust reddening component E_{dust} from Eq. 4.3 is interpreted as $E(B - V)$ so

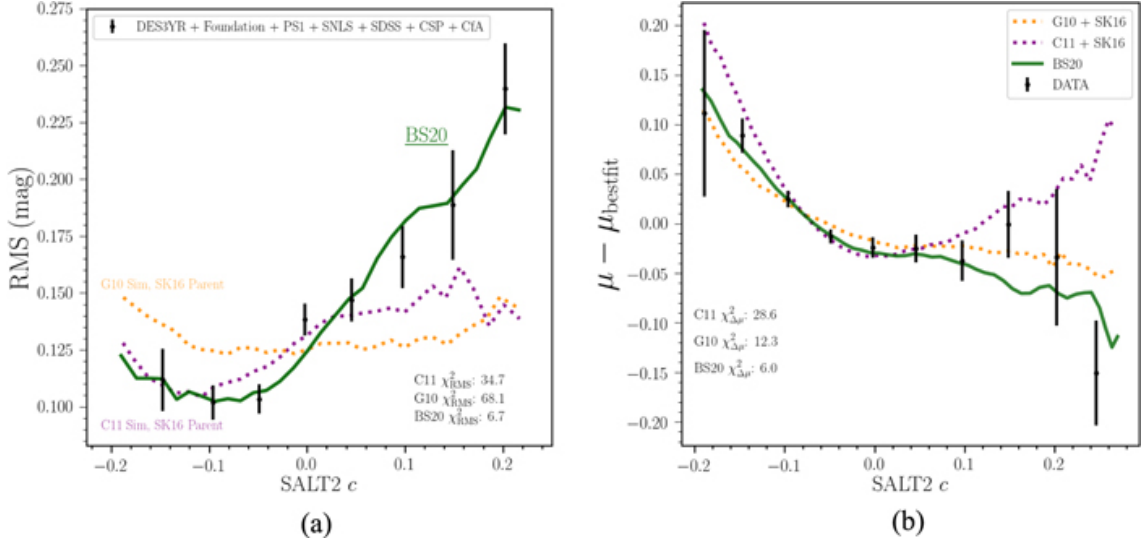


Figure 4.1: Panel (a) shows the RMS of the Hubble Residuals as a function of c for real data and three different models of intrinsic scatter. Real data is presented in black dots, the BS20 model is in green line, G10 is in yellow dotted line, and C11 is in purple dotted line. Panel (b) is the same but for the Hubble Residuals as a function of colour. From Brout & Scolnic (2021).

that the V -band extinction is given by

$$A_V = R_V \times E_{\text{dust}} \quad (4.4)$$

where R_V is selective extinction and $E_{\text{dust}} = E(B - V)$. The change in observed brightness is modeled as

$$\Delta m_B = \beta_{\text{SN}c_{\text{int}}} + (R_V + 1)E_{\text{dust}} + \epsilon_{\text{noise}}. \quad (4.5)$$

Figure 4.2, taken from the BS20 paper, shows a diagram of how this dust model affects different aspects of SNIa measurements. The observed colour distribution in the data can be intuitively explained by a symmetric parent population that is reddened by dust, rather than an asymmetric Gaussian parent population. The middle panel shows the RMS of the Hubble Residuals, which are well explained

by increasing extinction with colour. Finally, the shape of the Hubble Residuals themselves implies different colour-luminosity relationships for different subsets of colours in SNIa data.

This approach leaves arbitrary choices for parametric modeling of distributions. BS20 uses the following 7 parameters for SNIa:

- \bar{c} : the Gaussian mean of intrinsic colour distribution.
- σ_c : the Gaussian sigma of intrinsic colour distribution.
- $\bar{\beta}_{\text{SN}}$: the Gaussian mean of distribution for intrinsic colour-luminosity correlation.
- $\sigma_{\beta_{\text{SN}}}$: the Gaussian sigma of distribution for intrinsic colour-luminosity correlation.
- \bar{R}_V : the Gaussian mean of R_V distribution.
- σ_{R_V} : the Gaussian sigma of R_V distribution.
- τ_E : describes the exponential distribution for E_{dust} .

Note that β_{SN} and β_{SALT2} are different parameters. β_{SALT2} , along with α_{SALT2} , are determined from a global fit of the fitted SALT2 parameters. In the BS20 model, β_{SALT2} is a convolution of β_{SN} and other dust effects. Similarly, the observed colour distribution, c_{obs} , is described by a symmetric intrinsic distribution combined with a dust model that accounts for the red tail observed in the data. The c_{obs} distribution can be phenomenologically replicated with an asymmetric Gaussian as done in Scolnic & Kessler (2016) or Popovic et al. (2021).

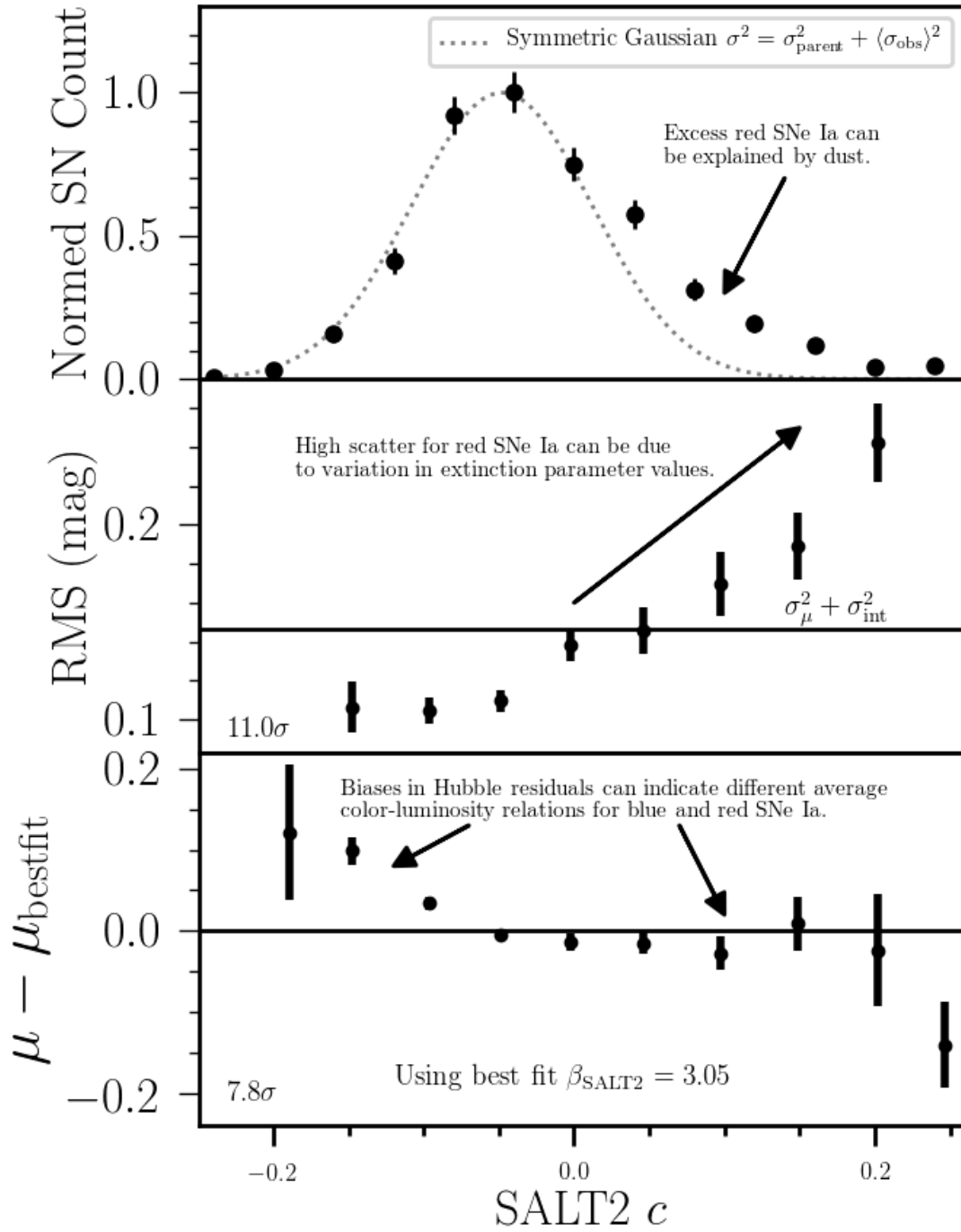


Figure 4.2: **Top:** An observed colour distribution in black circles with an intrinsic, dustless distribution overlaid in dotted line. **Middle:** The RMS of the Hubble Residuals as a function of colour. **Bottom:** The Hubble Residuals. For the bottom two panels, the significance of the deviation from a flat line is given. From Brout & Scolnic (2021).

The intrinsic colour is described as

$$P(c_{\text{int}}) = \frac{1}{\sqrt{2\pi}\sigma_c} e^{-(c_{\text{int}}-\bar{c})^2/2\sigma_c^2}. \quad (4.6)$$

Following Riess et al. (1996) and Jha et al. (2007), these E_{dust} values are drawn from an exponential distribution with probability

$$P(E_{\text{dust}}) = \begin{cases} \tau_E^{-1} e^{-E_{\text{dust}}/\tau_E} & , E_{\text{dust}} > 0 \\ 0 & , E_{\text{dust}} \leq 0 \end{cases} \quad (4.7)$$

where τ_E is described above.

The R_V distribution is characterised by

$$P(R_V) = \frac{1}{\sqrt{2\pi}\sigma_{R_V}} e^{-(R_V-\bar{R}_V)^2/2\sigma_{R_V}^2} \quad (4.8)$$

where \bar{R}_V and σ_{R_V} are model parameters described above. R_V values below 0.4 are excluded.

The correlation between SNIa luminosity and intrinsic colour, β_{SN} , is described with a Gaussian probability,

$$P(\beta_{\text{SN}}) = \frac{1}{\sqrt{2\pi}\sigma_{\beta_{\text{SN}}}} e^{-(\beta_{\text{SN}}-\bar{\beta}_{\text{SN}})^2/2\sigma_{\beta_{\text{SN}}}^2}. \quad (4.9)$$

with model parameters $\bar{\beta}_{\text{SN}}$ and $\sigma_{\beta_{\text{SN}}}$.

Equation 4.5 implies something unique that other models of intrinsic scatter lack; that is, a direct astrophysical explanation for changes in observed SNIa luminosity. This feature, combined with the range of galaxies that can host SNeIa, inspired BS20 to investigate how dust may explain that most famous of SNIa standardisation

Table 4.1: Fitted Parameters in BS20 Model

BS20 Param	N_{par}
Gaussian c_{int}	2
Gaussian β_{SN}	2
Gaussian R_V (low mass)	2
Gaussian R_V (high mass)	2
Exponential E_{dust} (low- z , low mass)	1
Exponential E_{dust} (low- z , high mass)	1
Exponential E_{dust} (high- z , low mass)	1
Exponential E_{dust} (high- z , low mass)	1
Total	12

mysteries, the mass step.

To account for host-galaxy correlations, BS20 split the R_V and E_{dust} distributions on host-galaxy stellar mass, specifically across galaxies with $M_{\text{stellar}} > 10^{10} M_{\odot}$ (high mass) and those with $M_{\text{stellar}} < 10^{10} M_{\odot}$ (low mass). The E_{dust} distributions were split between low z surveys and high z surveys as well as mass; however, the c_{int} and β_{SN} distributions are not split on host-galaxy stellar mass, as the model predicts that c_{int} and β_{SN} are intrinsic to SNIa and not their environments.

This splitting raises the number of fitted model parameters to 12. An accounting of the parameters and summary of the number of dimensions is shown in Table 4.1.

As Figure 4.3 shows, there is a significant difference between the Hubble Residuals of low mass and high mass galaxies - one that is, on average, 0.05 magnitudes.

4.1.2 Determining Dust Model Parameters

In contrast to Scolnic & Kessler (2016) and Popovic et al. (2021), which interpreted c_{obs} to come from a single underlying parameter, here the nature of the BS21 model is that several intrinsic populations (e.g c_{int} , R_V , $E(B - V)$, and β_{SN}) inform c_{obs} . This added model complexity results in the need to forward model, where simulations

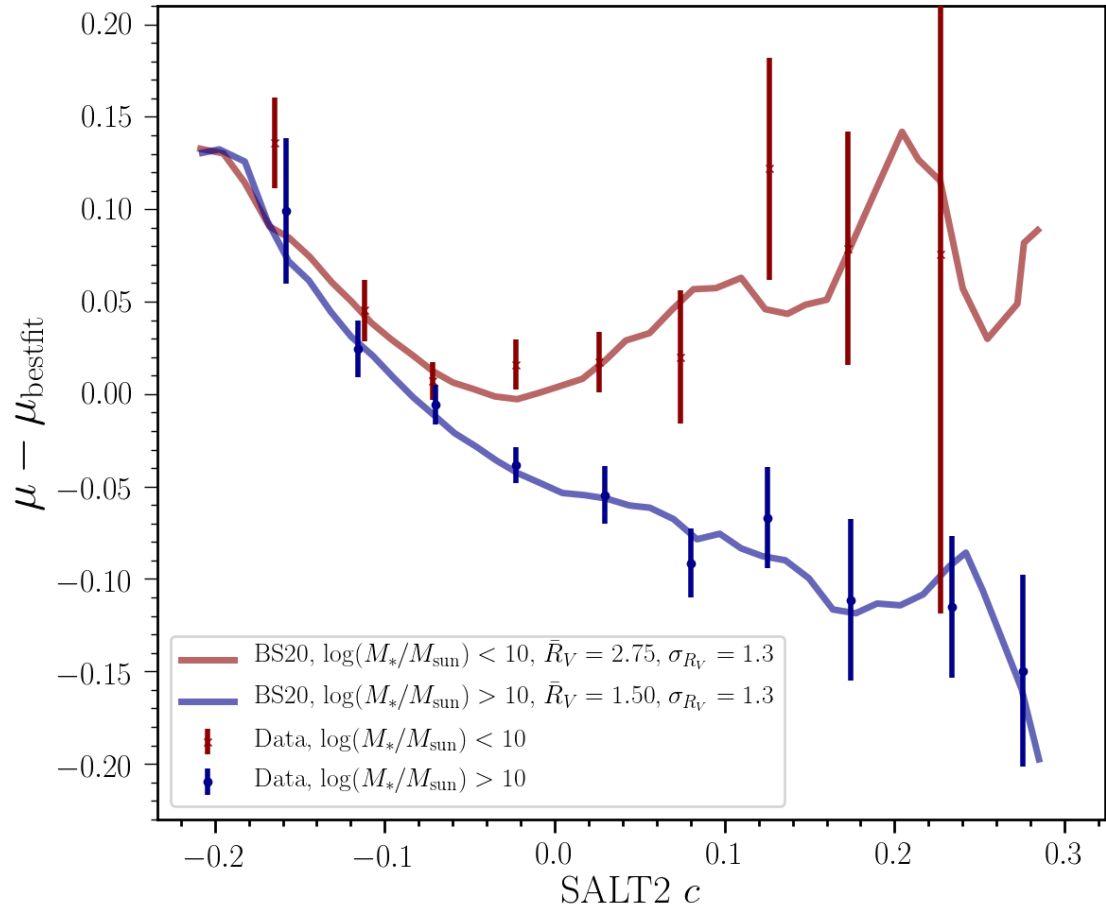


Figure 4.3: The binned Hubble Residuals as a function of c and split on host galaxy stellar mass. The points represent data and the lines are from simulations. Red is for low mass ($M_{\text{stellar}} < 10$) and blue represents high mass ($M_{\text{stellar}} > 10$). From Brout & Scolnic (2021).

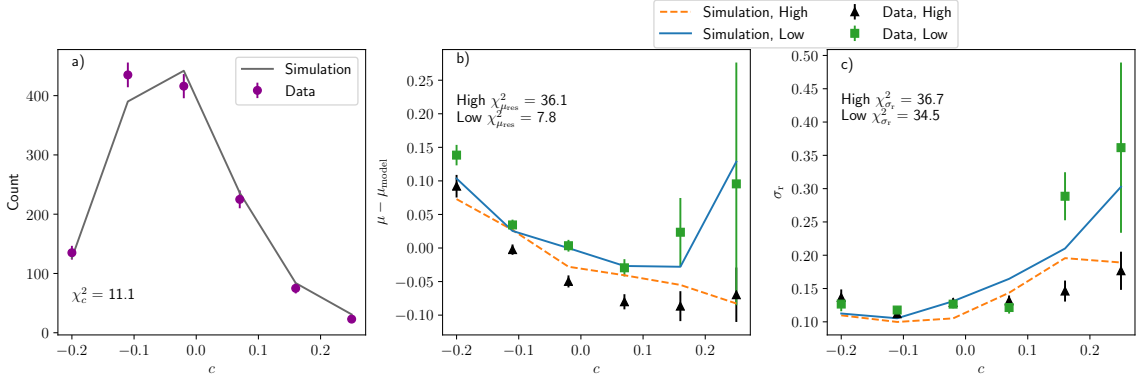


Figure 4.4: Plots of the metrics described in Section 4.1.2. The c histogram, c vs μ_{res} , and c vs σ_r are shown from left to right. The latter two plots are split on high and low mass. Plot a) is the observed colour (c) distribution with purple circles as histogram data and solid grey as simulated histogram. Plot b) is μ_{res} vs c split on high and low host-galaxy mass. Plot c) is σ_r of μ_{res} vs. c . Green squares are low mass data and black triangles are high mass data, while blue plot is low mass simulation and orange dotted plot is high mass simulation. We can see good agreement between data and simulation for our best fit parameters.

generated from a set of intrinsic parameters are analysed in the same way as the data in order to compare the observed and simulated distributions.

The BS21 paper found their model parameters by a coarse, 1-dimensional grid search, fixing all parameters but one and finding the local minimum. This process was time consuming, complex, and difficult to replicate. Their results are shown in Table 4.4. We aim to improve upon this by both speeding up the simulation generation process, automating the χ^2 search, and incorporating multi-dimensional fitting. But first, we must review the process by which we infer our dust parameters.

We infer these dust-model parameters from observables that exist in conventional SNIa cosmological analyses. Dust2Dust uses the three constraints illustrated in Figure 4.4, evaluated in 6 colour bins ranging from $c = -0.2$ to $c = 0.25$ (encompassing more than 99% of our sample). Scolnic & Kessler (2016) used Figure 4.4a, the histogram of observed c values; following BS21 we extend our constraints to include Hubble Residuals vs. c (Fig. 4.4b) and Hubble Residual scatter vs. c (Fig. 4.4c)

to better constrain models with additional complexity. A single colour χ^2 does not, by itself, contain enough information to separate the component pieces of the model. Broadly, the \bar{R}_V value dictates the slope of the Hubble Residual values as a function of colour (Fig. 4.4b), and σ_{R_V} drives both the colour-luminosity relation for the very reddest SNe (Fig. 4.4b), and separately, the Hubble Residual scatter vs. c (4.4c). The distribution of β_{SN} affects both the observed β_{SALT2} , as well as providing a scatter floor for Hubble Residual scatter vs. c (Fig. 4.4c). In addition to colour-dependent constraints, Dust2Dust includes a data-simulation constraint on β_{SALT2} and σ_{int} , though these do not have a graphical representation. The latter two constraints are determined by performing an ‘SALT2mu Fit’ (see 2.1.8) at each Markov-Chain Monte Carlo (MCMC) step. For quantities that define the constraints, uncertainties are determined from the data, with the exception of σ_{int} , which is discussed in detail later in the section.

The first Dust2Dust constraint (Figure 4.4a) is a χ^2 term of fitted c :

$$\chi_c^2 = \sum_i (N_{c_i}^{\text{data}} - N_{c_i}^{\text{sim}})^2 / e_{ni}^2 \quad (4.10)$$

where $N_{c_i}^{\text{data}}$ is the number of SNIa in colour bin i in the data, $N_{c_i}^{\text{sim}}$ is the number of SNIa in colour bin i in the simulation after scaling the integrated sum to match the data, and the uncertainty, e_{ni} , is

$$e_{ni} = 1/\sqrt{N_{c_i}^{\text{data}}} \quad (4.11)$$

The second constraint (Figure 4.4b) is based on the relationship between c and the distance modulus residual μ_{res} ,

$$\mu_{\text{res}} = \mu - \mu_{\text{model}} \quad (4.12)$$

where μ is the measured distance modulus from Equation 2.3 and μ_{model} is a reference cosmology. The Hubble residual constraint is

$$\chi_{\mu_{\text{res}}}^2 = \sum_i (\mu_{\text{res}_i}^{\text{data}} - \mu_{\text{res}_i}^{\text{sim}})^2 / e_{\mu_{\text{res}_i}}^2 \quad (4.13)$$

where $\mu_{\text{res}_{ci}}$ is the μ_{res} in each c bin and the error is

$$e_{\mu_{\text{res}_i}} = \frac{\sigma_{ri}}{\sqrt{N_{ci}}} \quad (4.14)$$

where σ_{ri} is the robust scatter:

$$\sigma_r(X) = 1.48 * \text{median}(|X|) \quad (4.15)$$

and N_{ci} is the number of SNIa in each c bin.

The third constraint (Figure 4.4c) is the relationship between c and the Hubble residual scatter

$$\chi_{\sigma_r}^2 = \sum_i (\sigma_{ri}^{\text{data}} - \sigma_{ri}^{\text{sim}})^2 / e_{\sigma_{ri}}^2 \quad (4.16)$$

where $e_{\sigma_{ri}}$ is defined as

$$e_{\sigma_r} = \frac{\sigma_{ri}}{\sqrt{2N_{ci}}} \quad (4.17)$$

from Group et al. (2020) Equation 40.7.

4.1.3 SALT2mu Fit

The colour-luminosity relationship, β_{SALT2} , and the post-standardisation intrinsic scatter, σ_{int} , along with α_{SALT2} and absolute luminosity $M(z_i)$, are determined from a global fit of the data following SALT2mu and Equation 3 in Kessler & Scolnic (2017). This SALT2mu fit is performed at each step of the MCMC chain as part

of the larger Dust2Dust method, and SALT2mu fit results are used to evaluate the following Dust2Dust constraints:

$$\chi_{\beta_{\text{SALT2}}}^2 = (\beta_{\text{SALT2}}^{\text{data}} - \beta_{\text{SALT2}}^{\text{sim}})^2 / e_{\beta_{\text{SALT2}}}^2 \quad (4.18)$$

and

$$\chi_{\sigma_{\text{int}}}^2 = (\sigma_{\text{int}}^{\text{data}} - \sigma_{\text{int}}^{\text{sim}})^2 / e_{\sigma_{\text{int}}}^2 \quad (4.19)$$

where $e_{\beta_{\text{SALT2}}}^2$ is given by the SALT2mu fit. SALT2mu does not provide uncertainties for σ_{int} ; therefore, we simulate 150 independent data-sized samples and estimate the uncertainty as the observed σ_{int} dispersion across these samples. We find $e_{\sigma_{\text{int}}} = 0.0036$.

The SALT2mu fit is implemented by the Beams with Bias Corrections (BBC) code from Kessler & Scolnic (2017), however, in our case, explicit bias corrections are not necessary because constraints (Eqs. 4.10, 4.13, 4.16) are based on data and sims that are processed with the same SALT2mu fit. Thus Dust2Dust accounts for selection effects from analysing simulated samples, not from BBC bias corrections.

4.1.4 Dust2Dust Model Fitting

Here, we improve on the BS21 fitting of parameters by developing a MCMC program, named Dust2Dust, to both provide robust error modeling and the simultaneous fitting of the model parameters. The forward-modeling process contains two steps: A SALT2mu fit is performed on the data and simulated supernova, and the results of this fit are used in the Dust2Dust likelihood to propose new steps in the MCMC chain.

A brief overview of the Dust2Dust process is provided in Figure 4.5 and summarised here:

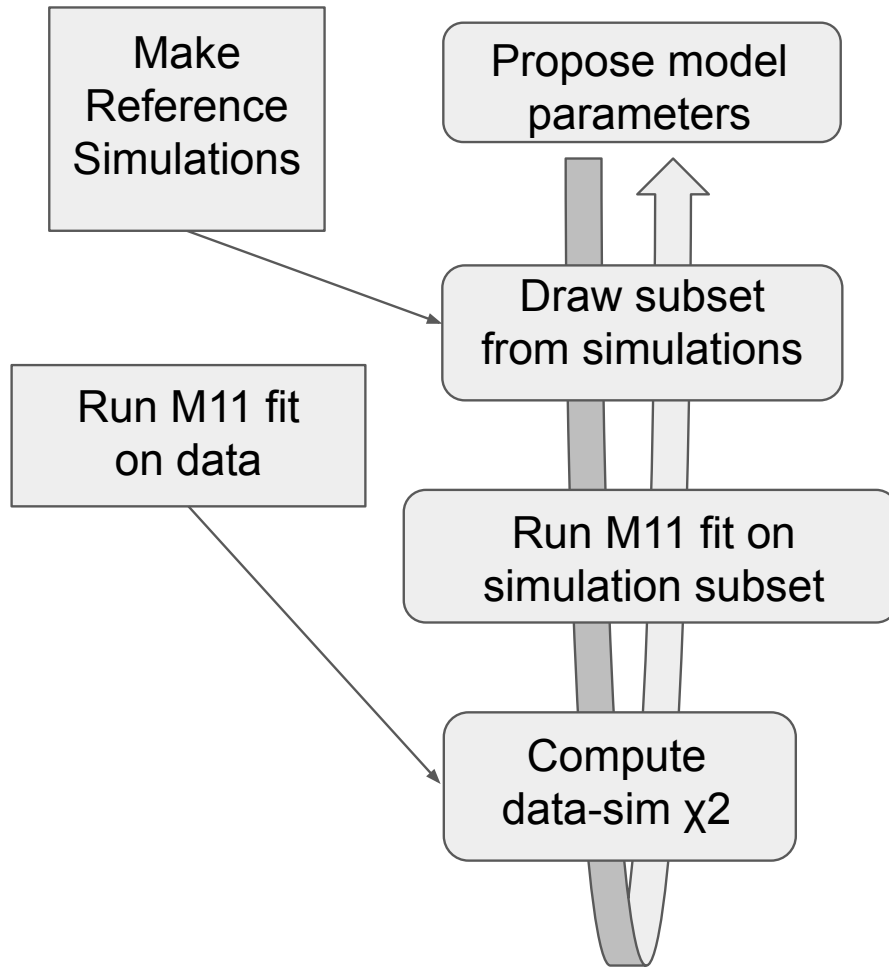


Figure 4.5: Pictograph of the Dust2Dust process. The requisite flat simulations are generated and SALT2mu is run on the data independently of the iterative process. The iterative steps are denoted with rounded corners; the model parameters from the BS21 model are proposed and a matching subset is drawn from the flat distributions. This subset then has the SALT2mu run on it, and the results are compared to the data.

- Before running Dust2Dust, a reference simulation is created for Dust2Dust to quickly sample the parameter space.
- Dust2Dust proposes a specific set of model parameters from the BS21 model.
- Dust2Dust importance-samples from the reference simulation to create a weighted simulation, characterised by the proposed set of model parameters.
- The SALT2mu fit is run on both the data and Dust2Dust-created weighted simulation.
- A data-sim χ^2 is computed for the proposed model parameters and is used to inform the next proposed model parameters.

Details of the Dust2Dust process are as follows. Dust2Dust begins with generating reference simulations (as described in Section 2.2) containing bounding distributions of our model parameters, both SNIa and host-galaxy properties. Of note, the simulated x_1 distribution is excluded from the Dust2Dust process, as the BS21 model does not propose a relationship between x_1 and host-galaxy mass. Instead, the simulations are generated with stretch distributions taken from Popovic et al. (2021), which include correlations with host-galaxy mass. These reference simulations are fitted with the SALT2 model and used in the MCMC process.

At each MCMC step, a new simulation is extracted by randomly selecting a subset of SNe from the reference simulation as follows. For SNIa parameters $\vec{\Theta} = \theta_i, i = 1, 2, 3, 4$, we define for each event

$$\begin{aligned}
 p_{\text{ref}} &= \prod_{i=1}^4 p_{\text{ref}_i}(\text{Ref Sim Params}) \\
 p &= \prod_{i=1}^4 p_i(\text{MCMC Params})
 \end{aligned}
 \tag{4.20}$$

where p_{ref_i} is the bounding function probability for the i_{th} parameter used to generate the reference/bounding simulation, and p_i is the probability of the SNe in the weighted simulation for the current MCMC step. The weight function for each event in the ref sim is

$$P(X) = \begin{cases} \text{if } \frac{p}{p_{\text{ref}}} < U([0, 1]), & 0 \\ \text{if } \frac{p}{p_{\text{ref}}} \geq U([0, 1]), & 1 \end{cases} \quad (4.21)$$

where $U([0, 1])$ is a random number in the range $[0, 1]$.

For τ_E , the bounding function is $(1/\tau)e^{-E_{\text{Dust}}/\tau}$. For Gaussian distributions, our bounding function is chosen to be a ‘flat top’ asymmetric Gaussian that is uniform between two boundaries, μ_1 and μ_2 (where $\mu_1 < \mu_2$), with standard deviations σ_1 and σ_2 :

$$P(X) = \begin{cases} e^{-(X-\mu_1)^2/2\sigma_1^2} & \text{if } X \leq \mu_1 \\ 1 & \text{if } \mu_1 < X < \mu_2 \\ e^{-(X-\mu_2)^2/2\sigma_2^2} & \text{if } X \geq \mu_2 \end{cases} \quad (4.22)$$

An example of this bounding function, along with the reweighting from Equation 4.21, is shown in Figure 4.6. Both the resulting distribution and the bounding function are normalised to have a peak probability of 1, though the bounding function does not integrate to unity by design.

This bounding function approach saves time by simulating fewer SNIa in parameter spaces that are unlikely to be used. The increase in efficiency can be approximated as the quotient of the areas covered by the bounding function and a uniform distribution, raised to the number of dimensions. In the case that all 4 of our reference distributions are bounded similarly to Figure 4.6, the quotient is ~ 1.3 , and the computational efficiency is approximately $1.3^4 \sim 4$ times more efficient than uni-

form distributions. The combination of reference simulation, bounding functions, SALT2mu fits, and the `emcee` package (from Foreman-Mackey et al. (2013)) is the basis for our MCMC named Dust2Dust.

In the case that $p/p_{\text{ref}} > 1$, the proposed distribution is considered to be out of range and flagged. The reference simulation can be iteratively regenerated with new centers and widths to cover the appropriate regions of parameter space. The number of such cases in our fit was on the order of 10^{-4} , and therefore negligible.

Dust2Dust initially keeps all simulated SNIa with a weight of 1. The resulting simulation size is heavily dependent on the proposed parameters - a tighter σ_β cut will naturally have fewer supernovae than a wider one. In order to avoid statistical fluctuations, the number of SNIa in the simulation are reduced to a uniform selected size, in this case 5,000 supernovae. In the case that Dust2Dust is not able to downsize the sample, the results are flagged as being a bad fit and a log-likelihood of -infinity is returned. For example, with the given fiducial results of the thesis, both σ_{R_V} values can be as low as 0.3 without triggering the 5,000 SNe threshold. $\sigma_{\beta_{SN}}$ can be as low as 0.05 without triggering the 5,000 SNe threshold. The number 5,000 was chosen to minimise statistical fluctuations. Neither this downsizing nor the selection of model parameters significantly affect non-model distributions such as redshift or stretch.

The design of Dust2Dust is to use the simulation frameworks developed in Kessler et al. (2009, 2019); Kessler & Scolnic (2017), and other works, while significantly reducing the simulation time compared to the naive approach of generating a new sample for each MCMC step. Minimising the time spent simulating is achieved via the use of the re-weighting algorithm, which generates an arbitrary desired distribution of SNIa properties after a single simulation. Table 4.3 shows the boundaries for the walkers generated by Dust2Dust. These bounds were determined after a number of iterations using Dust2Dust to ensure that our choice of prior does not impact the

results.

To fit our model, we minimise a modified version of Equation 8 in BS21:

$$\begin{aligned} \chi_{\text{Tot}}^2 = & \chi_{\text{c}}^2 + \chi_{\sigma_{\text{r}},\text{low}}^2 + \chi_{\sigma_{\text{r}},\text{high}}^2 + \chi_{\mu_{\text{res}},\text{low}}^2 \\ & + \chi_{\mu_{\text{res}},\text{high}}^2 + \chi_{\beta_{\text{SALT2}}}^2 + \chi_{\sigma_{\text{int}}}^2 \end{aligned} \quad (4.23)$$

where χ_{c}^2 is Equation 4.10, $\chi_{\sigma_{\text{r}},\text{low}}^2$ and $\chi_{\sigma_{\text{r}},\text{high}}^2$ are Equation 4.16 split on M_{stellar} , $\chi_{\mu_{\text{res}},\text{high}}^2$ and $\chi_{\mu_{\text{res}},\text{low}}^2$ are Equation 4.13 split on M_{stellar} , and $\chi_{\beta_{\text{SALT2}}}^2$ and $\chi_{\sigma_{\text{int}}}^2$ are Equations 4.18 and 4.19 respectively. A summary of these criteria is presented in Table 4.2.

Table 4.2: χ^2 Terms in Dust2Dust Population Fit

χ_{c}^2	c_{obs} distribution Not split on M_{stellar} .
$\chi_{\mu_{\text{res}},\text{high}}^2$	Colour vs. Hubble Residuals For high-mass galaxies.
$\chi_{\mu_{\text{res}},\text{low}}^2$	Colour vs. Hubble Residuals For low-mass galaxies.
$\chi_{\sigma_{\text{r}},\text{high}}^2$	Colour vs. HR Scatter For high-mass galaxies.
$\chi_{\sigma_{\text{r}},\text{low}}^2$	Colour vs. HR Scatter For low-mass galaxies.
$\chi_{\beta_{\text{SALT2}}}^2$	Error-weighted $\Delta \beta_{\text{SALT2}}$ Not split on M_{stellar} .
$\chi_{\sigma_{\text{int}}}^2$	Error-weighted $\Delta \sigma_{\text{int}}$ Not split on M_{stellar} .

The updated simulation is compared to the data and a log-likelihood is computed to determine the goodness-of-fit. The log-likelihood is defined as

$$\mathcal{L} = -\frac{1}{2} * \chi_{\text{Tot}}^2 \quad (4.24)$$

which `emcee` maximises, equivalent to minimising χ_{Tot}^2 .

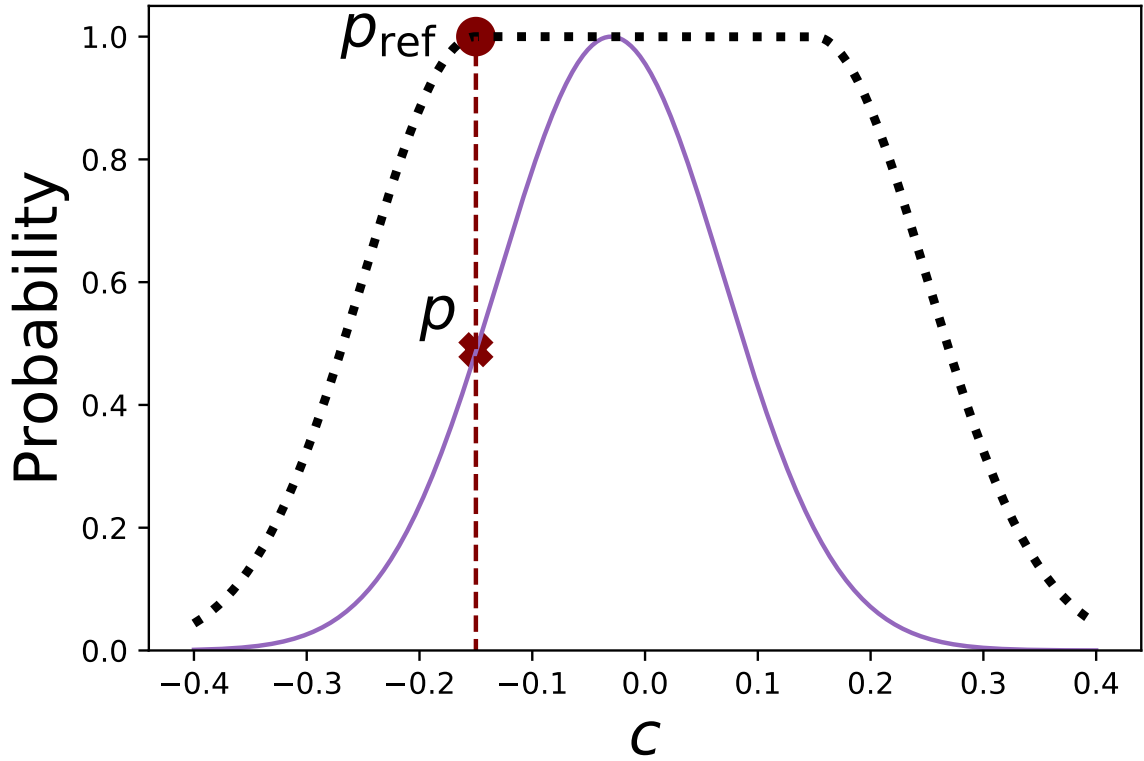


Figure 4.6: An example of the re-weighting done in Dust2Dust for the c parameter. The reference simulation is presented in black points and the proposed distribution is in purple histogram. The maroon p_{ref} point and p X are compared, and simulated SNIa are kept according to Equation 4.21.

For the purposes of this paper, we choose to split the BS21 model on host-galaxy M_{stellar} ; however, any arbitrary external property can be used.

Table 4.3: Ranges for Each Model Parameter

Parameter	Lower Bound	Upper Bound
\bar{c}	-0.3	-0.04
σ_c	0.01	0.2
$\overline{R_V}^a$	0.8	4
$\sigma_{R_V}^a$	0.25	4
τ_E^{ab}	0.05	0.2
$\overline{\beta}_{\text{SN}}$	1.0	3.0
$\sigma_{\beta_{\text{SN}}}$	0.0	1.0

^aThe same ranges are used for low and high M_{stellar}

^bThe same ranges are used for low and high z

4.2 Results

Here we evaluate and present the results from Dust2Dust run on the Pantheon+ data sample. Section 4.2.1 discusses the constraints on model parameters and how well they describe the data, including uncertainties and MCMC efficiency. Section 4.2.3 reviews the impact of statistical and systematic model uncertainties on w .

Table 4.4: Results from Dust2Dust and Comparison With Original Model Parameters

Model	Sample	\bar{c}	σ_c	$\overline{\beta}_{\text{SN}}$	$\sigma_{\beta_{\text{SN}}}$	$\overline{R_V}$	σ_{R_V}	τ_E
Mean:								
High-mass	CfA, CSP, Foundation	-0.077 ± 0.006	0.058 ± 0.005	2.064 ± 0.174	0.308 ± 0.08	2.138 ± 0.25	1.061 ± 0.429	0.107 ± 0.018
High-mass	DES, PS1, SNLS, SDSS							0.114 ± 0.015
Low-mass	CfA, CSP, Foundation					3.026 ± 0.375	1.481 ± 0.418	0.087 ± 0.016
Low-mass	DES, PS1, SNLS, SDSS							0.086 ± 0.021
Original:								
High-mass	CfA, CSP, Foundation	-0.084 ± 0.004	0.042 ± 0.002	1.98 ± 0.180	0.35 ± 0.200	1.50 ± 0.250	1.300 ± 0.200	0.190 ± 0.080
High-mass	DES, PS1, SNLS, SDSS							0.150 ± 0.020
Low-mass	CfA, CSP, Foundation					2.75 ± 0.350	1.300 ± 0.200	$0.010^{+0.050}_{-0.010}$
Low-mass	DES, PS1, SNLS, SDSS							0.120 ± 0.020

Table 4.5: Breakdown of different χ^2 criteria for the G10, C11, BS21-Original, and Dust2Dust scatter models.

χ^2	G10	C11	BS21 Original	Dust2Dust
χ_c^2	37	35	68	11
$\chi_{\mu_{\text{res,high}}}^2$	58	54	18	36
$\chi_{\mu_{\text{res,low}}}^2$	19	54	20	8
$\chi_{\sigma_r,\text{high}}^2$	158	162	95	37
$\chi_{\sigma_r,\text{low}}^2$	189	157	56	35
$\chi_{\beta_{SALT2}}^2$	7	31	1	0
$\chi_{\sigma_{\text{int}}}^2$	4	25	27	3
Sum	472	518	285	129

4.2.1 Fit of Model Parameters

The results for our best-fit parameters are given in Table 4.4, and these results are discussed below. Figure 4.7 shows the posterior likelihoods for our model parameters after discarding 100 steps for burn-in, a standard process to reduce spurious correlations in the MCMC. After this burn-in, our chains comprised 18,900 steps with 24 walkers. The acceptance fraction is 15%, and the autocorrelation time is 100. While this autocorrelation time could be improved by running Dust2Dust longer, we are already near the computation limits of our setup. In general, the posteriors are uni-modal, though not well approximated by a Gaussian. We give the mean values from the chains as our fiducial result.

As described in Section 4.1.2, Figure 4.4 shows three of the five criteria used to constrain the BS21 model parameters. A more specific breakdown of the χ^2 values is shown in Table 4.5. Dust2Dust returns a χ^2 that is $\times 2$ smaller than the original BS21 (BS21-Original) and nearly $\times 5$ smaller than two commonly used scatter models, G10 and C11. Both G10 and C11 follow SALT2 in not including an explicit dust-based colour law; G10 ascribes approximately 75% of observed scatter to achromatic effects

and the remaining 25% to chromatic effects. C11, in contrast, attributes 75% of scatter to chromatic variations and the remaining 25% grey. The equivalent criteria of Figure 4.4 for the G10 and C11 scatter models are shown in Figures 4.8 and 4.9, respectively. For both the G10 and C11 models, the Hubble Residual and σ_r distributions are poorly recreated by simulations.

Dust2Dust finds model parameters such that simulations predict the observed c distribution and μ_{res} behaviour, as well as β_{SALT2} and σ_{int} . The Hubble residual RMS term ($\chi_{\sigma_r}^2$) is the largest contributor to the overall χ^2 .

We test the robustness of Dust2Dust by analysing 16 data-sized simulations using parameters taken from the means in Table 4.4 and compare the aggregate results. The resulting χ_{tot}^2 ranges from 42 to 105, with an average of 70. These χ_{tot}^2 are significantly smaller than for the data ($\chi_{\text{tot}}^2 = 129$), which suggests that improvements to the model, notably σ_r , are likely needed.

The 12 fitted parameters are consistent with simulated inputs to within their uncertainties. Similar to our fiducial result, we use the mean values from the chains as the results for the 16 fits to data-sized simulations. From these fits, we compute the standard deviation of parameter values to compare to our estimated uncertainties. We find the medians of the 16 posterior widths agree to within 15% of the scatter (σ) of the 16 posterior means: the errors reported for the parameter fits are accurate to within 15% of the standard deviation of the 16 best fits, though they are underestimated. We then check how consistent the posterior means are to the true value of each parameter. We find of the 12 parameters, only one shows a 2.9σ bias - this is the low mass σ_{Rv} parameter. The median value of the distribution of recovered low mass σ_{Rv} values is within 2σ of the input value when using the medians of the posterior widths. To verify this, we ran on a single large simulated sample of 50,000 SNe to check for parameter recovery biases. Three of our recovered parameters are

more than 1σ from the input values; none are greater than 2σ .

Under the assumption of our model, we find evidence of different R_V distributions as a function of host-galaxy mass. The mean \bar{R}_V values in Table 4.4 differ between high and low mass galaxies by 2.8σ , and the σ_{R_V} values are within 1σ .

We find evidence that the β_{SN} distribution is not a delta function: $\sigma_{\beta_{\text{SN}}} > 0$ with $> 3\sigma$ confidence for the mean Dust2Dust results. G10 and C11 both assume a delta function for β_{SALT2} , which is not consistent with our Dust2Dust results.

4.2.2 Comparison with Original BS21 Parameters

For \bar{c} (Table 4.4), we find peak probability (-0.077 ± 0.006) comparable to that of BS21-Original (0.084 ± 0.004), though the standard deviation (0.058 ± 0.005) is higher than that of BS21-Original: 0.042 ± 0.002 .

Our $\bar{\beta}_{\text{SN}}$ and $\sigma_{\beta_{\text{SN}}}$ values are consistent with BS21-Original, and our values are more precise. Our $\sigma_{\beta_{\text{SN}}}$ uncertainty is $\sim 4\times$ smaller. Our $\bar{\beta}_{\text{SN}}$ is 2.064 ± 0.174 , compared to 1.98 ± 0.18 .

In contrast to BS21-Original, who found a low-mass \bar{R}_V value at 1.5 ± 0.25 , we find low-mass \bar{R}_V to be $\sim 2.0 \pm 0.25$. Our high-mass \bar{R}_V ($\sim 3.0 \pm 0.4$) is consistent with BS21-Original.

The Dust2Dust-recovered σ_{R_V} results are lower or consistent with those in BS21-Original. While the low-mass σ_{R_V} are consistent, our high-mass σ_{R_V} is smaller compared to BS21-Original.

Brout & Scolnic (2021) found that τ_E has little impact on the overall \mathcal{L} , particularly for the low- z subsample (BS21 Figure 9). Using Dust2Dust and a larger data sample, we find that all four τ_E values are similar (0.08 - 0.11), but the low and high mass components are more self-similar than the original BS21.

4.2.3 Systematic Uncertainties on Cosmological Parameters

For the SNIa-cosmology analysis (Brout et al. *in prep.*, B22), the fitted Dust2Dust parameters are used in simulations for bias corrections, and here we evaluate the associated systematic uncertainty on the dark energy equation-of-state w , matter density Ω_M , and the Hubble Constant H_0 . We compare two systematic evaluation methods: 1) a forward modeling approach using 100s of simulations, each analysed with a fast cosmology χ^2 minimiser, and 2) a covariance matrix approach with wfit.

We perform a cosmology analysis that includes

- SALT2 light-curve fitting to standardise the brightness (Section 2.1)
- Generating a large simulated sample for bias corrections to account for selection effects
- Using Beams with Bias Corrections (BBC) to produce a Hubble diagram corrected for biases in 4 dimensions: $\{c, z, x_1, M_{\text{stellar}}\}$ (Chapter 5)
- A cosmology fit

The first three steps are performed in the same manner as in B22. For our blinded cosmology fitting, we use a simple and fast minimisation program in SNANA (wfit) that uses a Planck-like Cosmic microwave background (CMB) prior based on the R-shift parameter (see σ_R tuning discussion at the end of Section 3 in Sánchez et al. (2021)).

To model the systematic uncertainty in w from BS21 parameter uncertainties, we generate 400 statistically independent data-sized simulations with BS21 model parameters drawn randomly from Dust2Dust chains, thus accounting for the uncertainty and covariance between model parameters. To account for the statistical uncertainty,

we additionally generated 400 statistically independent data-sized simulations with best fit BS21 model parameters. Each data-sized simulation is analysed using the 4 steps above.

We define the systematic uncertainty from population parameters to be

$$\sigma w_{\text{sys}} = \sqrt{\text{STDEV}(w_{\text{syst+stat}})^2 - \text{STDEV}(w_{\text{stat}})^2} \quad (4.25)$$

where $\text{STDEV}(w_{\text{syst+stat}})$ is the standard deviation of w values from 400 simulations including the randomly drawn parameters, and $\text{STDEV}(w_{\text{stat}})$ is the standard deviation of w values from 400 simulations using the best fit parameters. We find $\sigma w_{\text{sys}} = 0.014 \pm 0.001$.

While this simulation approach is effective for evaluating a single systematic, it is impractical for the commonly-used covariance matrix method that is used in the Pantheon+ cosmology analysis. Instead, we attempt to model the systematic uncertainty in the covariance matrix method using 4 bias correction perturbations that mimic the 400 simulations approach.

For this covariance matrix approach, we generate the nominal bias correction simulation using the maximum likelihood set of parameters. Next, we generate three bias correction simulations with model parameters that are $\Delta\chi^2 \sim 10$ (approximately 1σ away from the mean) away from our best-fit results. The resulting Hubble diagram and statistical+systematic covariance matrix is processed through wfit to determine cosmological parameters using a CMB prior from Planck Collaboration et al. (2016). A summary of this process is given in Section 2.2 of B22. While our forward modeling method only evaluated the w systematic, here we evaluate the systematic uncertainty on both w and H_0 .

Table 4.6: Cosmology constraints with systematics with Ω_M prior

Model	σH_0	σw_{sys}
Forward	-	0.014(1)
Covariance	0.145 km/s/Mpc	0.011

We define the systematic uncertainties from population parameters to be

$$\sigma w_{\text{sys}} = \sqrt{\sigma w_{\text{syst+stat}}^2 - \sigma w_{\text{stat}}^2} \quad (4.26)$$

$$\sigma H_{0\text{sys}} = \sqrt{\sigma(H_{0\text{syst+stat}})^2 - \sigma(H_{0\text{stat}})^2} \quad (4.27)$$

where $\sigma w_{\text{syst+stat}}$ is the w -uncertainty from wfit using a systematic+statistic covariance matrix, and σw_{stat} is the statistical-only w -uncertainty. Analogous definitions apply to $\sigma(H_{0\text{syst+stat}})$ and $\sigma(H_{0\text{stat}})$. We find $\sigma w_{\text{sys}} = 0.011$, and $\sigma H_{0\text{sys}} = 0.145$ km/s/Mpc.

The results from the forward-modeling and covariance matrix methods, while not within error, are similar in their impact on w . With only three different biasCor simulations, our covariance matrix approach may be affected by noise. Adding more biasCor simulations represents a significant computational challenge. To maintain consistency with the forward-modeling approach, we binned the Hubble Residuals for the covariance matrix approach. Implementing an unbinned approach from Brout et al. (2021) allows the data to “self correct” for certain systematics, and may decrease this systematic uncertainty from population modeling. The forward-modeling is therefore an upper bound on the associated systematic uncertainty.

This is the Accepted Manuscript version of an article accepted for publication in The Astrophysical Journal. IOP Publishing Ltd is not responsible for any errors or omissions in this version of the manuscript or any version derived from it. The Version of Record is available online at the following doi: 10.48550/arXiv.2112.04456

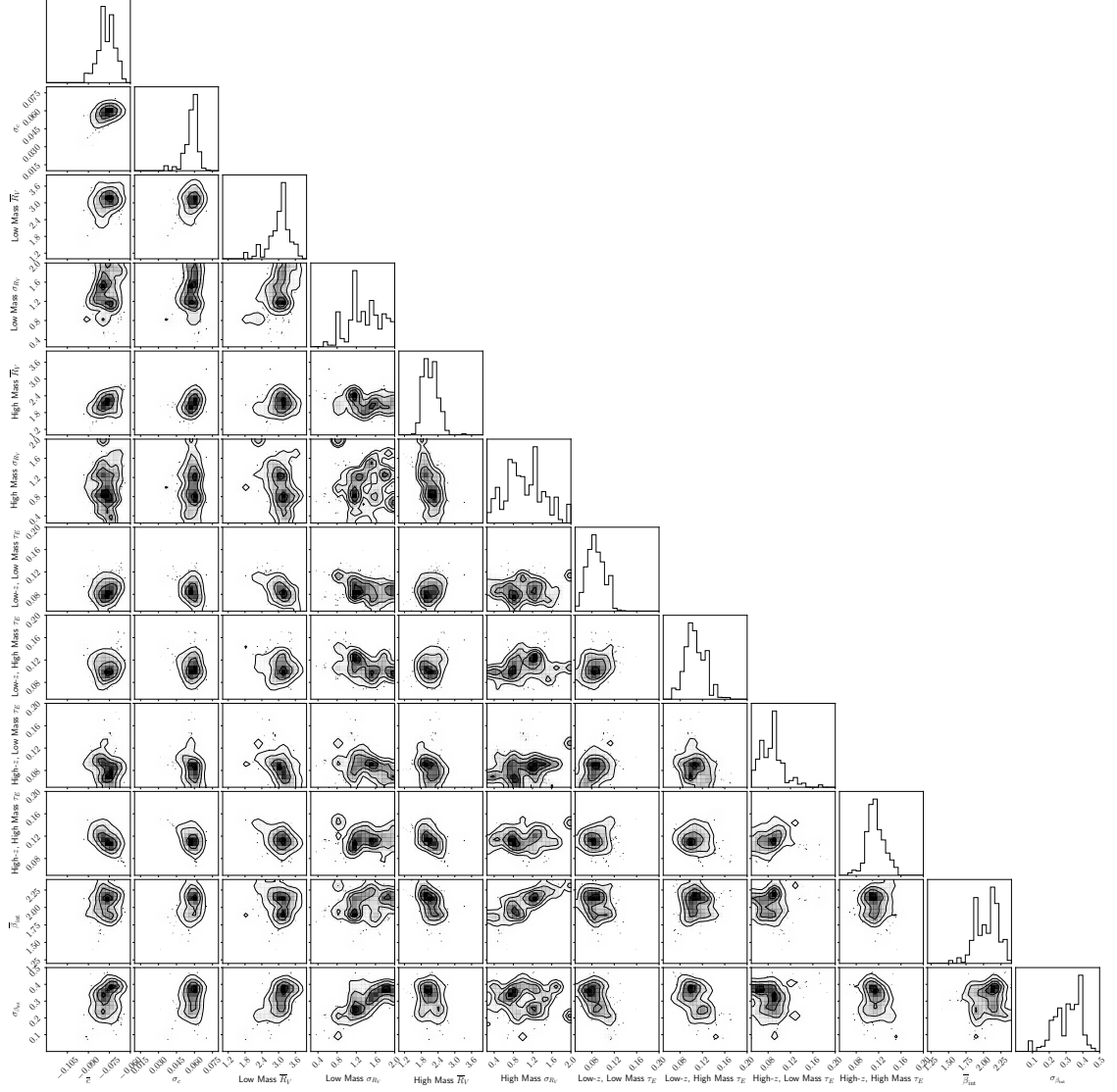


Figure 4.7: Triangle plot for fitted Dust2Dust parameters. Parameters were fit simultaneously and include covariances. \bar{c} , σ_c , $\bar{\beta}$, and σ_β are fit for the entire sample. $\bar{\tau}_V$, σ_{RV} are fit separately for low-mass and high-mass galaxies. τ_E is fit four times across z and M_{stellar} .

G10 Scatter Model

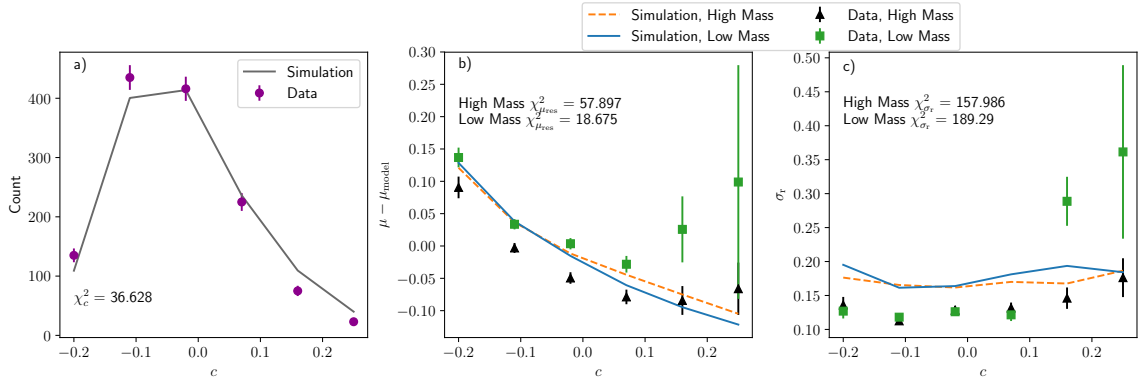


Figure 4.8: The c histogram, c vs μ_{res} , and c vs $\text{RMS}(\mu_{\text{res}})$ are shown here from left to right. The latter two plots are split on high and low mass. Purple circles are histogram data and solid grey is simulated histogram. Green squares are low mass data and black triangles are high mass data, while blue plot is low mass simulations and orange dotted plot is high mass simulation. The G10 model significantly overestimates the RMS and does not accurately replicate the μ_{res} split nor the change in RMS with c .

C11 Scatter Model

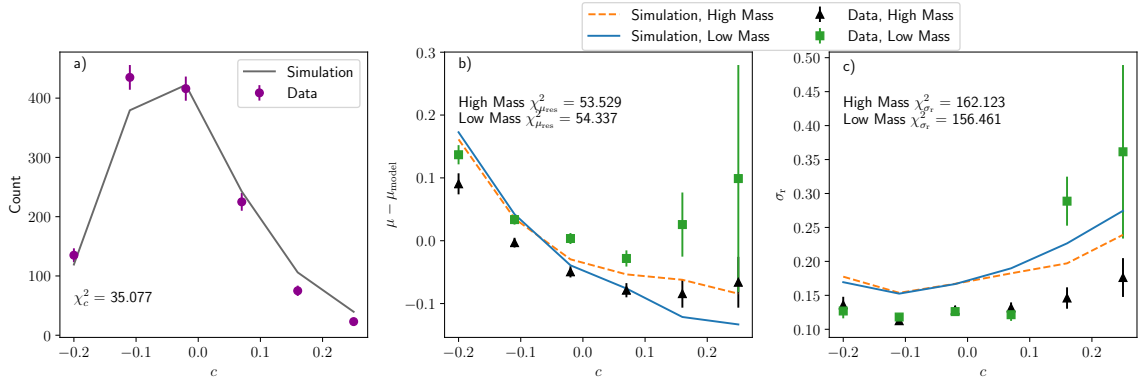


Figure 4.9: The c histogram, c vs μ_{res} , and c vs $\text{RMS}(\mu_{\text{res}})$ are shown here from left to right. The latter two plots are split on high and low mass. Purple circles are histogram data and solid grey is simulated histogram. Green squares are low mass data and black triangles are high mass data, while blue plot is low mass simulations and orange dotted plot is high mass simulation. The C11 model significantly overestimates the RMS and does not accurately replicate the μ_{res} split.

Chapter 5

Correcting Biases in SNIa

The results presented in this chapter, as well as some portions of text, are from Popovic et al. (2021). The text represents my own work, and the contributions of other authors is presented as such:

- *Dillon Brout: Implementation of BBC7D and BBC4D within the SNANA framework after development lead by myself.*
- *Richard Kessler: Alongside Dillon, implementation of BBC7D and BBC4D, as well as many fixes to SNANA code to enable SNANA to better use correlated parameters.*
- *Daniel Scolnic: Analysis and advising, particularly with respect to appropriate extra dimensions and computational power mitigation strategies.*
- *Lisa Lu: Code refactoring for the parent populations section.*

The previous sections have shown why the rudimentary, redshift-only bias corrections method covered in Section 2.1.9 is not sufficient, as redshift-only corrections do not take into account the shifts in fitted parameters, nor do they account for the difference in parameter corrections. Figure 5.1 shows the deviation in observed m_B , x_1 , and c as a function of redshift and the supernova parameters. These deviations clearly diverge, indicating that a bias corrections method that does not take light curve fit parameters into account is incomplete.

To address this issue, Kessler & Scolnic (2017) created the BEAMS with Bias Corrections (BBC) method. BEAMS has already been covered, and the groundwork

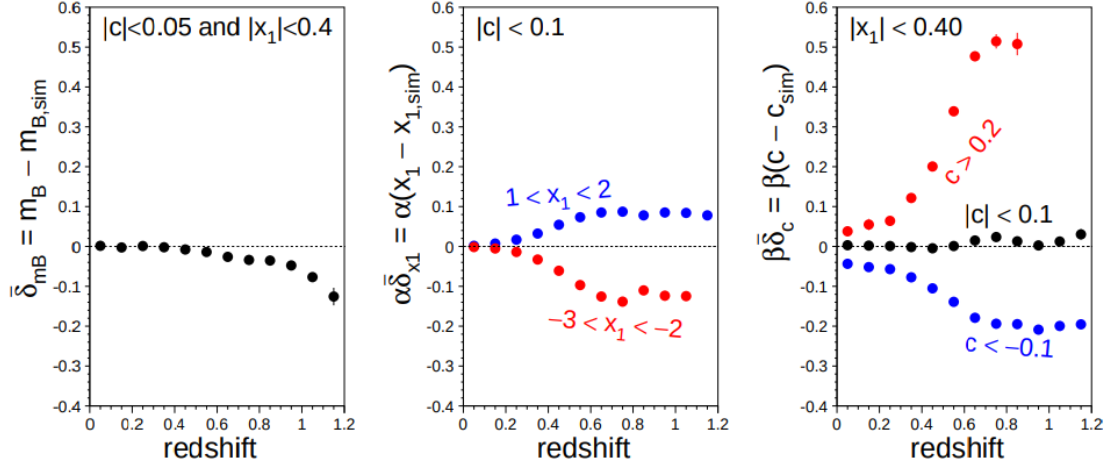


Figure 5.1: Bias corrections of m_B ($\bar{\delta}_{m_B}$), x_1 ($\alpha \bar{\delta}_{x_1}$), and c ($\beta \bar{\delta}_c$) as a function of redshift. The $\bar{\delta}$ is a matter of convention, it is equivalent to δ in this work. Figure from Kessler & Scolnic (2017).

for bias corrections has been laid, but here we lay out the construction and methodology of the 5D-dimensional corrections that comprise BBC5D from Kessler & Scolnic (2017).

Kessler & Scolnic (2017) expanded on the 1D method by defining a bias-corrected distance where the individual Tripp components of m_B , c , and x_1 are corrected. They define a bias-corrected distance,

$$\begin{aligned}
 \mu^* &= m_B^* + \alpha x_1^* - \beta c^* - M_{z_i} \\
 &= (m_B - \delta_{m_B}) + \alpha(x_1 - \delta_{x_1}) - \beta(c - \delta_c) - M_{z_i} \\
 &= m_B + \alpha x_1 - \beta c - M_{z_i} - \delta \mu_{\text{bias}}(z, x_1, c, \alpha, \beta)
 \end{aligned} \tag{5.1}$$

where bias-corrected quantities are denoted with a star superscript and

$$\delta \mu_{\text{bias}} \equiv (\delta_{m_B} + \alpha \delta_{x_1} - \beta \delta_c) \tag{5.2}$$

Measurement noise and intrinsic scatter preclude calculating the exact bias correction

for each event; therefore, $\delta\mu_{\text{bias}}$ is interpolated in 5D cells of $\{z, x_1, c, \alpha, \beta\}$. The $\delta\mu_{\text{bias}}$ term is calculated with a large simulation designated as a ‘BiasCor’, by comparing the observed values to the simulated ones for each SNIa parameter. The first three dimensions (z, x_1, c) are interpolated using the simulated populations. However, the luminosity correlation coefficients (α, β) are single valued and not described with a population model akin to z, x_1, c . Therefore, the bias corrections for α and β are determined on a 2×2 grid that brackets the values of α and β found in the data. This grid enables for an interpolation of the BiasCor sample at the value of the proposed α and β in each iteration of the BBC fit. This specific approach to the α and β nuisance parameters marks an improvement over the 1D bias correction method, which required assuming an α and β for the simulations used for bias corrections and therefore an iterative simulation approach.

5.0.1 Improving Bias Corrections for SNIa-Host Correlations

The first attempt to marry BBC5D and host-galaxy correlations was introduced by Smith et al. (2020). The technique used by Smith et al. 2020 differs from that introduced in Section 3.1.3 in that it did not attempt to introduce an underlying population, but rather directly used the observed correlations in the data to be replicated in the simulations.

The Smith et al. 2020 approach, while approximate, was sufficient to introduce correlations between simulated SNe Ia and their hosts. They found that including host galaxy correlations in the simulations and the BiasCor *reduced* the recovered mass step γ by up to 50%.

The cause of this γ reduction may initially seem like a perplexing problem, but in truth it originates from BBC5D not accounting for mass in the bias corrections.

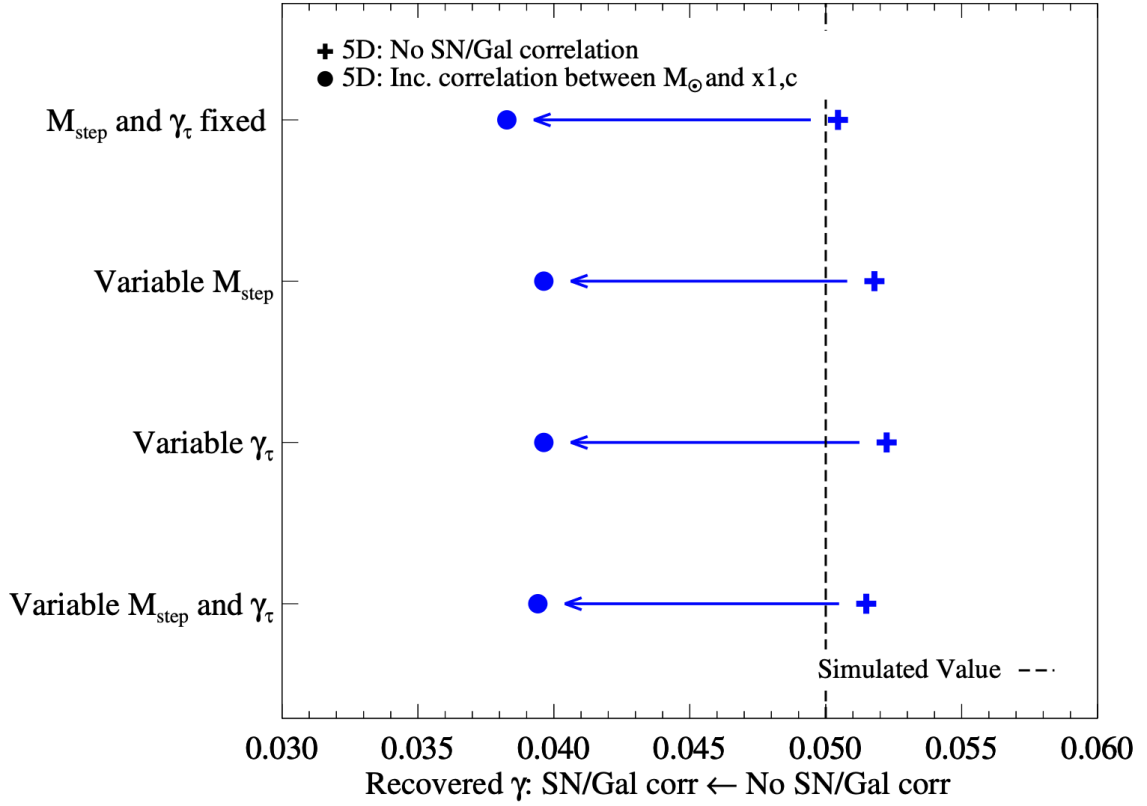


Figure 5.2: The best fit value of γ for a simulated DES 3-year sample when using BBC5D. The true, input γ is shown in dashed line, while the recovered γ for simulations without host galaxy correlations is shown in blue cross and simulations with host galaxy correlations are shown in blue circle. Different combinations of a fixed mass step location M_{step} and mass step magnitude γ_τ are shown on the y-axis. A significant (~ 0.012 reduction in the mass step is shown regardless of the choice of mass step location or size. From Smith et al. (2020).

This can best be shown in Figure 5.3, which shows the difference in the δ_{x_1} component of BBC5D bias corrections. The high mass x_1 values are being over-corrected compared to the low mass SNe Ia. This is because BBC5D does not account for an intrinsic change in the x_1 parameters as a function of mass, and therefore over-corrects a subset of supernovae.

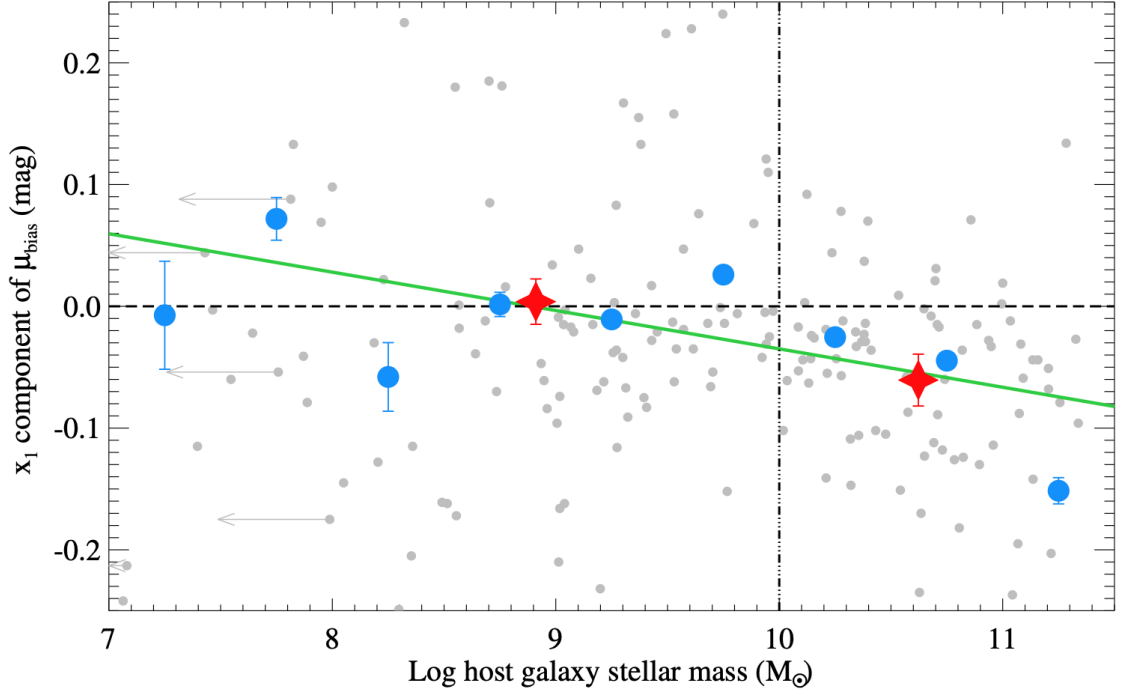


Figure 5.3: The δ_{x_1} component of BBC5D bias corrections as a function of the log host galaxy stellar mass. The individual corrections to SNe Ia are shown in grey point, the binned averages are in blue circle with statistical error, and the high (> 10) and low (< 10 mass averages are shown in red star. There is a 2.2σ discrepancy between the high and low mass bins. From Smith et al. (2020).

In short, because BBC5D marginalises over M_{stellar} , it expects all SNIa to share same underlying x_1 population. With this expectation, it over-corrects the high mass SNe because they appear to have an observed x_1 further from the population mean-simulated value. In fact they draw from a different population, see Figure 3.5, but this is not accounted for.

While the δ_{x_1} correction is, *on average*, correct, the γ bias results from the BBC5D corrections being applied before the mass step is fit in SALT2mu. When the δ_{x_1} component is applied, it removes some amount of the magnitude difference between high mass SNe and low mass SNe due to the difference in intrinsic x_1 distribution. However, the mass step is simply a magnitude difference between high mass and low mass SNIa. In effect, for a bias correction system that marginalises over mass, the magnitude difference arising from an x_1 population that correlates with redshift and the mass step γ are degenerate.

To account for these biases in the mass step, we introduce two new dimensions to the $\delta\mu_{\text{bias}}$ term in Equation 5.1: θ , which is a magnitude shift, and M_{stellar} .

The new θ dimension is incorporated into the BiasCor by adding a magnitude shift of $+\theta$ to a random half of the simulation, and $-\theta$ to the other half; there is no correlation between θ and host properties, and thus $\theta \neq \gamma$. Using BiasCor with θ , the BBC fit allows for a mag-shift ($\delta\mu_{\text{host}}$) as an arbitrary function of $X = \log_{10}M_{\text{stellar}}$ and other parameters. While previous cosmology analyses **have used** $\delta\mu_{\text{host}} = -\gamma/2$ **for** $X > 10$ **and** $\delta\mu_{\text{host}} = +\gamma/2$ **for** $X < 10$, here we adopt the more general $\delta\mu_{\text{host}}$ function with step location S and step width τ_M (Equation 2.4). At each step of the BBC fit, the value of $\delta\mu_{\text{host}}$ for each event is used to interpolate the BiasCor between $\pm\theta$ such that

$$\begin{aligned} \delta\mu_{\text{bias}} &= \delta\mu_{\text{bias}}(\vec{x}_5, X, -\theta) \\ &+ f \times [\delta\mu_{\text{bias}}(\vec{x}_5, X, +\theta) - \delta\mu_{\text{bias}}(\vec{x}_5, X, -\theta)] \end{aligned} \tag{5.3}$$

where $f = (\delta\mu_{\text{host}} + \theta)/2\theta$ and $\vec{x}_5 = \{z, x_1, c, \alpha, \beta\}$. It is important that $\theta > \delta\mu_{\text{bias}}$ to ensure a valid interpolation.

The addition of θ and M_{stellar} results in changing the 5D $\delta\mu_{\text{bias}}$ term in Equation 5.1 to a 7D $\delta\mu_{\text{bias}}$ as follows,

$$\begin{aligned} \delta\mu_{\text{bias}}(z, x_1, c, \alpha, \beta) \rightarrow \\ \delta\mu_{\text{bias}}(z, x_1, c, \alpha, \beta, \theta, M_{\text{stellar}}) . \end{aligned} \tag{5.4}$$

For the first six BiasCor dimensions, $\delta\mu_{\text{bias}}$ is interpolated. For the M_{stellar} dimension, $\delta\mu_{\text{bias}}$ is evaluated in discrete bins to avoid interpolating across the luminosity step at $10^{10}M_{\odot}$.

The effect of θ on the bias corrections is shown in Figure 5.4 as a function of redshift. Here we set $\theta = \pm 0.06$, the effects of which is negligible for $z < 0.8$ and increases to ~ 0.02 mag at high- z . Because θ is independent of supernova parameters, it can be used for investigating correlations between any host galaxy property and SNIa luminosity, not just host-galaxy stellar mass.

5.0.2 Changes to the BBC formalism for BS20

While the SALT2 model is an accurate description of SNIa light curves, it is nonetheless an approximation that ignores the difference between intrinsic color variation and dust. Previous SNIa cosmology analyses have used the same SALT2 model in both light curve fitting and BiasCor; this means that the BiasCor corrects for selection effects, but does not correct for biases in the SALT2 model. BS20 attempts to provide a more accurate light-curve model that can be used for the BiasCor, and here we update BBC to be compatible with BS20.

The BBC5D formalism is not compatible with BS20 for three reasons: 1) BBC intrinsic scatter is characterised by a single colour-independent σ_{int} while BS20 uses a dust-dependent scatter that is poorly characterised by a single σ_{int} , 2) BBC assumes the single SALT2 colour-luminosity relation β , whereas BS20 uses distributions for intrinsic β_{SN} and dust R_V (Eq. 4.5), and 3) c_{int} and β_{SN} in BS20 refer to intrinsic

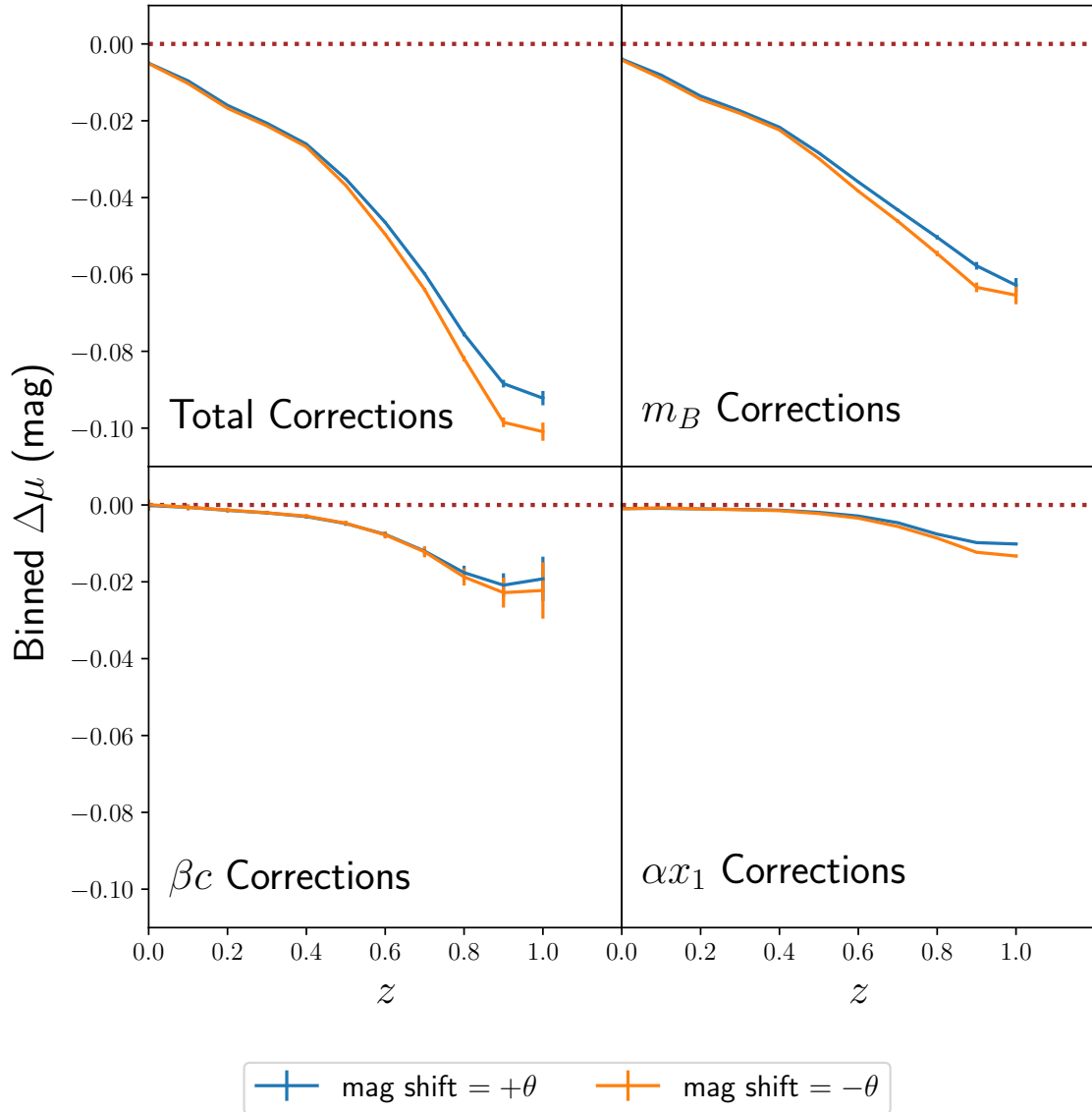


Figure 5.4: Bias correction vs. redshift for $\theta = +0.06$ (blue) and $\theta = -0.06$ (orange). The biased quantity is indicated on each panel.

colour and intrinsic colour-luminosity relationship, while SALT2 c and β include both dust and intrinsic properties.

Ideally, to incorporate BS20, we would decompose the fitted colour c into c_{int} and c_{dust} and compute a true β in the simulation. While we plan to address these issues in a future work, they require significant updates to both training and fitting code; instead, we make several approximations. Here we describe BBC updates to be compatible with the BS20 model:

1. Replace the SALT2 model in the BiasCor with the BS20 model.
2. Include M_{stellar} as in Section 5.0.1, but not θ because the mass step is predicted by the BS20 model without the γ parameter.
3. Remove grid-interpolation of α and β because the BS20 simulations are forward-modeled and result in BBC-fitted α and β that are in agreement with that of the data.
4. $\delta\mu_{\text{bias}}$ is computed for distances instead of bias-correcting each SALT2 parameter.

These changes are referred to as BBC-BS20 and result in a $\delta\mu_{\text{bias}}$ dimensionality of $\{z, x_1, c, M_{\text{stellar}}\}$. For BBC-BS20, Equation 5.1 becomes:

$$\mu^* = m_B + \alpha x_1 - \beta c - M_{z_i} - \delta\mu_{\text{bias}} \quad (5.5)$$

and Equation 5.2 becomes

$$\delta\mu_{\text{bias}} = m_B^{\text{BC}} + \alpha x_1^{\text{BC}} - \beta c^{\text{BC}} - M_{z_i} - \mu_{\text{true}} . \quad (5.6)$$

The true distance modulus for the BiasCor is μ_{true} , and the superscript BC denotes that these values are from SALT2 light-curve fits to the BiasCor events. We note that Equations 5.5 and 5.6 can be used with BBC5D and the SALT2 model, and yield consistent results compared to using Equations 5.1 and 5.2.

5.0.3 Impact on Cosmology with Host Properties

With our simulations from Section 2.2 and the parent populations shown in Figure 3.5, we create 100 simulated data sets and a large BiasCor to test the accuracy of our bias correction methods. We compare four different bias correction methods for the G10 and C11 models. Two methods use BBC1D, with and without M_{stellar} information included in the BiasCor (designated ‘No Mass’, similar to that of Betoule et al. (2014)). The other two methods use the BBC5D and new BBC7D method. Overall, we find our new method significantly improves upon BBC5D. In Table 5.1, we show the fitted nuisance parameters, Hubble scatter (RMS of $\mu_{\text{fit}} - \mu_{\text{true}}$), w and w -bias defined as $\Delta w = (w_{\text{fit}} - w_{\text{true}})$, averaged over the 100 simulations.

For the G10 scatter model, we find an α bias below 1% for all BBC methods. This broad agreement holds well for the recovery of β as well. The BBC5D approach results in a significant γ bias of $\Delta\gamma = 0.019 \pm 0.001$ magnitudes. BBC7D reduces this bias by a factor of ~ 5 , although a 2 milimag γ -bias remains with 2σ significance. These trends in α , β , and γ are qualitatively similar in the C11 results. However, it is worth noting that the BBC1D recovery of β and γ for the C11 scatter model is significantly biased.

For both G10 and C11, we see a general decrease in Hubble scatter with increasing dimensionality of the BBC methodology. BBC5D and BBC7D have comparable Hubble scatter with each other for both G10 and C11, and both are $\sim 10\%$ smaller

compared to using BBC1D.

The presence of host-galaxy correlations in the BBC1D BiasCor does not make a significant impact on recovered w values for G10 or C11. In the case with and without host-galaxy correlations, the w -bias is $\sim 0.02 \pm 0.005$ for G10 and $\sim 0.01 \pm 0.005$ for C11. BBC5D does not significantly effect this BBC1D w -bias, recovering -0.0201 ± 0.0048 and -0.0237 ± 0.0046 for G10 and C11 respectively. The BBC7D w -bias for both G10 and C11 is a factor of 2 smaller than their 5D counterparts: **w -bias= 0.0086 ± 0.0046 for G10 and 0.0105 ± 0.0046 for C11.** Both BBC7D biases have $\sim 2\sigma$ significance. Overall, BBC7D has the smallest w -bias as well as the smallest biases for other nuisance parameters and scatter.

In Figure 5.5, we show the binned distance modulus residuals as a function of redshift for BBC1D, BBC5D, and BBC7D. BBC7D has smaller μ residuals (mostly ~ 0.005 across the z range) than the BBC5D approach, **except for near $z = 0.1$. All BBC μ residuals have a significant excess around this range, which is most pronounced for BBC7D: $\mu_{\text{BBC}} - \mu_{\text{true}} = 0.01 \pm 0.004$ (2.4σ).**

The accuracy of the reported distance modulus error, σ_μ , in comparison to Hubble Residual (HR) scatter is another important metric in determining the effectiveness of BBC. Figure 5.6 shows BBC1D and BBC7D σ_μ and HR scatter as a function of SNIa colour, c . We see better agreement for BBC7D compared to BBC1D. Figure 5.6 and Table 5.1 show that for G10 and C11, the BBC7D methods have the smallest scatter.

Table 5.1: Fitted values and uncertainties ¹ averaged over 100 simulations

Method	Model	input $\alpha = 0.145$		input $\beta = 3.1$		input $\gamma = 0.05$		input $w = -1$	
		Fitted α	Fitted β	Fitted γ	Fitted w	Hubble scatter ²	Fitted w	$\Delta_w (N_{\sigma_w})$	
BBC1D (No Mass) ³	G10	0.1442 ± 0.0005	3.1154 ± 0.0062	0.0475 ± 0.0010	0.149 ± 0.005	-0.9828 ± 0.0047	0.017 (3.7 σ)		
BBC1D	G10	0.1443 ± 0.0005	3.1160 ± 0.0062	0.0474 ± 0.0010	0.149 ± 0.005	-0.9777 ± 0.0047	0.022 (4.7 σ)		
BBC5D	G10	0.1440 ± 0.0005	3.0901 ± 0.0061	0.0313 ± 0.0010	0.138 ± 0.005	-1.0201 ± 0.0046	-0.0201 (4.4 σ)		
BBC7D	G10	0.1451 ± 0.0005	3.0891 ± 0.0062	0.0464 ± 0.0010	0.137 ± 0.005	-1.0086 ± 0.0046	-0.0086 (1.9 σ)		
Method	Model	input $\alpha = 0.145$	input $\beta = 3.8$	input $\gamma = 0.05$	input $w = -1$				
		Fitted α	Fitted β	Fitted γ	Fitted w	Hubble scatter	$\Delta_w (N_{\sigma_w})$		
BBC1D (No Mass)	C11	0.1458 ± 0.0005	3.2285 ± 0.0068	0.0445 ± 0.0011	0.151 ± 0.005	-0.9896 ± 0.0048	0.0104 (2.6 σ)		
BBC1D	C11	0.1459 ± 0.0005	3.2283 ± 0.0068	0.0432 ± 0.0011	0.151 ± 0.005	-0.9961 ± 0.0048	0.0039 (0.8 σ)		
BBC5D	C11	0.1444 ± 0.0005	3.7740 ± 0.0073	0.0287 ± 0.0009	0.132 ± 0.005	-1.0237 ± 0.0046	-0.0237 (5.2 σ)		
BBC7D	C11	0.1460 ± 0.0005	3.7813 ± 0.0071	0.0466 ± 0.0010	0.131 ± 0.005	-1.0105 ± 0.0046	-0.0105 (2.3 σ)		
Method	Model	input $\alpha = 0.145$	input $\beta = \text{ND}$ ⁴	input $\gamma = 0$	input $w = -1$				
		Fitted α	Fitted β	Fitted γ	Fitted w	Hubble scatter	$\Delta_w (N_{\sigma_w})$		
BBC1D (No Mass)	BS20	0.1458 ± 0.0006	2.7526 ± 0.0075	0.0533 ± 0.0009	0.121 ± 0.005	-0.9545 ± 0.0045	0.0455 (10.1 σ)		
BBC1D	BS20	0.1461 ± 0.0006	2.7565 ± 0.0070	0.0467 ± 0.0009	0.116 ± 0.005	-0.9572 ± 0.0045	0.0428 (9.5 σ)		
BBC-BS20	BS20	0.1417 ± 0.0004	3.0770 ± 0.0050	0.0006 ± 0.0007	0.104 ± 0.005	-0.9943 ± 0.0040	0.0057 (1.4 σ)		

^aUncertainties are the average uncertainty among 100 simulations, divided by $\sqrt{100}$

^bThe error in the Hubble scatter is the R.M.S divided by $\sqrt{100}$.

^cDoes not include M_{stellar} dependent parent populations in the BiasCor.

^dNot Determined: For the BS20 model, input SALT2 β ($\beta \neq \beta_{\text{SN}}$) is not defined.

5.0.4 Impact on Cosmology Using Bias Corrections for BS20

The bottom tier of Table 5.1 shows how well BBC1D and BBC-BS20 perform on simulations generated with the BS20 model. While simulations of the BS20 model do not have an input γ like the aforementioned simulations G10 and C11, the simulation includes host-mass vs colour-luminosity dependence that matches that of the data. As reported in BS20, we find that using BBC1D results in $\gamma \sim 0.06$, consistent with the value found in the data. BBC-BS20 results in $\gamma = 0.0006 \pm 0.0007$, consistent with no mass step. Applying BBC1D to BS20 simulations performs well in recovering α ($\Delta\alpha \sim 0.001 \pm 0.0006$), while BBC-BS20 has a slightly larger α -bias ($\Delta\alpha \sim 0.003 \pm 0.0004$). To validate the predicted γ -reduction, we apply the BBC-BS20 method on real data and find

$$\gamma = 0.0166 \pm 0.0076 \quad (5.7)$$

which is **less than 1/3 the size of previous measurements.**

The BS20 model is characterised by a distribution of β_{SN} and R_V , and thus we cannot determine an input β for the simulation. For this reason, the BS20 section of Table 5.1 refers to the input β as Not Defined (ND), and we are unable to compute β biases. BS20 found their model parameters such that their BBC1D β from simulations matched that of the data ($\beta \sim 3.06 \pm 0.06$). Since BS20 used an overly simplistic assumption about M_{stellar} distributions, their fitted model parameters are approximate. Here we update the M_{stellar} distribution to match the data (Figure 3.2) but do not update the BS20 model parameters; we find BBC1D correction on BS20 simulations results in $\beta \sim 2.76 \pm 0.01$, which no longer matches that of the data. However, when running BBC-BS20 on our simulations and real data we find good agreement: $\beta = 3.077 \pm 0.005$ (sim) and $\beta = 3.165 \pm 0.045$ (data) respectively. This BBC1D β discrepancy warrants the need for further improvements to the BS20

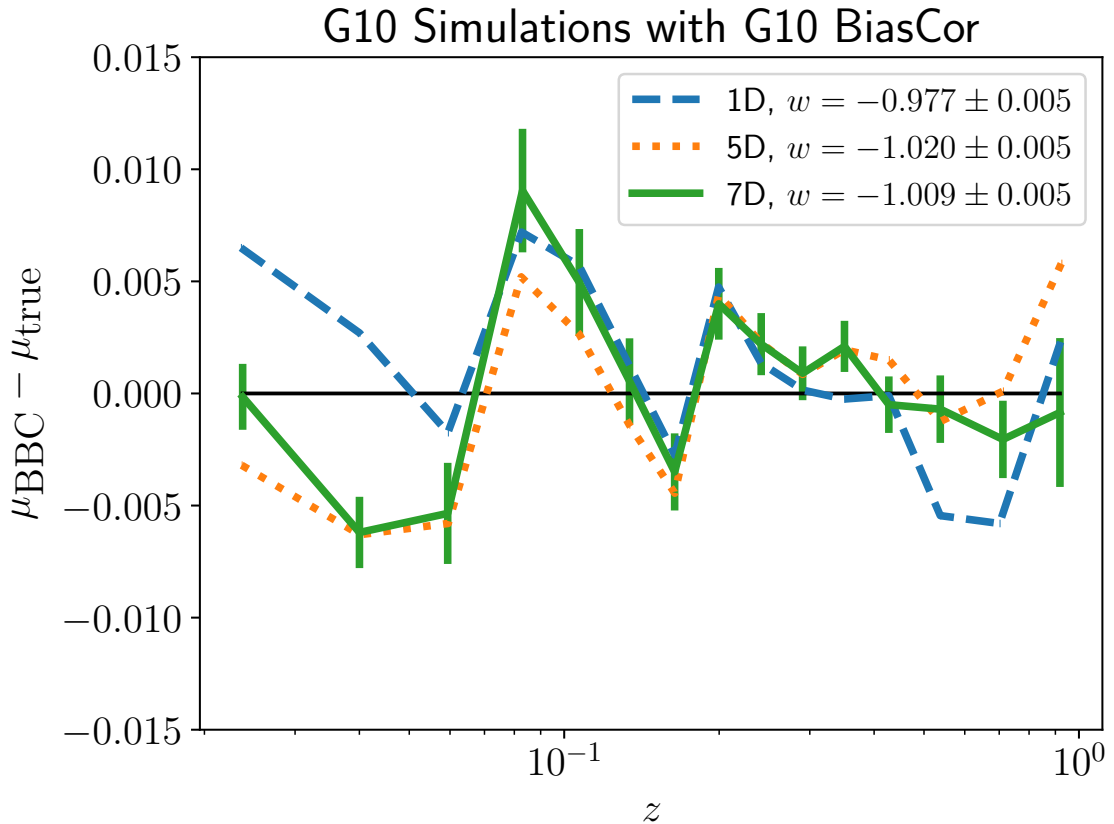


Figure 5.5: The binned μ residuals for the G10 scatter model using three different BBC methods on the same set of simulations. Uncertainties are shown for BBC7D only but are representative for the other methods.

modeling.

BBC1D results in a w -bias of $\sim 0.04 \pm 0.004$, while the BBC-BS20 w -bias is significantly reduced and consistent with 0, $\sim 0.006 \pm 0.004$. We find that the Hubble Scatter in the BS20 simulations is $\sim 10\%$ smaller than that of G10 or C11, which is illustrated in Figure 5.6.

This is the Accepted Manuscript version of an article accepted for publication in The Astrophysical Journal. IOP Publishing Ltd is not responsible for any errors or omissions in this version of the manuscript or any version derived from it. The Version of Record is available online at [10.3847/1538-4357/abf14f](https://doi.org/10.3847/1538-4357/abf14f)

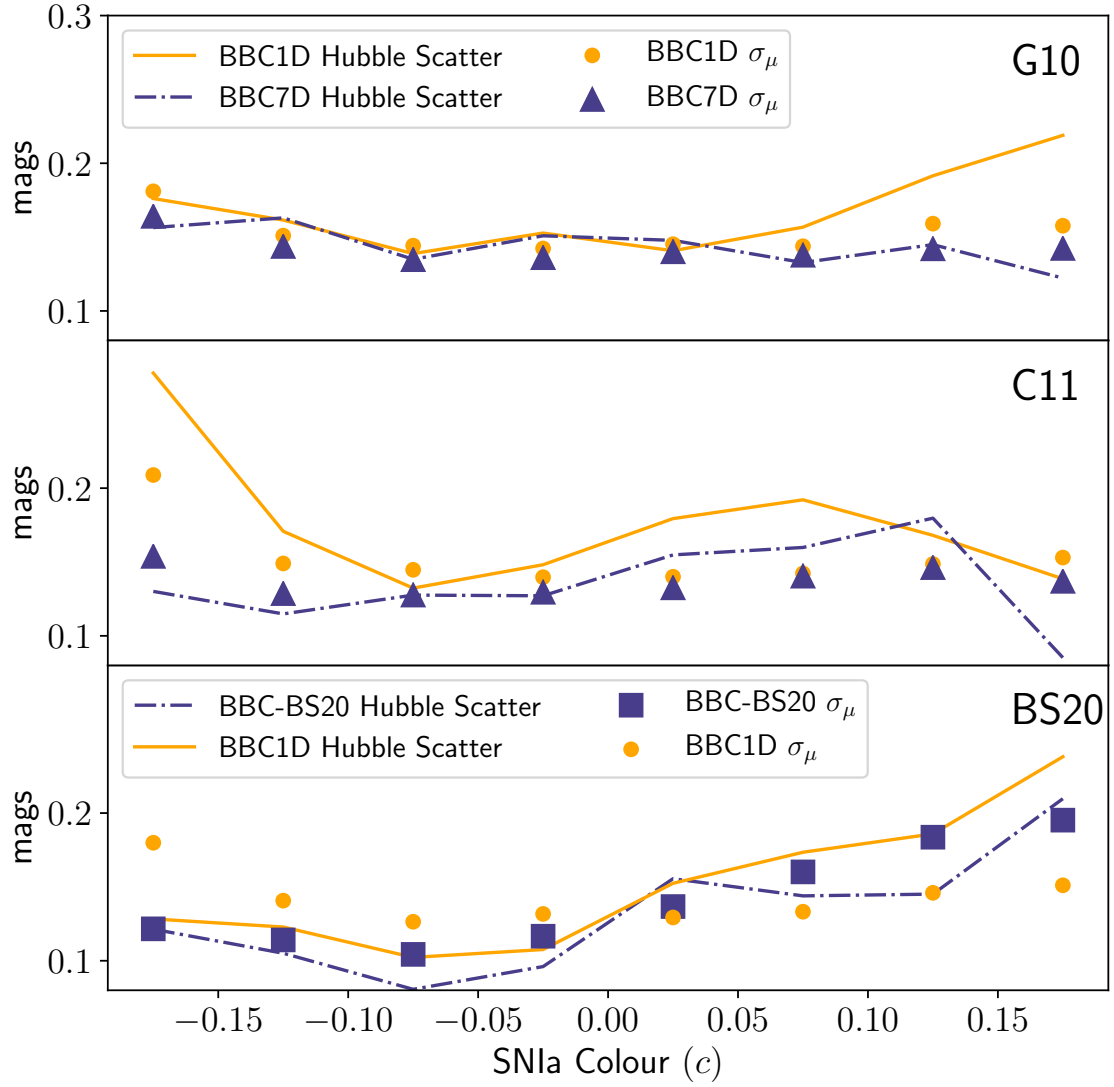


Figure 5.6: The Hubble Scatter (line) and the BBC-fitted distance modulus uncertainties, σ_μ , (triangle) are plotted for three different scatter models. We expect good agreement between the two for an effective BBC method.

Chapter 6

Biases in Photometric Samples

The results presented in this chapter, as well as some portions of text, are from Popovic et al. (2019). The text represents my own work, and the contributions of other authors is presented as such:

- *Daniel Scolnic: Analysis and advising. Dan is responsible for the initial scope of the paper and aided greatly in much of the analysis of my first paper.*
- *Richard Kessler: Implementation of code and analysis construction, particularly with regards to host mis-association within SNANA and the old Nearest Neighbour pipeline.*

By this chapter we have left the auspices of the simulation structure presented in Figure 2.9, but that is not to say it is not still helpful. Here we investigate a set of systematic uncertainties that are unique to photometric samples: those samples where the spectrum of the supernova is not acquired. As we shall see, our simulation framework will prove indispensable to this investigation. In this chapter we shall call back to simulations of non-Ia supernova as introduced in Chapter 2.5, which are used to estimate non-Ia contamination in photometric samples.

This chapter represents the first foray into photometric samples, those sets of SNe Ia that do not have spectroscopic measurements. Having no guarantee of their typing, we need to be able to account for potential contamination from SNe that are not standardisable. The switch from spectroscopic samples also introduces the question of what the true host galaxy of the supernova is. With spectroscopic measurements,

we obtain a redshift of the supernova, which can be compared to that of the galaxy. While the galaxy redshift is more accurate (on the order of 10^{-4}), and therefore preferentially used, an SN redshift provides a helpful check to ensure that an incorrect redshift is not used. Photometric samples do not have this check. Therefore, much like estimating the non-Ia contamination, we must estimate the mis-association and how that impacts our cosmological measurements. The BEAMS technique, as illustrated in Figure 2.7, will make its return here.

While photometric samples seem like they may introduce a whole host of new problems, we shall see through the course of this chapter and beyond that there are tools to mitigate these new challenges, and that the increased statistics and ease of modeling vastly outweigh any potential downsides to photometric samples.

6.1 Analysis

Measuring cosmological parameters with SNIa requires modeling and fitting the observed light-curves and using the results to standardize supernova brightness for distance measurements. Distances are evaluated with the Tripp equation, detailed in Equation 4 in Abbott et al. (2019) and Equation 3 in S18. Simulations are also needed to correct for distance biases and to generate training samples for classifiers. We review the main steps of the analysis here.

To better understand our systematic uncertainties, we simulated 30,000 events and split them into 40 data sized samples so that each simulated subsample is comparable in size to our real data sample (~ 700 SNe). The full analysis is performed on each simulated subsample as well as the true data sample.

6.1.1 Host Matching

To match a supernova to its most likely host galaxy, the d_{DLR} method is employed. This uses angular separation ($\Delta\theta$) and accounts for the galaxy spatial profile and orientation.

We start with the radial equation of an ellipse as measured from the center, with semi-major and semi-minor axes a and b and orientation angle θ :

$$r(\theta) = \frac{ab}{\sqrt{(a\sin\theta)^2 + (b\cos\theta)^2}} \quad (6.1)$$

We define the supernova angle as the angular difference between a line that goes through the supernova position and galaxy center and a line that passes through North and the galaxy center. Combined with the orientation of the galaxy as given by the galaxy position angle we define θ by subtracting the supernova angle from the position angle of the galaxy. With a , b , and θ , the directional light radius (DLR) is defined from equation 6.1 as the effective radius of the galaxy at angle θ .

The position angle of the galaxy can be found using the Stokes parameters Q and U given in the SDSS DR14 data release. DR14 uses a slightly unconventional notation for U ; this is corrected with a factor of 2 in the position angle.

Since these parameters are not fits to a model, but rather based on pixel data, they are more robust for fainter galaxies. The position angle ϕ can be expressed as

$$\phi = \frac{1}{2}\arctan\left(\frac{2U}{Q}\right) \quad (6.2)$$

The ratio of the semi-major and minor axes can also be computed with the Stokes parameters. Defining $\kappa \equiv Q^2 + U^2$, the ratio a/b is then expressed as

$$\frac{a}{b} = \frac{1 + \kappa + 2\sqrt{\kappa}}{1 - \kappa} \quad (6.3)$$

Following S14, we set a equal to the Petrosian half light radius within the r -band and b is determined using equation 6.3. Finally, we define a distance weighted d_{DLR}

$$d_{\text{DLR}} = \frac{\text{Angular separation}}{r(\theta)} \quad (6.4)$$

It is important to note that DLR and d_{DLR} are survey dependent quantities and are not easily comparable across surveys. Of particular note are magnitude cutoffs. Establishing a magnitude limit does allow for fine tuned control of $\Delta\theta$ density, but does not account for apparent ellipticity. At higher magnitudes, the apparent ellipticity as measured by the Stokes parameters begins to increase. At fainter brightness, noise begins to dominate the signal and leads to unrealistic ellipticity measurements. But differences in magnitude limits for different surveys, combined with those in image processing, can alter the apparent size of a galaxy. Self-consistent DLR measurements within the survey are more accurate than solely $\Delta\theta$ determinations, but cross comparison would not be effective.

For each SN, all galaxies within $30''$ are selected and sorted by ascending d_{DLR} values. The galaxy with the smallest d_{DLR} is considered to be the host galaxy.

6.1.2 Light-curve Fitting

Selection requirements (cuts) are applied to reduce CC contamination and to define a sample which has distance biases that can be modeled with a Monte Carlo simulation. Supernovae with properties within the SALT2 training range of colour ($-0.3 < c < 0.3$) and stretch ($-3 < x_1 < 3$) are selected. To ensure well-measured light-curve

fit parameters, we apply cuts on the uncertainties for stretch ($\sigma_{x_1} < 1$) and time of maximum brightness ($\sigma_{t_0} < 2$ observer frame days). We also require that the SALT2 fit probability (based on χ^2 per degree of freedom) is > 0.001 . Next, we define a rest-frame age, $T_{\text{rest}} = (\text{MJD} - \text{MJD}_{\text{peak}})/(1+z)$, where MJD is the observation date, MJD_{peak} is the date of peak brightness, and z is the redshift. We require that at least one observation satisfies $T_{\text{rest}} > 10$ days, and that at least one observation satisfies $T_{\text{rest}} < 0$ days. Finally, we require that at least two bands have an epoch in which the SNR is > 5 . A summary of these cuts on the data are shown in Table 6.1.

Table 6.1: Sequential selection requirements on the SDSS transient sample.

Cut	Number	Comments
Total Candidates	10,258	Data Release (Sako 2018)
Spec-z and d_{DLR}	4,356	Host galaxy redshift
$T_{\text{rest}} < 0$	3,852	Light-curve sampling
$T_{\text{rest}} > 10$	3,518	Light-curve sampling
SNR	2,717	Signal to Noise Ratio > 5
SALT2 Fit Parameters	1,219	$c, x_1, \sigma_{x_1}, \sigma_{t_0}$
NN Classifier	700	Nearest Neighbour classifier

6.1.3 Classification

We use a Nearest Neighbour (NN) classifier developed by Sako et al. (2018) and Kessler & Scolnic (2017). We simulate a large training sample of SN (Ia + CC) with the same selection requirements and light-curve fitting as for the data. The redshift, colour, and stretch ($z, c,$ and x_1) are used to define a 3-dimensional (3D) space for the NN analysis. In this space, each data point (real or simulated) is the center of a sphere at $\{z, c, x_1\}$. Classification is done by counting the number of Ia and CC SN within the sphere, and the data point is classified to be the type that is most frequent inside the sphere. The size of the sphere is set with a metric determined by

maximising the product of the efficiency and purity (Kessler & Scolnic (2017)). Data identified as SNIa with a probability of less than 0.5 are rejected.

6.1.4 BBC and Cosmology Fitting

Cosmological analysis within the BBC framework is done in three stages. The first stage classifies supernovae as Ia or CC using the NN method, and assigns a probability (P_{Ia}) for each event to be a SNIa. The second stage separates the data into redshift bins and determines a mean distance modulus in each bin, after accounting for selection biases and CC contamination (Kessler & Scolnic (2017)). Here we use 10 equal sized bins ranging from $z = 0.02$ to 0.5. The third stage performs a cosmological fit to the binned distances using BAO (Eisenstein et al. (2005)) and CMB (Komatsu et al. (2009)) priors, similar to Lasker et al. (2019) who found these priors to be sufficient for systematics studies.

6.2 Simulations

Simulated supernovae are needed to calculate bias corrections, create training samples, and assess the impact of our systematics. We use the SNANA software to simulate supernova light-curves using SDSS detection efficiencies, Point Spread Function (PSF) sizes, sky noise, and zeropoints. The observing history has previously been modeled for SDSS in Kessler et al. (2009). While Kessler et al. (2009) modeled the spectroscopic selection efficiency of the supernovae, here we model the efficiency of obtaining a spectroscopic redshift from the host galaxy, as described below. A complete description of how these simulations are generated for DES is given in Kessler et al. (2019); for this study we replace the survey description of DES with that for SDSS. We simulate our SNe with Λ CDM cosmology, with a flat universe ($k=0$),

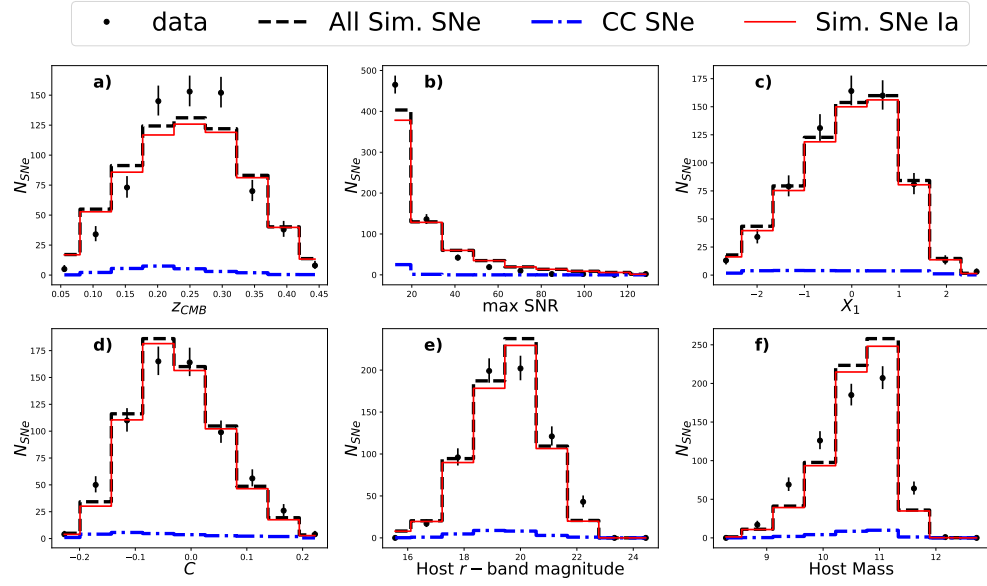


Figure 6.1: A comparison between the data and the Fiduciary simulation for various distributions. The data is shown in points with error bars, the dashed histogram shows the total simulated SNe (Ia + CC), the solid histogram shows the simulated SNIa only, and the dotted histogram shows simulated CC. The simulated CC contamination is $\sim 4\%$ of the total sample and is discussed further in section 6.3.

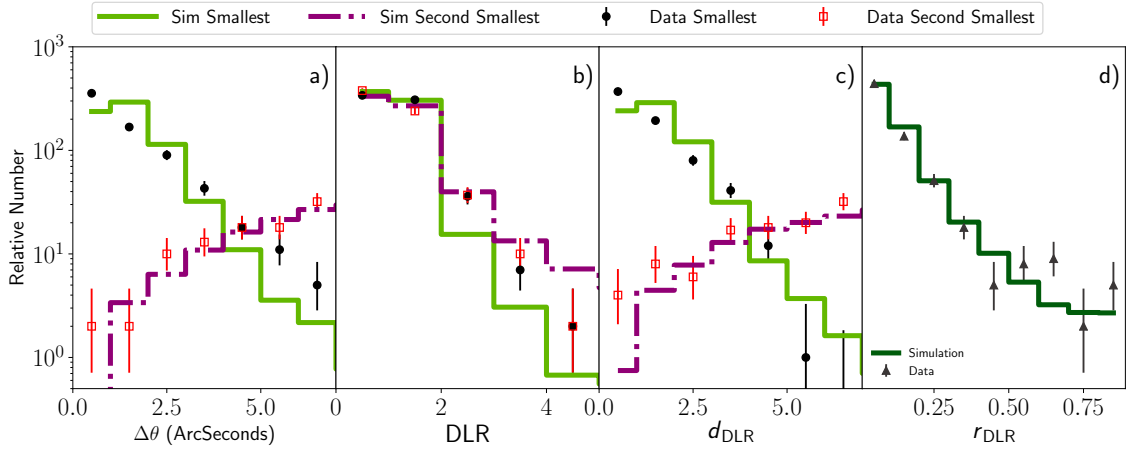


Figure 6.2: Distributions for data (filled circles and open squares) and Fiduciary SNIa-only simulation (histogram) for quantity indicated in each panel, as defined in section 6.1.1. For panels a), b), and c) the filled circles and solid histogram are for the smallest d_{DLR} value; open squares and dashed histogram are for the second smallest value. In d), r_{DLR} is shown by triangles for data and solid histogram for simulation.

$\Omega_{\text{Matter}} = 0.3$ and $w = -1$.

For this analysis, we simulate both Type Ia and CC light-curves. For SNIa, we use the SALT2 model with population parameters from Scolnic & Kessler (2016). Simulations were generated with the stretch-luminosity α and colour-luminosity β that were measured from the data as input ($\alpha = 0.14$ and $\beta = 3.2$; Sako et al. (2018)). We use the ‘‘G10’’ intrinsic scatter model from Kessler et al. (2013) using the error parameterisation from Guy et al. (2010). CC modeling is done with SED templates from Kessler et al. (2010c), Jones et al. (2018a), and the PLAsTiCC templates from Modelers (2019) and Kessler et al. (2019), further detailed in section 6.3.1. We denote our ‘Fiduciary’ analysis as using PLAsTiCC CC templates (excluding SNIax) in the training sample along with an adjusted luminosity function to match Jones et al. (2018b). Figure 6.1 shows the distributions of data are in good agreement with those from the Fiduciary simulations for redshift, SNR, colour and stretch.

6.2.1 Host Galaxy Libraries

To model the potential measurement biases of cosmological parameters based on selection of host galaxies, we first create a realistic library of host galaxies (HOSTLIB) with properties that match those of our data. We evaluate the quality of our HOSTLIB by comparing the distributions of smallest and second smallest d_{DLR} (section 6.1.1); these distributions are sensitive to galaxy spatial profile, survey depth, galaxy photo- z , and $\Delta\theta$.

We evaluated three different HOSTLIBs to use in our simulations. The first two, the Advanced Camera for Surveys General Catalog (ACS-GC) and the Marenstrum Institut de Ciències de l’Espai Simulations Catalogue (MICECAT), were used in Gupta et al. (2016). For these two HOSTLIBs, the simulated $\Delta\theta$ distribution does

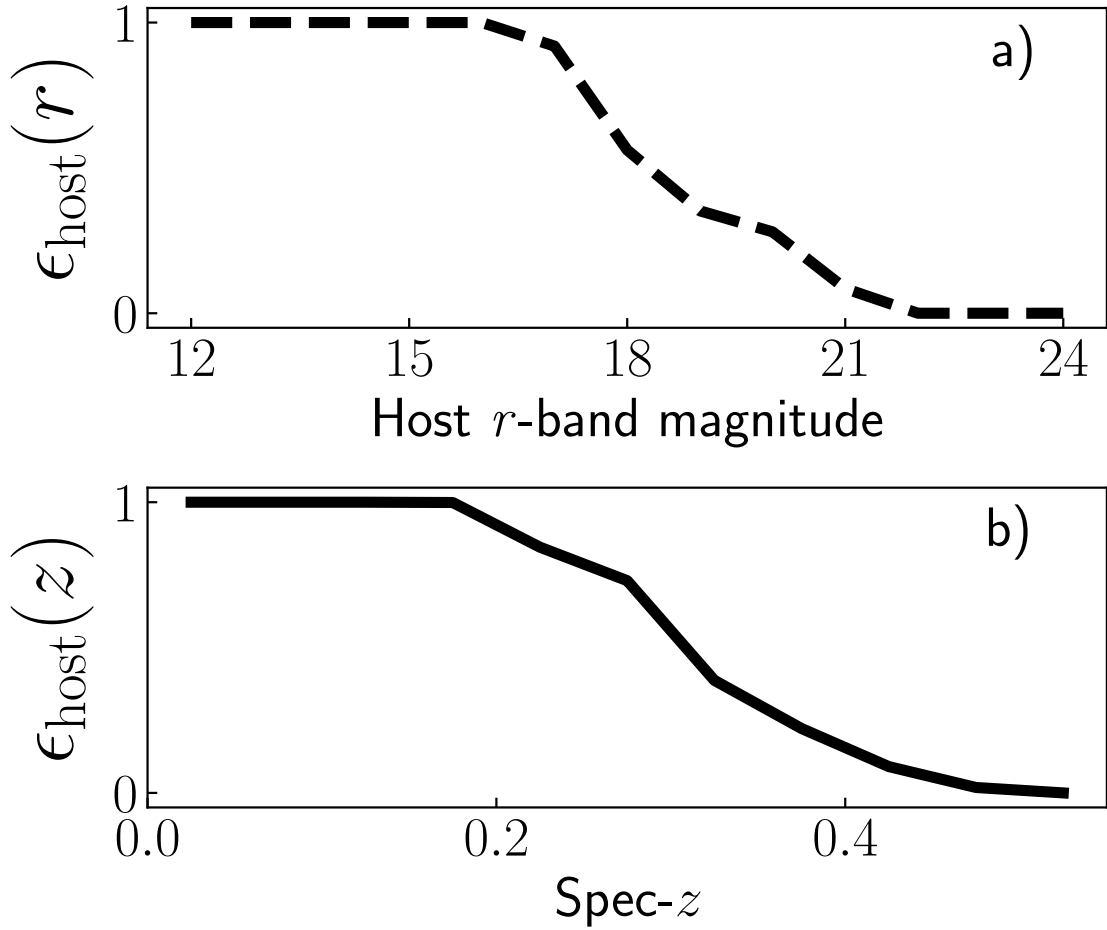


Figure 6.3: The measured r -band host magnitude efficiency is shown in black dashed line and the measured host spec- z efficiency is shown in solid black. The spec- z efficiency is roughly half at $z = 0.3$. The r -band host magnitude efficiency drops off at the faint end.

not match the SDSS data.

Therefore, we created a third library by compiling observed galaxies within Stripe 82 from the SDSS DR14 data release. To maximise completeness and exclude spectroscopic selection effects, we selected host galaxies with a photometric redshift. The HOSTLIB includes Sersic profile information calculated from the Stokes values. These profiles are used in simulations to place supernovae near a galaxy and to model Poisson noise from the host galaxy. The SNANA simulation only calculates the smallest d_{DLR} value for each SN, so the second smallest values were calculated separately from the HOSTLIB.

For data and simulation, Figure 6.2 compares distributions of $\Delta\theta$, DLR, and d_{DLR} . Each distribution is shown separately for the smallest and second smallest d_{DLR} value. Also shown is the ratio of smallest to second smallest d_{DLR} values (r_{DLR}). We find good agreement in all distributions. Note that a HOSTLIB with too-large separations between galaxies can result in good data/sim agreement for the smallest d_{DLR} in Figures 6.2a, b, and c, but would result in poor agreement for the second-smallest d_{DLR} , and also under-predict mis-associations. The good agreement for the second smallest d_{DLR} and r_{DLR} is therefore an important metric for reliably predicting the mis-association rate. We also show in Figure 6.1e that there is good agreement in the r -band magnitude of the host-galaxy distribution between data and simulations.

Past studies have shown that there is a correlation between the stretch-and-colour-corrected luminosity of SNIa and the host galaxy stellar mass (M_{stellar}). This effect has been found in the Supernova Legacy Survey (SNLS; Sullivan et al. (2010)), the SDSS sample (Lampeitl et al. (2010); Wolf et al. (2016); Hayden et al. (2013); Gupta et al. (2011)), and the PS1 sample (S18). In this SDSS analysis, we simulate these correlations to estimate biases arising from our spectroscopic galaxy selection. For every galaxy in our HOSTLIB, we calculate M_{stellar} using the methodology from

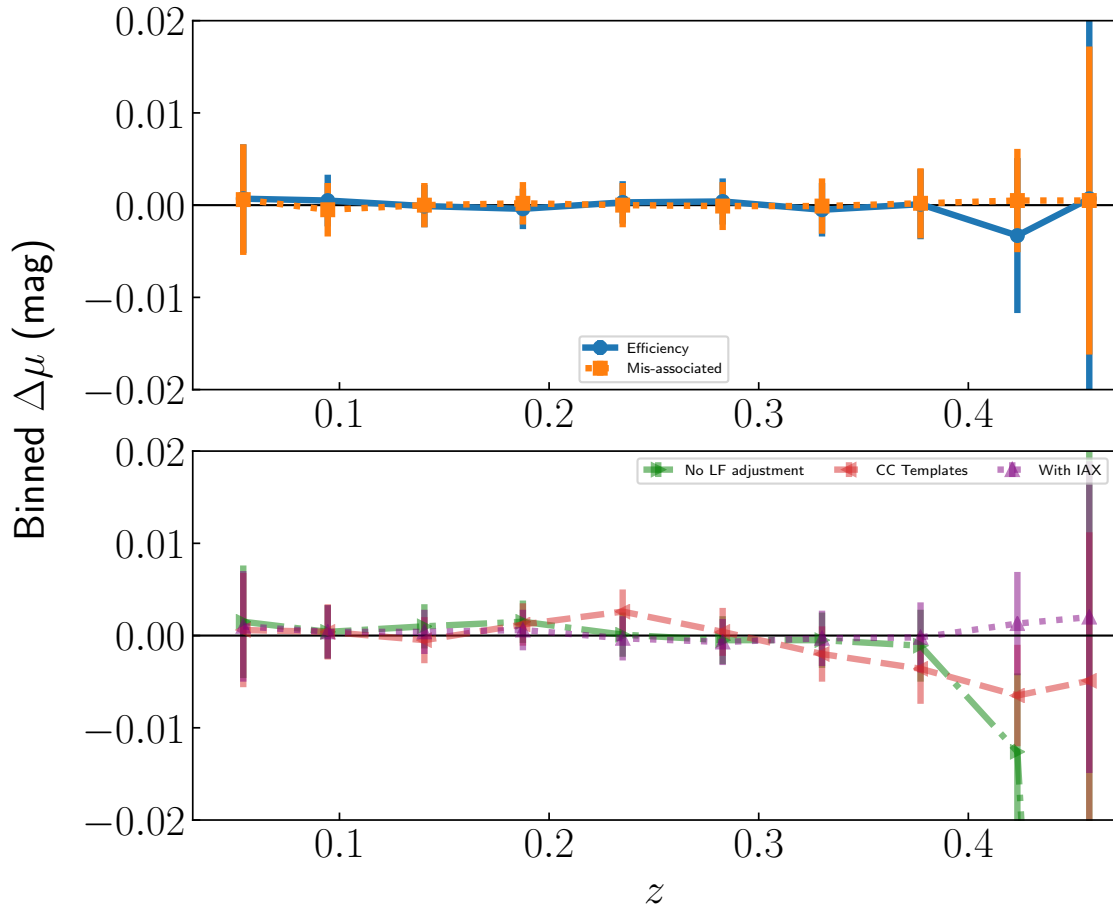


Figure 6.4: The difference between binned distance modulus residuals for each systematic are shown here, for simulated supernovae. The top panel shows the effect of host galaxy selection changes, the bottom shows the different CC options.

Taylor et al. (2011),

$$M_{\text{stellar}} = 1.15 + 0.7 \times (g - i - 0.4 \times (i - \mu_{\text{calc}})), \quad (6.5)$$

where g and i are the host galaxy magnitudes in the respective band, and μ_{calc} is the calculated distance modulus using the galaxy redshift and same Λ CDM cosmology parameters as in the simulations. Equation 6.5 is used to calculate masses for both the data and the HOSTLIB. A comparison of the host-mass distribution between data and simulations is shown in Figure 6.1f; while the agreement is not as good as for the host-galaxy magnitude comparison and could use further study, it is sufficient to assess systematics.

We introduce a -0.025 mag correction to the luminosity of supernovae in galaxies with stellar mass $M_{\odot} > 10^{10}$, and a $+0.025$ mag correction to those with $M_{\odot} < 10^{10}$. We do not include additional correlations of SNIa properties (c and x_1) with host galaxy properties, these correlations are discussed in Smith et al. (2014).

Using simulations generated with input from our HOSTLIB, we evaluate the selection efficiency of our host galaxy. In our Fiduciary analysis, we define the efficiency, $\epsilon_{\text{host}}(r)$, to be a function of host galaxy r -band magnitude as follows,

$$\epsilon_{\text{host}}(r) \equiv N_{\text{data}}(r)/N_{\text{sim}}(r) \quad (6.6)$$

where $N_{\text{data}}(r)$ is the number of SNe in each host galaxy r -band magnitude bin for data, and $N_{\text{sim}}(r)$ is the number of SNe in each host galaxy r -band magnitude bin for a simulation with $\epsilon_{\text{host}}(r) = 1$. We scale $\epsilon_{\text{host}}(r)$ so that the maximum is 1 (Figure 6.3a).

For a systematic test, we follow Jones et al. (2018b) and parameterize the selection

function to depend on host spec- z (Figure 6.3b),

$$\epsilon_{\text{host}}(z) \equiv N_{\text{data}}(z)/N_{\text{sim}}(z) \quad (6.7)$$

where z is the host galaxy spec- z , and $N_{\text{data}}(z)$ and $N_{\text{sim}}(z)$ are defined as in equation 6.6, but using z bins.

6.2.2 Core Collapse Simulations

An important systematic in cosmological analyses of photometric samples is the collection of CC models used to simulate training samples for classifiers. The most recent study on this systematic has been done by Jones et al. (2018b), which used a compendium of publicly available CC templates and adjusted the luminosity functions of the library to match the Hubble residual tail region after selection cuts. Light-curve templates of SNII were adjusted by 1.1 mag to be more luminous and SNIb/c were similarly adjusted by 1.2 mag.

Since Jones et al. (2018b), the PLAsTiCC library (Kessler et al. (2019); Modelers (2019)) was released, which has enhanced previous CC template libraries. Compared with Jones et al. (2018b), here we include MOSFiT (Modular Open-Source Fitter for Transients) for SNIbc (Kessler et al. (2010a); Pierel et al. (2018a); Guillochon et al. (2018a); Villar et al. (2017a)), NMF (Nonnegative Matrix Factorization) for SNII (Kessler et al. (2010b); Pierel et al. (2018b); Guillochon et al. (2018b); Villar et al. (2017b)), SNIax (Jha (2017a)), and SNIa-91bg. We included an additional 0.9 mag smear for SNII-NMF as discussed in Kessler et al. (2019). Our Fiduciary analysis includes SNII-NMF, SNIbc-MOSFiT, and SNIa-91bg. As we will discuss in the next section, SNIax were excluded from both the simulated training and data samples.

6.2.3 SNIax Simulations

The PLAsTiCC models include SNIax, which typically have lower luminosity, lower ejecta velocity, and greater variation in photometric parameters than their SNIa counterparts. The SED model used in PLAsTiCC is based on the real SNIax, 2005hk. The SED model was augmented with other spectra and the luminosity function was inferred from the sample studied in Jha (2017b). Light-curves are generated to match the absolute magnitude (M_V), rise time (t_{rise}), and decline rate in the B and R bands ($\Delta m_{15}(B)$ and $\Delta m_{15}(R)$) detailed in Stritzinger et al. (2015) and Magee et al. (2016).

6.2.4 Simulation Analysis

We apply the analysis (Section 3) to our simulated data sample, and fit for nuisance parameters α , β , γ , and cosmological parameter w . The recovered values for these parameters in our Fiduciary analysis are consistent with their input values of 0.14, 3.2, 0.05, and -1 , respectively. More precise validation tests with simulations are described in Section 6 of Brout et al. (2018).

6.3 Results

Here we assess the impact on our cosmological measurements of the systematics studied in this analysis, such as different CC templates used in classifier training sets, the frequency of host galaxy mis-association, and the modeling of selection efficiency. A summary of the various cosmological biases from these uncertainties is presented in Table 6.2. The mean bias in w is determined with the 40 simulated subsamples for each systematic listed in Table 6.2, which has previously been discussed individually. In addition, the error on the mean and the scatter, or robust standard deviation,

have also been calculated for the simulations. We define

$$\Delta w \equiv w_{Fid} - w_{sys} \quad (6.8)$$

as the w -bias. For data, w_{Fid} is the measured w value for the Fiduciary analysis. For simulations, w_{Fid} is the mean measured w of our subsamples. The bias in recovered distances as a function of redshift due to each systematic uncertainty is shown in Figure 6.4. We define the statistical error (w_{stat}) as

$$w_{stat} = w_{RMS} / \sqrt{N_{sub}} \quad (6.9)$$

where w_{RMS} is the RMS of Δw and N_{sub} is the number of subsamples. With 40 subsamples, the statistical error in our mean Δw is below 0.004, which is sufficiently small for this analysis.

Host galaxy mis-association and shifts in the CC luminosity function result in a w -bias that can be corrected, and the resulting systematic uncertainty is typically smaller than the correction. Here we use the size of each correction as a systematic uncertainty, and in future work will evaluate the reliability of these corrections along with the associated systematic uncertainties.

6.3.1 Galaxy Association and Mis-association

Figure 6.2 shows the properties used to validate the simulations from which the mis-association rate was determined. Comparing each true host galaxy in our simulation to the d_{DLR} -selected galaxy, we determine the host galaxy mis-association to be 0.6%.

Figure 6.5 shows the effect of mis-associated hosts on redshifts (6.5a), as well as the distributions of $\Delta\theta$ (6.5b) and d_{DLR} (6.5c) for those mis-associated hosts; figure

Table 6.2: w Differences for Systematic Tests

Systematic Test (Host)	Δw_{sim}^a	w_{RMS}^b	Δw_{data}^c	N_σ^d
Mis-associated Host	+0.0007(09)	0.0059	N/A	N/A
Host Efficiency	-0.0072(37)	0.0237	-0.006	0.05 σ
Systematic Test (Contamination)	Δw_{sim}	w_{RMS}	Δw_{data}	N_σ
No LF adjustment	-0.0109(03)	0.0192	-0.041	1.57 σ
Choice of CC model	-0.0028(14)	0.0089	-0.002	0.09 σ
Include Iax	-0.0022(09)	0.0059	+0.001	2.07 σ

^aMean Δw of the 40 simulated subsamples.

^bThe Root Mean Square of the simulated subsamples.

^cThe Δw measured by the data.

^dThe number of standard deviations of Δw for data away from Δw for sim, defined in equation 6.10.

6.5d is a histogram of r_{DLR} for mis-associated SN. In each panel, the distribution for mis-associated hosts is much broader compared to correctly identified hosts.

We find that the recovery of w is biased by $\Delta w = 0.0007$ by this mis-association, which is consistent with 0.

6.3.2 Impact of Host Galaxy Selection Efficiency

We evaluate the bias on w due to our host galaxy selection by comparing our recovered distances using $\epsilon_{\text{host}}(r)$ to those using $\epsilon_{\text{host}}(z)$. The impact on the binned distances is shown in Figure 6.4. For most of the redshift range, the impact is less than 2 milli-mags and the only significant impact is at the higher end of our redshift range. This produces a w -bias of $\Delta w = -0.0072 \pm 0.0037$, significantly smaller than the statistical uncertainty. The RMS around this value is 0.05 σ .

6.3.3 Impact of Core Collapse Templates

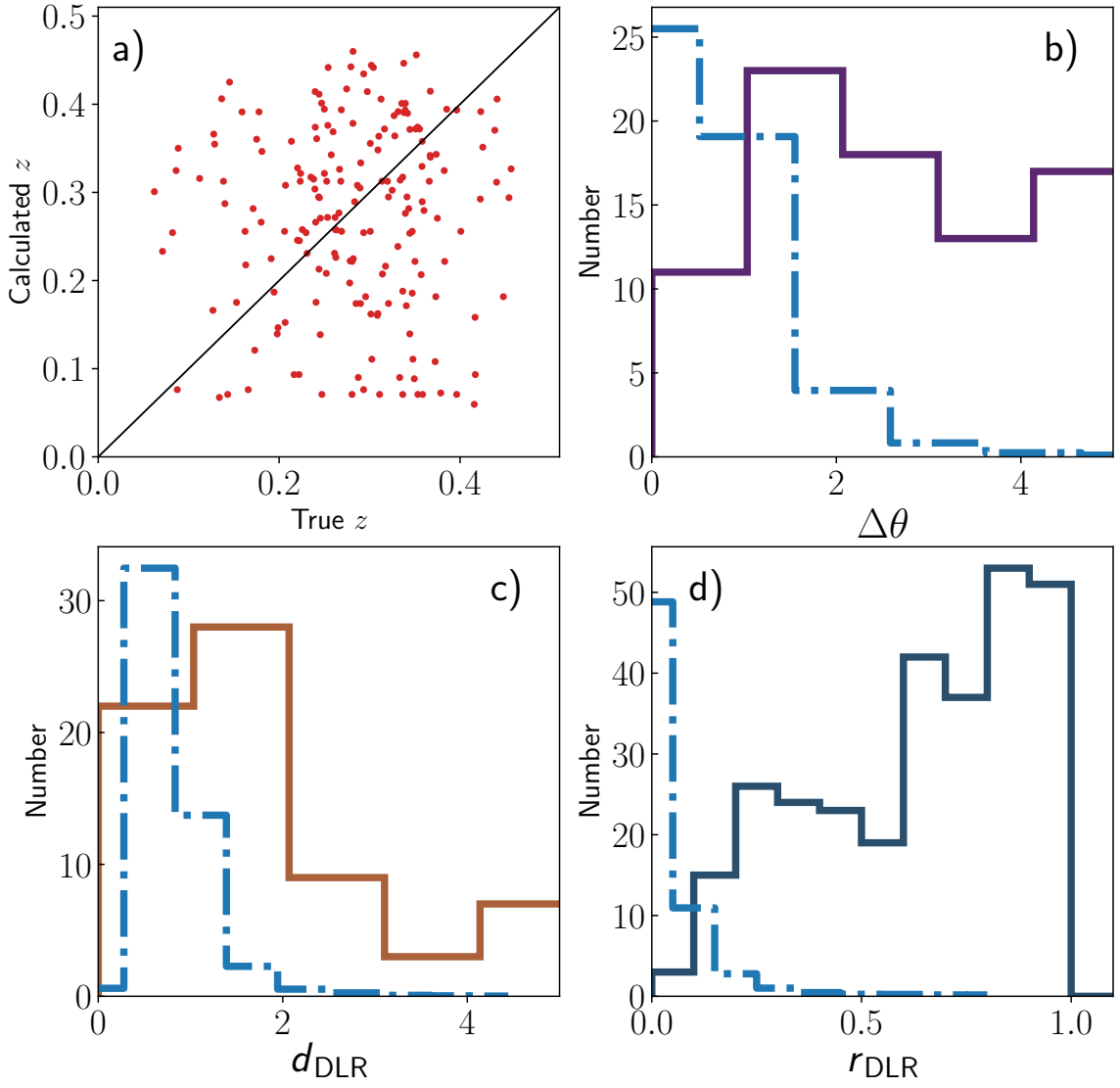


Figure 6.5: For simulated supernovae with mis-associated hosts, Panel a) shows true values of redshift versus the calculated values, with the black line showing correct association for reference. The solid histograms in panels b), c), and d) show distributions only for the mis-associated supernovae, the dash-dotted histogram for all supernovae (normalised to mis-associated population). When the galaxy is mis-associated, we attribute SNe to higher-redshift hosts 56% of the time and lower-redshift hosts 44% of the time.

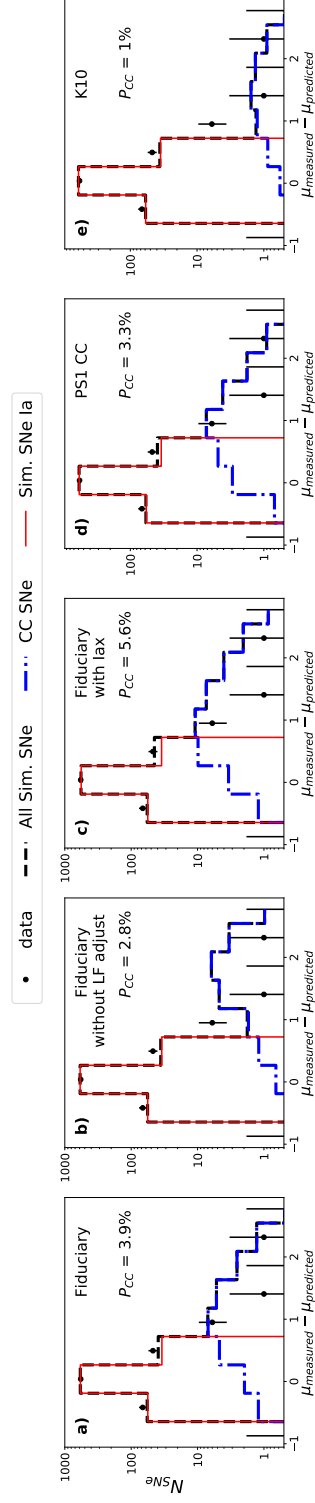


Figure 6.6: The Hubble residual distribution for data, and for simulations using different CC models as indicated on each panel. $\mu_{measured}$ is the measured Tripp distance modulus and $\mu_{predicted}$ is the predicted distance modulus from Λ CDM cosmology. The training sample is the Fiduciary CC model in all cases. Data is shown with points, simulated SNIa are shown with a red histogram, and simulated CC SNe are shown with a blue dashed histogram. The combined simulated distribution of CC and Ia SNe is shown with a black dashed histogram. The non-SNIa contamination (P_{CC}) is shown for each panel.

Figure 6.6 shows the Hubble residual distributions using five different CC models in the analysis, and each model is indicated in the panel. Figure 6.6 contains our Fiduciary case, where CC templates used in the simulations are from: the PLAsTiCC models with an adjusted luminosity function and without SNIax; the PLAsTiCC model with neither adjusted luminosity function nor SNIax; the PLAsTiCC model with adjusted luminosity function and SNIax; the CC templates from Kessler et al. (2010c) without luminosity adjustments (K10); and the CC templates from Jones et al. (2018a) with adjustments. The smallest contamination (P_{CC}) is 1% for K10, and the highest is 5.9% for the Fiduciary with Iax analysis. Still, we see that the contamination in the data for the positive tail of the Hubble residual distribution is better predicted in some cases than others. We find that the PLAsTiCC and K10 models do not match the data well in this region, confirming the need for luminosity function corrections to match the high Hubble residual tail suggested in Jones et al. (2018a).

For the case of Fiduciary with SNIax, the SNIax make up 40% of the CC contamination. While the SNIax luminosity distribution is fainter than SNIa, we also find that the x_1 and c values satisfy the selection requirements (see section 2.2), and therefore the NN classification poorly separates SNIa from SNIax. Jones et al. (2018b) do not include SNIax in the contamination library due to the expectation that they are too red ($c > 0.3$), and because the SNIax model was not available. As discussed in section 6.2.3, only a single SN was used to generate the SNIax model. However, if we perform SALT2 light-curve fits on the four known SNIax in SDSS (including 2005hk), we find that all the SNIax have fitted colour values $c > 0.3$ and thus fail our selection requirements. Therefore, these light-curve fits suggest that the SNIax contamination is overestimated and further study is needed.

From simulations, the impact on w due to the systematics related to core collapse

libraries is given in Table 6.2. We find the mean bias due to the CC systematics is $\Delta w < |0.01|$ with a statistical uncertainty of ~ 0.001 . The RMS in w from the simulations due to the systematics is 0.01-0.02.

6.3.4 Data and Simulation Comparison

In the last two columns of Table 6.2, we show the impact on w of the systematics studied in this analysis for the real data sample. This is shown for all the systematics except for the mis-associated host, as there we can not apply the same technique on the data as we did for the simulations. To assess whether the changes seen for the data sample are consistent with predictions from the simulations, we define the number of standard deviations (N_σ) for each systematic as

$$N_\sigma = (\Delta w_{\text{sim}} - \Delta w_{\text{data}})/w_{\text{RMS}} \quad (6.10)$$

where Δw_{sim} is the Δw recovered in simulations, Δw_{data} is the Δw recovered from the data, and w_{RMS} is the RMS of the Δw recovered from simulations. We find that the highest deviation compared to the simulations is seen for the ‘No LF adjustment’ systematic at 2.1σ . All other deviations near or below $< 1\sigma$. Therefore, we conclude that the impacts of the systematics seen in the simulations are consistent with those seen for the data.

This is the Accepted Manuscript version of an article accepted for publication in The Astrophysical Journal. IOP Publishing Ltd is not responsible for any errors or omissions in this version of the manuscript or any version derived from it. The Version of Record is available online at the following doi: 10.3847/1538-4357/ab6deb

Chapter 7

Amalgame

7.1 Introduction

This chapter is the amalgamation of the previous chapters, pulling together the techniques for simulation, bias correction, and the new systematic uncertainties. Compilation surveys such as Pantheon and Pantheon+ have been common in the past decade, representing the pinnacle of this generation’s cosmological measurements with SNIa. **But never before has a compilation been attempted with photometric samples.** With the previous chapters of this thesis finished, and the necessary tools and data to perform a cosmology analysis introduced, I apply these techniques to the Amalgame data set. Amalgame is comprised of SDSS, PS1, Low-z, and Foundation. With 2259 likely SNIa, spanning $z = 0.01$ to 0.62, it is the largest-ever SNIa sample and the first combined photometric sample. In this chapter, we shall first go over a handful of changes to formalism introduced in the Amalgame sample, then review the systematic uncertainties of the sample in Section 7.5. After that, I present the combined cosmological results in Section 7.6.1 before comparing different combinations of the Amalgame sample in Section 7.6.2. Finally, I go over the impact and meaning of the systematic uncertainties in Section 7.6.3 before discussing the implications for future works.

Table 7.1: Number of SNe that pass SALT3 fitting before and after cosmology cuts.

Survey	Before Cuts	After Cuts
SDSS	2015	721
PS1	2478	1202
Foundation	174	170
Low-z	200	166

The cosmology cuts instituted for our data and simulations are shown below; Table 7.1 shows a breakdown of the number of likely SNIa before and after our cosmology cuts.

- $\sigma_{x_1} < 1$: SALT3 x_1 uncertainty < 1 .
- $\sigma_{\text{PKMJD}} < 2$: Uncertainty on fitted peak brightness < 2 days.
- $-3 < x_1 < 3$
- $-0.3 < c < 0.3$
- $T_{\text{rest,min}} < 5$: Requires at least 1 observation 5 days before peak brightness (rest frame)
- $T_{\text{rest,max}} > 0$: Requires at least 1 observation after peak brightness (rest frame)
- $-20 < T_{\text{rest}} < 60$: Requires at least one observation between -20 and 60 days (rest frame)

7.2 Updates to Dust2Dust

Proper modeling of dust parameters for photometric samples requires improvements to the methodology introduced previously. Chapter 4 assumed a spectroscopic sample free from core collapse contamination; this is no longer the case. Here we detail

updates to the Dust2Dust approach to incorporate the presence of core collapse supernovae in the Dust2Dust fit:

- We fix α and β in the Dust2Dust fit, instead of floating them in the SALT2mu minimisation.
- We institute a cut on the probability of being a Ia from our classifiers ($PIa > 0.5$).
- We do not include core collapse supernovae in the bounded simulations for Dust2Dust.
- We utilise BEAMS with the Hlozek et al. (2012) core-collapse prior.

In P22, the β (β_{obs} in P22) parameter is used as a metric criteria (Section 4.1 of P22). However, this presents issues with the colour vs. Hubble Residuals metric, which is calculated by subtracting out observed distances from the best fit cosmology for both data and simulations. When β_{obs} is floated, the resulting β_{obs} for the data and simulations are not guaranteed to be the same, therefore resulting in a bias in distance moduli that is not constrained by the more impactful colour vs. Hubble Residual metric (Table 6 of P22).

To fix this issue, the β_{obs} of the data is measured via a SALT2mu fit (Kessler & Scolnic (2017) find negligible differences between β determinations with 1D bias corrections and none) and then used as the nominal β_{obs} for both the simulations and the data. While this approach does remove β_{obs} as a metric criteria, it is not an effective constraint on dust model parameters, contributing little to the overall χ^2 .

To mitigate core collapse supernovae from contaminating the Dust2Dust fits, we implement a probability cut on the likelihood of being a Type Ia as assigned by our classifiers. The inclusion of obvious ($PIa < 0.5$) core collapse supernova impacts all

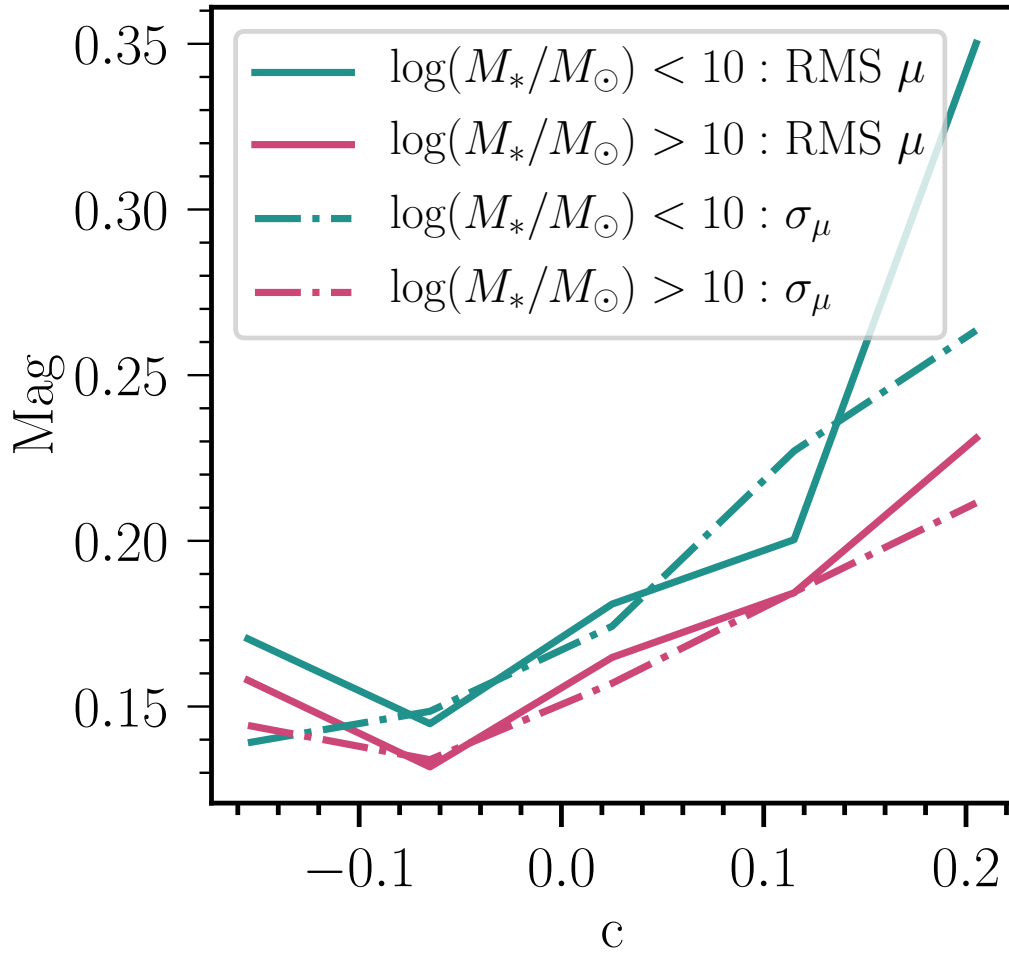


Figure 7.1: A comparison of the Root Mean Square of the Hubble residuals (solid) with the median distance modulus error (dash dotted) for the data as a function of colour. This is shown for high and low mass host galaxies.

of the Dust2Dust criteria, and in particular the colour distribution, Hubble Residual scatter, β_{obs} , and σ_{int} metrics are not able to be mitigated with the inclusion of BEAMS. Our nominal probability cut is an SNN-likelihood of greater than 0.5. As a quick test, we use our nominal dust model parameters with a probability cut of $PIa > 0.9$ to compare the results, and find a $\Delta\chi^2 = 11$.

We make the assumption that the probability cut removes enough non-Ia that the effects of not simulating core-collapse supernovae into the bounded simulations that comprise Dust2Dust are negligible. This approach has the added benefit of allowing us to use Vincenzi et al. (2019b) core collapse models, which include accurate dust information for core collapse supernovae.

Finally, we utilise the BEAMS methodology to mitigate the effect of any remaining core collapse supernovae on our colour vs. Hubble Residual metric. We present the best-fit Dust2Dust Amalgame samples along with a breakdown of their χ^2 in Table 7.2.

7.3 Updates to σ_{int}

Equations 2.6 and 2.7 in Section 2.1.8 detail the calculation of σ_{int} . Here we detail a small correction to the calculation.

When calculating μ for SNIa in the biasCor files, a β must be assumed. Brout et al. (2022) follow Popovic et al. (2021) in using the input β_{SALT} when calculating μ ; however, μ_{ERR} was calculated with β_{SN} due to an overlooked variable. Calculating μ and μ_{ERR} with inconsistent β values incorrectly increased the calculated σ_{int} values. This has since been fixed to use a consistent β_{SALT} .

Table 7.2: P22 Model Parameters and Criteria Fit for this paper.

Parameter	Value	Metric Criteria	χ^2
c_{int}	-0.074	χ_c^2	5.3
c_{std}	0.055	$\chi_{\mu_{\text{res}},\text{high}}^2$	27.3
High mass $\overline{R_V}$	3.17	$\chi_{\mu_{\text{res}},\text{low}}^2$	13.1
High mass σ_{RV}	1.23	$\chi_{\sigma_r,\text{high}}^2$	62.3
Low mass $\overline{R_V}$	1.71	$\chi_{\sigma_r,\text{low}}^2$	20.9
Low mass σ_{RV}	0.82	$\chi_{\beta_{\text{int}}}^2$	N/A
Low z , low mass τ_{EBV}	0.13	$\chi_{\sigma_{\text{int}}}^2$	0.64
Low z , high mass τ_{EBV}	0.12		
High z , low mass τ_{EBV}	0.11		
High z , high mass τ_{EBV}	0.13		
$\overline{\beta}_{\text{int}}$	1.50		
$\sigma_{\beta_{\text{int}}}$	0.29		

7.4 Sims and Data

Here we present the data-sim overlays for the SDSS and PS1 surveys. There is good agreement between the data and simulations. The redshift distribution for SDSS is slightly discrepant; this discrepancy is addressed in the efficiency modeling systematic in Section 7.5.4.

7.5 Systematic Uncertainty Sources

Here we introduce and detail the assumptions and approaches in our cosmological analysis that lead to possible systematic uncertainties. Each assumption is discussed and motivated, along with a complementary method of modeling to account for systematic uncertainties. The *purpose*, *baseline* treatment, and *systematic* uncertainties are given. For each of the systematics, we strive to maximise the consistency between the samples, applying the same techniques to all of the samples in Amalgame. The effect of these systematics are shown in Section 7.6; the detailed description of the systematics themselves are given here.

SDSS

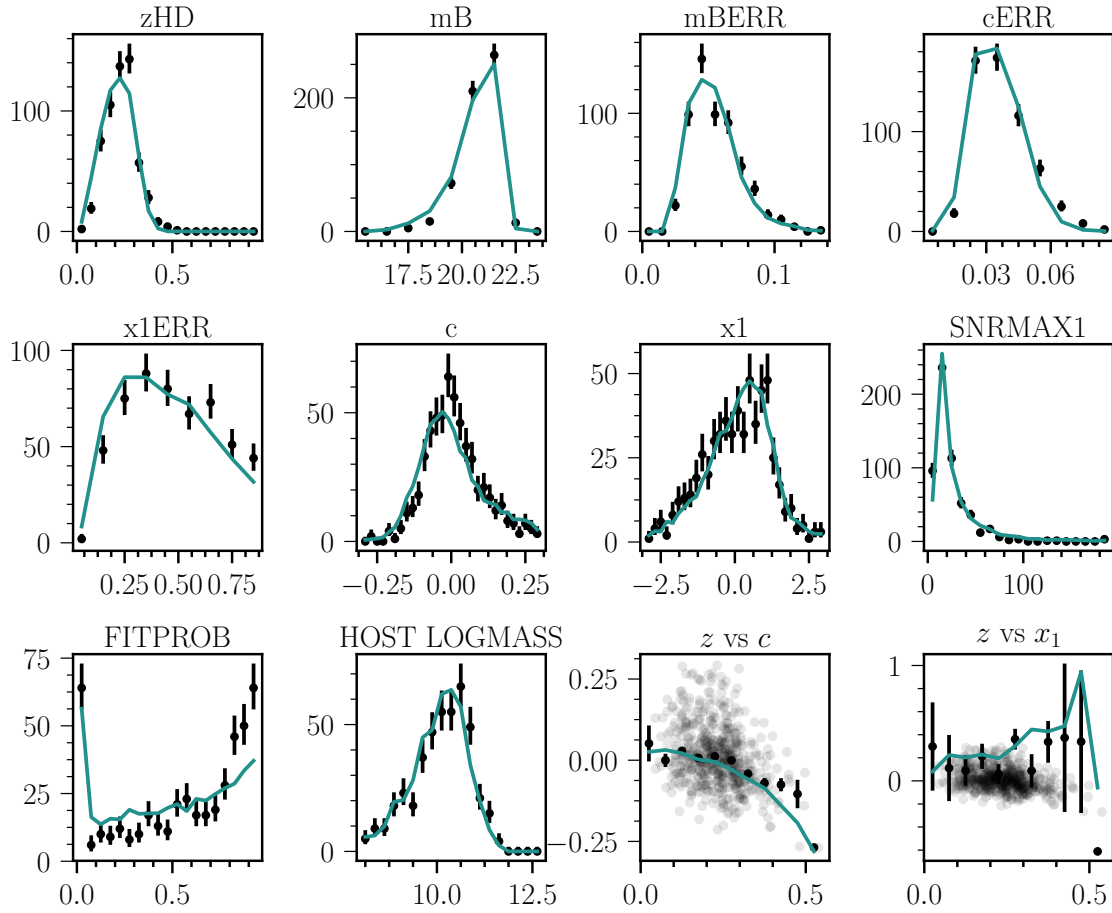


Figure 7.2: Metrics for goodness-of-fit for SDSS.

PS1

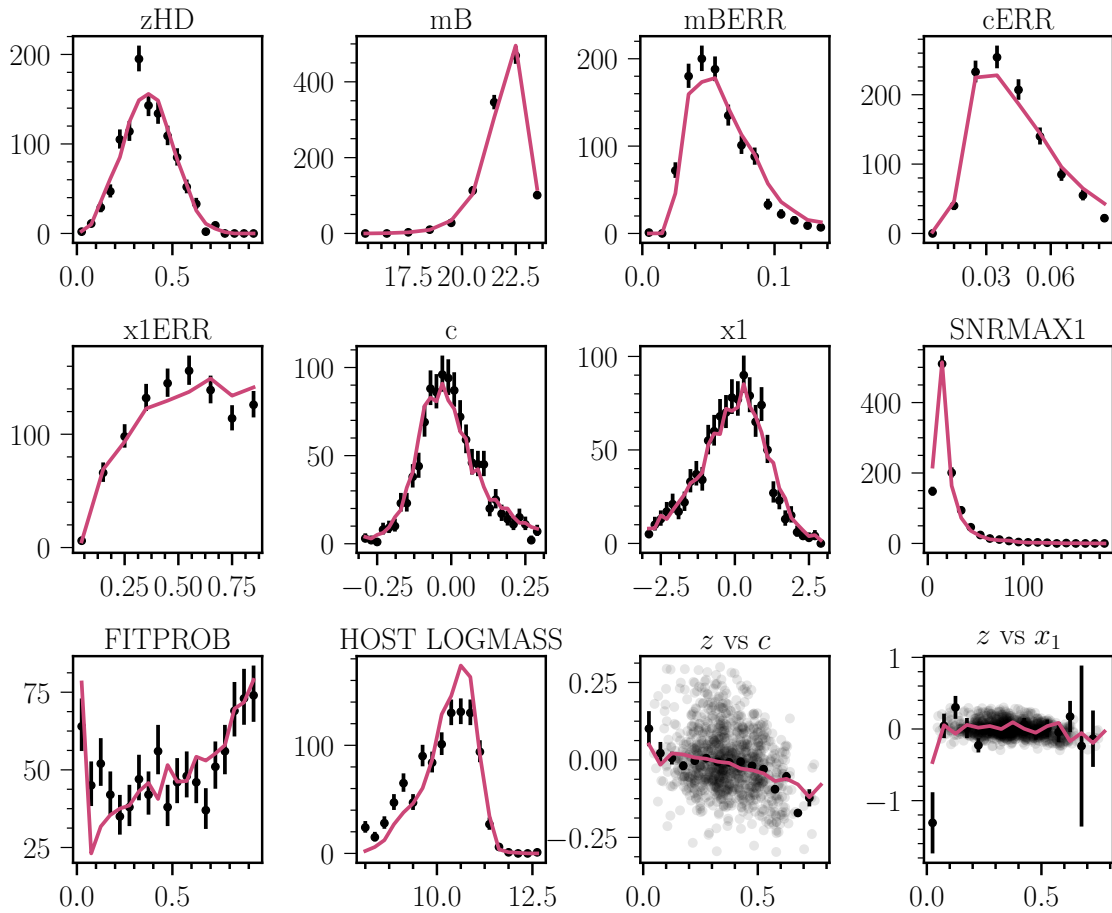


Figure 7.3: Metrics for goodness-of-fit for PS1.

Data

Section 7.5.1 Host-Galaxy Properties (Also see 7.5.10)

Calibration and Light-Curve Fitting

Section 7.5.2 Calibration

Section 7.5.3 SALT3 Model

Simulations

Section 7.5.4 Survey Modeling

Section 7.5.5 Intrinsic Scatter Models

Section 7.5.6 Core Collapse Models

Other

Section 7.5.7 Nuisance Parameters with z

Section 7.5.8 Fixed Nuisance Parameters

Section 7.5.9 Validation

Section 7.5.10 Other

7.5.1 Host-Galaxy Properties

Purpose: The host-galaxy mass is used to standardise SNIa brightnesses in two ways: simulations include correlations between x_1 and the host-galaxy mass from Popovic et al. (2021) and correlations between c , dust, and host-galaxy mass from Popovic et al. (2021); and a residual luminosity step related to the host galaxy mass (the ‘mass step’ γ) is corrected in the Tripp Eq. 2.13 (Appendix 7.2).

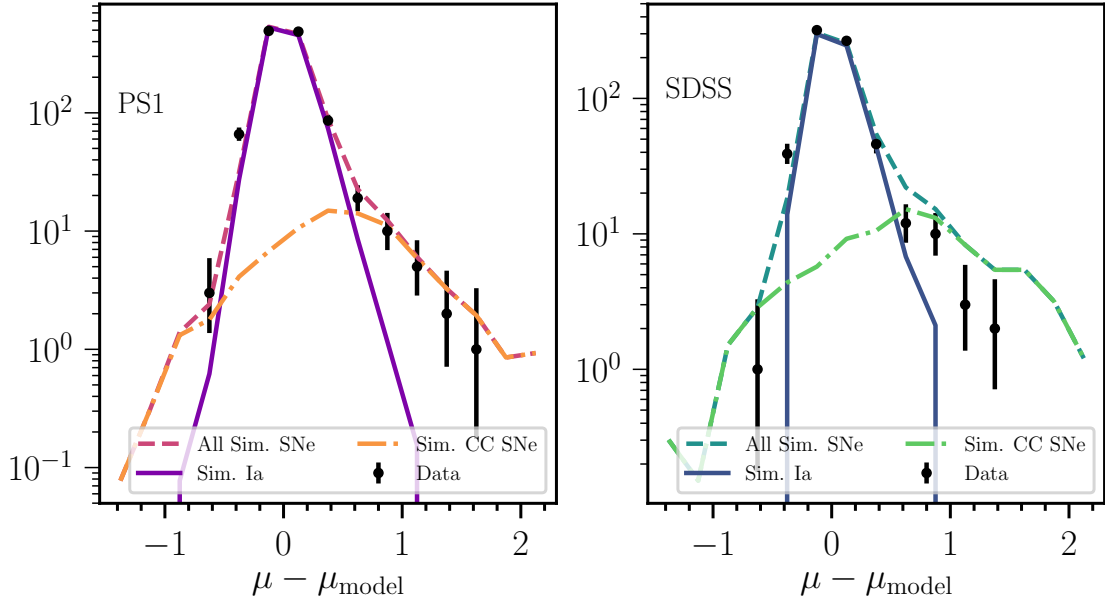


Figure 7.4: Hubble Residuals for PS1 (left) and SDSS (right). The data is shown in black points, simulations are broken down into All Simulated SNe in dashed histogram, Simulated Ia Only in solid histogram, and only Simulated Core Collapse Only in dash-dotted histogram. Both surveys show good agreement between sim and data.

Baseline: For the baseline analysis, we place the mass step at $10^{10} M_{\odot}$.

Systematics: Analyses such as Sullivan et al. (2011), Childress et al. (2014), and Kelsey et al. (2020) have found evidence that a more appropriate location of the mass step may not be at $10^{10} M_{\odot}$. Following Pantheon+, we include a systematic placing the mass step at $10^{10.2} M_{\odot}$.

7.5.2 Calibration

Purpose: The compilation of different instruments, filters, and telescopes requires photometric calibration of the passbands in each survey in order to fit light curves and standardise SN brightnesses. This same calibration is needed for the SALT3 model training.

Baseline: We use the calibration presented by Fragilistic from Brout et al. (2021). Alongside the nominal calibration, we make use of the relevant subset of their 105×105 covariance matrix that describes the zeropoint calibrations. This 105×105 matrix includes the bands from SDSS, PS1, and the low redshift surveys in this analysis.

Systematics: A more in-depth description of the calibration and its systematics is given in Brout et al. (2021). To estimate the calibration systematic, we refit SALT3 for 9 realisations of calibration zero points drawn from the Fragilistic covariance matrix. The value of $\sigma_\psi^2 = 1/9$ is chosen such that the quadrature sum of the calibration systematic is unity. Additional changes to the wavelength range and tertiary stellar magnitudes are given in Section 3.2.1 in Brout et al. (2022), but summarised here. The σ_ψ for the uncertainty in modelling primary standard star C26202 is $\sigma_\psi = 3$, and the recalibration of CSP tertiary stellar magnitudes from Krisciunas et al. (2017) is reflected in setting $\sigma_\psi = 1$.

7.5.3 SALT3 Model

Purpose: SNIa light curves are fit with the SALT3 model to determine the light-curve parameters m_B, c, x_1 for each SN for use in Equation 2.13.

Baseline: We use the SALT3 model from Kenworthy et al. (2021) with the calibration from Brout et al. (2021).

Systematics: Following Brout et al. (2022), we use 9 SALT3 models retrained on the the Fragilistic zero-points. The calibration shifts in the retrained models are coherently propagated through training and light curve fitting.

7.5.4 Survey Modeling

Purpose: SNIa surveys require additional followup for the acquisition of redshifts, be

it from the supernova itself or its host galaxy. This followup can give rise to a number of potential biases, including Malmquist bias and other selection effects. These potential biases can be mitigated with the use of simulations and error modeling.

Baseline: Figures 7.3 and 7.2 shows a comparison between simulations and real data for distributions of c , x_1 , and z for SDSS and PS1. This cosmology analysis requires host-galaxy spectroscopic redshifts for placement in the Hubble Diagram. To incorporate the spectroscopic redshifts from host galaxies, which itself effects the supernova detection efficiency and the mass step, modeling is needed. In the fiducial analysis, this host galaxy efficiency is modeled as a function of the r -band magnitude of the host galaxy, and is shown in Figure 7.5.

Systematics: As a systematic we follow Jones et al. (2019) and to model the efficiency as a function of redshift (Equations 2 and 3 of Popovic et al. (2019)) for both SDSS and PS1. As an additional systematic to measure selection effects, we increase the Signal-to-Noise Ratio (SNR) of each simulation by 20%, changing our simulated distributions.

7.5.5 Intrinsic Scatter Models

Purpose: We use SNANA to generate catalogue-level simulations for use in bias corrections and to correct for inefficiencies in measuring intrinsic distributions. A model of intrinsic scatter, the remaining scatter in SNIa measurements post-standardisation, is required for realistic simulations.

Baseline: To model the SNIa intrinsic scatter shown in Equation 2.6 in our simulations, we use the Brout & Scolnic (2021) (BS20) dust model with parameters updated in Popovic et al. (2021), hereafter P22. Dust-based scatter models instead include dust in modeling SNIa properties. The SN light curves are reddened and

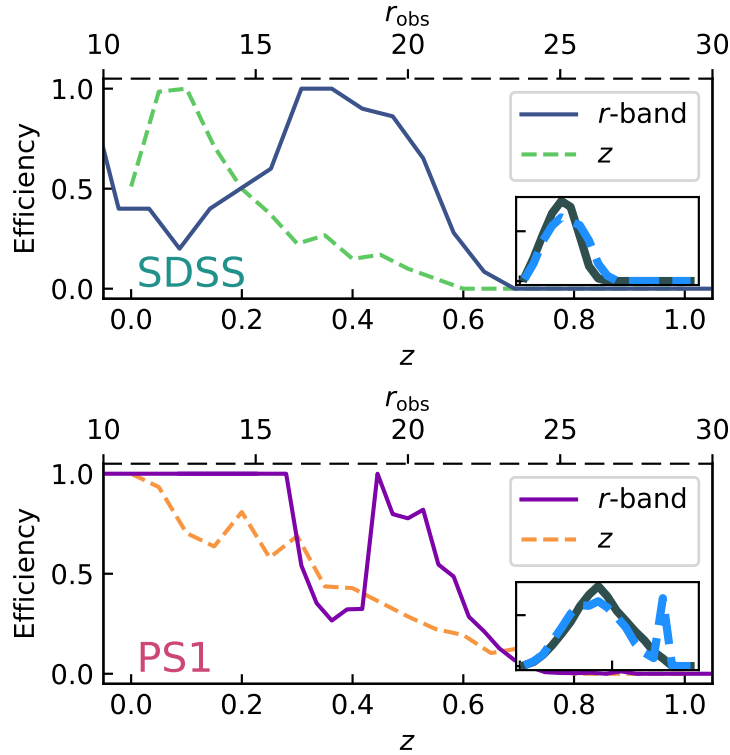


Figure 7.5: A comparison of the host galaxy redshift efficiencies for SDSS (top) and PS1 (bottom). The r -band magnitude efficiency used in the fiducial analysis is presented in dashed line, and the z efficiency is presented in solid line. The resulting redshift distributions are presented in the inset plots for the r -band magnitude in dashed histogram and z efficiency in solid histogram.

dimmed by dust. A more detailed analysis of the model is available in Brout & Scolnic (2021) and Popovic et al. (2021). P22 simulations are used to generate BBC-4D bias corrections. As P22 does not include x_1 effects, the x_1 values are drawn from the method in Popovic et al. (2021).

We use the Dust2Dust program as presented in Popovic et al. (2021) to derive the dust model parameters ($c_{\text{int}}, R_V, E(B - V), \beta_{\text{SN}}$) for the combined SDSS, PS1, Low-z, and Foundation sample. These model parameters (hereafter constituting the P22) are given in Table 7.2, and we generate our baseline bias correction simulations with these parameters. The simulations are used for the BBC-4D/BBC-BS20 bias correction method presented in Chapter 4; in review, c is

$$c_{\text{obs}} = c_{\text{int}} + E_{\text{dust}} + \epsilon_{\text{noise}}. \quad (7.1)$$

where ϵ_{noise} is measurement noise otherwise unaccounted for. The change in observed brightness is modeled as

$$\Delta m_B = \beta_{\text{SN}} c_{\text{int}} + (R_V + 1) E_{\text{dust}} + \epsilon_{\text{noise}}. \quad (7.2)$$

Systematics: To reflect fitting uncertainties in Dust2Dust, we follow P22 and Brout et al. (2022) and draw 4 realisations of model parameters from Dust2Dust as alternative bias correction models. Parent populations for x_1 are calculated for the SDSS+PS1 photometric sample using the methodology in Popovic et al. (2021) and the parent populations for Foundation and Low-z are taken from the same paper.

7.5.6 Core Collapse Models

Purpose: We use simulations for the BEAMS method (2.1.10) to model the relative

luminosities of Ia and non-Ia SNe. This prior is used to model the BEAMS likelihood and subsequently the weighting for the supernova in the cosmological fit.

Baseline: We use simulations of SDSS and PS1 using core-collapse SED inputs from Vincenzi et al. (2021) to train SNN. We include Iax, 91-bg, SNIi, and SNIb/SNIc simulations alongside SNIa simulations.

Systematics: In place of non-Ia simulations, we use the z -dependent polynomial expansion approximation from Hlozek et al. (2012) to model non-Ia populations. This z -dependent polynomial adds additional parameters to the BBC fit, increasing the complexity.

7.5.7 Redshift Evolution of Nuisance Parameters

Purpose: Equation 2.13 includes a colour-luminosity component β and a stretch-luminosity component α that are fit for the entire supernova sample. These nuisance parameters describe the slope of the SNIa-parameter (e.g. c or x_1) vs. luminosity graph.

Baseline: We follow Brout et al. (2022) and other cosmology analyses and assume that α and β are constant in redshift while they are fit in the BBC process.

Systematics: We include two similar systematics, allowing α and β to evolve with redshift. They are modelled as

$$\alpha(z) = \alpha_0 + \alpha_1 \times z \tag{7.3}$$

and

$$\beta(z) = \beta_0 + \beta_1 \times z. \tag{7.4}$$

We allow one nuisance parameter to evolve with redshift at a time.

7.5.8 Fixed Nuisance Parameters

Purpose: The model parameters for the P22 scatter model are determined through a complex, multidimensional fit that requires that the simulations and the data have the same nuisance parameters α and β . A different assumed β between the real data and simulations used to compute model parameters can cause biased recovery of model parameters and therefore biased cosmology. A preliminary fit on the data is done with redshift-only bias corrections, and this resulting β is used as the β for the simulations.

However, β is an output of the P22 scatter model, and can be influenced by non-Ia contamination in the fitting process. Fixing the α and β values in the fitting process is a necessary step ensuring consistency between data and simulations, but it is not clear how this impacts the 4D-biasCor α and β values.

Baseline: We let the BBC process fit for α and β in the minimisation procedure, as done in historical analyses.

Systematics: The presence of non-Ia SNe, which does not follow the SALT3 standardisation procedure, may impact the recovered β from the Dust2Dust fitting procedure. This is in part because CC SNe are dimmer than their Ia counterparts, which may lead to be interpreted as a greater quantity of dust causing this dimming. Therefore, we fix the α and β values to those found in a fit of the data using only redshift-based corrections.

7.5.9 Validation

Purpose: Proper analysis with simulations requires validation to ensure that we are able to recover our input parameters and not produce biases. These validation tests track biases due to BBC, light-curve fitting, and simulation inputs, but do not track

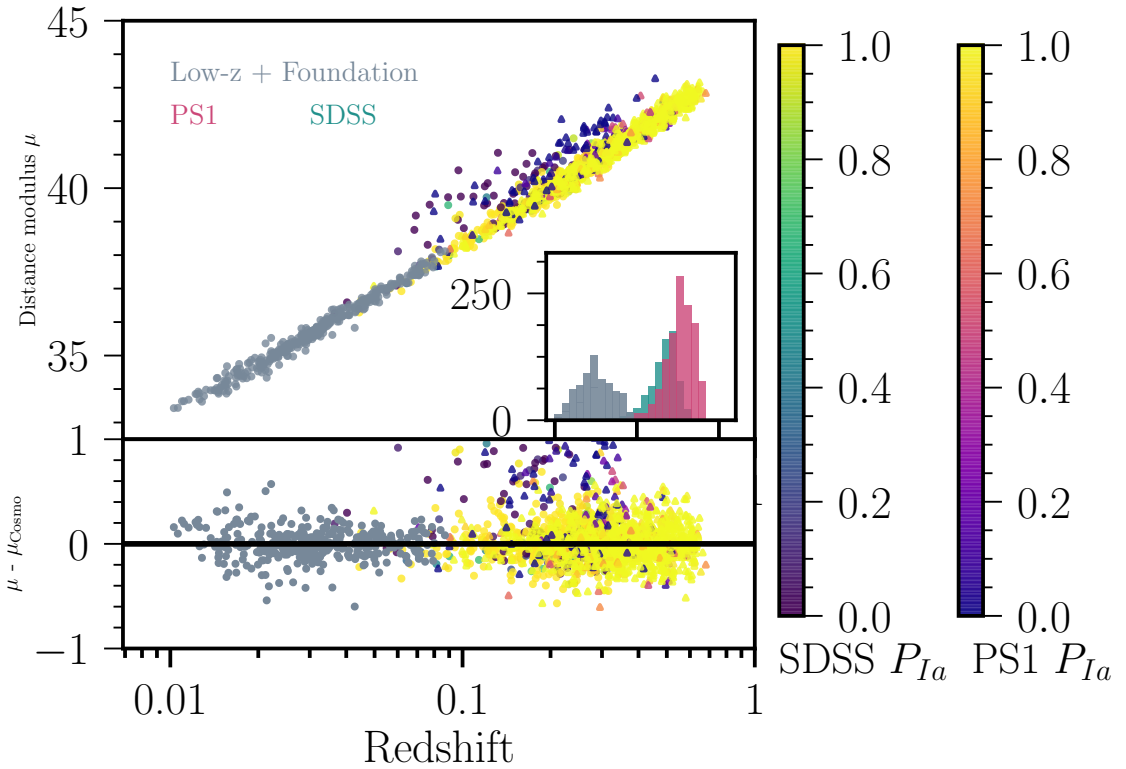


Figure 7.6: Top panel: Distance Modulus μ versus redshift z (“Hubble Diagram”) for the Amalgame sample. SDSS (Viridis) and PS1 (Plasma, triangles) are coloured according to their classification probability P_{Ia} from **SuperNNova**; the Low- z and Foundation surveys are dark grey as they contain no Core collapse supernovae. **Bottom panel:** the distance modulus residual relative to a best-fit cosmological model (“Hubble Residuals”).

assumptions made about photometry or calibration.

Baseline: The analysis is repeated, end to end, on 10 data-sized simulations using the P22 scatter model.

7.5.10 Other

We include the following systematics as they were in Brout et al. (2022): Redshift, Peculiar Velocities, and Milky Way Reddening. These are summarised in Table 7.4, and a more detailed description is given in Brout et al. (2022).

7.6 Results

Here we present the results of the Amalgame analyses. Our nominal approach to cosmology uses the unbinned covariance matrix from Section 2.1.9.

7.6.1 Nominal Cosmological Results

Validation

We perform our nominal analysis on 10 simulated subsamples with the P22 model, with realistic distributions of SNIa parameters and core collapse contamination. We find we recover our input cosmology, with $w_{\text{reco}} = -0.999 \pm 0.005$. Table 7.3 shows a comparison of the nuisance parameters from simulated SNIa and real data. The β discrepancy is discussed further in Section 7.5.8.

Hubble Diagram

The Amalgame Hubble Diagram of 2259 SNIa light curves is shown in the top panel of Figure 7.6. It spans a redshift range of 0.01 to 0.62, containing supernovae from SDSS, PS1, Low-z, and Foundation. In the case of SDSS and PS1, the data points are coloured according to their probability of being an SNIa (2.1.10). Inset to the top panel is the redshift distribution of each of the constituent subsurveys. The bottom panel of Figure 7.6 shows the residuals to the best-fit cosmology, the results of which are presented in the following subsections.

7.6.2 Subsample Cosmological Results

Here we present the cosmological results and error budgets from various combinations of Amalgame subsamples: SDSS+PS1+Foundation, SDSS+PS1, SDSS+Foundation,

Table 7.3: Comparison of BBC output between data and simulations.

Amalgame+Low- z	Data	Sim
N_{SNe}	2259	2245
α	0.138 (0.003)	0.137 (0.003)
β	3.075 (0.039)	2.851 (0.034)
γ_{M_\star}	0.0215 (0.0073)	0.0012 (0.0063)
σ_{gray}	0.0656	0.0000
RMS	0.247	0.219

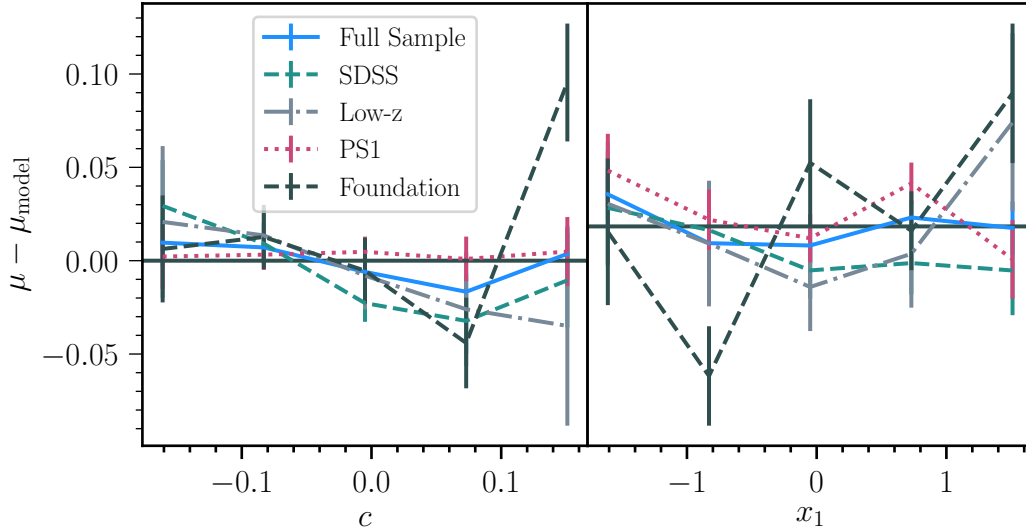


Figure 7.7: Hubble Residuals $\mu - \mu_{\text{model}}$ vs. c and x_1 for the entire sample and subsamples. The entire sample is shown in blue.

PS1+Foundation, and SDSS+Low- z . This is the first time that two photometric samples have been combined; here we investigate their consistency across the subsamples and the full sample.

To motivate these combinations, we present the correlation of bias-corrected Hubble Residuals with c and x_1 for the overall sample in blue and the constituent subsamples in Figure 7.7. The x_1 correlation with Hubble Residuals is consistent with 0 for the full sample and the subsamples, indicating that the bias corrections are accounting for any such correlations. There is evidence of non-zero residuals vs. colour for SDSS, though the full sample residuals are consistent with zero.

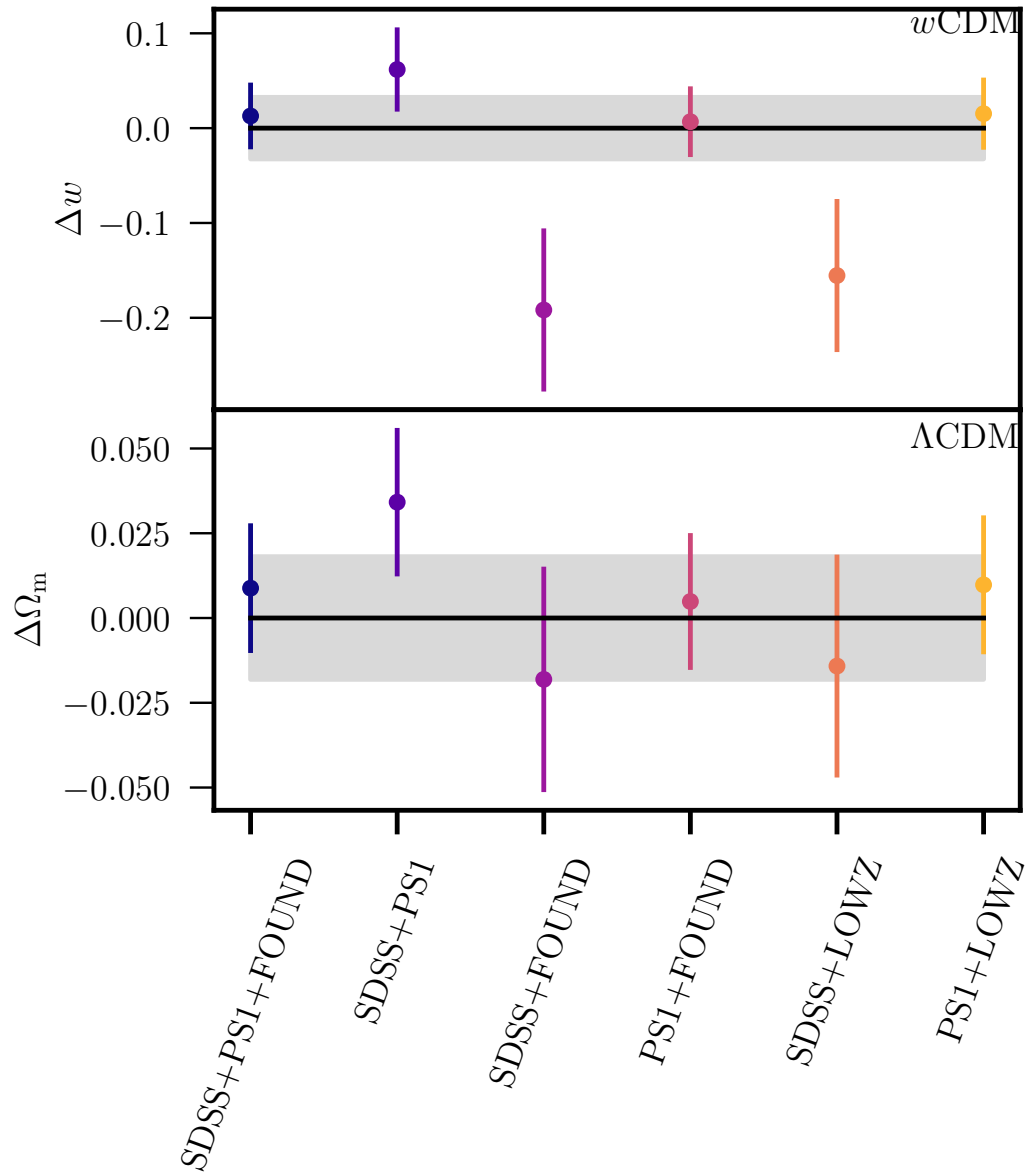


Figure 7.8: Top panel: Changes in measured w from the fiducial Amalgame survey for w CDM. The SDSS+Lowz and SDSS+Foundation subsamples are inconsistent with our fiducial results, likely due to the lack of a high redshift anchor respectively. **Bottom panel:** Changes in measured Ω_m from the fiducial Amalgame survey for Λ CDM. Results are similar to that of the top panel.

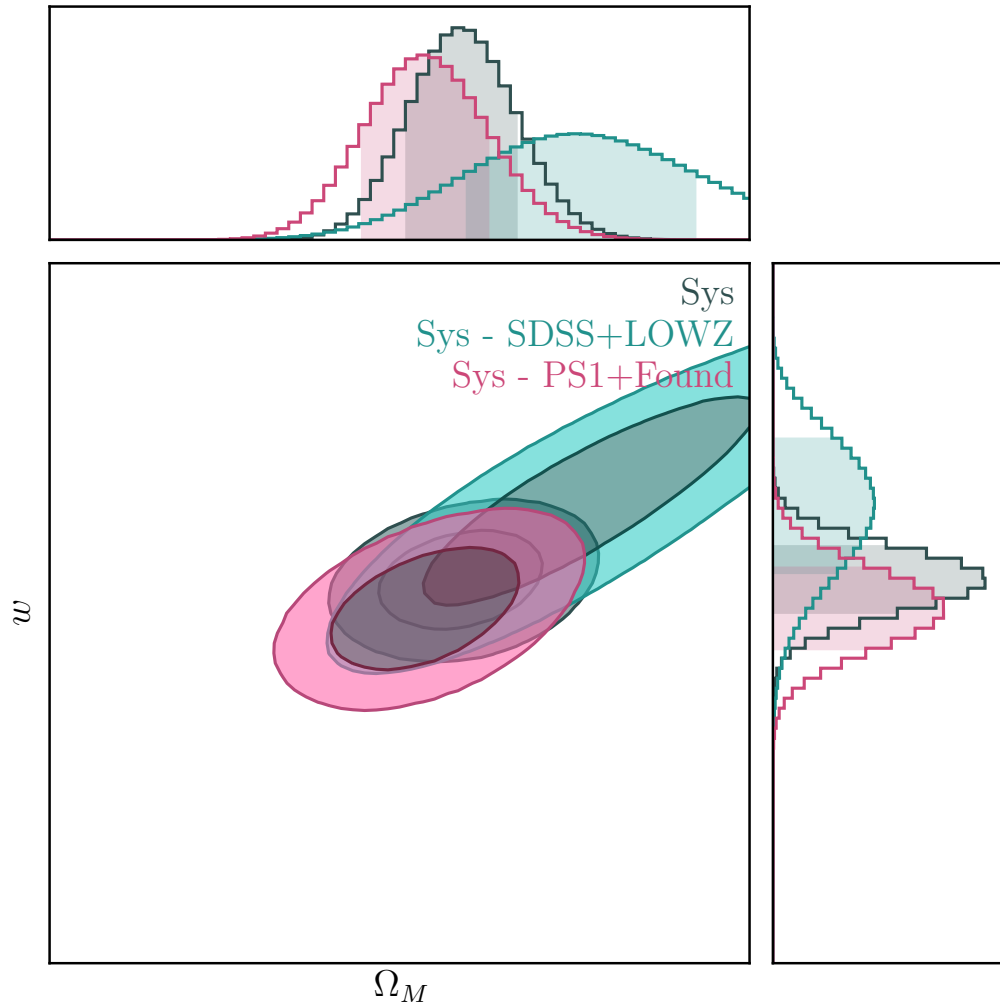


Figure 7.9: The blinded w/Ω_{matter} contour for the Amalgame sample. The full sample is presented in dark grey, next to PS1+Foundation in fuchsia and SDSS+Low-z in cyan. The constraints from SDSS+Low-z are noticeably weaker than the full sample or PS1+Foundation. An offset between the two measured cosmologies is present, though the results are consistent within 1.3σ .

The difference in Hubble Residuals between the fiducial Amalgame sample and the subsample combinations is presented in Figure 7.11. Two subsample combinations are more than 1σ outside the uncertainties of Amalgame in grey fill: SDSS+FOUND and SDSS+LOWZ. The commonality between these two subsamples is the use of SDSS as the high-redshift sample - this is discussed further in Section 7.7.1. Figure 7.8 shows this discrepancy on measurements of w and Ω_m .

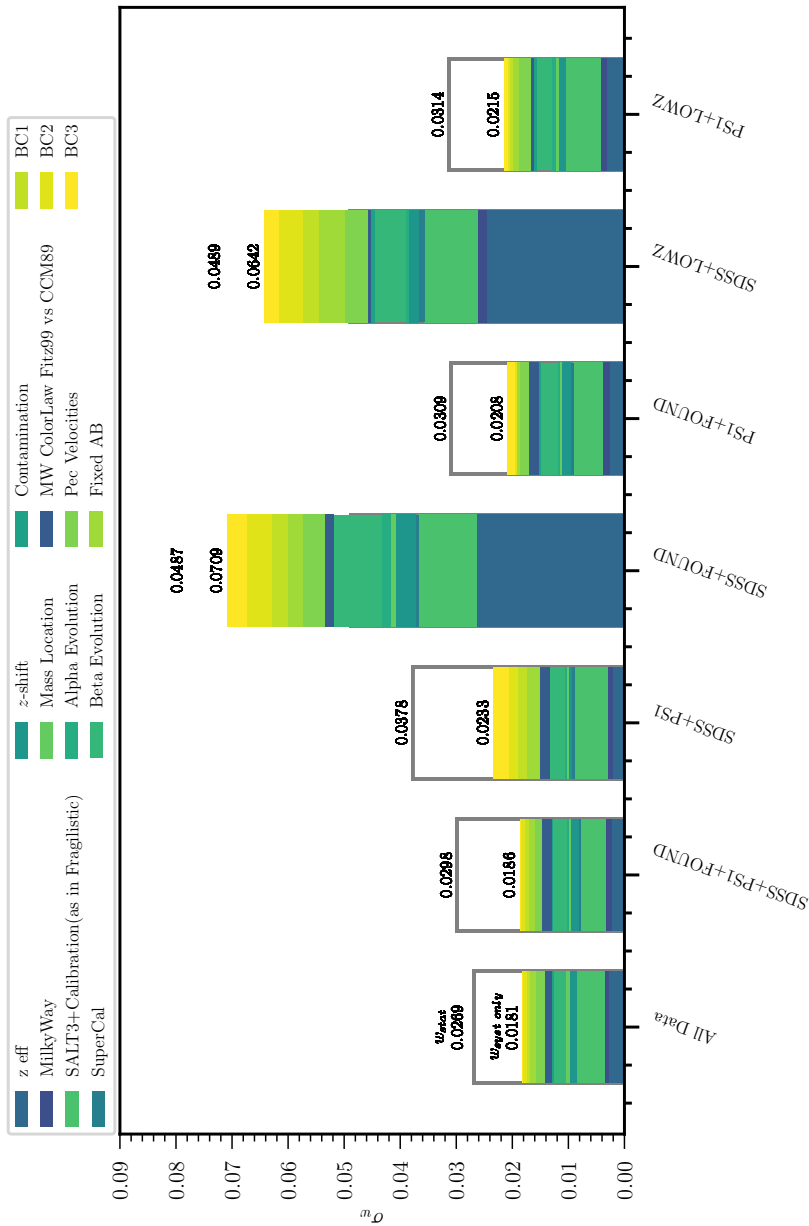


Figure 7.10: Error Budget comparison for the subsample combinations presented in this paper. The full sample is presented first, followed by SDSS+PS1+Foundation, SDSS+PS1, SDSS+Foundation, and PS1+Foundation. The subsample uncertainties are comparable except for SDSS+Lowz and SDSS+Foundation, which lack the higher redshift statistics of PS1.

The increased statistical *and* systematic uncertainties in the SDSS+LOWZ and SDSS+FOUND subsamples are shown in Figure 7.10: the statistical uncertainties alone are nearly double that of the nominal sample, and the systematic uncertainty is similarly scaled up. Given that the redshift range of SDSS is $z \sim 0.4$, the increased statistical uncertainty is not unexpected, as the statistical uncertainty reflects the diminished constraining power from the smaller redshift range. Nonetheless, this increased uncertainty is not sufficient to explain the difference in measured cosmological parameters (a 1.9σ difference in w), which is discussed further in Section 7.7.

Figure 7.10 shows the error budgets for each of the subsample combinations side by side. The statistical w -uncertainty increases as expected, but alongside it the systematic w -uncertainty also increases. This indicates that systematic uncertainties are not statistically-independent, and future, larger surveys using covariance matrix measurements of cosmology may enjoy further reductions in systematic uncertainty. The statistical uncertainties of SDSS+Found and SDSS+Low- z are the largest, indicating un-ideal coverage of the redshift range compared to PS1+Low- z , which has similar numbers but extends to $z \sim 0.7$ rather than $z \sim 0.5$.

Constraints on Cosmological Parameters

Here we present the constraints on cosmological parameters from the Amalgame sample. Figure 7.13 shows the SN-only cosmological contours for the Amalgame and Pantheon+ for comparison. The Amalgame is wider in Ω_m space than Pantheon+, which is expected due to the lower redshift range. Nonetheless, the two samples are broadly consistent with each other, and the Amalgame measurement is competitive.

Figure 7.14 shows the w/Ω_{matter} constraints when combined with the results from Planck Collaboration et al. (2020) from the full Amalgame sample, for the fiducial alongside the statistical-only constraints and different cosmological binning schemes.

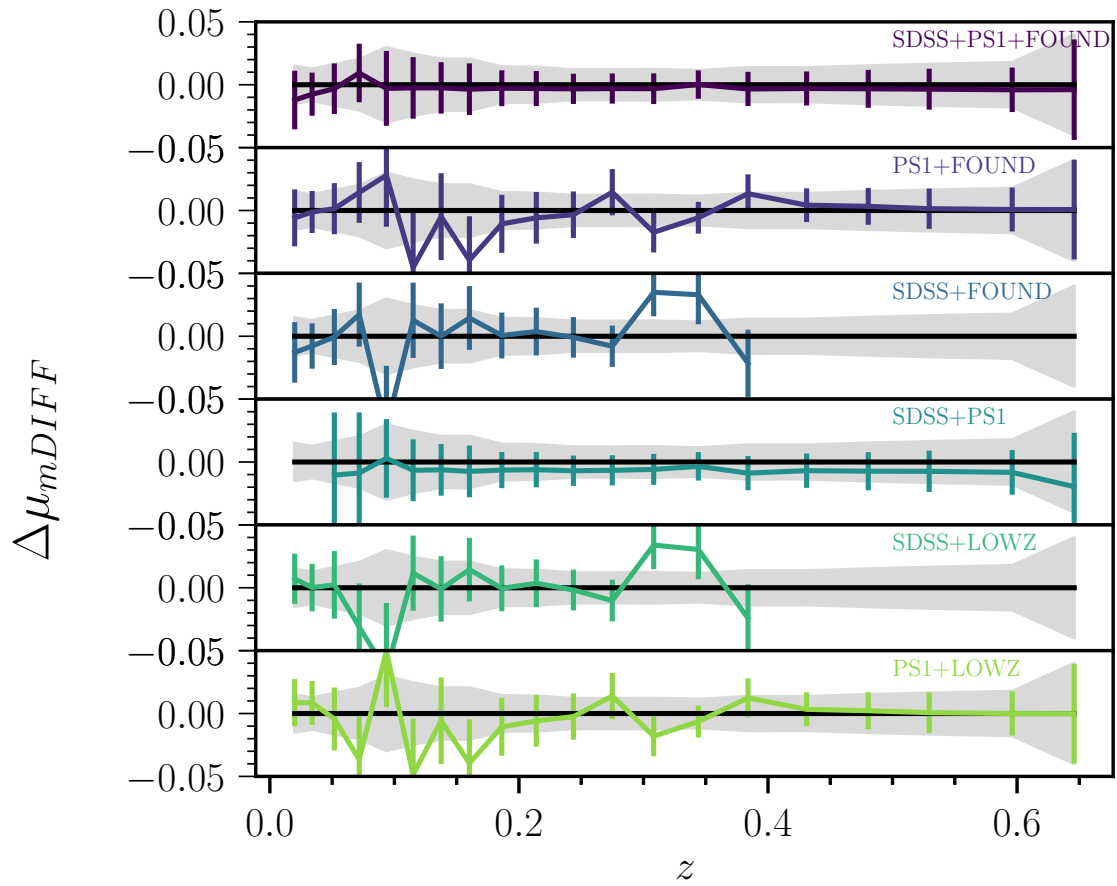


Figure 7.11: Binned difference in Hubble Residuals between the fiducial Amalgame sample and various subsamples. Uncertainties for the fiducial sample are presented in grey fill.

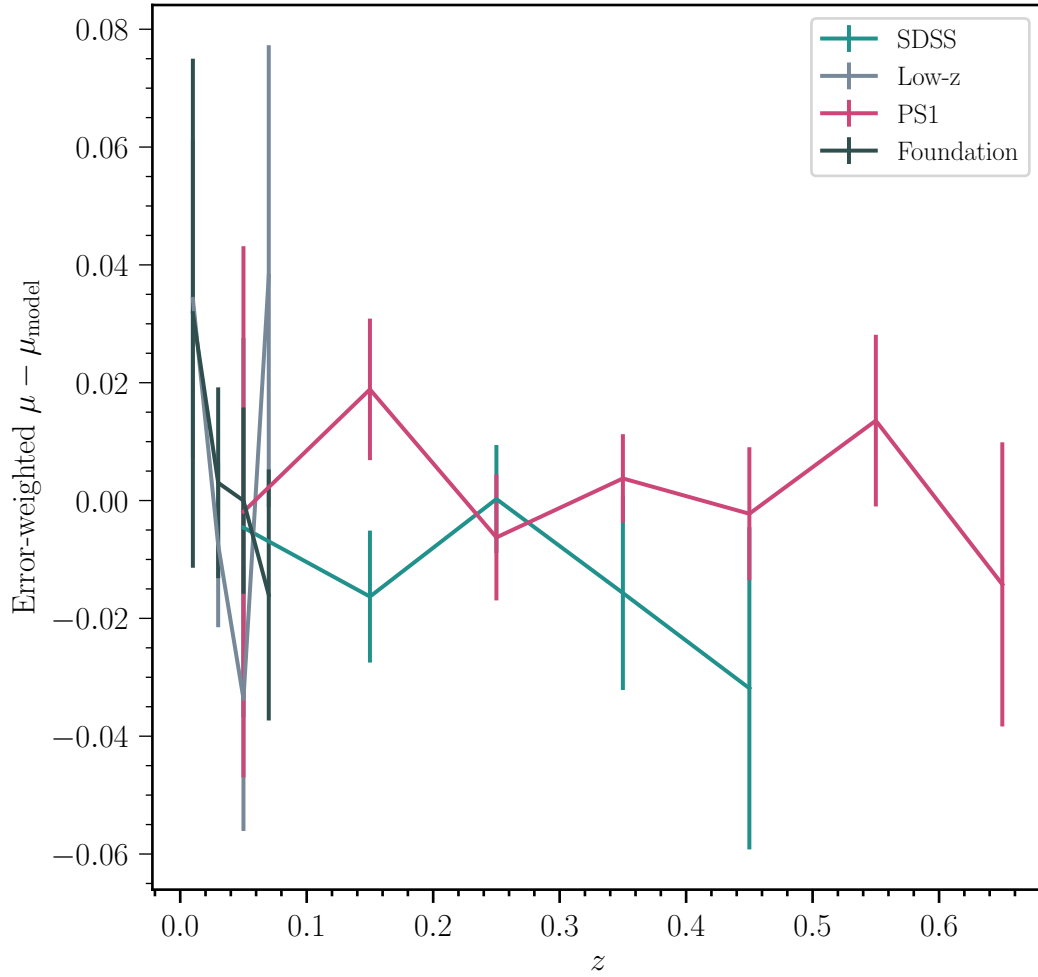


Figure 7.12: Hubble Residuals $\mu - \mu_{\text{model}}$ for subsample surveys. PS1 residuals are presented in fuchsia plot, SDSS residuals in turquoise, Low-z residuals in grey, and Foundation residuals in black plot. PS1 dominates the Hubble Residuals over SDSS.

The results are consistent with each other, and the increase in cosmological measurement fidelity from the use of an unbinned Hubble Diagram is apparent. The rebinned contour shows a slight shift in the contour, though still within error.

The Amalgame sample offers a prime opportunity to directly compare cosmological measurements that do not share common SNe. Here, we compare the cosmological measurements from the SDSS+Low- z sample and the PS1+Foundation sample. Figure 7.9 shows the contours from these two subsamples compared to the full Amalgame sample. The PS1+Foundation sample is consistent with the measurements from the full Amalgame sample, indicating that PS1 and Foundation are the main drivers of the cosmological measurement. SDSS+Low- z , on the other hand, is offset from the full Amalgame measurement, and the errors are more than twice as large as the full Amalgame sample. SDSS+Low- z does not provide strong cosmological constraints, (on the order of ~ 0.1 in w), nor is it a particularly strong driver of the cosmological measurement from Amalgame. Further discussion of SDSS+Low- z can be found in 7.7.1.

7.6.3 Systematic Uncertainties

Table 7.4 provides a comprehensive overview of the sources of systematic uncertainty for the Amalgame analysis. These uncertainties, and their relative contribution to the overall w systematic uncertainty, are displayed in Figure 7.10. Overall, the individual systematics are subdominant to the statistical uncertainty, and for the most part on the order of $< 1\%$. The largest systematic contribution remains the calibration and SALT3 surfaces as detailed in Brout et al. (2021) and Section 7.5.3. This systematic uncertainty contribution, about $\sim 40\%$ of the statistical uncertainty, is comparable to that of Pantheon+, which found a calibration and SALT3 uncertainty of 38% of

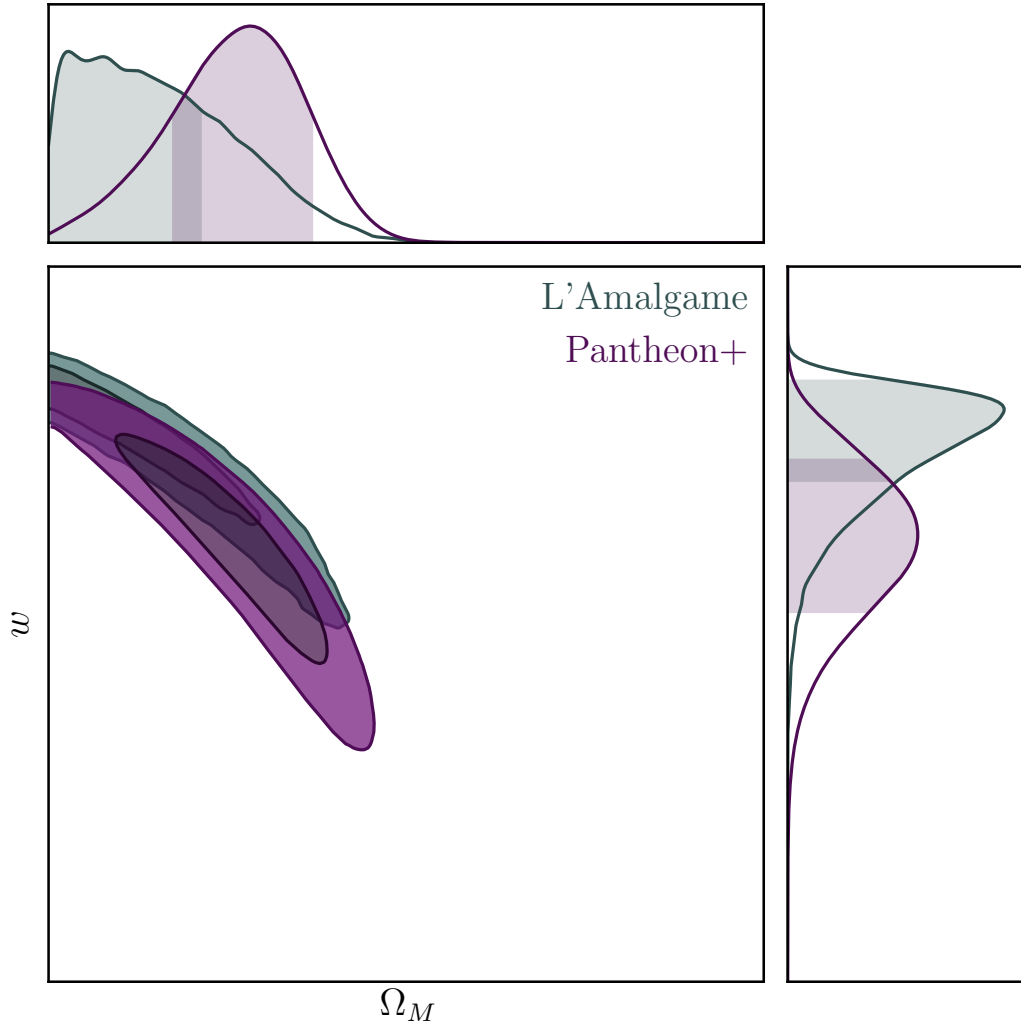


Figure 7.13: The w/Ω_{matter} contour for the Amalgame sample for SN-only measurement. The Amalgame is plotted in grey, alongside the purple SN-only results from Pantheon+. The results for both are blinded, but not shifted.

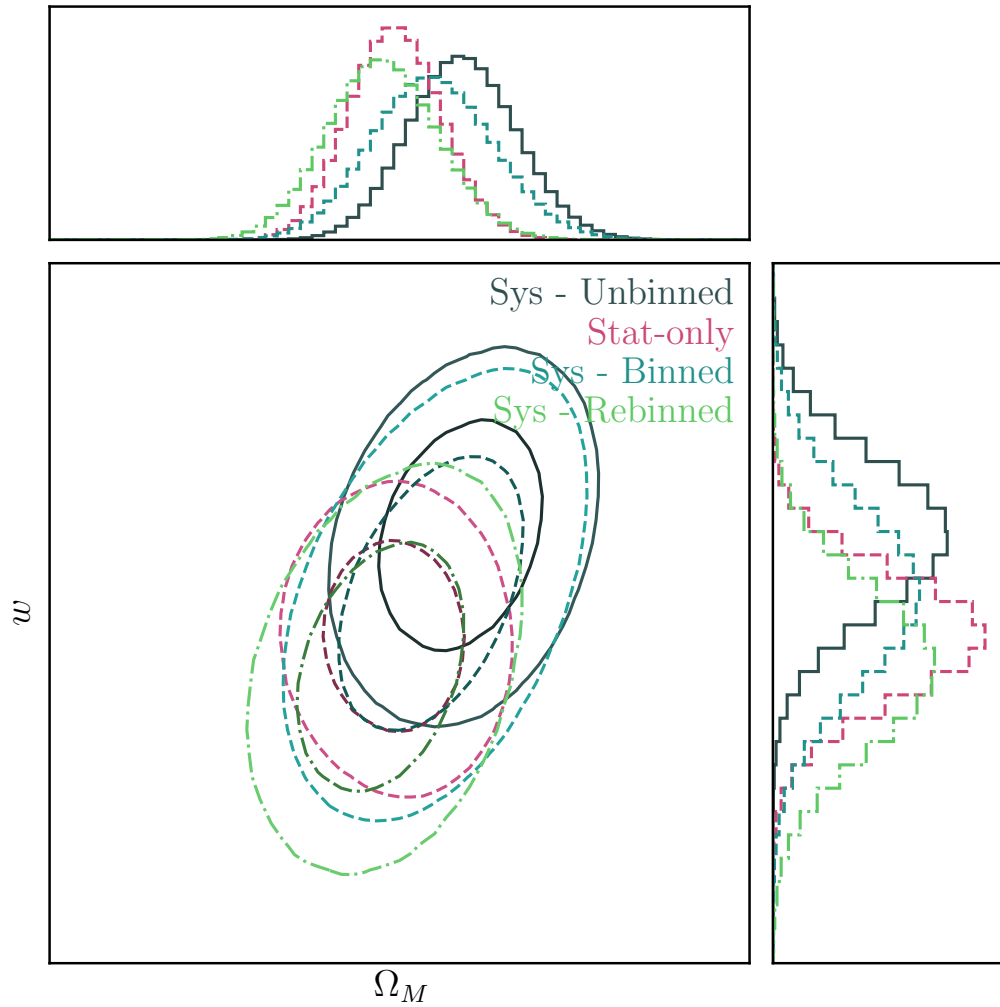


Figure 7.14: The w/Ω_{matter} contour for the Amalgame sample with the Planck prior, blinded. The full sample is presented in dark grey, alongside the statistical uncertainty only sample in dashed fuchsia. The alternate binning approaches are presented in dash dotted green for the rebinned sample and blue dotted line for the binned sample. The results are consistent within error of each other.

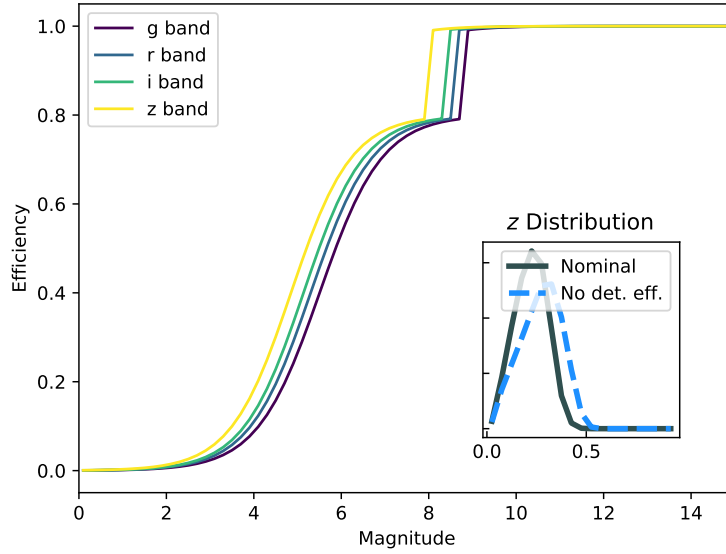


Figure 7.15: The SDSS detection efficiency for simulated supernovae as a function of SNR. The g band is presented in purple, r band in blue, i band in green, and z band in yellow. In the inset plot is the redshift distribution for the nominal simulations (grey histogram) and no detection efficiency simulation (blue dashed histogram).

the statistical uncertainty.

Those systematics shared with Pantheon+ are largely similar, instead, we shall mostly focus on those systematics unique to this analysis.

$\alpha(z)$ and $\beta(z)$

We allow the stretch-luminosity coefficient α and the colour-luminosity coefficient β to change with z . We find no evidence of an α that evolves with redshift, nor any noteworthy systematic uncertainty associated with such an evolution. The $\beta(z)$ systematic has a greater contribution to the overall systematic uncertainty - 0.0052 - though this is still less than 1% on w .

Fixed α and β

We find a noticeable difference in the fitted α and β values between the BBC-4D recovered values and a preliminary redshift-only bias correction. The $\Delta\alpha \sim 0.03$ and $\Delta\beta \sim 0.4$, outside statistical error. Despite this change in the nuisance parameters,

the $\Delta w = -0.0015$, and the systematic uncertainty is similarly small at $\sim 0.002\%$.

Changing follow-up efficiency

Redshift determination for photometric surveys is a function of the host-galaxy properties, not the supernovae. This systematic is the largest of the non-intrinsic scatter model systematics, with a $\sigma_{w,\text{syst}} = 0.0065$, and a $\Delta w = -0.0012$. Our fiducial case of using the r -band magnitude of the host galaxy, rather than a statistical redshift efficiency, is a more realistic approach. The conservative z -based efficiency systematic is still subdominant to the statistical uncertainty, but represents an upper ceiling for future surveys.

Intrinsic Scatter Model

The three dust systematics result in a combined systematic uncertainty of ~ 0.002 , one of the lower systematic contributions. While the individual contributions are not approximately equal, the low $\sigma_{w,\text{syst}}$ and Δw do indicate that three biasCor are sufficient to approximate the impact of this systematic.

Classifier

The choice of using a simulated core collapse SNe sample as the prior for BEAMS versus using the Hlozek et al. (2012) analytical solution results in a negligible difference in Δw and σ_w . While the simulated set is a more realistic approximation of the core collapse population, the CC contamination as identified by SNN effectively marginalises issues due to contamination.

Figure 7.16 visualises the Δw values from each of the included systematics, without the Covariance Matrix from Section 2.1.9. These represent the worst-case Δw for this analysis, and are all within the statistical uncertainty.

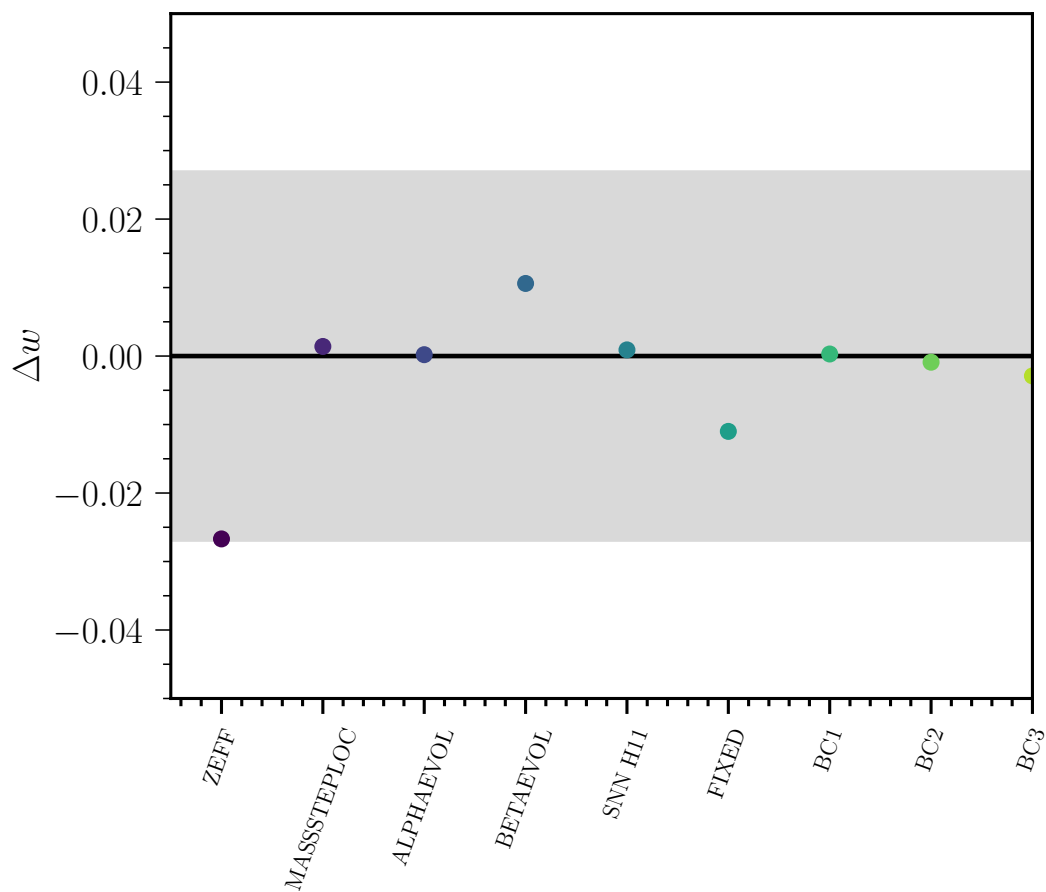


Figure 7.16: Changes in measured w between systematics for the fiducial Amalgame sample. Grey fill is the statistical uncertainty from the fiducial analysis. These measurements do not include the Covariance Matrix from Section 2.1.9.

Table 7.4: Sources of Uncertainty

Sec. and description	Baseline	Systematic	Scale	$\sigma_{w,\text{syst}}$	$\frac{\sigma_{w,\text{syst}}}{\sigma_{w,\text{stat}}}$	$\Delta w_{\text{syst}}^\dagger$
Total Statistical				N/A	1.00	-0.0111
Total Systematic (Unbinned Covariance Matrix Approach)				0.0181	0.6729	N/A
Total Systematic (Binned Covariance Matrix Approach)				(0.028)	(0.84)	0.014
Data						
- Redshift (7.5.10)	shift nominal redshift	$\Delta z = 10^{-4}$	1	0.0029	0.1078	0.0015
- Peculiar (7.5.10)	velocities 2M++ velocity map	2MRS velocity map	1	0.0039	0.145	0.0044
- Host Galaxy Properties (7.5.1)	Mass step at $M_\star = 10$	Mass step at $M_\star = 10.2$	1	0.0013	0.0483	0.0015
- α Evolution (7.5.7)	constant α	$\alpha(z) = \alpha_0 + \alpha_1 \times z$	1	0.0	0.0	0.0001
- β Evolution (7.5.7)	constant β	$\beta(z) = \beta_0 + \beta_1 \times z$	1	0.0052	0.1933	0.0036
- Not floating α and β in BBC Fit (7.5.8)	Floated α and β	Fixed α and β values	1	0.0023	0.0855	-0.0015
Calibration and Light-curve modelling						
- HST Calspec (7.5.2)	Calspec 2020 Update	5 mmag/7000Å	3	0.0	0.0	-0.0001
- SALT3 (7.5.3) & ZP	surfaces SALT3 trained on fragilistic best-fit of K21	10 covariance realizations	1/3	0.0114	0.4238	-0.017
- MW scaling (7.5.10)	Schlafly & Finkbeiner (2011)	5% scaling	1	0.0018	0.0669	-0.0003
- MW colour law (7.5.10)	$R_V=3.1$ and F99	$R_V=3.0$ and CCM	1/3	0.0027	0.1004	0.0007
Simulations						
- Survey Modelling ϵ_z^{spec} [X] (7.5.4)	r-band magnitude efficiency	z -based efficiency	1	0.0065	0.2416	-0.0012
- Intrinsic scatter model (7.5.5)	Dust model parameters from Appendix Table 7.2	Separate dust parameters within 1σ				
		Sys 1	$1/\sqrt{3}$	0.001	0.0372	-0.0001
		Sys 2	$1/\sqrt{3}$	0.0016	0.0595	0.0014
		Sys 3	$1/\sqrt{3}$	0.0	0.0	-0.0008
- Core-collapse prior (7.5.6)	SN Vincenzi et al. (2021) CC Templates	Polynomial fit as in Holzek 2012	1	0.0007	0.026	-0.0001

\dagger Shift in w when including when including ONLY this systematic

7.7 Discussion

7.7.1 SDSS Consistency

Of particular interest is the inclusion of SDSS into the nominal sample, given the 1.3σ difference in measured w between PS1+Low- z and SDSS+Low- z . The measurements of w between the nominal sample and PS1 as the sole high-redshift anchor are consistent ($< 1\sigma$), however, there are noteworthy decreases in the statistical and systematic uncertainties when including SDSS. The driver of the observed Δw between SDSS-only high redshift anchor and the nominal case is a 1.9σ change in average observed distance around $z = 0.3$. In this redshift area, there are ~ 100 SDSS SNIa, compared to ~ 300 PS1 SNIa.

This difference is driven by the lack of effective detection efficiency modeling for the supernovae in the SDSS SN sample. The true efficiency is as-of-yet unknown and requires further research - for now, we have assumed a detection efficiency similar to that of the Dark Energy Survey 5-year sample in the shallow fields (Sánchez et al. (2021)). The efficiency we have used is shown in Figure 7.15.

Further improvements in the understanding of the SDSS detection efficiency will further reduce this discrepancy; alternatively, we suggest from Figure 7.11 that the SDSS contribution be truncated at $z = 0.25$ to abrogate the worst of the detection efficiency issues.

7.7.2 Cosmological Parameters

It may have been noticed by this point that I have avoided giving specific cosmological measurements. This is intentional; the Amalgame sample is still actively being developed at the time of writing this thesis, and we are not yet at the point where

it is appropriate to unblind. Nonetheless, there is still information to be drawn from the blinded results given thus far - our systematic uncertainty budget shows that a combined photometric sample is a viable candidate for measuring cosmology, on par with conventional spectroscopic samples.

7.7.3 Comparison of Binned and Unbinned Results

Table 7.4 shows the binned Hubble Residual results for comparison to our nominal unbinned case. Using the unbinned Hubble Diagram results in a reduction of the systematic uncertainty $\sigma_{w,syst}$ by 0.007, or 25%. The w shift of $\Delta w = 0.014$ between the binned and unbinned Hubble Diagrams is on the order of magnitude of the statistical uncertainty, though smaller, indicating no strong bias on recovered cosmological parameters from using the unbinned Hubble Diagrams.

Additionally, we compare a *re*-binned Hubble Diagram, finding an overall systematic uncertainty $\sigma_{w,syst} = 0.019$, similar to the unbinned approach though noticeably higher. The $\Delta w = -0.017$ between the unbinned and rebinned approach is still below the statistical uncertainty threshold, though notably in the opposite direction as the Δw_{binned} .

Chapter 8

Conclusions and Future Work

In this thesis, I have presented two distinct methods of improving cosmological measurements with SNIa. Chapter 4 showed how to infer model parameters for intrinsic scatter models with dust, while Chapter 5 used these parameters, alongside historical intrinsic scatter models, to correct potential biases. Moving forwards, work must be done to combine these processes. Presently, our cosmology pipelines are a combination of forward modeling and ad-hoc bias corrections; future research will ideally combine these approaches into the light curve fitting process itself.

On the other hand, Chapter 6 presented a collection of systematic uncertainties unique to photometrically confirmed samples of SNIa; that is, those samples where spectroscopy of the SNe itself is not taken. The confluence of these two approaches, improved bias corrections and unique photometric systematic uncertainties, is presented in Chapter 7, where I show that a combined photometric sample is competitive with contemporary measurements of the dark energy equation-of-state parameter w . In this summary, we shall return to the questions that were asked at the beginning of the thesis, in Figure 1.2.

8.1 How do we observe the universe?

Distance measurements, and therefore cosmology measurements, with SNIa are done with a light curve fitter. The most common light curve fitter in modern supernova cosmology is SALT, the Spectral Adaptive Light-curve Template. SALT uses an input

sample of photometric and spectroscopic measurements to estimate the spectrum of supernova light curves it is fitting, returning a handful of standardisation parameters that make SNIa the most precise distance measurement tools in cosmology. However, SALT assumes a single dust extinction law for all SNe. This approach marginalises over natural variations in the quantity and size of dust particulates in galaxies.

It is known that dust reddens and dims light due to scattering, and even if we were to disregard the effects of dust entirely, as has been done in the past, we know that there is still some intrinsic population of SNIa parameters that is skewed and smeared by measurement noise and imperfect telescopes.

8.2 How do we simulate the universe?

This begs the question: if we want to recover these intrinsic parameters, or determine the impact of dust on our sample, how do we simulate these effects?

The SuperNova ANalysis program, SNANA, provides a robust and extensive platform for simulating supernova light curves. SNANA starts with the SALT model, using a redshift, distance, and input parent populations to construct a ‘perfect’ SNIa SED. This SED then undergoes cosmological effects and redshifting before it is integrated into filters. Telescope noise and cadence are then applied, before cuts are made based on detection and selection effects.

While the improvements and changes to SNANA I have introduced through the course of my PhD may not be explicitly published, I have introduced a host of now widely-used features that are crucial to the current and next generation of cosmological analysis, such as a built-in host mis-association feature, the ability to correlate SNIa properties with their host galaxy, and a suite of improvements to the host library functionality within SNANA.

The pippin program, which has been referenced before, is a convenient wrapper for the various SNANA functions that comprise the modern cosmology pipeline, and is a great step forwards in terms of a single incorporated cosmology analysis. However, the SALT training, light curve fitting, and bias corrections generation are still conceptually isolated and require a great amount of human hours to assemble, even for re-analysing existing surveys. There is still more work to be done in combining these and granting them more iterative power.

8.3 How are our measurements biased?

Using features of the data and SNANA, particularly the relationship between SNIa colour c and the Hubble Residuals, we are able to infer these dust parameters, alongside select intrinsic SNIa parameters. I introduced this process in Popovic et al. (2021), providing the first robust and moreover, replicable, method to determine dust parameters from SNIa optical data. This code is public, and integrated into SNANA such that it can be used for both past and future surveys. This code has been used not only for Amalgame, but for the Pantheon+ survey and the upcoming DES 5-year photometric survey, making it a crucial part of world-class cosmological analyses three times over.

However, this work is by no means complete. In the interest of time, computational power, and scope, several things I consider important were left on the cutting room floor. The most obvious of these is that dust parameters, and the requisite fitting code Dust2Dust, only describe extrinsic ‘dust’ effects of SNIa light curves. The potential progenitor effects, much less the x_1 parameter, are unmodeled. I find this conceptually disappointing and entirely incomplete. Unfortunately, there currently exists no good model for tying intrinsic progenitor effects into observed x_1 values as

there exists for dust and c ; this obviously presents a large impediment to accurate simultaneous modeling.

Secondly, there is the question of binning. The current approach relies on a binned, uninterpolated interpretation of dust parameters for host galaxies. While this does fit the data better, it is unphysical and unintuitive. I would ideally love to have some smooth, connected analytical description of these parameters that has more of an astrophysical meaning. Alongside this, a more elegant way of propagating the uncertainties to cosmology is desired. Simulating different biasCor to estimate the uncertainties is an effective, but brute force, method. Ideally, I would be able to propagate the parameter uncertainties without ‘redundant’ simulations.

Alongside these new parameter uncertainty propagation, we will need to fix the issue of the assumed cosmology. It is desirable, and with more streamlined simulations, imminently possible, to vary the assumed cosmology of the simulations alongside the dust and SN parameters, permitting more varied and thorough estimates of the impact of cosmology on fitted light curve parameters.

Before dust was reintroduced into the field, I was focused on phenomenological descriptions of intrinsic populations as in Popovic et al. (2021). These intrinsic populations, and their correlation to host parameters, are equally as widespread as their physical dust counterparts.

This phenomenological approach is lightweight, and with the advent of new SALT training methods, has become widely used. It may sound strange to say I have no qualms with its design or implementation, but I feel it’s effective at what it set out to do, and I have been pleasantly surprised by its usage within the community.

8.4 How do we fix these biases?

However, these improvements are only helpful in cosmological measurements if they can be used to reduce systematic biases and uncertainties. Previous bias correction methods were not able to incorporate intrinsic populations that correlate with host galaxy parameters, resulting in significant (upwards of 50%) biases in recovered nuisance parameters. Even worse, dust based scatter models were incompatible with conventional bias corrections methods. To this end, I introduced two new methods of bias corrections in Popovic et al. (2021), BBC7D and BBC4D.

BBC7D expands the previous iteration, BBC5D, from

$$\begin{aligned} \delta\mu_{\text{bias}}(z, x_1, c, \alpha, \beta) &\rightarrow \\ \delta\mu_{\text{bias}}(z, x_1, c, \alpha, \beta, \theta, M_{\text{stellar}}) &. \end{aligned} \tag{8.1}$$

BBC7D was, unfortunately, from its inception out of date. The obvious improvements that dust modeling affords us sounded the death knoll for BBC7D. I don't mind this, however. While it works, the extra two dimensions added exponentially increase the simulation size needed for bias corrections. This works, for now, but would present significant problems for future surveys. This is because as the sample size increases, the volume in $(z, x_1, c, \alpha, \beta, \theta, M_{\text{stellar}})$ phase space it covers also increases, thereby necessitating more simulated events to correct for.

BBC4D, on the other hand, *reduces* the number of dimensions. This has, surprisingly, not been that much of an issue, but BBC4D has been beset by other problems, some of which are self made and others are not. I believe we have, well after the release of the paper, fixed many of the unintended bugs that arose from incorrect assumptions within the BBC code. Things like internally using `SIM beta` without declaration caused many issues in the transition from SED-variational models like

G10 and C11 to dust models.

But other issues lay with BBC4D. This is where it gets complicated - the only blame that can be laid squarely at the feet of BBC4D is that it does not provide meaningful corrections to α or β . The lack of α corrections is certainly a systemic shortcoming, albeit one that does not seem to matter; cosmological and even α biases are very low.

β corrections, or lack thereof, lead us to our next issue. Conceptually, the Dust2Dust process should already provide a corrected β value for BBC4D, such that the β -correcting process is already finished at the simulation stage. In the case of simulations, this works, and we recover the correct β . In the case of data, this does not work. We see a difference in simulation and data β that is larger than the uncertainty, and this leads me to the biggest concern with BBC4D - its reliance on the simulation inputs in the biasCor.

BBC4D works - it recovers input cosmology with the smallest biases of any bias corrections method. But this efficacy does require good agreement between the biasCor and the ‘data’. There are plenty of signs to indicate that we have this with the data - Dust2Dust uncertainties are on the order of 1% for binned covariance matrices, much less for unbinned. Nonetheless, this β discrepancy indicates that there is work to be done on the modeling side, and further progress to be made correcting potential biases.

8.5 What biases inhere in photometric surveys?

Those systematic uncertainties unique to photometric surveys that I focused on in Popovic et al. (2019) - non-Ia contamination, host mis-association, and host galaxy follow-up efficiency - are all remarkably small. Up until recently, non-Ia contamina-

tion was believed to be the largest extant systematic facing cosmology with SNIa. Today, it barely registers among our error budgets.

That is only considering the first order effects, however. Amalgame briefly investigated the impact of non-Ia contamination on training dust model parameters. With a probability cut instituted on the data, this appears to be a non-issue, but it remains an area that requires further research.

Host galaxy mis-association turns out to be a self-solving problem. An incorrect redshift measurement on a SNIa is, from the point of view of a Hubble Diagram, indistinguishable from a non-Ia with the correct redshift. Quality cuts and Chauvenet’s criteria end up removing the worst offenders, minimising the mis-association. However, this similarity between non-Ia contamination and incorrect redshifts could lead to ‘*z*-BEAMS’, a method of fitting for and selecting multiple potential redshifts for a given SNIa.

I find the host galaxy followup efficiency to be the most compelling of the photometric sample uncertainties, and even this one presents an obvious solution. Selecting based on the host galaxy magnitude is far more realistic than a statistical redshift based efficiency, and is therefore preferable. Nonetheless, this ends up being the largest of the systematics presented in Popovic et al. (2019). I think it’s telling that, of those systematics presented in my first paper, only one made it to Amalgame. The rest are, at the moment, solved problems.

8.6 Cosmology

The Sloan Digital Sky Survey is 20 years old. Astronomy is improving around it - superior imaging, subtraction, calibration, depth, and cadence. And yet, alongside PS1 and the low redshift sample, it is able to constrain cosmological parameters equal

to that of the best modern samples. But the Amalgame sample is likely the last of its kind. Our low redshift sample is wholly unequal to the task of the next generation of samples of SNIa: the low- z systematics are too large, and while Foundation fares better, it is too small. Several new low redshift samples are in the works, the Zwicky Transient Facility and Young Supernova Experiment among them. These will lay the groundwork for LSST and Nancy Grace Roman, surveys that will demand even further reductions in systematic uncertainty but will reward them in equal measure.

Bibliography

- Abbott, T. M. C., Allam, S., Andersen, P., et al., 2019, *The Astrophysical Journal Letters*, 872, 2, L30, arXiv:1811.02374
- Alard, C., Lupton, R. H., 1998, *The Astrophysical Journal*, 503, 325, arXiv:astro-ph/9712287
- Amanullah, R., Lidman, C., Rubin, D., et al., 2010, *The Astrophysical Journal*, 716, 712, arXiv:1004.1711
- Baker, S., Cousins, R., 1984, *Nucl. Instrum. Methods Phys. Res.*, 221, A437
- Bautista, J. E., Paviot, R., Vargas Magaña, M., et al., 2021, *The Monthly Notices of the Royal Academy of Science*, 500, 1, 736, arXiv:2007.08993
- Betoule, M., Kessler, R., Guy, J., et al., 2014, *Astronomy and Astrophysics*, 568, A22, arXiv:1401.4064
- Branch, D., Garnavich, P., Matheson, T., et al., 2003, *The Astronomical Journal*, 126, 3, 1489
- Brout, D., Hinton, S. R., Scolnic, D., 2021, *The Astrophysical Journal Letters*, 912, 2, L26, arXiv:2012.05900
- Brout, D., Scolnic, D., 2021, *The Astrophysical Journal*, 909, 1, 26, arXiv:2004.10206
- Brout, D., Scolnic, D., Kessler, R., et al., 2018, arXiv e-prints, arXiv:1811.02377, arXiv:1811.02377
- Brout, D., Scolnic, D., Popovic, B., et al., 2022, *The Astrophysical Journal*, 938, 2, 110, arXiv:2202.04077
- Brout, D., Taylor, G., Scolnic, D., et al., 2021, *The Pantheon+ Analysis: SuperCal-Fragilistic Cross Calibration, Retrained SALT2 Light Curve Model, and Calibration Systematic Uncertainty*, arXiv:2112.03864
- Brout, e., D., 2021, in prep
- Chambers, K. C., Magnier, E. A., Metcalfe, N., et al., 2016, ArXiv e-prints, arXiv:1612.05560
- Childress, M. J., Wolf, C., Zahid, H. J., 2014, *Monthly Notices of the Royal Academy of Science*, 445, 1898, arXiv:1409.2951
- Chotard, N., Gangler, E., Aldering, G., et al., 2011, *Astronomy and Astrophysics*, 529, L4, arXiv:1103.5300

- Conley, A., Guy, J., Sullivan, M., et al., 2011, *Astrophysical Journal Supplement*, 192, 1, arXiv:1104.1443
- Contreras, C., Hamuy, M., Phillips, M. M., et al., 2010, *The Astronomical Journal*, 139, 519, arXiv:0910.3330
- Crocce, M., Castander, F. J., Gaztañaga, E., Fosalba, P., Carretero, J., 2015, *The Monthly Notices of the Royal Academy of Science*, 453, 2, 1513, arXiv:1312.2013
- Dawson, K. S., Schlegel, D. J., Ahn, C. P., et al., 2013, *The Astronomical Journal*, 145, 10, arXiv:1208.0022
- du Mas des Bourboux, H., Rich, J., Font-Ribera, A., et al., 2020, *The Astrophysical Journal*, 901, 2, 153, arXiv:2007.08995
- Eisenstein, D. J., Zehavi, I., Hogg, D. W., et al., 2005, *The Astrophysical Journal*, 633, 560, astro-ph/0501171
- Eldridge, J. J., Maund, J. R., 2016, *Monthly Notices of the Royal Academy of Science*, 461, 1, L117, arXiv:1604.05050
- Filippenko, A. V., Richmond, M. W., Branch, D., et al., 1992, *The Astronomy Journal*, 104, 1543
- Fitzpatrick, E. L., 1999, *Publications of the Astronomical Society of the Pacific*, 111, 63, arXiv:astro-ph/9809387
- Foley, R. J., Challis, P. J., Chornock, R., et al., 2013, *The Astrophysical Journal*, 767, 1, 57, arXiv:1212.2209
- Foley, R. J., Scolnic, D., Rest, A., et al., 2018, *Monthly Notices of the Royal Academy of Science*, 475, 193, arXiv:1711.02474
- Foreman-Mackey, D., Hogg, D. W., Lang, D., Goodman, J., 2013, *Publications of the Astronomical Society of the Pacific*, 125, 925, 306, arXiv:1202.3665
- Fraser, M., 2020, *Royal Society Open Science*, 7, 7, 200467
- Gaskell, C. M., Sparke, L. S., 1986, *The Astrophysical Journal*, 305, 175
- Group, P. D., Zyla, P. A., Barnett, R. M., et al., 2020, *Progress of Theoretical and Experimental Physics*, 2020, 8, ISSN 2050-3911, 083C01, <https://academic.oup.com/ptep/article-pdf/2020/8/083C01/34673722/ptaa104.pdf>
- Guillochon, J., Nicholl, M., Villar, V. A., et al., 2018a, *The Astrophysical Journal Supplement*, 236, 6, arXiv:1710.02145

- Guillochon, J., Nicholl, M., Villar, V. A., et al., 2018b, *The Astrophysical Journal Supplement*, 236, 6, arXiv:1710.02145
- Gupta, R. R., D'Andrea, C. B., Sako, M., et al., 2011, *The Astrophysical Journal*, 740, 92, arXiv:1107.6003
- Gupta, R. R., Kuhlmann, S., Kovacs, E., et al., 2016, *The Astronomical Journal*, 152, 154, arXiv:1604.06138
- Guy, J., Astier, P., Nobili, S., Regnault, N., Pain, R., 2005, in *22nd Texas Symposium on Relativistic Astrophysics*, 368–373
- Guy, J., Sullivan, M., Conley, A., et al., 2010, *Astronomy and Astrophysics*, 523, A7, arXiv:1010.4743
- Hayden, B. T., Gupta, R. R., Garnavich, P. M., Mannucci, F., Nichol, R. C., Sako, M., 2013, *The Astrophysical Journal*, 764, 191, arXiv:1212.4848
- Hicken, M., Challis, P., Jha, S., et al., 2009, *The Astrophysical Journal*, 700, 331, arXiv:0901.4787
- Hicken, M., Challis, P., Kirshner, R. P., et al., 2012, *Astrophysical Journal Supplement*, 200, 12, arXiv:1205.4493
- Hlozek, R., Kunz, M., Bassett, B., et al., 2012, *The Astrophysical Journal*, 752, 79, arXiv:1111.5328
- Holtzman, J. A., Marriner, J., Kessler, R., et al., 2008, *The Astronomical Journal*, 136, 2306, arXiv:0908.4277
- Hubble, E., 1929, *Proceedings of the National Academy of Science*, 15, 3, 168
- Hubble, E., Humason, M. L., 1931, *The Astrophysical Journal*, 74, 43
- Humason, M. L., 1931, *The Astrophysical Journal*, 74, 35
- Jha, S., Kirshner, R. P., Challis, P., et al., 2006, *The Astronomical Journal*, 131, 527, astro-ph/0509234
- Jha, S., Riess, A. G., Kirshner, R. P., 2007, *The Astrophysical Journal*, 659, 122, astro-ph/0612666
- Jha, S. W., 2017a, *Type Iax Supernovae*, 375
- Jha, S. W., 2017b, *Type Iax Supernovae*, 375
- Jones, D. O., Riess, A. G., Scolnic, D. M., et al., 2018a, *The Astrophysical Journal*, 867, 108, arXiv:1805.05911

- Jones, D. O., Scolnic, D. M., Foley, R. J., et al., 2019, *The Astrophysical Journal*, 881, 1, 19, ISSN 1538-4357
- Jones, D. O., Scolnic, D. M., Riess, A. G., et al., 2018b, *The Astrophysical Journal*, 857, 51, arXiv:1710.00846
- Kasen, D., Woosley, S. E., 2007, *The Astrophysical Journal*, 656, 2, 661
- Kelsey, L., Sullivan, M., Smith, M., et al., 2020, arXiv e-prints, arXiv:2008.12101, arXiv:2008.12101
- Kenworthy, W. D., Jones, D. O., Dai, M., et al., 2021, *The Astrophysical Journal*, 923, 2, 265, arXiv:2104.07795
- Kessler, R., Bassett, B., Belov, P., et al., 2010a, *Publications of the Astronomical Society of the Pacific*, 122, 1415, arXiv:1008.1024
- Kessler, R., Bassett, B., Belov, P., et al., 2010b, *Publications of the Astronomical Society of the Pacific*, 122, 1415, arXiv:1008.1024
- Kessler, R., Bernstein, J. P., Cinabro, D., et al., 2009, *Publications of the Astronomical Society of the Pacific*, 121, 1028, arXiv:0908.4280
- Kessler, R., Conley, A., Jha, S., Kuhlmann, S., 2010c, arXiv e-prints, arXiv:1001.5210, arXiv:1001.5210
- Kessler, R., Guy, J., Marriner, J., et al., 2013, *The Astrophysical Journal*, 764, 48, arXiv:1209.2482
- Kessler, R., Narayan, G., Avelino, A., et al., 2019, *Publications of the Astronomical Society of the Pacific*, 131, 1003, 094501, arXiv:1903.11756
- Kessler, R., Scolnic, D., 2017, *The Astrophysical Journal*, 836, 56, arXiv:1610.04677
- Komatsu, E., Dunkley, J., Nolte, M. R., et al., 2009, *Astrophysical Journal Supplement*, 180, 2, 330, arXiv:0803.0547
- Krisciunas, K., Contreras, C., Burns, C. R., et al., 2017, *The Astronomical Journal*, 154, 5, 211, arXiv:1709.05146
- Lampeitl, H., Smith, M., Nichol, R. C., et al., 2010, *The Astrophysical Journal*, 722, 566, arXiv:1005.4687
- Lasker, J., Kessler, R., Scolnic, D., et al., 2019, *Monthly Notices of the Royal Academy of Science*, 485, 4, 5329, arXiv:1811.02380
- Leavitt, H. S., Pickering, E. C., 1912, *Harvard College Observatory Circular*, 173, 1

- Li, T. S., DePoy, D. L., Marshall, J. L., et al., 2016, *The Astronomical Journal*, 151, 157, arXiv:1601.00117
- Li, W., Filippenko, A. V., Chornock, R., et al., 2003, *Publications of the Astronomical Society of the Pacific*, 115, 806, 453, arXiv:astro-ph/0301428
- Magee, M. R., Kotak, R., Sim, S. A., et al., 2016, *Astronomy and Astrophysics*, 589, A89, arXiv:1603.04728
- Mandel, K. S., Scolnic, D. M., Shariff, H., Foley, R. J., Kirshner, R. P., 2017, *The Astrophysical Journal*, 842, 93, arXiv:1609.04470
- Marriner, J., Bernstein, J. P., Kessler, R., et al., 2011, *The Astrophysical Journal*, 740, 72, arXiv:1107.4631
- Martin, J., 2012, *Comptes Rendus Physique*, 13, 6-7, 566, arXiv:1205.3365
- Modelers, P., 2019, *Libraries & Recommended Citations for using PLAsTiCC Models*
- Möller, A., de Boissière, T., 2019, arXiv e-prints, arXiv:1901.06384, arXiv:1901.06384
- Perlmutter, S., Aldering, G., Goldhaber, G., et al., 1999, *The Astrophysical Journal*, 517, 565, astro-ph/9812133
- Perrett, K., Sullivan, M., Conley, A., et al., 2012, *The Astronomical Journal*, 144, 2, 59, arXiv:1206.0665
- Phillips, M. M., 1993, *The Astrophysical Journal Letters*, 413, L105
- Pierel, J. D. R., Rodney, S., Avelino, A., et al., 2018a, *Publications of the Astronomical Society of the Pacific*, 130, 11, 114504, arXiv:1808.02534
- Pierel, J. D. R., Rodney, S., Avelino, A., et al., 2018b, *Publications of the Astronomical Society of the Pacific*, 130, 11, 114504, arXiv:1808.02534
- Planck Collaboration, Ade, P. A. R., Aghanim, N., et al., 2016, *Astronomy and Astrophysics*, 594, A14, arXiv:1502.01590
- Planck Collaboration, Aghanim, N., Akrami, Y., et al., 2020, *Astronomy and Astrophysics*, 641, A6, arXiv:1807.06209
- Popovic, B., Brout, D., Kessler, R., Scolnic, D., 2021, arXiv e-prints, arXiv:2112.04456, arXiv:2112.04456
- Popovic, B., Brout, D., Kessler, R., Scolnic, D., Lu, L., 2021, 913, 1, 49

- Popovic, B., Scolnic, D., Kessler, R., 2019, arXiv e-prints, arXiv:1910.05228, arXiv:1910.05228
- Riess, A. G., Filippenko, A. V., Challis, P., et al., 1998, *The Astronomical Journal*, 116, 1009, astro-ph/9805201
- Riess, A. G., Kirshner, R. P., Schmidt, B. P., et al., 1999, *The Astronomical Journal*, 117, 707, astro-ph/9810291
- Riess, A. G., Press, W. H., Kirshner, R. P., 1996, *The Astrophysical Journal*, 473, 88, arXiv:astro-ph/9604143
- Sako, M., Bassett, B., Becker, A., et al., 2008, *The Astronomical Journal*, 135, 348, arXiv:0708.2750
- Sako, M., Bassett, B., Becker, A. C., et al., 2018, *Publications of the Astronomical Society of the Pacific*, 130, 064002, arXiv:1401.3317
- Sánchez, B., Kessler, R., Scolnic, D., et al., 2021, arXiv e-prints, arXiv:2111.06858, arXiv:2111.06858
- Schlafly, E. F., Finkbeiner, D. P., 2011, *The Astrophysical Journal*, 737, 103, arXiv:1012.4804
- Schlafly, E. F., Meisner, A. M., Stutz, A. M., et al., 2016, *Astrophysical Journal*, 821, 2, 78, arXiv:1602.03928
- Scolnic, D., Brout, D., Carr, A., et al., 2022, *The Astrophysical Journal*, 938, 2, 113, arXiv:2112.03863
- Scolnic, D., Kessler, R., 2016, *The Astrophysical Journal Letters*, 822, L35, arXiv:1603.01559
- Scolnic, D., Kessler, R., Brout, D., et al., 2018, *The Astrophysical Journal Letters*, 852, L3, arXiv:1710.05845
- Scolnic, D. M., Riess, A. G., Foley, R. J., et al., 2014, *The Astrophysical Journal*, 780, 37, arXiv:1306.4050
- Slipher, V., 1917, *Proceedings of the American Philosophical Society*, 56, 403
- Smith, M., Bacon, D. J., Nichol, R. C., et al., 2014, *The Astrophysical Journal*, 780, 24, arXiv:1307.2566
- Smith, M., Sullivan, M., Wiseman, P., et al., 2020, arXiv e-prints, arXiv:2001.11294, arXiv:2001.11294
- Smoot, G., Bennett, C., Weber, R., et al., 1990, *The Astrophysical Journal*, 360, 685

- Stoughton, C., Lupton, R. H., Bernardi, M., et al., 2002, *The Astronomical Journal*, 123, 485
- Stritzinger, M. D., Phillips, M. M., Boldt, L. N., et al., 2011, *The Astronomical Journal*, 142, 156, arXiv:1108.3108
- Stritzinger, M. D., Valenti, S., Hoefflich, P., et al., 2015, *Astronomy and Astrophysics*, 573, A2, arXiv:1408.1093
- Sullivan, M., Conley, A., Howell, D. A., et al., 2010, *Monthly Notices of the Royal Academy of Science*, 406, 782, arXiv:1003.5119
- Sullivan, M., Guy, J., Conley, A., et al., 2011, *The Astrophysical Journal*, 737, 102, arXiv:1104.1444
- Sullivan, M., Le Borgne, D., Pritchet, C. J., et al., 2006, *The Astrophysical Journal*, 648, 2, 868, arXiv:astro-ph/0605455
- Taylor, E. N., Hopkins, A. M., Baldry, I. K., et al., 2011, *Monthly Notices of the Royal Academy of Science*, 418, 1587, arXiv:1108.0635
- Taylor, G., Lidman, C., Tucker, B. E., Brout, D., Hinton, S. R., Kessler, R., 2021, *Monthly Notices of the Royal Academy of Science*, 504, 3, 4111, arXiv:2104.00172
- Tripp, R., 1998, *Astronomy and Astrophysics*, 331, 815
- Villar, V. A., Berger, E., Metzger, B. D., Guillochon, J., 2017a, *apj*, 849, 70, arXiv:1707.08132
- Villar, V. A., Berger, E., Metzger, B. D., Guillochon, J., 2017b, *apj*, 849, 70, arXiv:1707.08132
- Vincenzi, M., Sullivan, M., Firth, R. E., et al., 2019a, *The Monthly Notices of the Royal Academy of Science*, 489, 4, 5802, arXiv:1908.05228
- Vincenzi, M., Sullivan, M., Firth, R. E., et al., 2019b, *The Monthly Notices of the Royal Academy of Sciences*, 489, 4, 5802, arXiv:1908.05228
- Vincenzi, M., Sullivan, M., Graur, O., et al., 2021, *Monthly Notices of the Royal Academy of Science*, 505, 2, 2819, arXiv:2012.07180
- Wolf, R. C., D'Andrea, C. B., Gupta, R. R., et al., 2016, *The Astrophysical Journal*, 821, 115, arXiv:1602.02674